NONEQUILIBRIUM RADIATION AND CHEMISTRY MODELS FOR AEROCAPTURE VEHICLE FLOWFIELDS

Volume I

AEROSPACE ENGINEERING DEPARTMENT

Semiannual Progress Report
July 1990 -- December 1990

TEXAS A&M UNIVERSITY

TAMRF Report No. 6382-91-01-(I)

February 1991

(NASA-CR-188196) NONEQUILIBRIUM RADIATION AND CHEMISTRY MODELS FOR AEROCAPTURE VEHICLE FLOWFIELDS, VOLUME 1 Semiannual Progress Report, Jul. - Dec. 1990 (Texas A&M Univ.) 165 p
N91-24100
Unclas
CSCL 01A G3/02 0012584

NASA Grant No. NAG-1-1003

Leland A. Carlson
Professor of Aerospace Engineering
Texas A&M University
College Station, TX 77843-3141

TEXAS ENGINEERING EXPERIMENT STATION

NONEQUILIBRIUM RADIATION AND CHEMISTRY MODELS FOR AEROCAPTURE VEHICLE FLOWFIELDS

Volume I

Semiannual Progress Report

July 1990 -- December 1990

TAMRF Report No. 6382-91-01-(I)

February 1991

NASA Grant No. NAG-1-1003

Leland A. Carlson
Professor of Aerospace Engineering
Texas A&M University
College Station, TX 77843-3141

NONEQUILIBRIUM RADIATION AND CHEMISTRY MODELS FOR AEROCAPTURE VEHICLE FLOWFIELDS

I. Introduction

This report covers approximately the period July 1990 thru December 1990. The primary tasks during this period have been the study of nonequilibrium chemical and radiation models and coupling, the evaluation of various electron-electronic energy models, the continued development of improved nonequilibrium radiation models for molecules and atoms, the development of precursor models and investigation of precursor phenomena, and the development of vibrational nonequilibrium models.

II. Personnel

The staff associated with this project during the present reporting period have been Dr. Leland A. Carlson, Principal Investigator, and Thomas A. Gally, Scott Stanley, and Derek Green, Graduate Research Assistants. It should be noted that Mr. Gally is currently supported by a NASA Graduate Student Researchers Fellowship from NASA Johnson Space Center and will use the results of his research on this project in his Ph.D. dissertation. His research is primarily in the areas of nonequilibrium chemical and radiation models, electron-electronic energy models, and the development of the radiation coupled nonequilibrium viscous shock layer code. Mr. Stanley, who was supported by this project, used the results of his research into precursor phenomena for his masters' thesis and graduated in December 1990. Mr. Green was supported by the department during this reporting period and has been developing vibrational nonequilibrium models for the VSL code. Beginning January 1, 1991 he will be supported by the project. In addition, an additional departmentally supported graduate student,

Rajeev Koteshwar, is conducting masters' research on flowfields involving carbon species; and it is anticipated that portions of his work will have applications to the present project.

III. Nonequilibrium Chemical and Radiation Models and Coupling Phenomena

Most of the effort conducted in this area during the present reporting period is summarized in detail in AIAA Paper 91-0569. This paper was presented in January at the AIAA 29th Aerospace Sciences Meeting and a copy is included in this report in Appendix I. Briefly the work has involved the development of detailed nonequilibrium radiation models for molecules along with appropriate models for atoms, the inclusion of nongray radiation gasdynamic coupling in the VSL code, the development and evaluation of various electron-electronic energy models, and an examination of the effects of shock slip.

As a result an engineering flowfield model suitable for analyzing the stagnation region of high altitude entry vehicles having extensive nonequilibrium has been developed. This model includes nonequilibrium chemistry, multi-temperature, viscous conduction, and diffusion effects. It also, as indicated, includes coupled nongray radiative transfer in a form that contains the effect of local thermodynamic nonequilibrium phenomena resulting from chemical and thermal nonequilibrium on the emission and absorption characteristics of atoms and molecules. The boundary conditions include multi-temperature shock slip and a partially catalytic wall having frequency dependent radiative properties. After comparing with flight data from five Fire 2 trajectory points, which verified that the model has the correct behavior and is reasonably accurate, it has been applied to a variety of cases including two AFE

trajectory points, a condition representative of high speed return from Mars of a small vehicle, a series of points at 80 km for velocities 12 to 16 km/sec, and a study of the effects of altitude at 16 km/sec.

These studies have shown the following:

(1) Shock slip phenomena is important at all conditions investigated.

(2) Radiation cooling/coupling is important for many cases. Specifically,

(a) It is measureable even in the early portions of the Fire 2 trajectory.

(b) It is minor effect for the AFE conditions investigated.

(c) At 80 km, it is small at 12 km/sec, important by 14 km/sec, and the dominant phenomena at 16 km/sec at all altitudes.

(d) It is very important for the high speed Mars return case.

(3) Radiation heat transfer should be included and varies as to source. Specifically,

(a) In the early stages of the Fire 2 entry, the radiative transfer is primarily molecular and infrared lines. Later, atomic VUV continuum and line radiation becomes very important.

(b) For the AFE, radiation, while small, is imporant and primarily molecular. It is probably mostly $N_2^+(1-)$.

(c) At 12 km/sec and above radiation is a significant portion of the total heating and is primarily due to atomic processes. By 14 km/sec it is dominant.

(4) Local thermodynamic nonequilibrium (LTNE) is important and should be included in all models. In addition,

(a) LTNE depopulates the excited states of atoms and N_2 molecules in the post-shock nonequilibrium region.

(b) LTNE can lead to an overpopulation of excited states in regions of radiative cooling and in the wall thermal layer.

(c) $N_2^+(1-)$ is relatively unaffected by LTNE.

(d) The importance of LTNE is independent of radiative coupling.

(e) The inclusion of LTNE reduces the magnitude of radiation cooling effects.

Again, details are presented in Appendix I.

In addition, during this reporting period work has continued on the development of the second order nonequilibrium atomic radiation model discussed in the last progress report. Instead of assuming that the excited states of atoms are in equilibrium with the free electrons and ions, this improved model uses finite rates to actually determine the population of a pseudo-excited species. In this model, all of the excited states are represented as a single species, N^*, and work is in progress to determine the appropriate reaction rates associated with the population and depopulation of such excited states. As a first effort, only collisional mechanisms are being considered.

In Figure 1 some very preliminary results obtained using this second order nonequilibrium atomic radiation model approach in conjunctrion with the nonequilibrium molecular model are presented. The flowfield conditions and boundary conditions for this stagnation line case are 14 km/sec at 80 km with R_{nose} = 2.3 m. These results were

obtained using the full electron-electronic equation model, and thus they can be compared to those on Fig. 12 of AIAA 91-0569, which were obtained using the first order nonequilibrium atomic radiation model. Examination of these preliminary data indicates that compared to those obtained with the first order model, the post shock chemical nonequilibrium region is smaller and the electron temperature peak is slightly closer to the shock front at a slightly lower value. Also, the outer twenty-five percent and inner ten percent of the stangation region is in local thermodynamic nonequilibrium in that the N^* population is not that predicted by a Boltzmann distribution. Further, unlike the first order model, the new excitation rate is sufficiently fast to maintain local thermodynamic equilibrium in the interior of the flowfield, even with extensive radiative cooling and coupling. In fact the new rates, which are very preliminary at this point, lead to higher radiative cooling in the outer portions of the shock layer. The subsequent effect is to cool the shock layer, which leads to slightly lower wall radiative heating predictions than those obtained with the first order model (See AIAA 91-0569).

Again it is emphasized that the results on Figure 1 are very preliminary; and definite conclusions should not be inferred at this point.

IV. Precursor Studies

During the past six months, the initial research into shock wave precursors and their subsequent affect on the nonequilibrium shock layer around AOTV type vehicles has been completed. The theory and primary results of this effort are presented in detail in the masters' thesis of Scott Stanley, which comprises Volume II of this report. In

addition, a user's manual for the precursor has been written; and it is included as Volume III of this report.

As discussed in previous progress reports, this initial precursor study only included precursor effects resulting from photoprocesses involving continuum absorption phenomena and neglected in the pre-shock region collisional chemistry and atomic line absorption. However, in the treatment of the shock layer, radiative gasdynamic coupling and cooling and local thermodynamic nonequilibrium atomic line and continuum as well as LTE molecular processes were included in the radiation analysis. Also, in the shock layer multi-temperature effects were included by using the quasi-equilibrium electron energy model (QEE). However, in the precursor, because of the sensitivity to electron and electronic energy, a full electron-electronic energy model was utilized. In all cases, the vehicle was considered to have a nose radius of 2.3 m; and the freestream was assumed to be nitrogen.

In Volume II detailed results are presented for the precursor and the shock layer for the vehicle at 16 km/sec at an altitude of 72 km since at this condition the magnitude of the precursor effects was the largest of the cases investigated. In addition, parametric studies are presented for the precursor at 72, 75, and 80 km at 16km/sec and for velocities of 12, 14, and 16 km/sec at 80 km. While not presented in Volume II, many other cases were investigated; and these are summarized in a series of miscellaneous figures included in this volume in Appendix II.

An attempt was also made to compare results obtained with the present model with experimental data measured by Omura and Presley[1], who, using a shock tube having an initial pressure of 0.2 torr, measured electron densities in

front of a 11.89 km/sec shock wave in nitrogen. Since the present model is for the stagnation region of a blunt body, a direct comparison with an incident normal shock could not be made. Consequently, two approaches were tried. The first attempted to simulate the Omura and Presley case using binary scaling, assuming that the corresponding nose diameter for the shock tube case was 30.48 cm (1 foot). This value was selected since it would give the correct area of the radiating shock layer. The conditions for this case were U_{inf} = 11.89 km/sec, T_{inf} = 300 ^{o}K, p_{inf} = 38.61 dynes/cm^2, and R_{nose} = 210 cm. The second case used Omura and Presley's freestream conditions "directly" and assumed R_{nose} to be 15.24 cm (6 in.). Unfortunately, neither of these approaches is a true simulation since actually the radiating shock layer should be the same thickness as the slug of shock tube gas between the shock front and the contact surface. However, the latter dimension was unknown.

Results obtained using the present precursor model by these two approaches are shown on Figure 2. Interestingly the predictions using binary scaling and that using the actual Omura and Presley conditions yield virtually identical nondimensional results, which indicates that for these conditions precursor phenomena appear to scale binarly. However, what is even more surprising is that the prediction for the electron densities in the region immediately in front of the bow shock are in reasonable agreement with those measured immediately in front of the incident shock wave in the shock tube. Also, far away from the shock front, the present predictions are below the measured values of Omura and Presley. This behavior would be expected since in the shock tube wall reflection would increase the radiation intensity, and thus the photoionization, to values above those expected for a similar sized flight vehicle. While the results presented

in Figure 2 do not verify the present model and program because the simulation is not "perfect", they do indicate that it has the correct phenomenological behavior and that its predictions as to magnitudes are reasonable.

In summary, the precursor studies of this project have developed a method to calculate the chemical and thermal nonequilibrium precursor flowfield resulting from continuum radiative absorption processes in the pre-shock region. In particular, a model which properly includes photoprocesses in the electron-electronic energy formulation has been developed; and a similar approach could be used to include these processes in the shock layer model. In addition, it has been shown that precursor effects in front of the shock wave significantly change the pre-shock electron temperature and induce significant ionization. However, a series of detailed parametric tests indicate that these effects, while significant, have negligible effect on the shock layer and the radiative flux to the body.

In examining these results and conclusions, it should be noted that they are for a nitrogen freestream only and do not include in the precursor region line absorption by atoms or collisional chemistry effects. While the latter two phenomena probably tend to have counteracting effects, the absorption of radiation by oxygen in an air precursor could be significant. Nevertheless, the results of this study indicate that precursor phenomena, while interesting and significant, have little effect on the actual shock layer chemistry, flow properties, or radiative transfer.

V. Vibrational Nonequilibrium Studies

During the past six months, an effort has been initiated to develop for inclusion in the nonequilibrium radiating viscous shock layer code a vibrational

nonequilibrium model, which would convert the present code from a two-temperature to a three-temperature approach. While it is eventually planned to also include as an option the Park $(T*T_{vib})^{0.5}$ model, the present effort has concentrated on the MCVDV model[2]. This approach retains the CVDV vibration dissociation model of Treanor and Marrone[3], but it has been appropriately modified to include the vibrational translational relaxation cutoff time and diffusive nature coefficient suggested by Park[4]. In addition, the present model also includes electron-vibrational coupling in both the vibrational energy model and in the electron-electronic model. It should be noted that in the present formulation, unlike the original CVDV and MCVD models which utilized separate vibrational temperatures for each species, the present model utilizes a vibrational temperature which is representative of the total energy of all vibrating species. In other words, like Park[4] and Gnoffo[5], only a single vibrational temperature is utilized.

Quite obviously, in all current vibrational models there are several terms, such as the relaxation time cutoff, diffusive factor form, electron-vibration coupling term, etc. which are to a great extent empirical or which contain empirical coefficients. Thus, as part of the present effort, the code is being formulated so that these various terms can be included or excluded at the user's option. In this way the effect and importance of these terms can be investigated.

Figures 3 shows some very preliminary results obtained using the three temperature model at one of the CFD points associated with the AFE. This condition is of interest because it is in a flight regime where vibrational nonequilibrium phenomena should be important. The present

results are for a nitrogen freestream, include shock slip, assume a Lewis number of 1.4, and are similar to that on Fig. 7 in AIAA 91-0569. While the method is still under development and being debugged, these results show significant three temperature nonequilibrium in the chemical nonequilibrium zone behind the shock front with, due to vibration-dissociation coupling, a consequent decrease in the rate of dissociation.

In addition, and perhaps somewhat suprisingly, they also indicate thermal nonequilibrium in the thermal boundary layer near the wall. Examination of the results indicate that this thermal nonequilibrium is due to diffusion of cooler vibrating molecules away from the wall, which lowers the average T_{vib} below T_{tran}. Then strong electron-vibrational coupling leads to a lowering of the electron-electronic temperature below the translational values. This strong influence of diffusional phenomena is one of reasons it is planned to examine diffusion modeling during the next reporting period.

VI. Publications

In January 1991, AIAA Paper 91-0569, "Nonequilibrium Chemical and Radiation Coupling Phenomena in AOTV Flowfields", was presented by L. A. Carlson and T. A. Gally. A copy of this paper is included in this report as Appendix I.

In addition, abstracts of two proposed papers were submitted to the 22nd AIAA Fluid Dynamics and Plasma Dynamics Conference to held in June 1991. The first, by Thomas A. Gally and L. A. Carlson is entitled "A Flowfield Coupled Excitation and Radiation Model for Nonequilibrium Reacting Flows"; and second is "The Effects of Shock Wave Precursors Ahead of Hypersonic Entry Vehicles" by Scott A. Stanley and L. A. Carlson. Both of these papers have been

accepted for presentation, and copies of the abstracts are included as Appendices III and IV.

Finally, based upon information from the AIAA, the paper "The Effect of Electron Temperature and Impact Ionization on Martian Return AOTV Flowfields" by Carlson and Gally should appear in the January 1991 issue of the Journal of Thermophysics and Heat Transfer.

VII. Future Efforts

During the next reporting period it is planned to continue the development of the nonequilibrium radiating reacting shock layer model. Particular emphasis will be placed on the development and refinement of the second order atomic nonequilibrium radiation model and on the inclusion of vibrational nonequilibrium effects. It is planned to include not only the MCVDV type of model but also a Park type model and to compare the two approaches.

As mentioned above, there have been many instances in the cases investigated to date in which diffusion phenomena have strongly influenced the result. Unfortunately, most of the current multicomponent diffusion models have various limitations. For example, the Moss[6] model in its presented form does not explicitly account for multiple temperatures and is complicated; while the model used by Gnoffo[5], which includes multi-temperature phenomena, is only "exact" if the diffusing species is a trace species[7]. Likewise the model in the present code, while implicitly accouting for multi-temperature effects only via the species concentrations, is highly approximate in its use of a single constant Lewis number.

Consequently, during the next reporting period it is planned to examine diffusion models and perhaps to

incorporate an improved multi-component multi-temperature model into the shock layer code. It is anticipated that this model will still utilize the ambipolar concept and assume that electrons and ions diffuse together.

Finally, it is hoped that during the next reporting period the present studies will be extended to include a portion of the forward face of a vehicle. Also, initial efforts to model air as well as nitrogen will be conducted.

VIII. References

1. Omura, M. and Presley, L. L., "Electron Density Measurements Ahead of Shock Waves in Air", AIAA Journal, Vol. 7, No. 12, Dec. 1969, pp. 2363-2365.

2. Carlson, L. A., Bobskill, G. J., and Greendyke, "Comparison of Vibration-Dissociation Coupling and Radiative Transfer Models for AOTV/AFE Flowfields," Journal of Thermophysics and Heat Transfer, Vol. 4, No. 1, January 1990, pp. 16-26.

3. Marrone, P. V., "Inviscid, Nonequilibrium Flow Behind Bow and Normal Shock Waves, Part I. General Analysis and Numerical Examples," Report No. QM-1626-A-12(I), Cornell Aeronautical Lab., Inc., May 1963.

4. Park C., "Assessment of Two-Temperature Kinetic Model for Ionizing Air," AIAA Paper 87-1574, June 1987.

5. Gnoffo, P. A., Gupta, R. N., and Shinn, J. L., "Conservation Equations and Physical Models for Hypersonic Air Flows in Thermal and Chemical Nonequilibrium," NASA TP 2867, Feb. 1989.

6. Moss, J. N., "Reacting Viscous Shock Layer Solutions with Multicomponent Diffusion and Mass Injection," NASA TR-R-411, June 1974.

7. Curtiss, C. F. and Hirschfelder, J. O., "Transport Properties of Multi-Component Gas Mixture," Journal of Chemical Physics, Vol. 17, No. 6, June 1949, pp. 550-555.

IX. Technical Monitor

The NASA technical monitor for this grant is Lin C. Hartung, Aerothermodynamics Branch, Space Systems Division, NASA Langley Research, Center, Hampton, Virgina

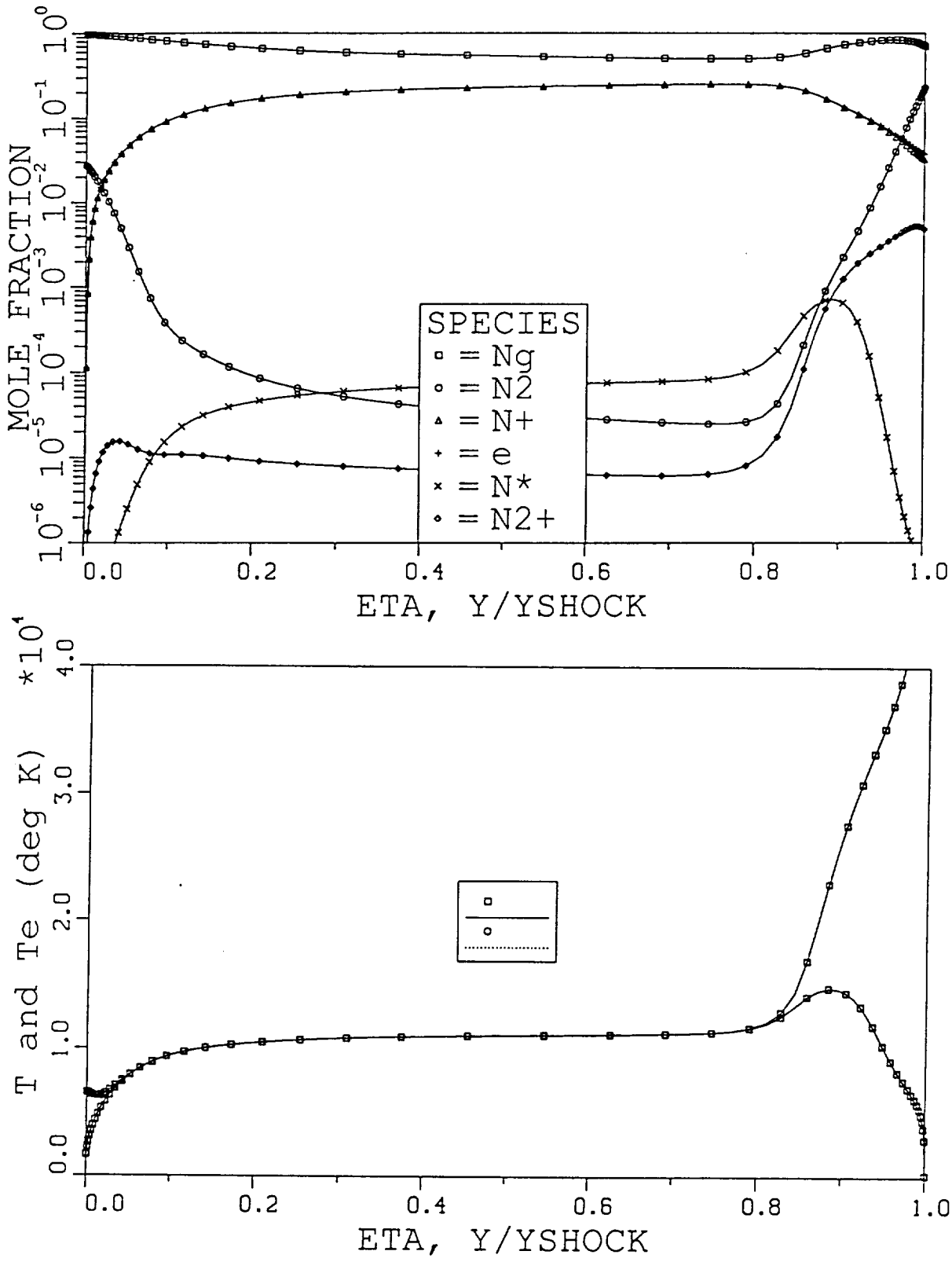

Fig. 1 -- Stagnation Profiles Using Second Order Nonequilibrium Atomic Radiation Model
U=14 km/sec, H = 80 km, R_{nose}= 2.3 m
QR = 105.6 watts/cm^2, QC = 60.3 watts/cm^2, Y_{shock} = 8.82 cm

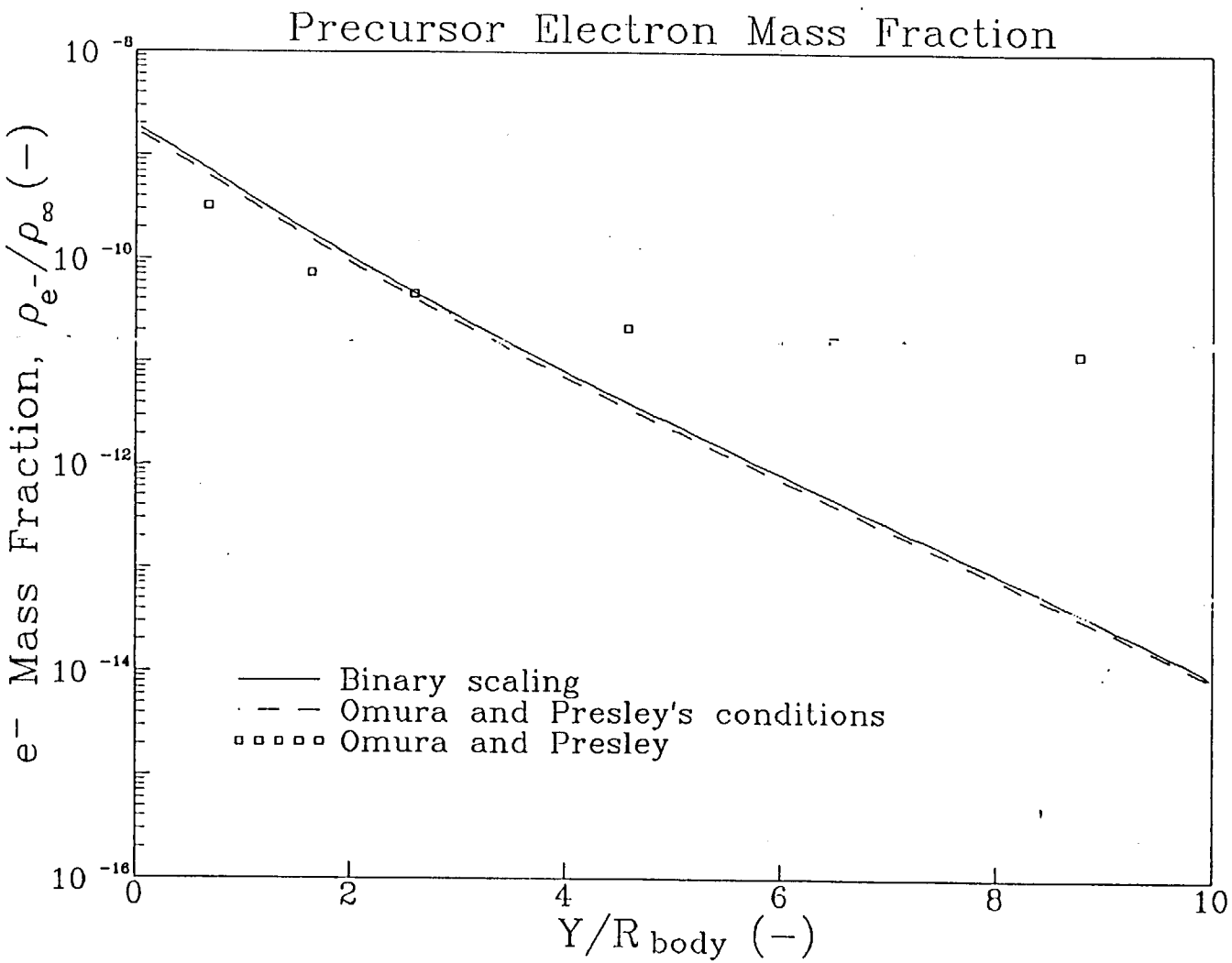

Fig. 2 -- Comparison of Present Precursor Predictions with Those Measured by Omura and Presley

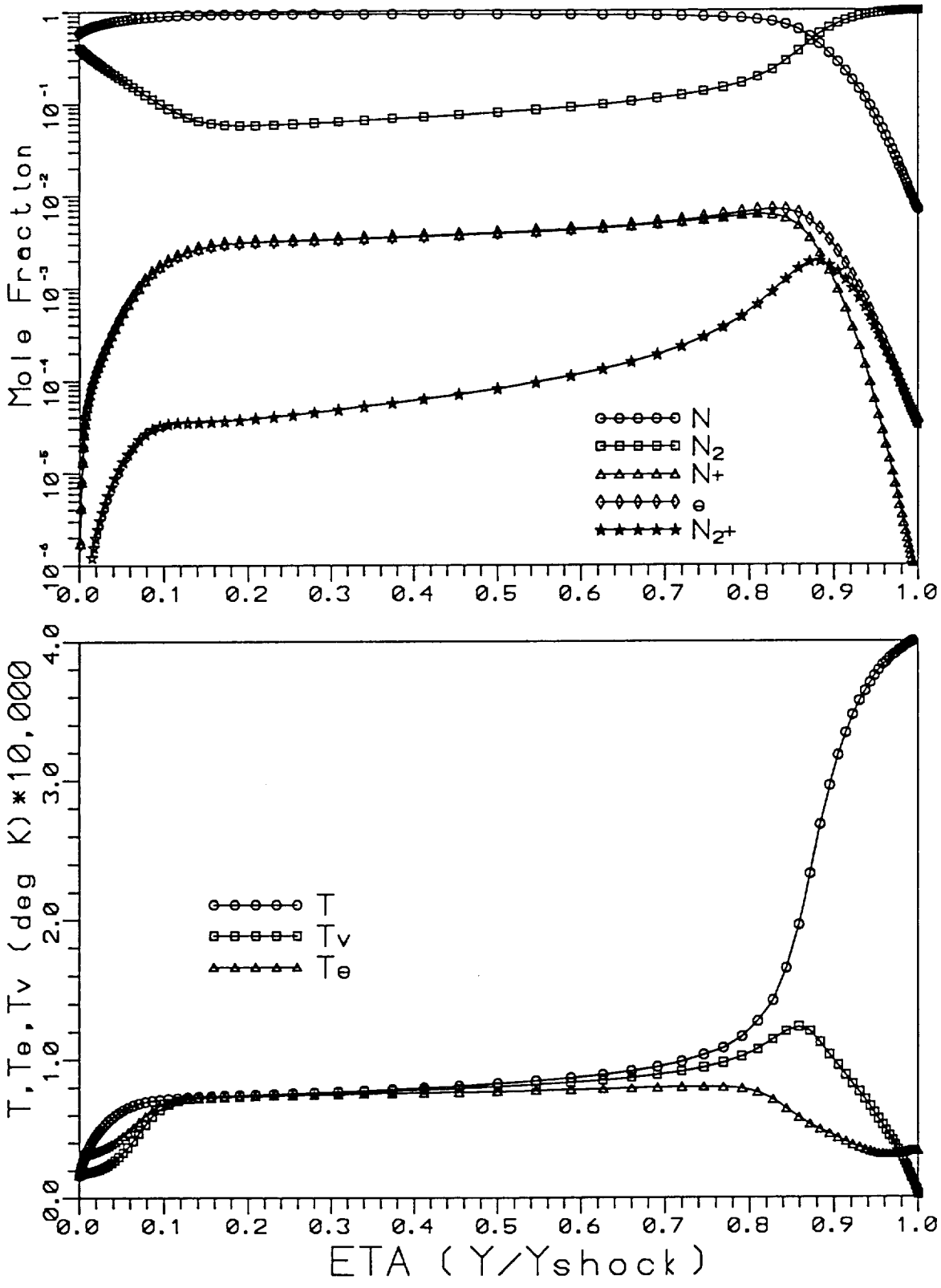

Fig. 3 -- Preliminary Vibrational Nonequilibrium Results for AFE CFD Point 4 with QEEE and MCVDV Models
9.326 kmn/sec, H = 75.2 km, Y_{shock} = 13.6 cm

APPENDIX I

AIAA Paper 91-0569

Nonequilibrium Chemical and Radiation Coupling Phenomena in AOTV Flowfields

AIAA 91-0569

Nonequilibrium Chemical and Radiation Coupling Phenomena in AOTV Flowfields

L. A. Carlson and T. A. Gally
Texas A&M University
College Station, TX

29th Aerospace Sciences Meeting
January 7–10, 1991/Reno, Nevada

r permission to copy or republish, contact the American Institute of Aeronautics and Astronautics
0 L'Enfant Promenade, S.W., Washington, D.C. 20024

Nonequilibrium Chemical and Radiation Coupling Phenomena in AOTV Flowfields

Leland A. Carlson*
and
Thomas A. Gally**
Texas A&M University
College Station, Texas

Abstract

A flowfield model for the nonequilibrium stagnation region of high altitude entry vehicles which includes nonequilibrium chemistry, multi-temperature, viscous, conduction, and diffusion effects is presented. It contains coupled nongray nonequilbrium radiative transfer for atoms and molecules and local thermodynamic nonequilibrium phenomena. Comparison with Fire 2 flight data verifies that the model is reasonably accurate; and it has been applied to two AFE trajectory points, a high speed return from Mars, a series of points at 80 km for 12 to 16 km/sec, and three altitudes at 16 km/sec. Based on these results shock slip is significant, radiation cooling/coupling is minor at AFE conditions but important by 14 km/sec and dominant at 16 km/sec, radiation for the AFE is small but important and primarily molecular, above 12 km/sec atomic radiation is a significant or dominant portion of the total heating, and local thermodynamic nonequilibrium is important and should be included in all models.

Nomenclature

c_e = mean thermal velocity of electrons
c_p = specific heat at constant pressure
E = ionization potential
h = enthalpy
k = Boltzmann constant
m = mass
N = number density
n, s, ϕ = coordinate axis
p = pressure
Q = rate of inelastic energy exchange
T = Temperature
u, v, w = mass averaged velocity components
U = diffusional velocity
y_s = shock standoff distance
$\mathcal{D}$ = binary diffusion coefficient
ϵ = Reynolds number parameter
e = magnitude of electron charge
η = heat conduction coefficient
ξ_e = rate of elastic electron energy exchage
ρ = density
Φ = wall sheath electric potential

subscripts
e = electron
eI = electron impact reaction
r = species
s = value behind shock

superscripts
e = electronic
$n, n+1$ = iteration step
tr = translational

Introduction

In the future, various space programs will be conducted which will require the efficient return of large payloads from missions to the moon or to planets such as Mars. To accomplish this task, the return vehicles will either utilize direct entry at very high velocities or aerocapture techniques. In either case, a significant portion of the entry will involve high velocities at high altitudes; and, during this part of the trajectory, the vehicle flowfields will be dominated by chemical, thermal, and radiative nonequilibrium phenomena. To design and operate such vehicles, it is essential to develop engineering flowfield models which appropriately and accurately describe these chemical, thermal, and radiative nonequilibrium processes and the coupling between them.

Previously[1], the importance of properly predicting electron temperature and modeling electron impact ionization was investigated and a quasi-equilibrium free electron energy model and a two step ionization model formulated. In addition, an approximate method of handling nonequilibrium atomic radiation, which assumed that the excited states of atoms are in equilibrium with the local free electrons and ions, was developed[1-3] and applied to an eight step nongray emission-absorption radiation model. While the results obtained with these models were informative, the lack of detail in the radiation model, particularly with respect to atomic lines and the bands associated with molecular ions, and the highly approximate nature of the nonequilibrium molecular radiation portion of the model, which for some molecular bands appeared to underestimate the actual radiation, indicated a need for improvement. Further, while the quasi-equilibrium free electron energy model and its associated assumption that the electronic temperature was determined solely by the free electron temperature should be a good approximation for many conditions of interest in aerocapture and entry, it was felt that additional models should be developed in an effort to improve the modeling of electron energy, and hence temperature, due to its importance in determining nonequilbirum ionization chemistry and radiative transfer.

* Professor Aerospace Engineering, Associate Fellow AIAA
** NASA Graduate Student Researcher, Student Memeber AIAA
Copyright ©1991 by the American Institute of Aeronautics and Astronautics, Inc. All rights reserved.

closely predicted by a Boltzmann distribution. Likewise $N_2(1+)$ typically displays only a slight correction (from unity) for the source function but a significant decrease from that predicted using Boltmann distributions in the absorption coefficient. This trend is also "expected" since $N_2(1+)$ involves two excited states, B and A. On the other hand, while the absorption coefficient factor for $N_2(2+)$ is similar to that for $N_2(1+)$, the source function for $N_2(2+)$ is typically significantly reduced in the chemical and thermal nonequilibrium region behind the shock front, indicating that pre-dissociation is significantly depleting the population of the C electronic state.

The most interesting result, however, is that the $N_2^+(1-)$ radiation is usually only slightly affected by nonequilibrium phenomena. This result is in agreement with experiments which, at least at lower velocities, have indicated a strong $N_2^+(1-)$ contribution. However, since the number density of N_2^+ is often only significant in the region immediately behind the shock front, any $N_2^+(1-)$ radiation should originate from that region. This feature will be discussed further in the results section.

Another interesting phenomena associated with the molecular nonequilibrium radiation is that often in the thermal boundary layer near the wall, several of the factors accounting for LTNE exceed unity and become large. This behavior indicates an overpopulation of excited states above values which would be predicted by a Boltzmann distribution when intuitively an equilibrium distribution might be expected due to the increased density near the wall. However, the thermal boundary layer is often in significant nonequilibrium since the chemical reaction rates are finite and cannot keep up with the true local equilibrium, which leads to atom and sometimes ion concentrations above local equilibrium. In addition, diffusion tends to perturb the species population densities and leads to atom and ion densities above equilibrium values, which in turn creates enhanced molecular excited state populations. This enhancement, however, does not lead to increased radiative emission near the wall; and in fact, probably due to the lower electron-electronic temperature in that region, it does not, for the cases examined, appear to affect the radiative heat transfer. Thus, in the present studies limitations on the molecular nonequilibrium correction factors have not been imposed.

Nonequilibrium Atomic Radiation Model

Local thermodynamic nonequilibrium effects (LTNE) on atomic radiation are also computed by applying correction factors which account for the deviations in state populations from Boltzmann distributions to the absorption coefficient and source function values utilized in the radiative analysis. Such atomic LTNE definitely exists in the chemical nonequilibrium region immediately behind the shock front[1-3,6,7] where, due to ionization via excited states, the populations of the electronic states will be lower than predicted by an LTE assumption using the ground state. Likewise, in regions of recombination the reverse processes can lead to state populations above those obtained using LTE.

The current model, which should probably be termed a first order approximation, has been presented previously in Ref. 1-3 and similar models have been used for monatomic gases[8-11]. Briefly, this model assumes that atomic ionization proceeds by excitation from the three low ground states (for nitrogen) to the high excited states followed by rapid ionization. Consequently, the model assumes that excitation from the ground states to the higher states is a rate limiting step for the ionization process and that the excited states, because of their energy proximity to the ionized state, are in equilibrium with the free electrons and ions. With this approach, for example[1-3], the atomic nitrogen LTNE correction factor, which represents the ratio of the actual population in an excited state to that which would exist for a Boltzmann distribution, can be written as

$$\frac{N_{N+} N_e Q_N^e exp(169000/T_e)}{N_N Q_{N+}^e Q_e} \qquad (1)$$

This factor is usually less than one in ionization regions and can be greater than one in zones involving extensive deionization. For the results presented later, it was usually applied with no restrictions.

In contrast, Park[12] and Kunc et al[13] handle atomic LTNE by using a quasi-steady analysis in which, while rate processes between all the bound states and between the bound states and the ionized state are assumed finite, they are assumed to be fast relative to changes induced by the flowfield. Thus, at any point in a flowfield an equilibrium between the states will exist which is perturbed from a Boltzmann distribution due to radiative effects. Kunc et al have performed calculations in which they specify the electron temperature and the total number of charged particles (defined as two times the number of atoms plus the number of ions plus the number of electrons), leaving the actual number of ions and free electrons to be determined as part of the unknown populations.

Park, on the other hand, in the application of his method[6] assumes the number of ions and electrons to be given by a flowfield solution. Under this approach, a non-Boltzmann distribution can be achieved even in the absence of radiation, if the number of ions and electrons differs from equilibrium. To be totally correct, however, the excitation and ionization rates associated with each level must overall be consistent with the ionization rates used in the flowfield solution.

Obviously, the present first order approach and those of Park and Kunc et al represent the extremes of modeling LTNE atomic phenomena. While the present first order approach is simplified in its assumption that the rates between the excited states and the free ions and electrons are infinitely fast (i.e. local equilibrium), it does directly couple the predicted excited state populations to the flowfield and, unlike the detailed quasi-steady approaches, it is not computationally intensive. In addition, the latter are sensitive to the choice of the individual rates; and it is difficult to know which rate to adjust when comparing with experimental results and attempting to improve the correlation. Finally, the present model when coupled with a compatible electron impact ionization rate has been shown to yield good agreement with experimental ionization distances[1].

and h_1 and h_3 are geometric factors for the axisymetric coordinate system.

This full electron energy equation is integrated into the VSL code by setting up the terms in the same form as those for the global energy equation and then solving the equations using the existing routine for solving the global energy equation. In the cascade order of solving the governing conservation equations typical of VSL methods, the electron energy equation is included folowing the global energy equation, which is where the QEE or QEEE equation is normally included. Initially, the electron energy equation was not well behaved when solved in this manner primarily due to the large order of magnitude of the elastic and inelastic exchange terms, which, since they are nonlinear, were originally included explicitly in the calculations. Consequently, to provide iterative stability, these terms have been linearized as follows:

$$[(\dot{w}h)^e]^{n+1} = [(\dot{w}h)^e]^n + (T_e^{n+1} - T_e^n)\left(\frac{\partial}{\partial T_e}(\dot{w}h)^e\right)^n \quad (9)$$

$$\xi_{er}^{n+1} = \xi_{er}^n + (T_e^{n+1} - T_e^n)\left(\frac{\partial \xi_{er}}{\partial T_e}\right)^n \quad (10)$$

Another item which needs to be considered in modeling electron-electronic energy is the proper boundary condition on electron temperature at the wall. In most past analyses[1,12], it has been assumed that at the wall the electron temperature is equal to the wall temperature. Since the heavy particle temperature is also assumed equal to the wall temperature at the wall, this approach effectively assumes that the electron temperature is equal to the heavy particle temperature. At first, this approach seems reasonable and follows the philosophy that in the thermal boundary layer near the wall the flow should be near equilibrium and collision dominated. However, in the thermal boundary layer the chemical rection rates are finite and often cannot keep up with local equilibirum. This lag combined with diffusion leads to atom, ion, and electron densities above equilibrium values and in turn enhanced excited state populations. In addition, as can be seen in the electron-electronic energy equation, ionic recombination yields an increase in electron energy and tends to force the electron temperature above the heavy particle temperature.

Further, since almost all walls are catalytic to ions and electrons, there exists a thin plasma sheath adjacent to the wall across which a potential develops in order to maintain zero charge flux at the sheath edge. Since the thickness of the plasma sheath is negligible in comparison to that of the wall thermal layer, the edge of the sheath can be construed as being physically at the wall. Thus, the proper wall boundary conditions on the continuum equations should be obtained by matching the particle description in the plasma sheath to the corresponding continuum description at the wall. Examination of appropriate sheath models shows that continuity of electron energy flux requires

$$\left(\eta_e \frac{\partial T_e}{\partial n} - \rho_e U_e h_e\right)_{n=0} = [2kT_e + |e\Phi|]\frac{N_e c_e}{4} exp\left(\frac{-|e\Phi|}{kT_e}\right) \quad (11)$$

where the sheath potential is determined by enforcing charge neutrality at the sheath edge. Further analysis indicates that the heavy particle species, being in good contact with the wall, should be at the wall temperature. An approximation of this type of electron boundary condition has been incorporated as an option into the present full electron-electronic equation model.

Since the present flowfield formulation does not include vibrational nonequilibrium, the above electron-electronic energy models do not include vibrational-electronic coupling. While this phenomena should not be important at higher entry velocities due to the rapid dissociation of diatomic species in and near the shock front, it could be important at lower velocities. Thus, efforts are in progress to include vibrational nonequilibrium and vibrational electronic coupling; and these will be reported in a later paper.

Discussion of Results

Several sets of results obtained using the above methods and models are presented in this section. In all cases, results are for the stagnation streamline, utilize ninety-nine points between the shock front and the wall, and, for simplicity, assume a nitrogen freestream. The nonequilibrium chemistry model is similar to the Case II set of Ref. 1 and is shown in Table I; and it should be representative of high temperature radiating air. For diffusion, the approximate multi-component model of Ref. 18 has been used with a Lewis number of 1.4. Since in a high temperature ionized diatomic gas, charge exchange and ambipolar effects cause atoms, ions, and electrons to all have to a first approximation similar diffusion velocities, such a gas should be dominated by only two diffusion velocities, that of the molecules and that of the atoms, ions, and electrons. Thus, the present model should adequately represent the diffusion phenomena present, including multi-component effects. In addition, except for the Fire 2 cases, the wall has been assumed to be radiatively black, noncatalytic to atomic recombination, fully catalytic to ionic recombination, and at 1650°K. This value, which corresponds approximately to the maximum possible for a nonablating surface, has been used for convenience and to illuminate cool wall phenomena. However, it is recognized that for many cases of interest the heat transfer load will be more than adequate to induce ablation and to raise the wall temperature to significantly higher values. Finally, in all cases, unless stated otherwise, shock slip is assumed, coupled nongray radiative transfer has been included, and local thermodynamic nonequilibrium effects have been accounted for using the molecular and first order atomic models described above.

Fire 2 Cases

In order to ensure that the present method and models are reasonably correct and appropriate, results have been obtained for five trajectory points along the Fire 2 entry profile covering the time period from 1634 through 1637.5 sec. These points were selected because they encompass a period of the flight involving extensive chemical and thermal nonequilibrium and changing radiative behavior. These results have been computed assuming a fully catalytic wall at the wall temperature measured in flight, and the full electron-electronic energy model has been used in

The results, presented on Figs. 6(a) and 6(b), were obtained using the quasi-equilibrium free electron energy model without the electron impact molecular dissociation reaction, and profiles obtained with both fixed and slip shock jump conditions using a Lewis number of 1.4 are portrayed. As shown, the electron temperature rapidly rises behind the shock front and equilibrates with the heavy particle temperature. However, as evidenced by the continual decrease in temperature and the variations in composition across the shock layer, the stagnation flow for this case is always in chemical nonequilibrium. Also, the wall thermal layer comprises approximately twenty percent of the 12.2 cm thick shock layer. For this case, the convective heating was 13.55 watts/sq cm, the total radiative heat flux to the wall was 1.56 watts/sq cm, and radiative cooling effects were insignificant.

With respect to temperature, the effects of slip versus fixed shock jump conditions seem to be confined to a small region immediately behind the shock front. However, the impact on concentration and particularly on total enthalpy are significant. In fact, the total enthalpy profiles clearly show that the fixed shock boundary condition results in an incorrect value for enthalpy in the interior of the shock layer, leading to incorrect species concentration values. Interestingly, when a Lewis number of one is used with the fixed shock boundary conditions the enthalpy profile appears to be correct and when a value less than unity is used, the enthalpy is high in the flow interior. However, for the shock slip condition, the enthalpy profiles are unaffected by Lewis number. Since a Lewis number of 1.4 is more appropriate for describing atom molecule diffusion, which is the dominant diffusion mechanism in this flow, and since the enthalpy ratio in the flow interior in the absence of significant radiative cooling should be unity, these results demonstrate the importance of using slip shock boundary conditions at these conditions.

Since at these conditions, vibrational nonequilibrium should also be important, it is planned in a future paper to present results which include vibrational nonequilibrium. Also, it should be noted that since the results shown on Fig. 6 are for a nitrogen freestream, the radiative heating values in air, based upon the Fire 2 data, will probably be slightly higher.

AFE CFD Point 4

This condition corresponds to a "max Q" point for a heavier AFE vehicle at which the freestream conditions are 9.326 km/sec, 26.4 dynes/ sq cm, and 200°K. Stagnation line temperature and concentration profiles are presented on Fig. 7, which compares results obtained using the quasi-equilibrium electron-electronic model (QEEE) including the electron impact dissociation reaction with those using the quasi-equilibrium electron (QEE) energy model only. The primary effect of using the QEEE model is more extensive thermal nonequilibrium and a lower electron temperature through much of the shock layer. Also, the combined effect of electron impact dissociation and the QEEE model leads to a more dissociated flow having slightly different N_2 and N_2^+ profiles.

However, the most significant difference in the two models is the radiative heat transfer. For the QEEE case, the lower electron temperature yields a total radiative flux of 1.18 watts/sq cm, a shock standoff distance of 11.96 cm, and a convective heating of 25.8 watts/sq cm. For the QEE model it is 2.91 watts/sq cm., 11.89 cm, and 25.7 watts/sq cm respectively.

Fig. 8(a) shows the stagnation point continuum and line radiation distributions predicted with the QEEE model. In the actual radiative transfer analysis, lines are considered and integrated individually, but they are presented on Fig. 8(a) as average values for various line groups for convenience. While there are many infrared line groups and some in the ultra-violet, the line contributions are negligible compared to the continuum. Also, most of the continuum radiation (about 90%) is in the visible and infrared below 6.2 eV; and most of that is between 2 and 4 eV. At these conditions, this radiation is due to the $N_2^+(1-)$ band. In addition, there is some continuum contribution in the ultra-violet, probably due to nitrogen free-bound processes and $N_2(BH)$ bands.

Fig. 8(b) shows the same information as Fig. 8(a) except each line is shown individually. Many of the VUV lines above 10 eV are absorbing in their line centers, but the IR lines are essentially transparent and appear to be strongly emitting. However, line radiation at this condition is insignificant compared to the continuum contribution.

As part of this study computations were also conducted using the QEE model without including molecular LTNE effects; and the resulting radiative heat transfer result was 8.90 watts/sq cm. Obviously, molecular LTNE is important at AFE conditions and leads to lower radiative heating. Examination of the results indicate that the LTNE induced by chemical and thermal nonequilibirum drastically reduces radiation from the $N_2(1+)$ and $N_2(2+)$ bands and significantly decreases that due to $N_2(BH)$. However, $N_2^+(1-)$ is virtually unaffected by chemical and thermal nonequilibrium phenomena. Thus, on Fig. 8, the primary stagnation point radiation is in the continuum between 2 and 4 eV and is from the $N_2^+(1-)$ band.

At shock speeds below 10 km/sec, shock tube radiative intensity photomultiplier mesurements indicate a sharp rise to a peak immediately behind the shock front followed by a decrease until equilibrium is achieved[25]. Similar results have been obtained computationally for nonequilibrium flows for the visible region of the spectrum assuming the gas to be transparent[7]. Fig. 9 shows for the present QEEE model the variation along the stagnation line of radiative flux towards the stagnation point, QR+, and its negative derivative, -D(QR+)/DY. The latter is essentially what Candler[7] and others have termed radiation intensity. As can be seen, -D(QR+)/DY is similar to observed photomultiplier traces in having a peak near the shock front followed by a steady decrease towards the wall. For this case, no equilibrium plateau is achieved since the flow never reaches chemical equilibrium prior to the wall thermal boundary layer. (The oscillations near the wall are an artifact due to significant digit error resulting from providing the plot routine formatted data. The actual curve is smooth.) Comparison with the temperature plots indicates that the "intensity" peak corresponds to the maximum value in electron temperature; and near the wall the "intensity" is negative, indicating absorption. However, as shown by only the slight decrease in QR(+), the amount of absorption near the wall is negligible at these conditions.

The temperature and composition profiles for the 14 km/sec case are shown on Fig. 12. Since the freestream velocity is higher, the post-shock nonequilibrium zone is shorter than at 12 km/sec, occupying only the outer 30-40% of the 9.1 cm shock layer. The electron-electronic temperature rises rapidly and peaks at a value several thousand degrees above the equilibrium temperature, and the wall sheath representation only affects the electron temperature in a small zone near the wall. For this case the convective heating is 56.4 watts/cm^2 and the radiative flux is 110.7 watts/cm^2. Interestingly, especially when compared to the AFE cases, only about ten percent of this radiative heating is due to molecular processes.

As part of this study, several cases were also conducted at this condition using the quasi-equilibirum electron-electronic and quasi-equilibrium electron energy models; and the only difference between the models was that the peak in electron temperature was slightly higher and slightly further from the shock front with the exact model than with the quasi-equilibrium models. This behavior has been observed at freestream velocities of 12 km/sec and higher and is in sharp contrast to the trends displayed at the AFE velocities. At the higher velocities there are more electrons and the flow is dominated by ionization processes. Consequently, the electron-electronic energy is dominated by the free electrons. At the lower AFE speeds, there is very little ionization and the electronic energy portion dominates the combination. Thus, the shape and character of the electron temperature profiles appears to be significantly different at the higher velocities than at AFE speeds.

The spectral variation in radiative heat flux to the wall at 14 km/sec is shown on Fig. 13(a), where the contributions due to line and continuum processes have been combined and the convenient representation of lines as group averages has been utilized. Here, the heating due to continuum and lines is similar in magnitude with extensive infrared and UV lines as well as significant VUV bound-free processes. In fact, only about twenty-eight percent of the wall flux is from the visible and infrared below 6.2 eV. Notice that a measureable portion of the visible radiation is between 2 and 4 eV and is due to $N_2^+(1-)$ molecular radiation. Nevertheless, while this type of presentation is informative and useful, especially for continuum radiation, the characteristics and number of lines is not evident on this type of plot.

As mentioned previously, the actual radiative transfer analysis treats lines individually, and Fig. 13(b) displays the same information but with each line shown separately. From this representation, it is evident that in the visible and infrared the line radiation is primarily transparent. However, in the VUV, many of the line centers are highly absorbing with most of the line emission reaching the wall originating from the line wings.

In contrast to results below 10 km/sec, shock tube photomultiplier results at higher speeds show that the radiative intensity peak behind a shock front changes from a single peak to a double hump peak system[25]. Experimental spectral data indicates that the first is due to molecular radiation near the shock front while the second is atomic radiation coupled to the ionization process. Figure 14 shows for the 14 km/sec condition theoretical predictions of the radiative flux towards the wall, QR+, and the negative of its derivative, -DQR(+),DY. As discussed previously, the latter is closely related to radiative intensity.

The present profile clearly exhibits this double hump behavior. The first peak corresponds to the maximum value of the electron temperature, while the second occurs at the onset of thermal equilibrium and the establishment of near Boltzmann distributions in the excited states. Subsequently, radiative cooling occurs and the "intensity" rapidly decreases. During this period, examination of the species concentrations and of LTNE phenomena indicates nonequilibrium recombination is induced with resultant overpopulation, compared to a Boltzmann distribution, of the excited states. Around y/yshock of 0.3 the flow begins to absorb more than it emits and QR+ begins to decrease. However, as shown by the QR+ profile, which only decreases slightly between 0.3 and the wall, the absorption in the wall thermal layer only results in a mild decrease in QR+ at this condition.

The temperature and composition profiles at 16 km/sec are shown on Fig. 15, and the corresponding predicted radiative and convective heating rates are 272.6 and 87.3 watts/cm^2 respectively. Here, the electron temperature rises very rapidly and peaks near 20,000°K, confirming the trend that as speed increases, the peak electron-electronic temperature increases in magnitude and occurs nearer to the shock front. Likewise, again due to the increase in velocity, the nonequilibrium zone is shorter at about 20-25% of the 7.5 cm shock layer. Finally, on Fig. 15 notice that radiation cooling effects induce both atomic and ionic recombination starting near the end of the post-shock nonequilibrium zone and continuing all the way to the wall.

The effect on the temperature and ionization profiles of including radiative gasdynamic coupling in the flowfield and local thermodynamic nonequilibrium effects in the radiation is shown for the 16 km/sec case on Fig. 16. The curves denoted uncoupled do not include either radiation cooling or LTNE phenomena and indicate for this case that nominally the nonequilibrium post-shock zone and the wall thermal layer each affect about 20% of the shock layer. For this case, the shock standoff distance is 8.16 cm. However, when radiation coupling is included but LTNE is excluded, the shock layer thickness is reduced to 7.15 cm due to the lower temperature and increased density. The resultant profiles, designated as uncorrected, show that without LTNE effects significant cooling occurs in the nonequilibrium region with corresponding decreases in the electron and heavy particle temperatures and in the apparent length of the relaxation zone. Further, radiative losses through the shock front from the high temperature nonequilibrium zone reduce the total enthalpy forty percent, which leads to a cooler equilibrium zone having less than half the ionization of the uncoupled case.

Fortunately, when both radiation coupling and LTNE effects are included, the radiative losses are much less. As shown on the curves denoted as corrected, the corresponding temperature and ionization variations in the nonequilibrium post-shock region are only slightly affected since in that region the radiative losses are low due to LTNE effects. However, once equilibrium is nearly established around 0.8, radiative cooling becomes the dominant feature, the temperature steadily decreases, and the degree of ionization rapidly decreases. Obviously, at these conditions both LTNE phenomena and radiation coupling are important and need

Regions," *J. of Thermophysics and Heat Transfer*, vol. 3, No. 4, October 1989, pp. 380-388.

[3] Carlson, L. A., Bobskill, G. J., and Greendyke, R. B., "Comparison of Vibration Dissociation and Radiative Transfer Models for AOTV/AFE Flowfields," *J. of Thermophysics and Heat Transfer*, vol. 4, No. 1, January 1990, pp. 16-26.

[4] Thompson, R. A., "Comparison of Nonequilibrium Viscous Shock Layer Solutions with Windward Surface Shuttle Heating Data," AIAA Paper 87-1473, June 1987.

[5] Nicolet, W. E., "User's Manual for the Generalized Radiation Transfer Code (RAD/EQUIL or RADICAL)," NASA CR 116353, October 1969.

[6] Park, C., "Assessment of Two Temperature Kinetic Model for Ionizing Air," AIAA Paper No. 87-1574, June 1987.

[7] Candler, G. and Park, C., "The Computation of Radiation from Nonequilibrium Hypersonic Flows," AIAA 88-2678, June 1988.

[8] Foley, W. H. and Clarke, J. H., "Shock Waves Structered by Nonequilibrium Ionizing and Thermal Phenomena," *Physics of Fluids*, vol. 16, No. 3, March 1973, pp. 1612-1620.

[9] Nelson, H. F., "Nonequilibrium Structure of Argon Shock Waves," *Physics of Fluids*, vol. 16, No. 12, December 1973, pp. 2132-2142.

[10] Nelson, H. F. and Goulard, R., "Structure of Shock Waves with Nonequilibrium Radiation and Ionization," *Physics of Fluids*, vol. 12, No. 8, August 1969, pp. 1605-1617.

[11] Chapin, C. E., "Nonquilibrium Radiation and Ionization in Shock Waves," AA&ES Report, June 1967, Purdue, Univ., Lafayette, Ind.

[12] Park, C., "Calculation of Nonequilibrium Radiation in the Flight Regimes of Aeroassisted Orbital Transfer Vehicles," in ***Thermal Design of Aeroassisted Orbital Transfer Vehicles***, Progress in Astronautics and Aeronautics, Vol. 96, Ed. H. F. Nelson, AIAA, 1985, pp. 395-418.

[13] Kunc, J. A. and Soon, W. H., "Collisional Radiative Nonequilibrium in Partially Ionized Atomic Nitrogen," *Physical Review A*, vol. 40, No. 10, November 15, 1989, pp. 5822 ff.

[14] Gnoffo, P. A., Gupta, R. N., and Shinn, J. L.,, "Conservation Equations and Physical Models for Hypersonic Air Flows in THermal and Chemical Nonequilibrium," NASA TP 2867, February 1987.

[15] Lee, J. H., "Basic Governing Equations for the Flight Regimes of Aeroassisted Orbital Transfer Vehicles," in ***Thermal Design of Aeroassisted Orbital Transfer Vehicles***, Progress in Astronautics and Aeronautics, Vol. 96, Ed. H. F. Nelson, AIAA, 1985, pp. 3-53.

[16] Carlson, L. A., "Radiative Gasdynamic Coupling and Nonequilibrium Effects Behind Reflected Shock Waves," *AIAA Journal*, vol. 9, No. 5, May 1971, pp. 858-865.

[17] Chapman, S. and Cowling, T. G., ***The Mathematical Theory of Non-Uniform Gases***, Cambridge, 1964.

[18] Miner, E. W. and Lewis, C. H., "Hypersonic Ionizing Air Viscous Shock Layer FLows over Nonanalytic Blunt Bodies," NASA CR-2550, May 1975.

[19] Cauchon, D. L., "Radiative Heating Results from the Fire II Flight Experiments at a Reentry Velocity of 11.4 Kilometers Per Second," NASA TM X-1402, 1966.

[20] Cauchon, D. L., McKee, C. W., and Cornette, E. S., "Spectral Measurements of Gas-Cap Radiation During Project Fire Flight Experiments at Reentry Velocities Near 11.4 Kilometers per Second," NASA TM X-1389, October 1967.

[21] Gupta, R. N., "Navier Stokes and Viscous Shock Layer Solutions for Radiating Hypersonic Flows," AIAA Paper No. 87-1576, June 1987.

[22] Balakrishnan, A., C. Park, and Green, J. M., "Radiative Viscous Shock Layer Analysis of Fire, Apollo, and PAET Flight Data," in ***Thermophysical Aspects of Re-Entry Flows***, Progress in Astronauticss and Aeronautics, Vol. 103, Ed. J. N. Moss and C. D. Scott, AIAA, 1986, pp.514-540.

[23] Sutton, K., "Air Radiation Revisited," in ***Thermal Design of Aeroassisted Orbital Transfer Vehicles***, Progress in Astronautics and Aeronautics, Vol. 96, AIAA, 1985, pp. 419-442

[24] Bird, G. A., "Nonequilibrim Radiation During Re-Entry at 10 km/sec," AIAA Paper No. 87-1543, June 1987.

[25] Wilson, J., "Ionization Rate of Air Behind High Speed Shock Waves," *The Physics of Fluids*, vol. 9, No. 10, October 1966, pp. 1913-1921.

[26] Park, C. and Milos, F. S., "Computational Equations for Radiating and Ablating Shock Layers," AIAA Paper 90-0356, January 1990.

[27] Nicolet, W. E., Waterland, L. R., and Kendall, R. M., "Methods for Predicting Radiation Coupled Flowfields about Planetary Entry Probes," in ***Aerodynamic Heating and Thermal Protections Systems***, Progress in Astronautics and Aeronautics, Vol. 59, Ed. L. S. Fletcher, AIAA, 1978, pp. 120-136.

[28] Sutton, K. and Hartung, L. C., "Equilibrium Radiative Heating Tables for Earth Entry," NASA TM 102652, May 1990.

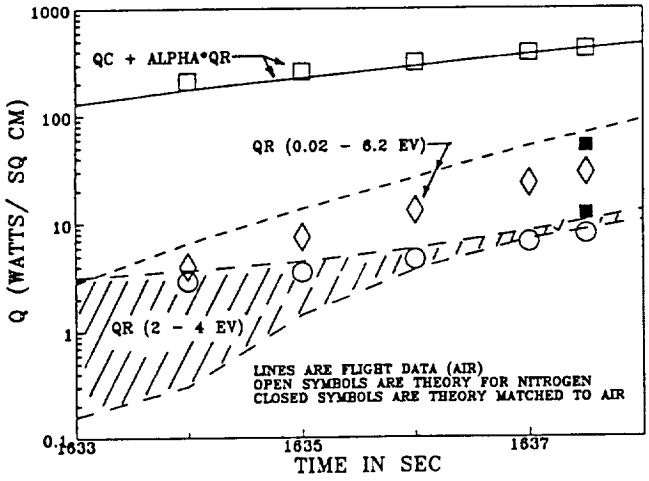

Fig. 4 – Comparison of Present Fire 2 Predictions (Nitrogen) with Flight Data (Air)

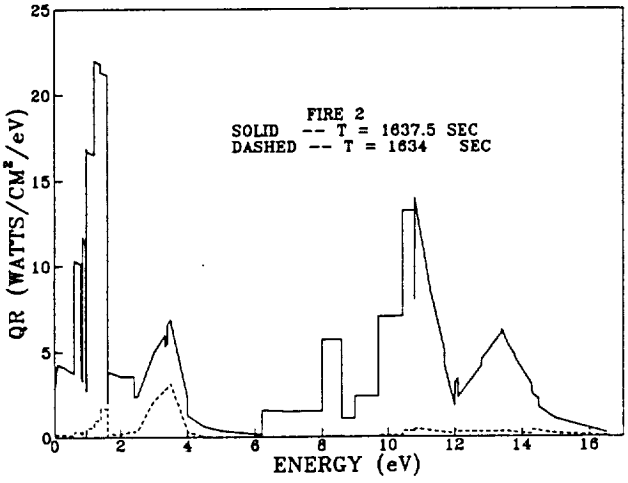

Fig. 5 – Spectral Variation of Stagnation Point Radiative Heat Transfer for Fire 2

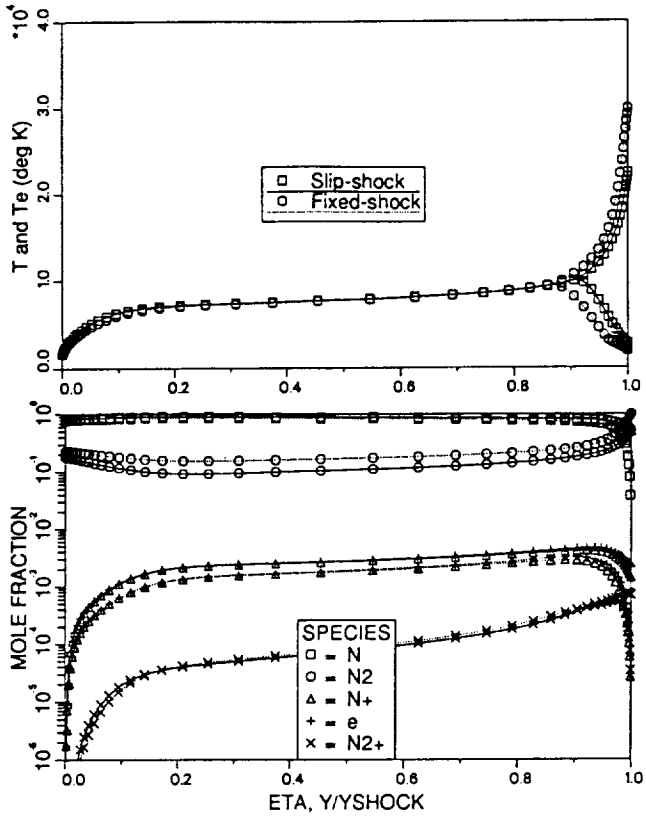

Fig. 6(a) – Stagnation Profiles for AFE CFD Point 2 Using QEE Model, U = 8.915 km/sec, H = 77.9 km, QR = 1.56 watts/cm^2, QC = 13.6 watts/cm^2, YSHOCK = 12.2 cm

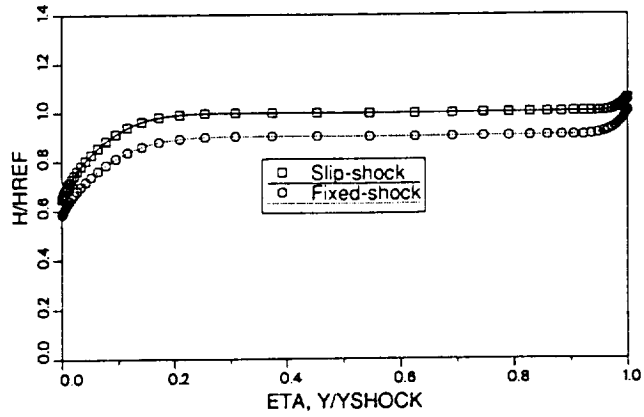

Fig. 6(b) – Enthalpy Profiles for AFE CFD Point 2 Using QEE Model

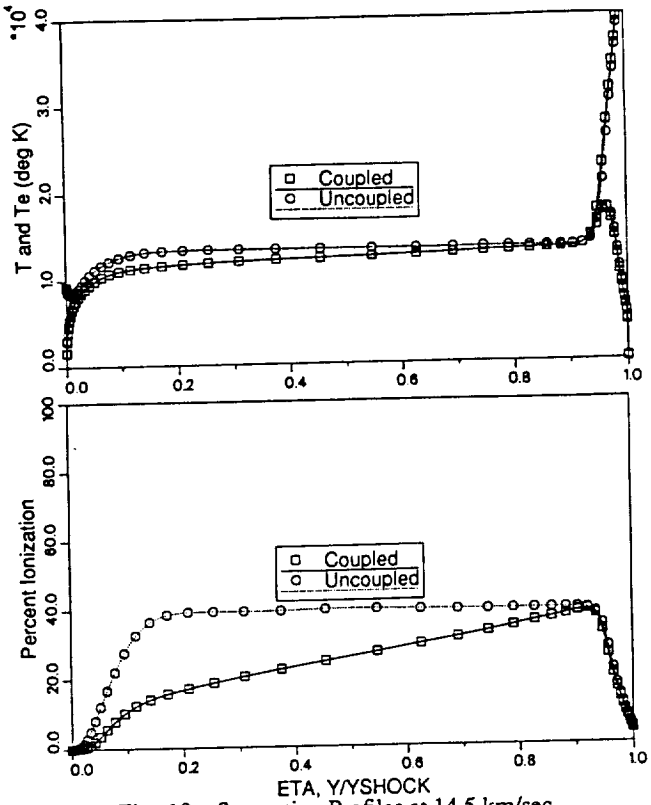

Fig. 10 – Stagnation Profiles at 14.5 km/sec, 65 km, Rnose = 1 m
Uncoupled: QR = 2831 watts/cm^2, QC = 426 watts/cm^2, YSHOCK = 3.92 cm
Coupled: QR = 1347 watts/cm^2, QC = 430 watts/cm^2, YSHOCK = 3.67 cm

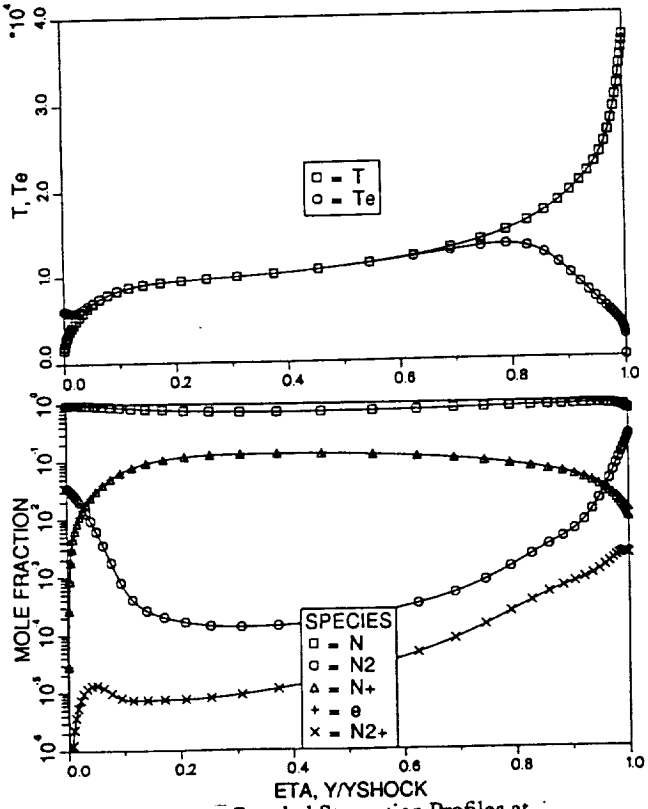

Fig. 11 – Coupled Stagnation Profiles at 12 km/sec, 80 km, Rnose = 2.3 m, QR = 24.3 watts/cm^2, QC = 33 watts/cm^2, YSHOCK = 11.5 cm

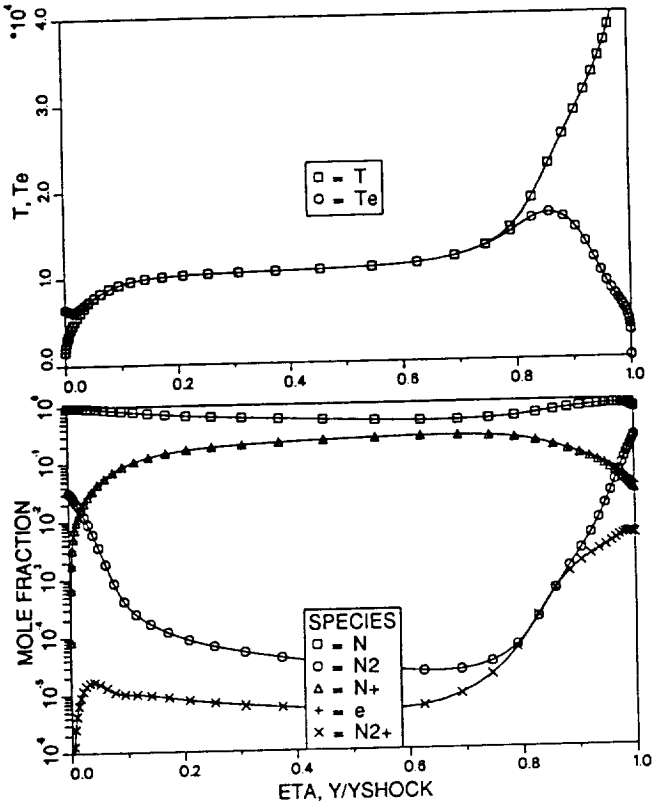

Fig. 12 – Coupled Stagnation Profiles at 14 km/sec, 80 km, Rnose = 2.3 m, QR = 111 watts/cm^2, QC = 56.4 watts/cm^2, YSHOCK = 9.1 cm

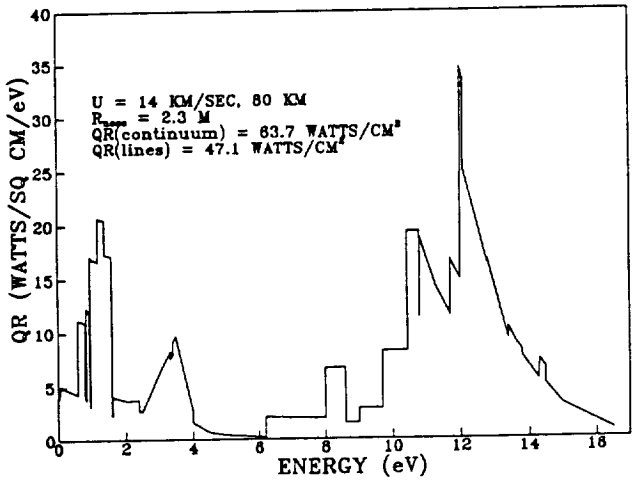

Fig. 13(a) – Usual Presentation of Spectral Variation of Stagnation Radiative Heat Transfer

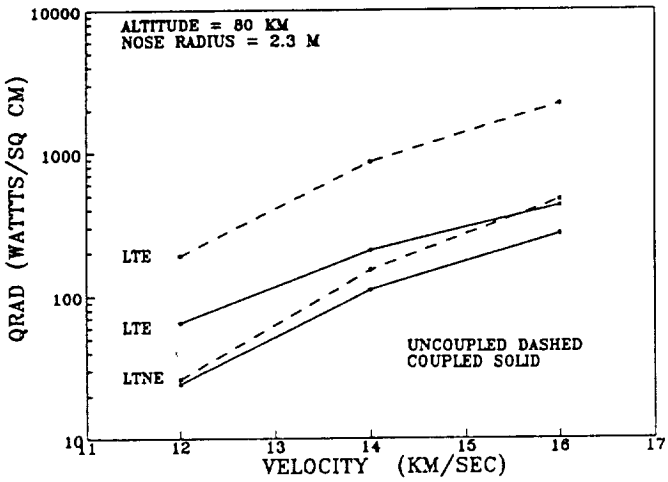

Fig. 17 – LTNE and Coupling Effects on Radiative Heat Transfer

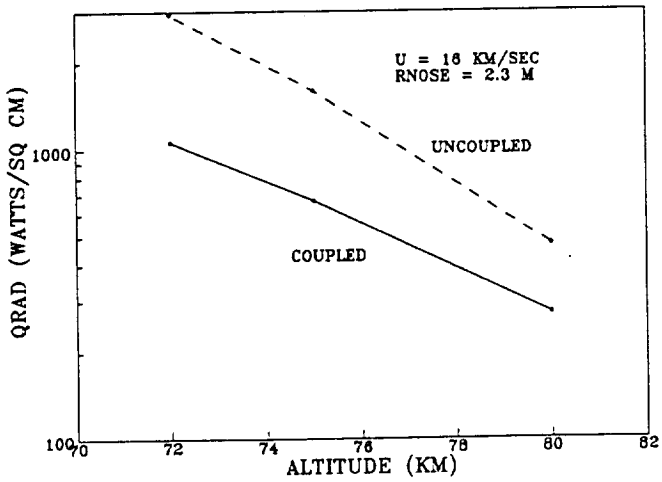

Fig. 18 – Radiative Gasdynamic Coupling Effects on Radiative Heat Transfer

APPENDIX II

Miscellaneous Results from Precursor Studies

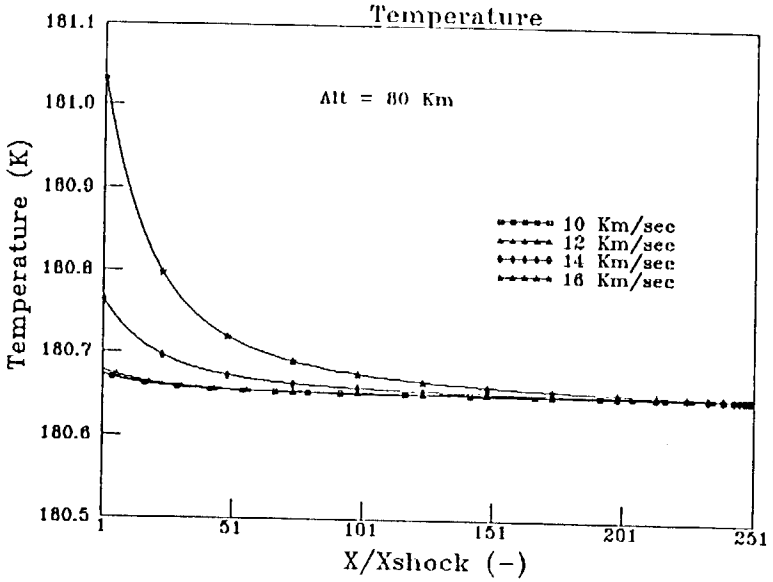
Temperature
Alt = 80 Km
10 Km/sec
12 Km/sec
14 Km/sec
16 Km/sec
Temperature (K)
181.1
181.0
180.9
180.8
180.7
180.6
180.5
1
51
101
151
201
251
X/Xshock (-)

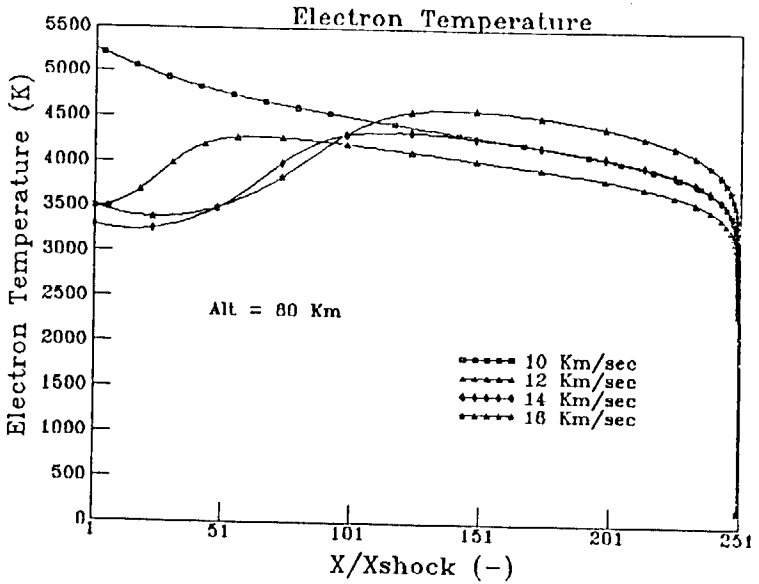
Electron Temperature
Alt = 80 Km
10 Km/sec
12 Km/sec
14 Km/sec
16 Km/sec
Electron Temperature (K)
5500
5000
4500
4000
3500
3000
2500
2000
1500
1000
500
0
1
51
101
151
201
251
X/Xshock (-)

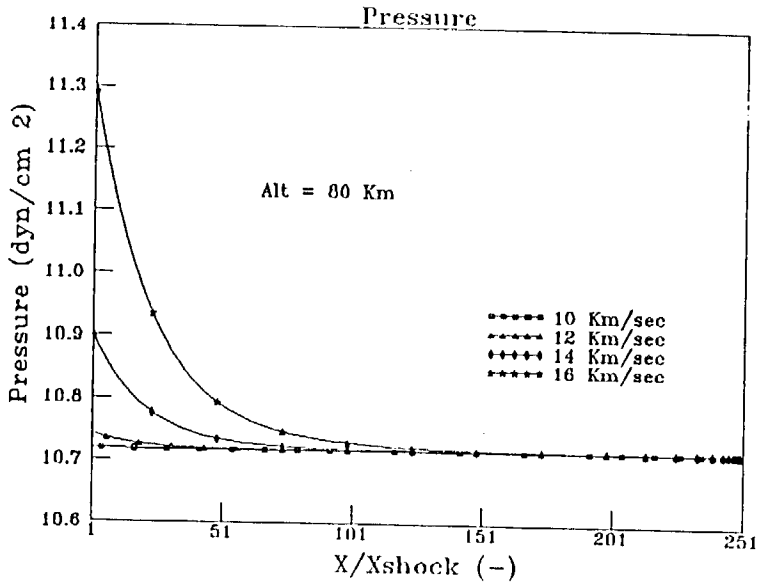
Pressure
Alt = 80 Km
10 Km/sec
12 Km/sec
14 Km/sec
16 Km/sec
Pressure (dyn/cm 2)
11.4
11.3
11.2
11.1
11.0
10.9
10.8
10.7
10.6
1
51
101
151
201
251
X/Xshock (-)

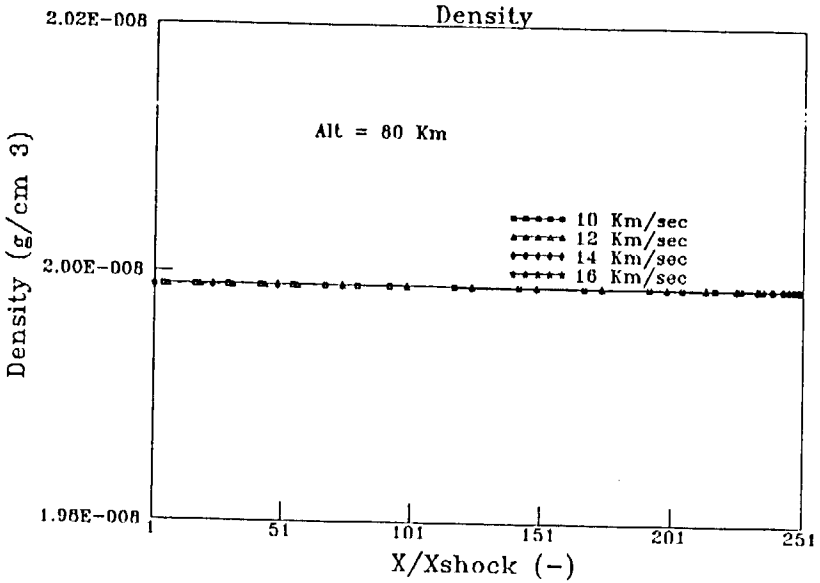
Density
Alt = 80 Km
10 Km/sec
12 Km/sec
14 Km/sec
16 Km/sec
Density (g/cm 3)
2.02E-008
2.00E-008
1.98E-008
1
51
101
151
201
251
X/Xshock (-)

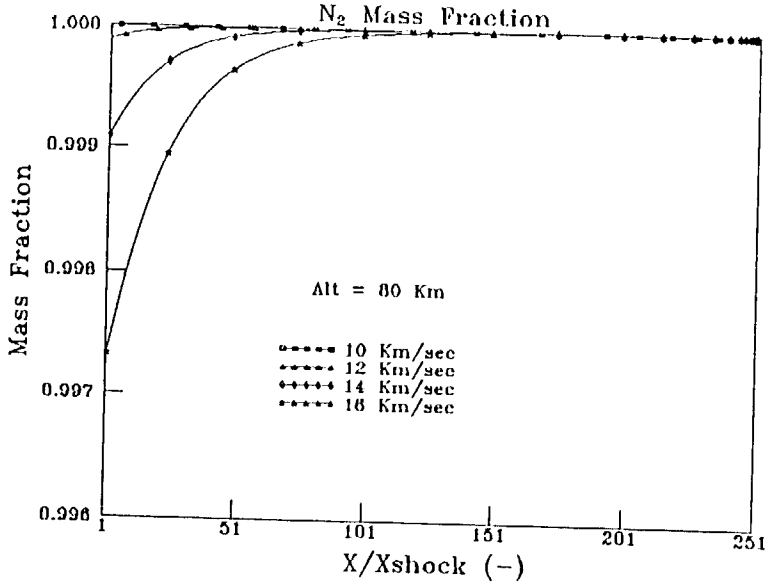
N_2 Mass Fraction
1.000
0.999
0.998
0.997
0.996
Mass Fraction
Alt = 80 Km
10 Km/sec
12 Km/sec
14 Km/sec
16 Km/sec
1
51
101
151
201
251
X/Xshock (-)

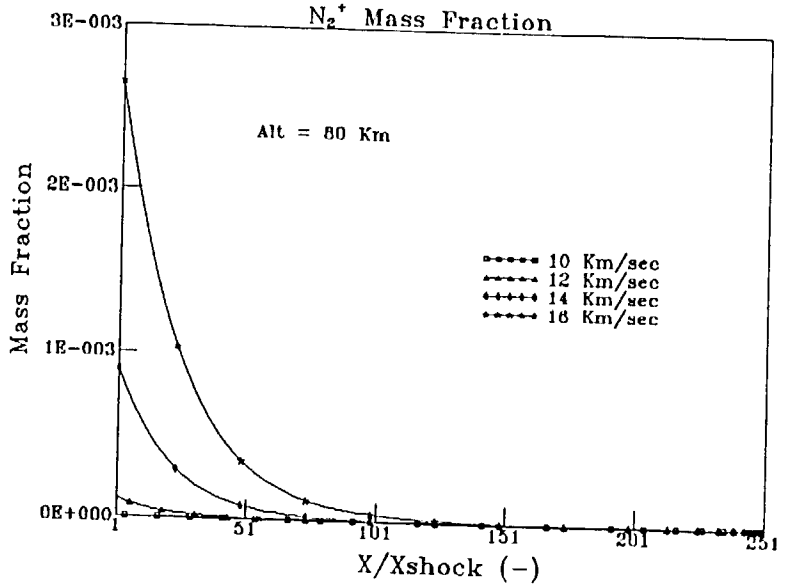
N_2^+ Mass Fraction
3E-003
2E-003
1E-003
0E+000
Mass Fraction
Alt = 80 Km
10 Km/sec
12 Km/sec
14 Km/sec
16 Km/sec
1
51
101
151
201
251
X/Xshock (-)

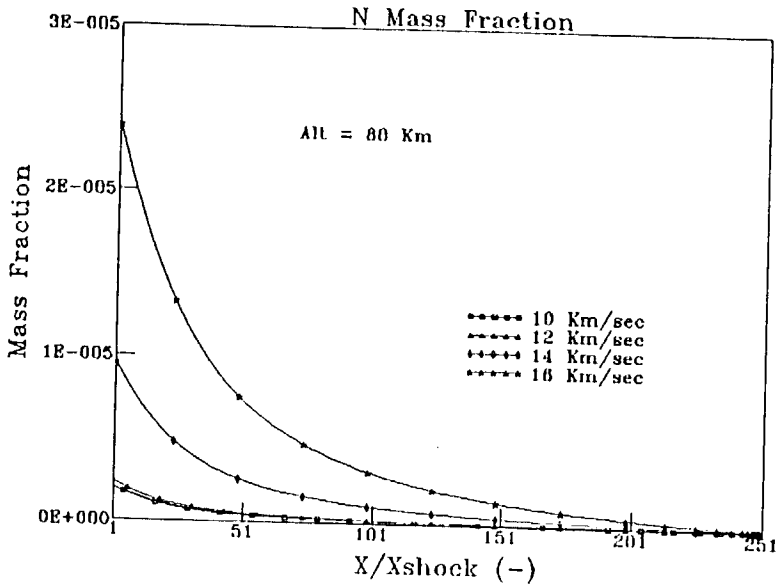
N Mass Fraction
3E-005
2E-005
1E-005
0E+000
Mass Fraction
Alt = 80 Km
10 Km/sec
12 Km/sec
14 Km/sec
16 Km/sec
1
51
101
151
201
251
X/Xshock (-)

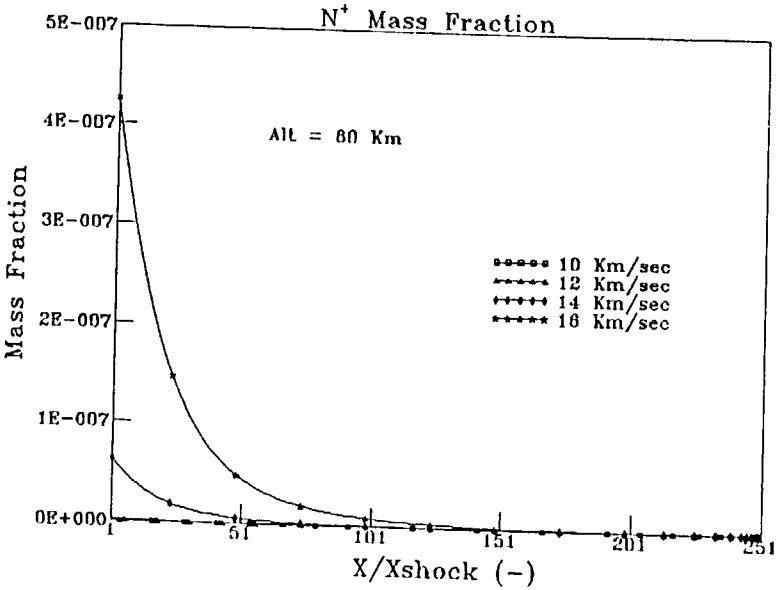
N^+ Mass Fraction
5E-007
4E-007
3E-007
2E-007
1E-007
0E+000
Mass Fraction
Alt = 80 Km
10 Km/sec
12 Km/sec
14 Km/sec
16 Km/sec
1
51
101
151
201
251
X/Xshock (-)

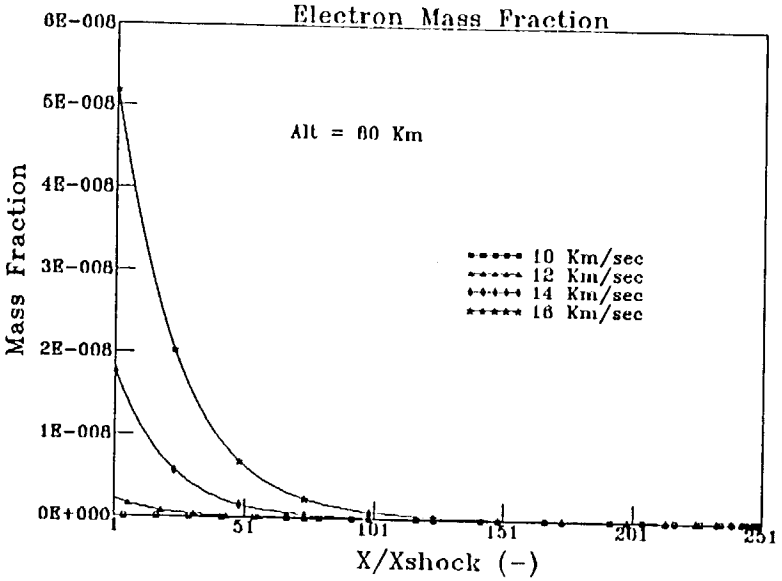
Electron Mass Fraction
Alt = 80 Km
10 Km/sec
12 Km/sec
14 Km/sec
16 Km/sec
Mass Fraction
6E-008
5E-008
4E-008
3E-008
2E-008
1E-008
0E+000
1
51
101
151
201
251
X/Xshock (-)

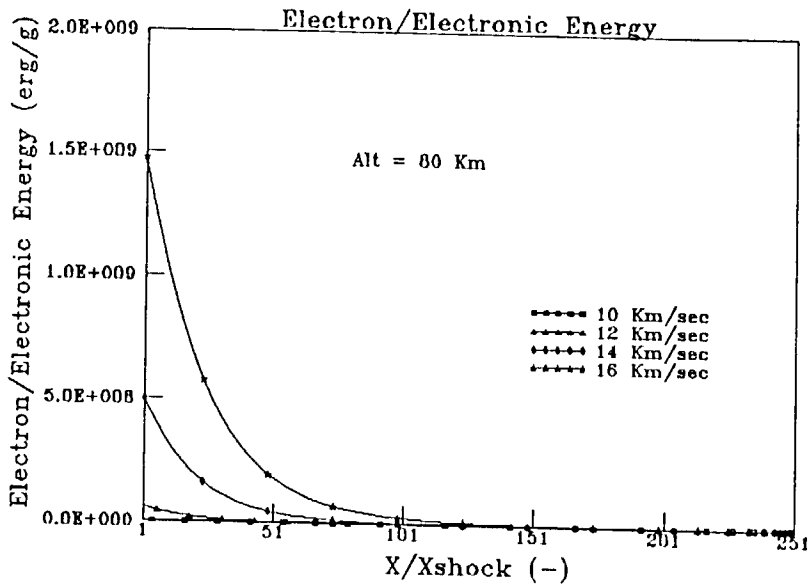
Electron/Electronic Energy
Alt = 80 Km
10 Km/sec
12 Km/sec
14 Km/sec
16 Km/sec
Electron/Electronic Energy (erg/g)
2.0E+009
1.5E+009
1.0E+009
5.0E+008
0.0E+000
1
51
101
151
201
251
X/Xshock (-)

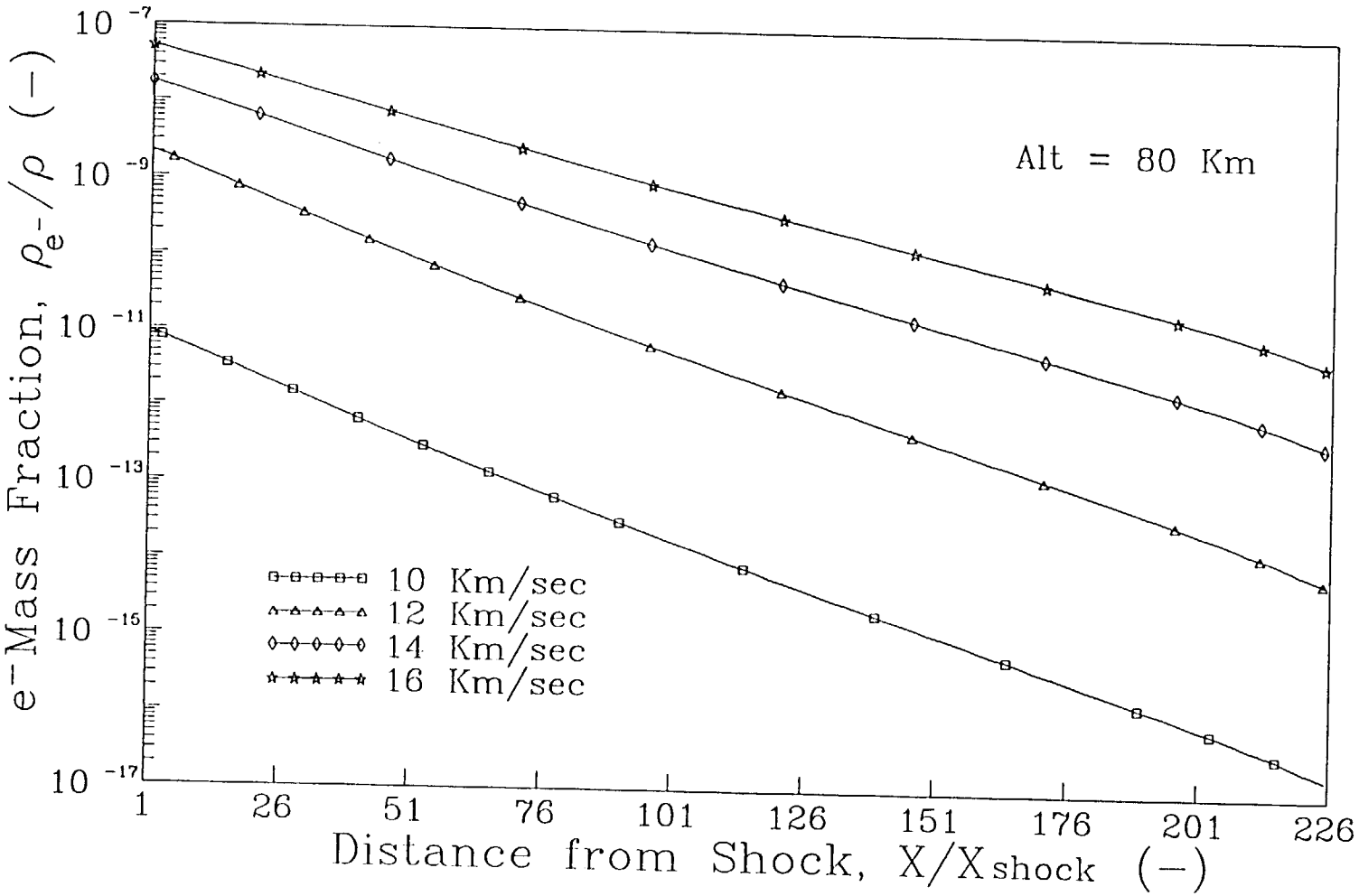
Alt = 80 Km
10 Km/sec
12 Km/sec
14 Km/sec
16 Km/sec
e⁻ Mass Fraction, ρ_{e^-}/ρ (−)
Distance from Shock, X/Xshock (−)
10 -7
10 -9
10 -11
10 -13
10 -15
10 -17
1
26
51
76
101
126
151
176
201
226

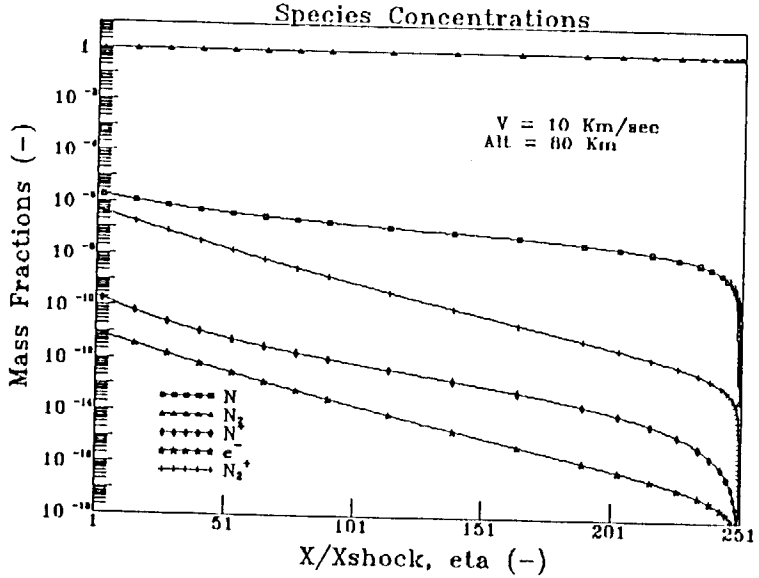
Species Concentrations
V = 10 Km/sec
Alt = 80 Km
Mass Fractions (-)
N
N2
N+
e-
N2+
X/Xshock, eta (-)

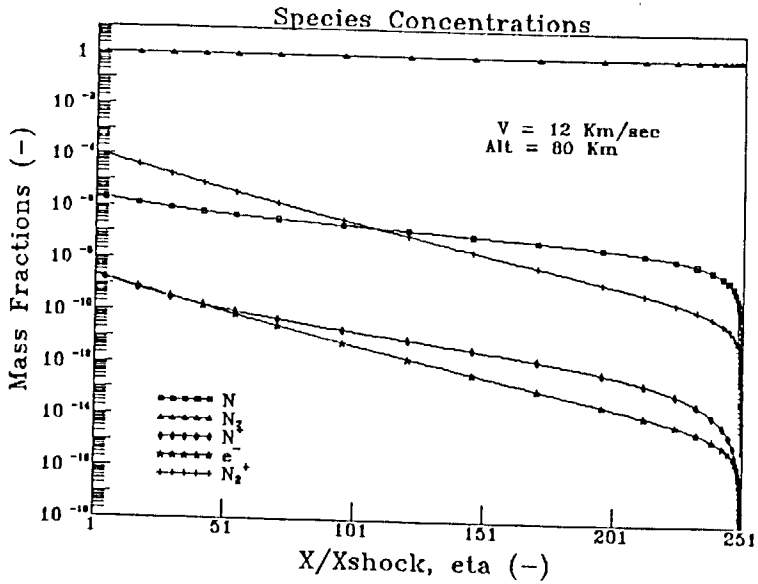
Species Concentrations
V = 12 Km/sec
Alt = 80 Km
Mass Fractions (-)
N
N2
N+
e-
N2+
X/Xshock, eta (-)

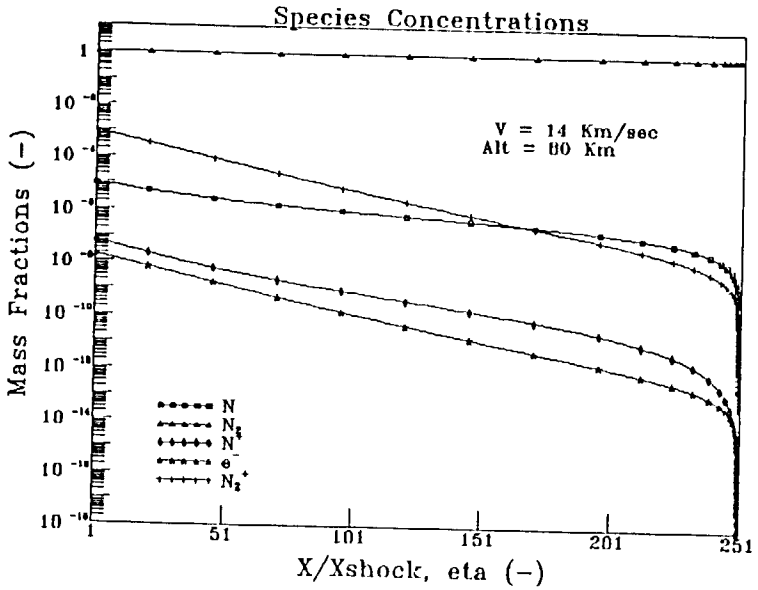
Species Concentrations
V = 14 Km/sec
Alt = 80 Km
Mass Fractions (-)
N
N2
N+
e-
N2+
X/Xshock, eta (-)

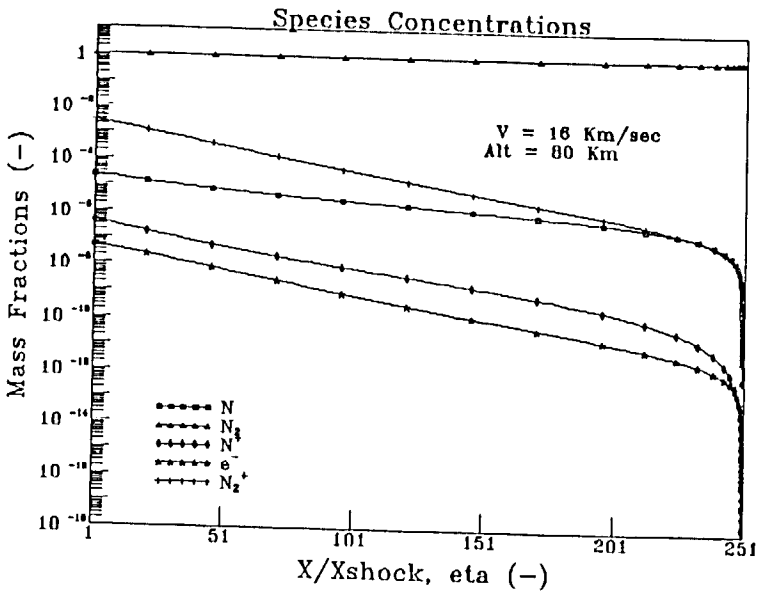
Species Concentrations
V = 16 Km/sec
Alt = 80 Km
Mass Fractions (-)
N
N2
N+
e-
N2+
X/Xshock, eta (-)

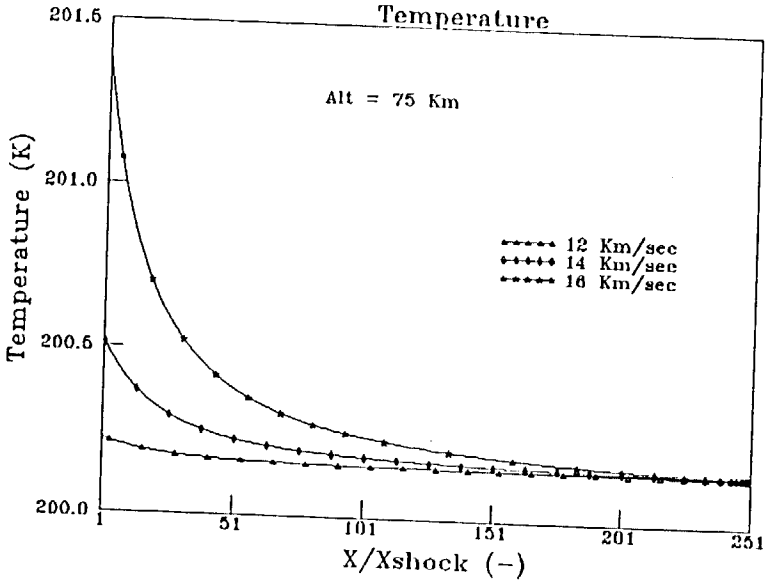
Temperature
Alt = 75 Km
12 Km/sec
14 Km/sec
16 Km/sec
Temperature (K)
201.5
201.0
200.5
200.0
1
51
101
151
201
251
X/Xshock (-)

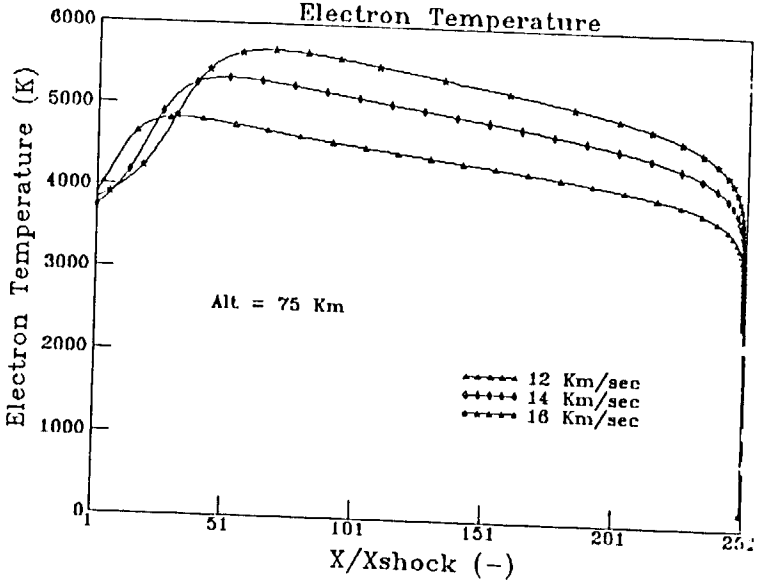
Electron Temperature
Alt = 75 Km
12 Km/sec
14 Km/sec
16 Km/sec
Electron Temperature (K)
6000
5000
4000
3000
2000
1000
0
1
51
101
151
201
X/Xshock (-)

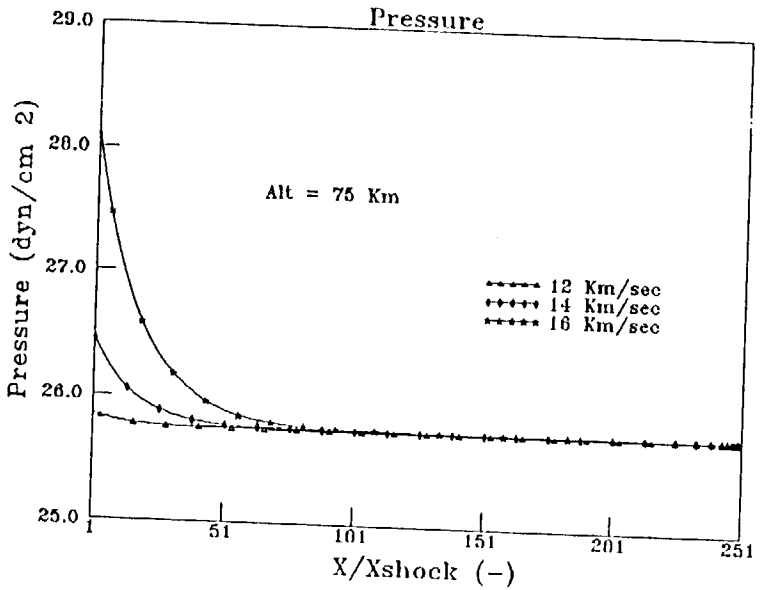
Pressure
Alt = 75 Km
12 Km/sec
14 Km/sec
16 Km/sec
Pressure (dyn/cm 2)
29.0
28.0
27.0
26.0
25.0
1
51
101
151
201
251
X/Xshock (-)

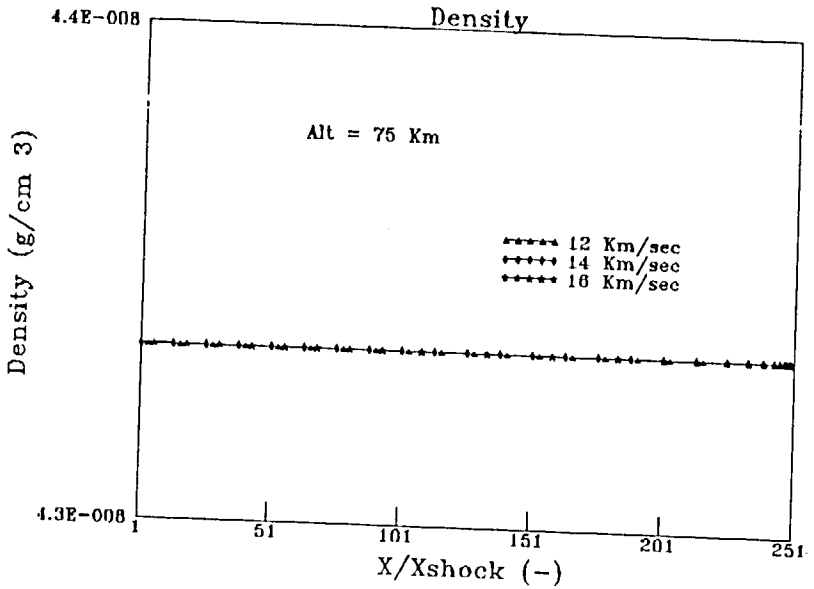
Density
Alt = 75 Km
12 Km/sec
14 Km/sec
16 Km/sec
Density (g/cm 3)
4.4E-008
4.3E-008
1
51
101
151
201
251
X/Xshock (-)

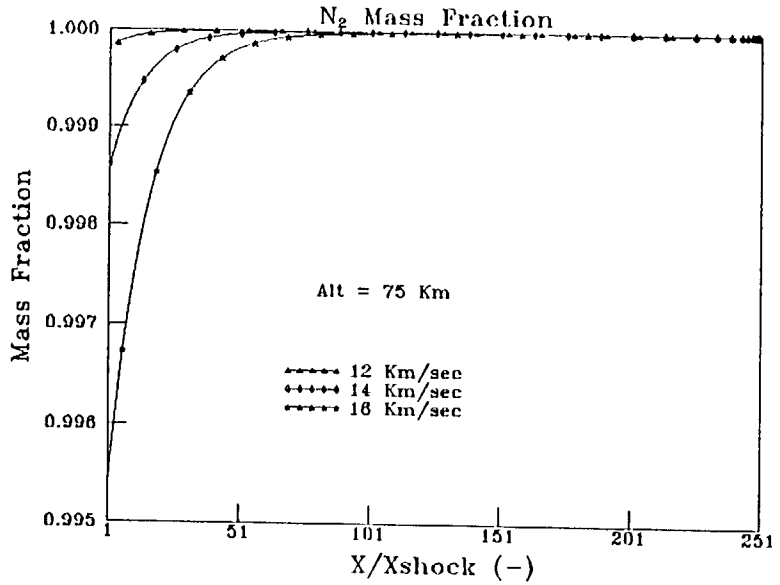
N_2 Mass Fraction
1.000
0.999
0.998
0.997
0.996
0.995
Mass Fraction
Alt = 75 Km
12 Km/sec
14 Km/sec
16 Km/sec
1
51
101
151
201
251
X/Xshock (-)

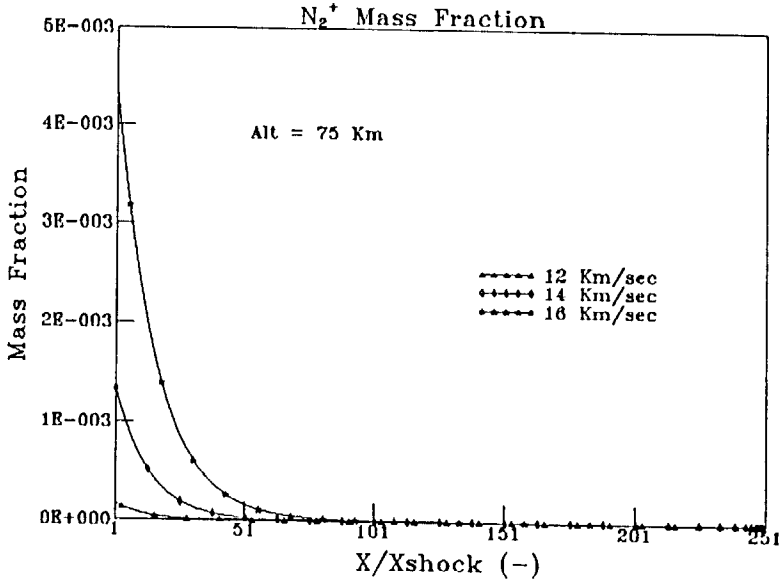
N_2^+ Mass Fraction
5E-003
4E-003
3E-003
2E-003
1E-003
0E+000
Mass Fraction
Alt = 75 Km
12 Km/sec
14 Km/sec
16 Km/sec
1
51
101
151
201
251
X/Xshock (-)

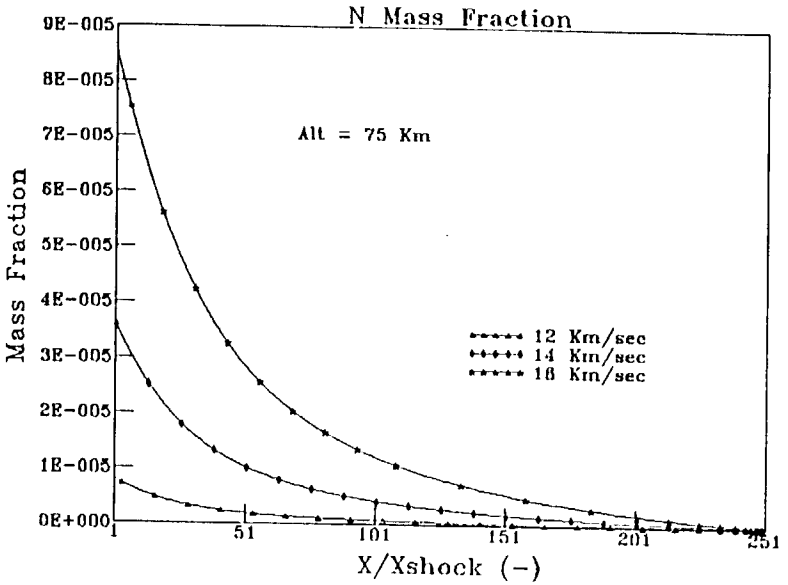
N Mass Fraction
9E-005
8E-005
7E-005
6E-005
5E-005
4E-005
3E-005
2E-005
1E-005
0E+000
Mass Fraction
Alt = 75 Km
12 Km/sec
14 Km/sec
16 Km/sec
1
51
101
151
201
251
X/Xshock (-)

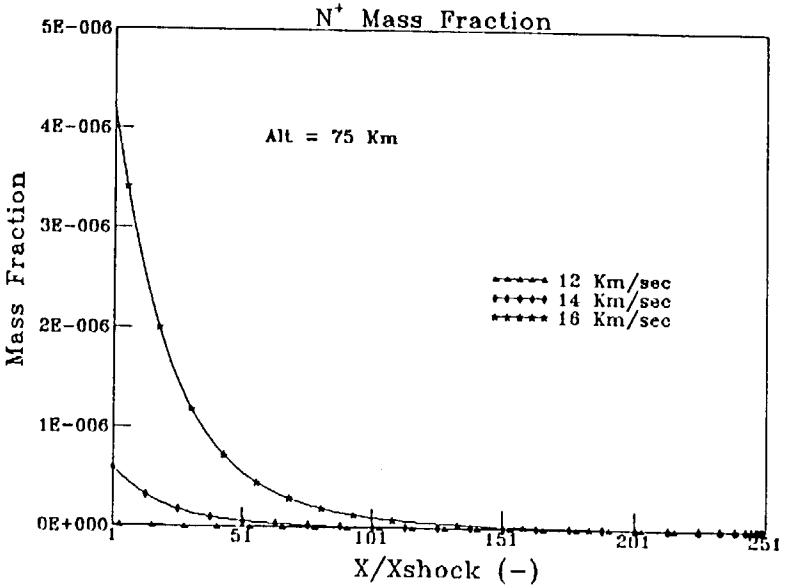
N^+ Mass Fraction
5E-006
4E-006
3E-006
2E-006
1E-006
0E+000
Mass Fraction
Alt = 75 Km
12 Km/sec
14 Km/sec
16 Km/sec
1
51
101
151
201
251
X/Xshock (-)

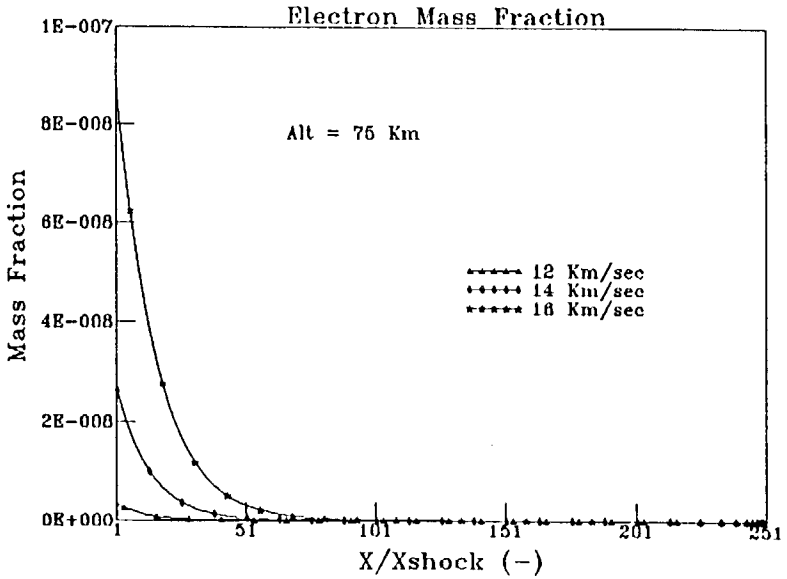
Electron Mass Fraction
Alt = 75 Km
12 Km/sec
14 Km/sec
16 Km/sec
Mass Fraction
1E-007
8E-008
6E-008
4E-008
2E-008
0E+000
1
51
101
151
201
251
X/Xshock (-)

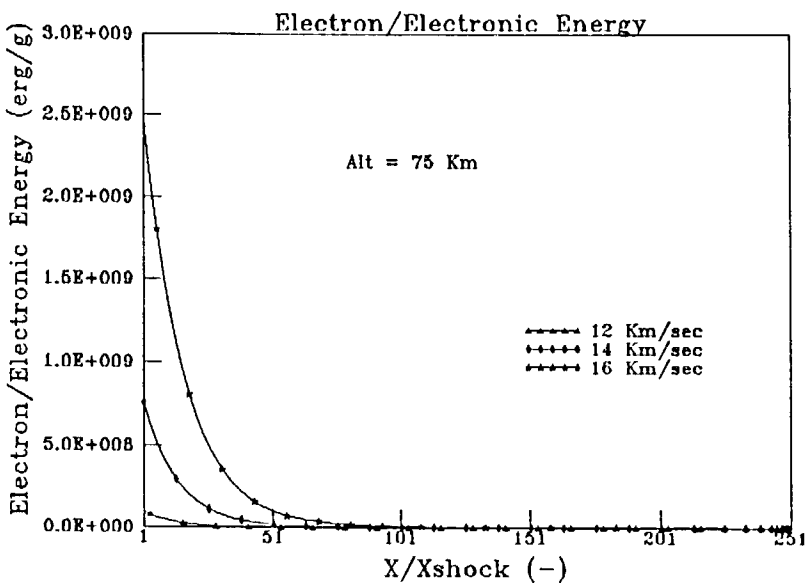
Electron/Electronic Energy
Alt = 75 Km
12 Km/sec
14 Km/sec
16 Km/sec
Electron/Electronic Energy (erg/g)
3.0E+009
2.5E+009
2.0E+009
1.5E+009
1.0E+009
5.0E+008
0.0E+000
1
51
101
151
201
251
X/Xshock (-)

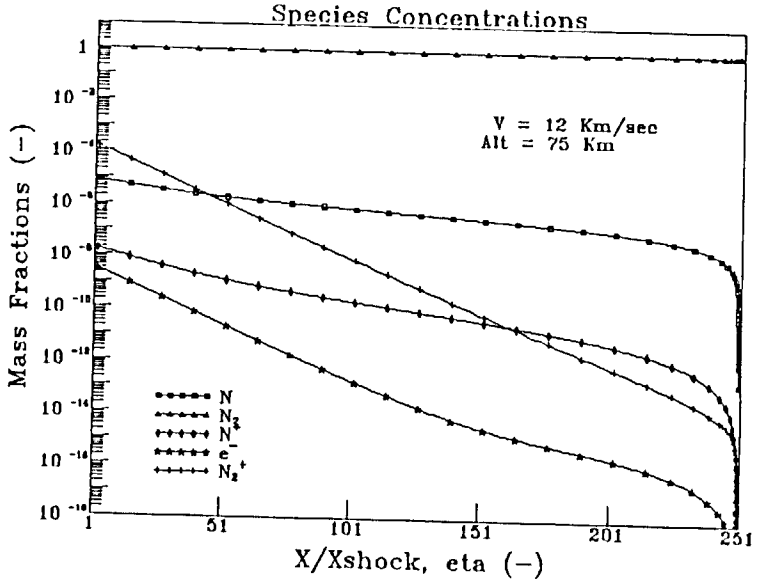
Species Concentrations
V = 12 Km/sec
Alt = 75 Km
Mass Fractions (-)
X/Xshock, eta (-)
N
N2
N+
e-
N2+

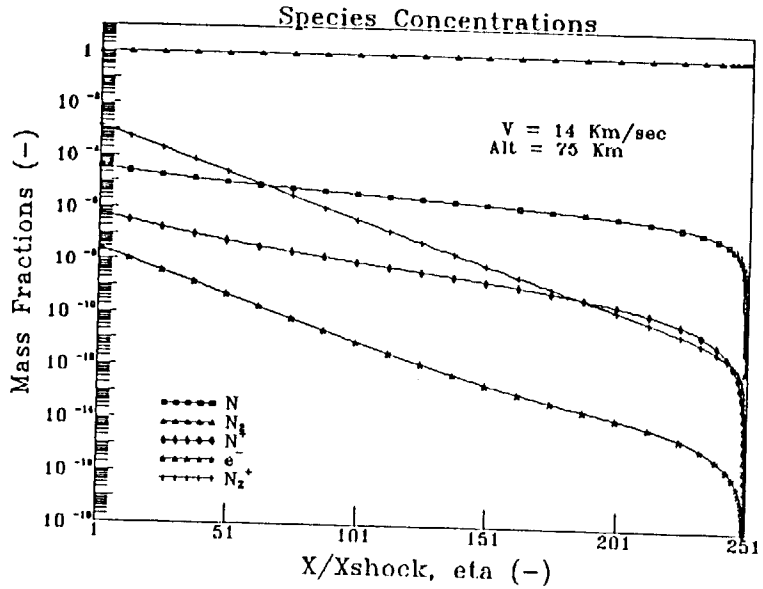
Species Concentrations
V = 14 Km/sec
Alt = 75 Km
Mass Fractions (-)
X/Xshock, eta (-)
N
N2
N+
e-
N2+

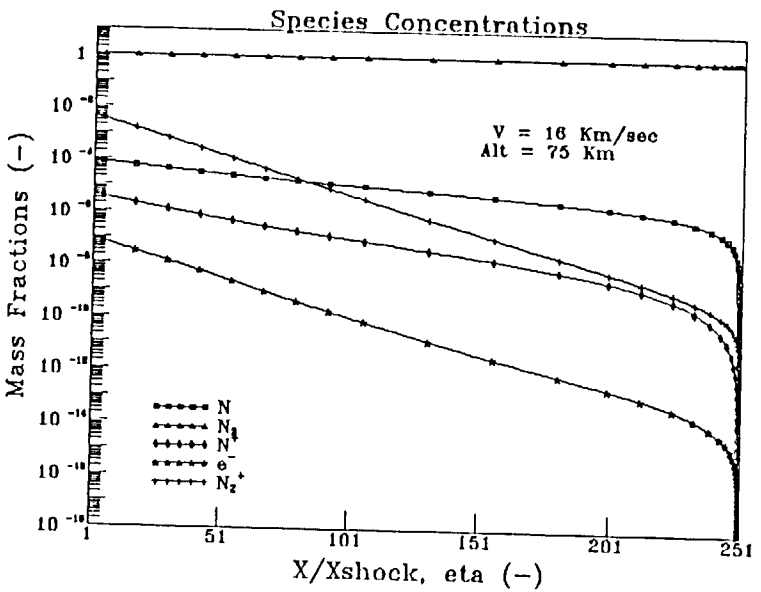
Species Concentrations
V = 16 Km/sec
Alt = 75 Km
Mass Fractions (-)
X/Xshock, eta (-)
N
N2
N+
e-
N2+

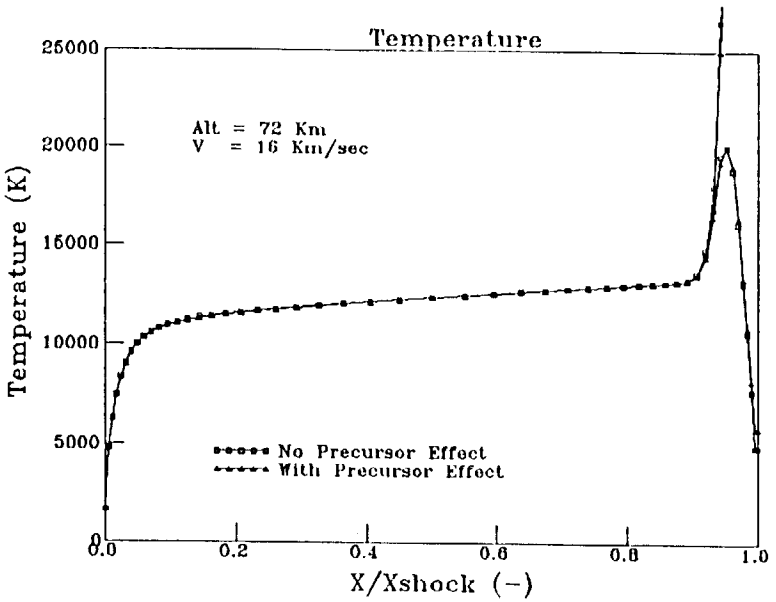
Temperature
Alt = 72 Km
V = 16 Km/sec
No Precursor Effect
With Precursor Effect
Temperature (K)
X/Xshock (-)
25000
20000
15000
10000
5000
0
0.0
0.2
0.4
0.6
0.8
1.0

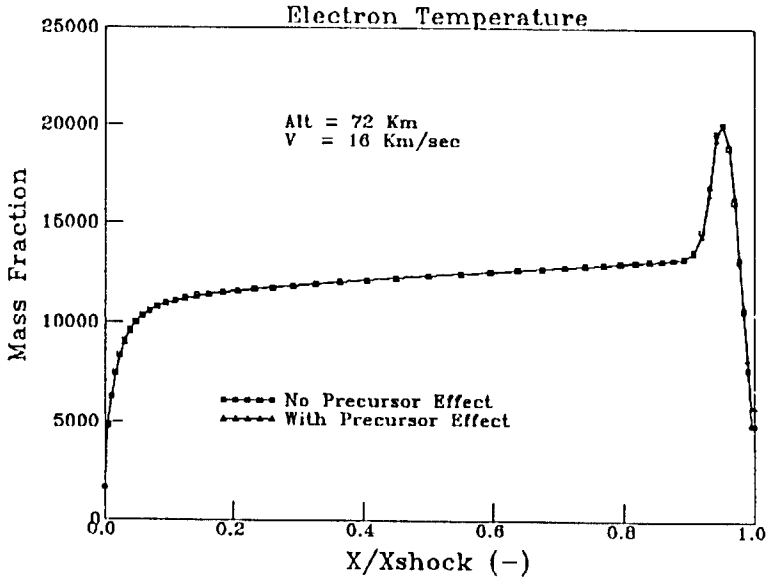
Electron Temperature
Alt = 72 Km
V = 16 Km/sec
No Precursor Effect
With Precursor Effect
Mass Fraction
X/Xshock (-)
25000
20000
15000
10000
5000
0
0.0
0.2
0.4
0.6
0.8
1.0

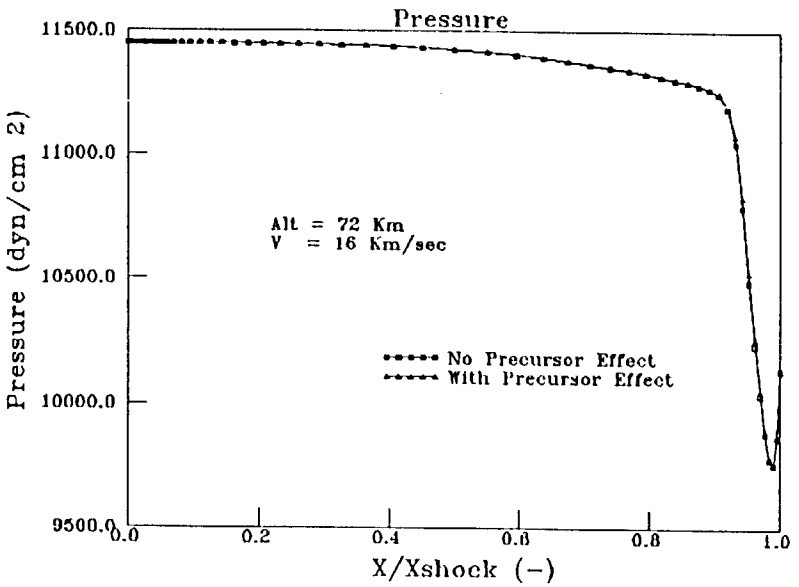
Pressure
Alt = 72 Km
V = 16 Km/sec
No Precursor Effect
With Precursor Effect
Pressure (dyn/cm 2)
X/Xshock (-)
11500.0
11000.0
10500.0
10000.0
9500.0
0.0
0.2
0.4
0.6
0.8
1.0

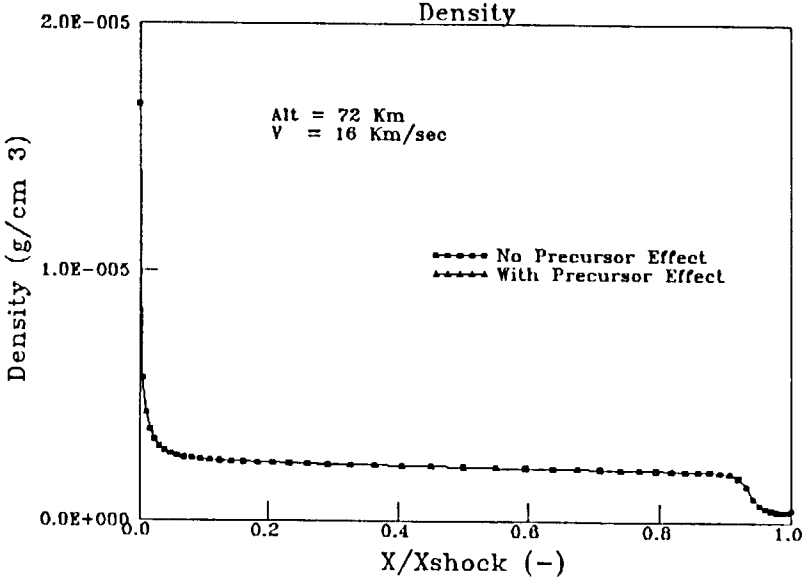
Density
Alt = 72 Km
V = 16 Km/sec
No Precursor Effect
With Precursor Effect
Density (g/cm 3)
X/Xshock (-)
2.0E-005
1.0E-005
0.0E+000
0.0
0.2
0.4
0.6
0.8
1.0

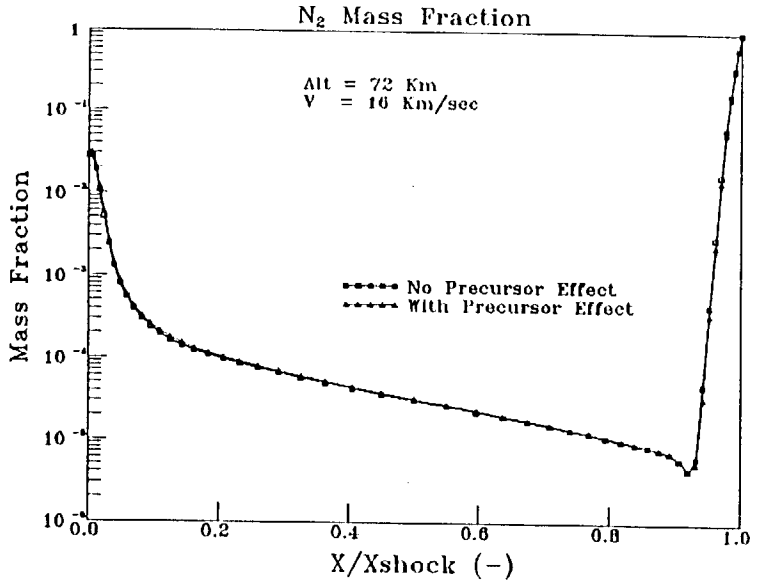
N_2 Mass Fraction
Alt = 72 Km
V = 16 Km/sec
No Precursor Effect
With Precursor Effect
Mass Fraction
X/Xshock (-)

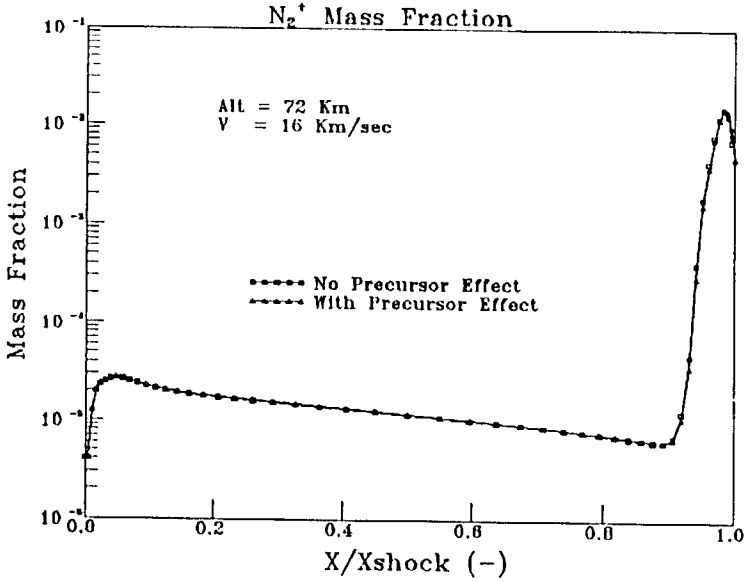
N_2^+ Mass Fraction
Alt = 72 Km
V = 16 Km/sec
No Precursor Effect
With Precursor Effect
Mass Fraction
X/Xshock (-)

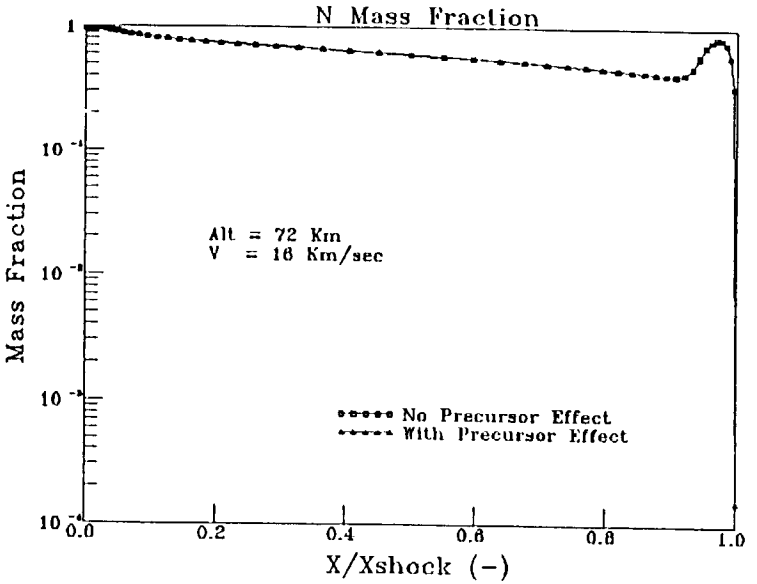
N Mass Fraction
Alt = 72 Km
V = 16 Km/sec
No Precursor Effect
With Precursor Effect
Mass Fraction
X/Xshock (-)

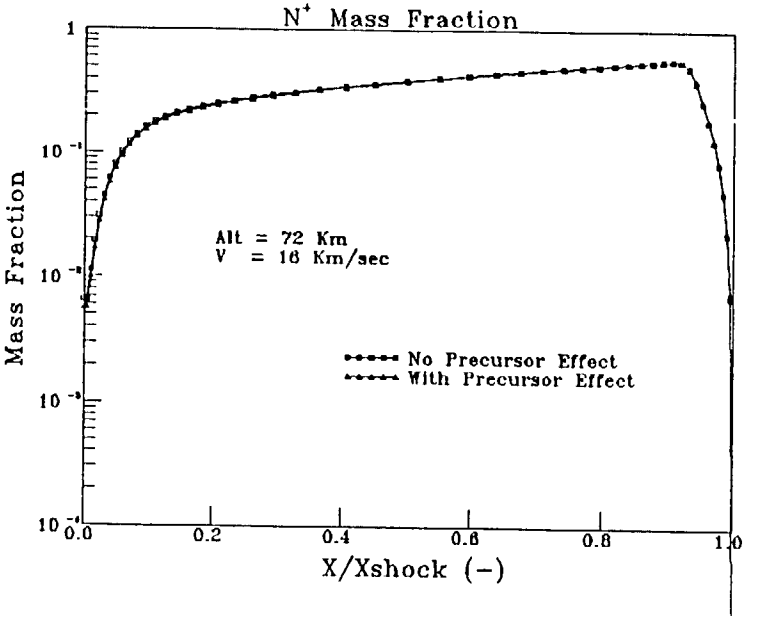
N^+ Mass Fraction
Alt = 72 Km
V = 16 Km/sec
No Precursor Effect
With Precursor Effect
Mass Fraction
X/Xshock (-)

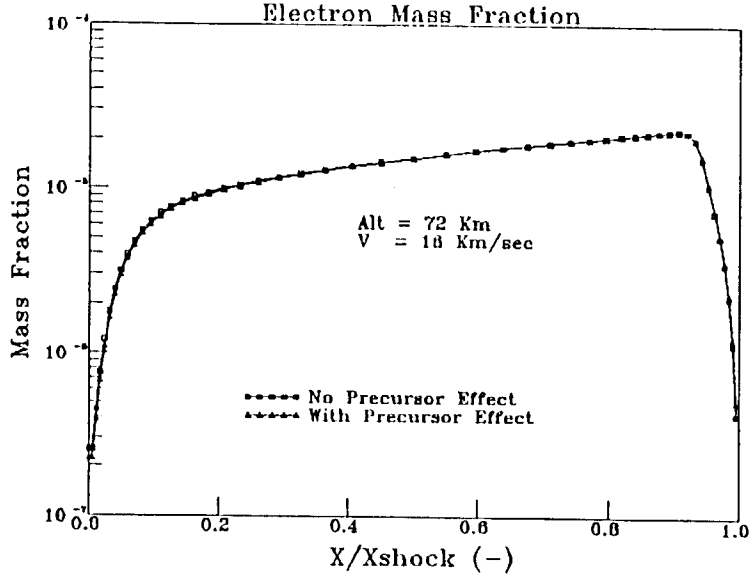
Electron Mass Fraction
Mass Fraction
Alt = 72 Km
V = 16 Km/sec
No Precursor Effect
With Precursor Effect
X/Xshock (-)

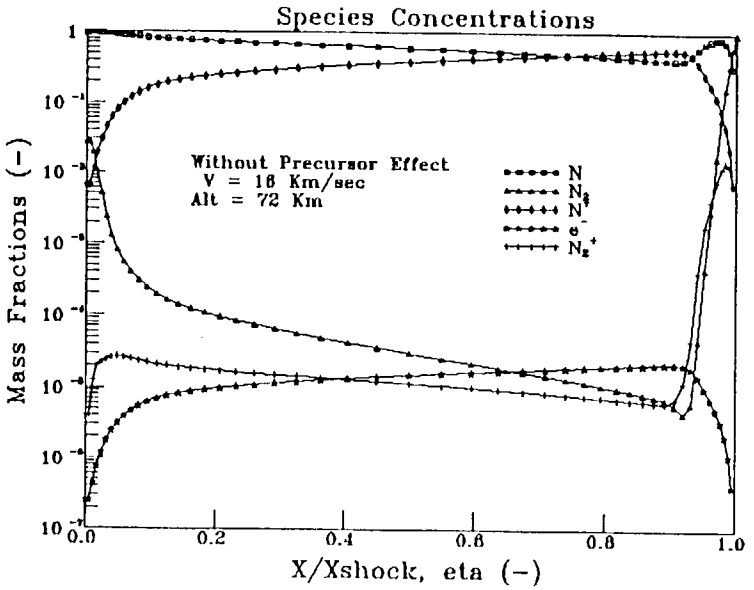
Species Concentrations
Mass Fractions (-)
Without Precursor Effect
V = 16 Km/sec
Alt = 72 Km
N
N2
N+
e-
N2+
X/Xshock, eta (-)

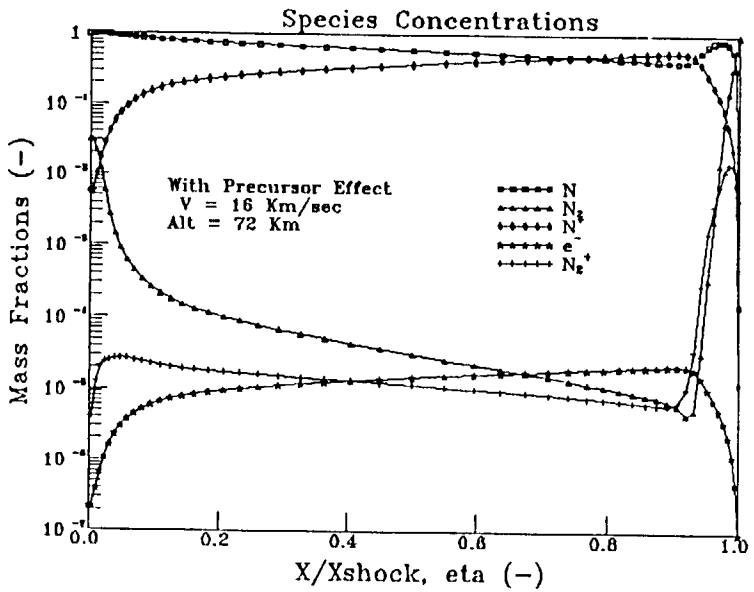
Species Concentrations
Mass Fractions (-)
With Precursor Effect
V = 16 Km/sec
Alt = 72 Km
N
N2
N+
e-
N2+
X/Xshock, eta (-)

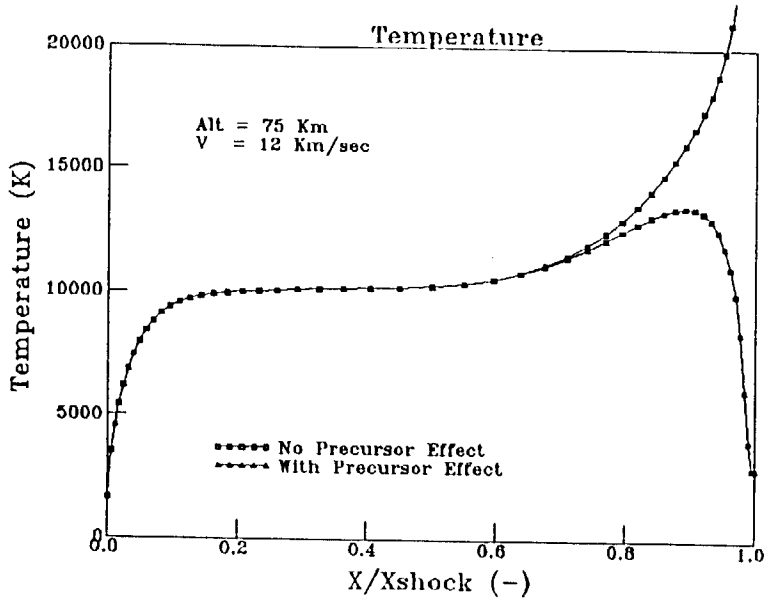
Temperature
Alt = 75 Km
V = 12 Km/sec
No Precursor Effect
With Precursor Effect
Temperature (K)
20000
15000
10000
5000
0
0.0
0.2
0.4
0.6
0.8
1.0
X/Xshock (-)

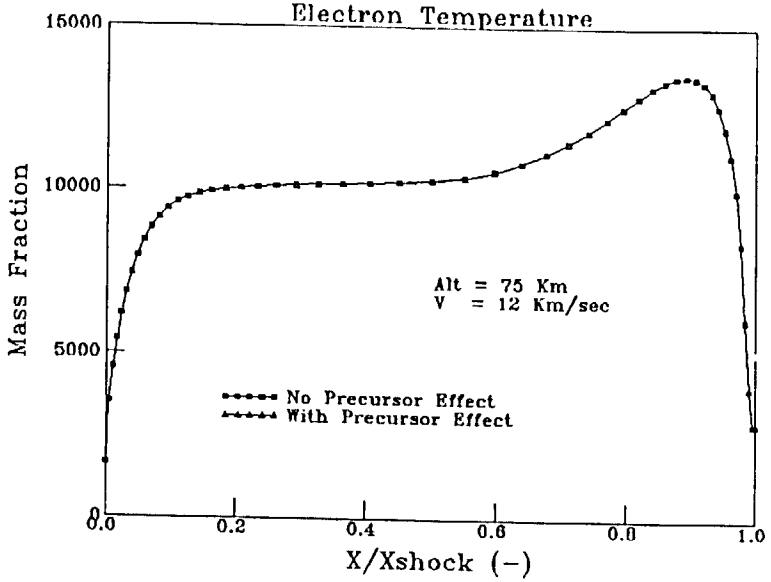
Electron Temperature
Alt = 75 Km
V = 12 Km/sec
No Precursor Effect
With Precursor Effect
Mass Fraction
15000
10000
5000
0
0.0
0.2
0.4
0.6
0.8
1.0
X/Xshock (-)

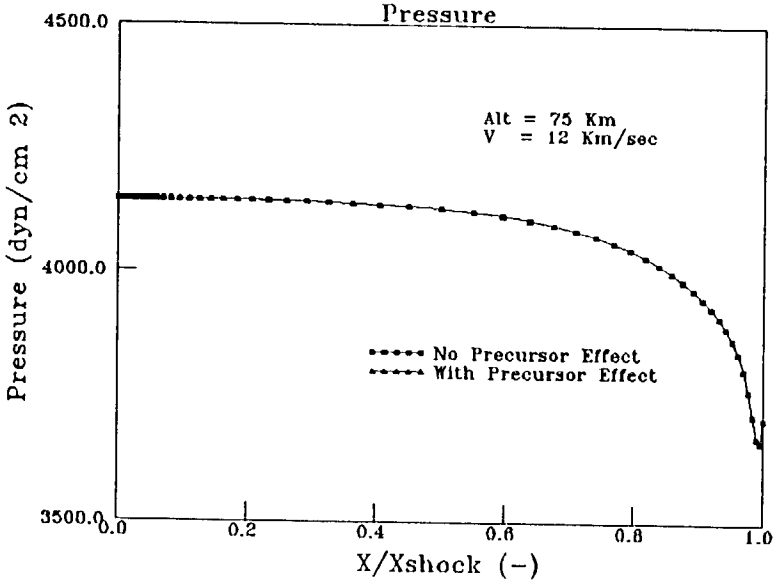
Pressure
Alt = 75 Km
V = 12 Km/sec
No Precursor Effect
With Precursor Effect
Pressure (dyn/cm 2)
4500.0
4000.0
3500.0
0.0
0.2
0.4
0.6
0.8
1.0
X/Xshock (-)

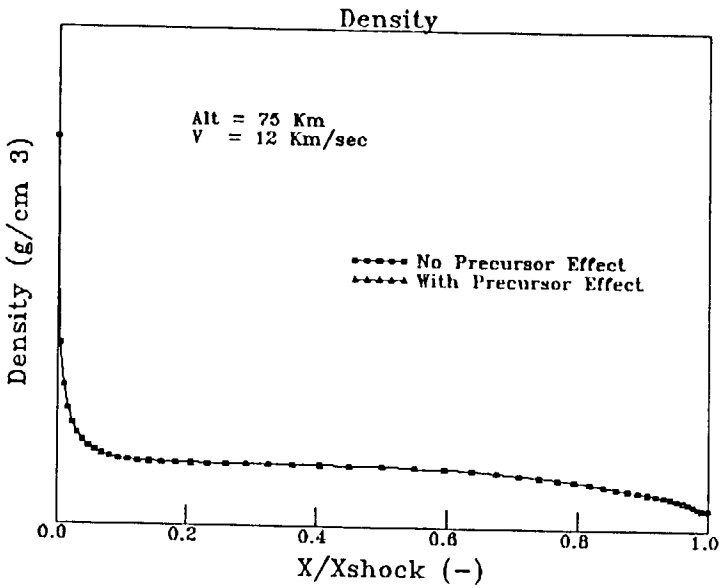
Density
Alt = 75 Km
V = 12 Km/sec
No Precursor Effect
With Precursor Effect
Density (g/cm 3)
0.0
0.2
0.4
0.6
0.8
1.0
X/Xshock (-)

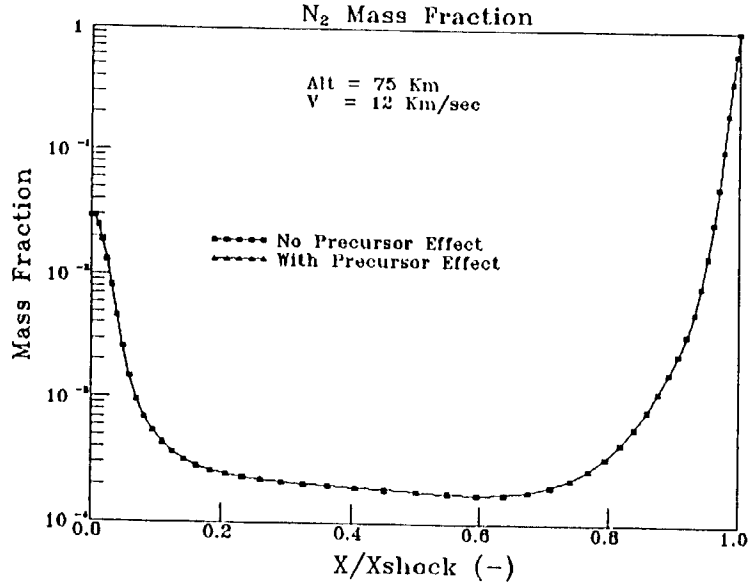
N_2 Mass Fraction
Alt = 75 Km
V = 12 Km/sec
No Precursor Effect
With Precursor Effect
Mass Fraction
X/Xshock (-)

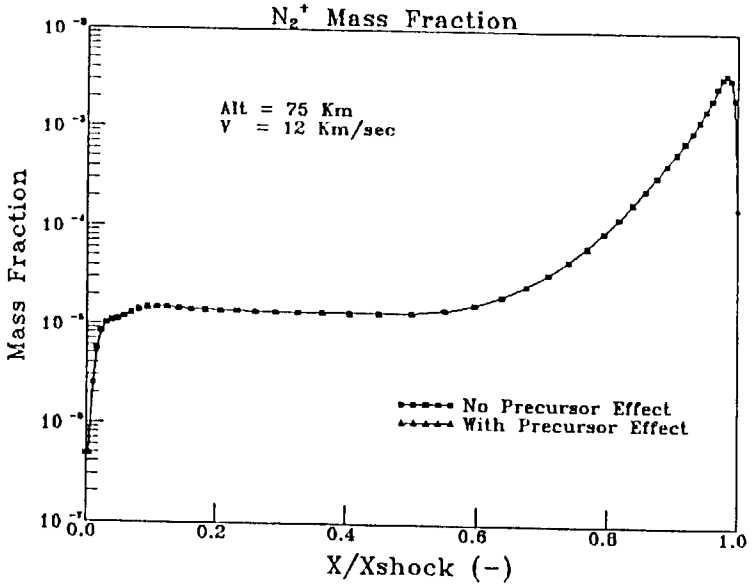
N_2^+ Mass Fraction
Alt = 75 Km
V = 12 Km/sec
No Precursor Effect
With Precursor Effect
Mass Fraction
X/Xshock (-)

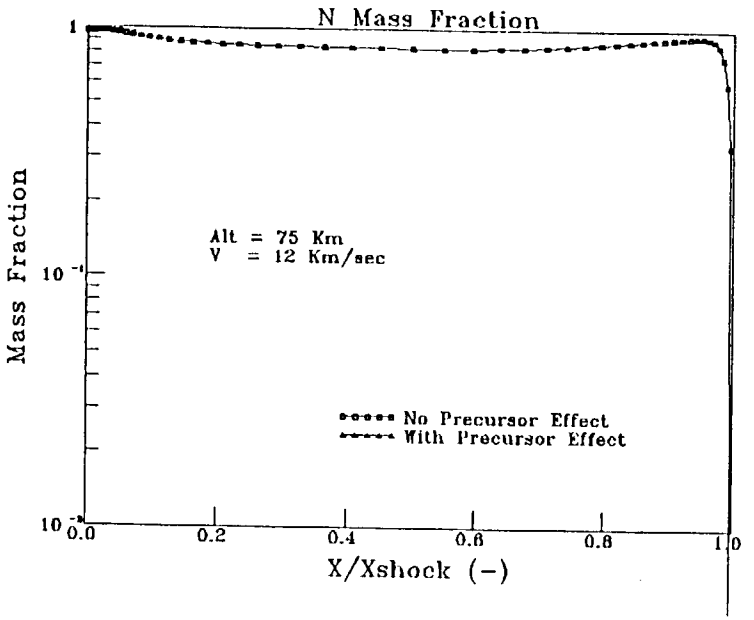
N Mass Fraction
Alt = 75 Km
V = 12 Km/sec
No Precursor Effect
With Precursor Effect
Mass Fraction
X/Xshock (-)

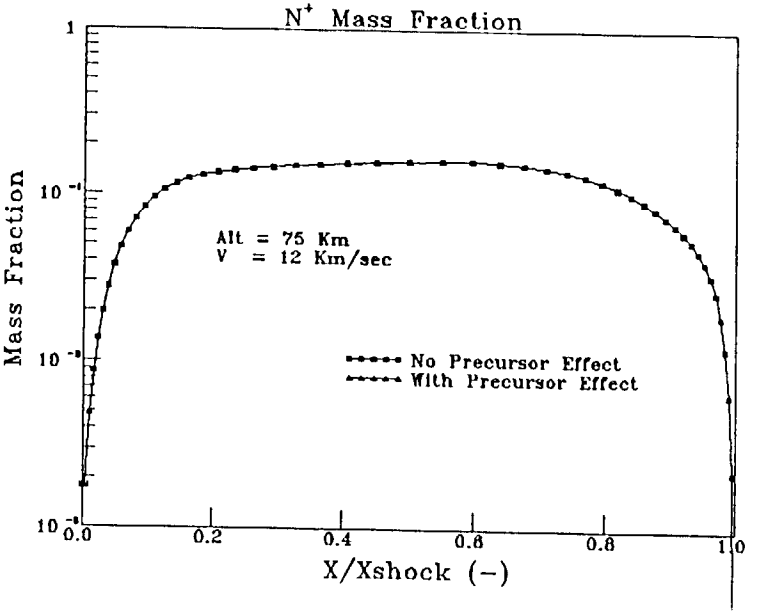
N^+ Mass Fraction
Alt = 75 Km
V = 12 Km/sec
No Precursor Effect
With Precursor Effect
Mass Fraction
X/Xshock (-)

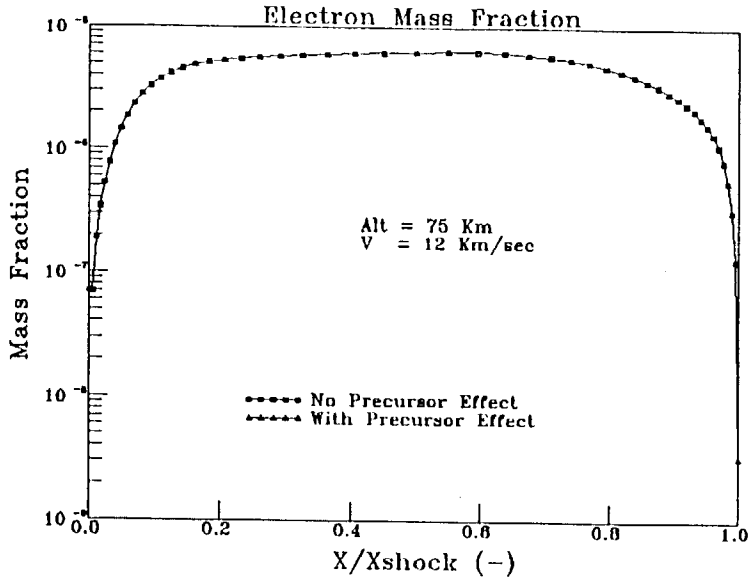
Electron Mass Fraction
Mass Fraction
Alt = 75 Km
V = 12 Km/sec
No Precursor Effect
With Precursor Effect
X/Xshock (-)

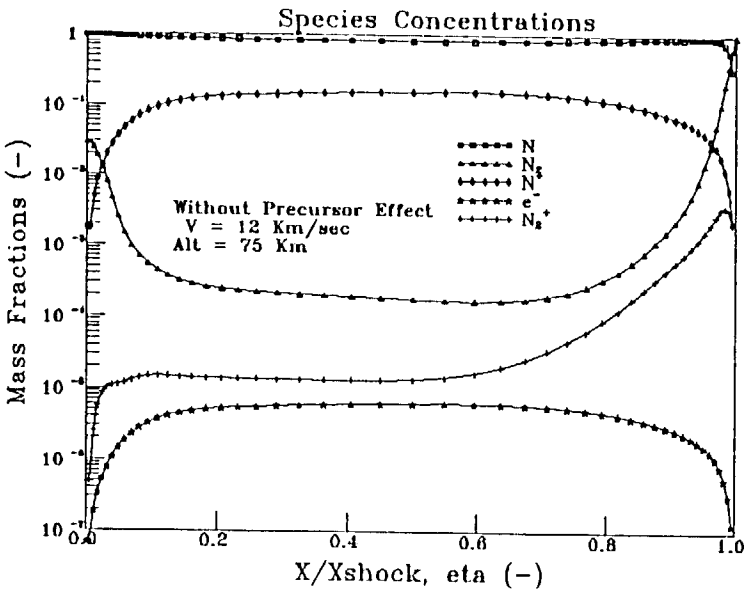
Species Concentrations
Mass Fractions (-)
Without Precursor Effect
V = 12 Km/sec
Alt = 75 Km
N
N_2
N^+
e^-
N_2^+
X/Xshock, eta (-)

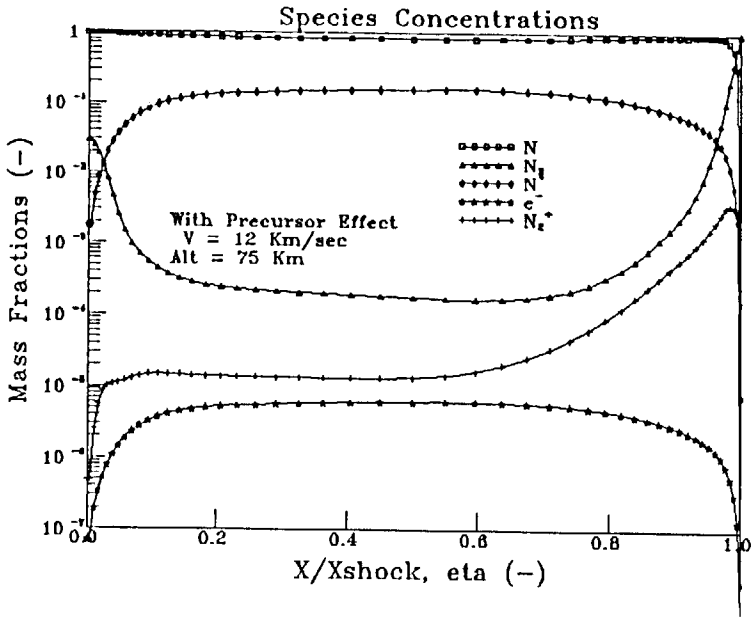
Species Concentrations
Mass Fractions (-)
With Precursor Effect
V = 12 Km/sec
Alt = 75 Km
N
N_2
N^+
e^-
N_2^+
X/Xshock, eta (-)

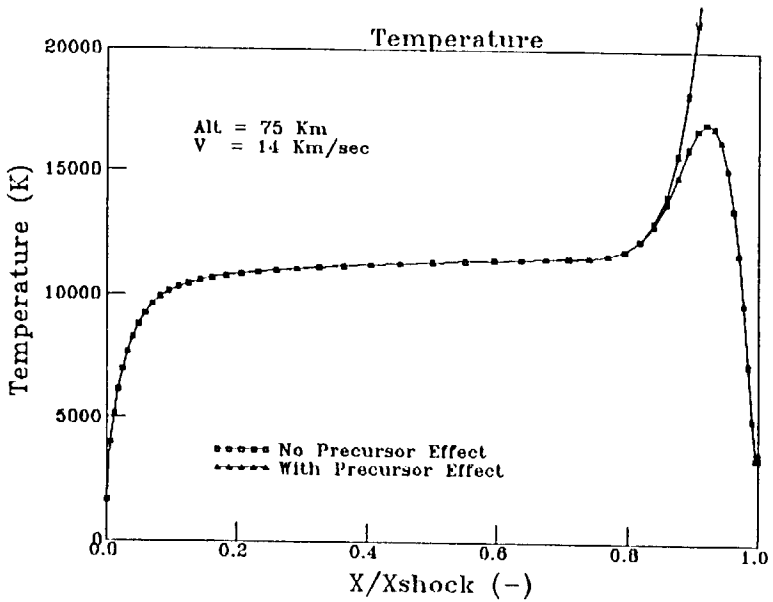
Temperature
Alt = 75 Km
V = 14 Km/sec
No Precursor Effect
With Precursor Effect
Temperature (K)
X/Xshock (-)
20000
15000
10000
5000
0
0.0
0.2
0.4
0.6
0.8
1.0

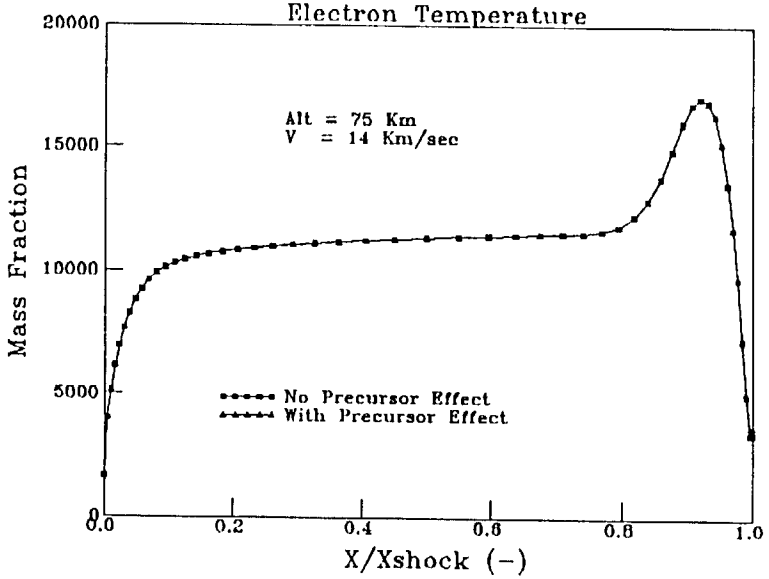
Electron Temperature
Alt = 75 Km
V = 14 Km/sec
No Precursor Effect
With Precursor Effect
Mass Fraction
X/Xshock (-)
20000
15000
10000
5000
0
0.0
0.2
0.4
0.6
0.8
1.0

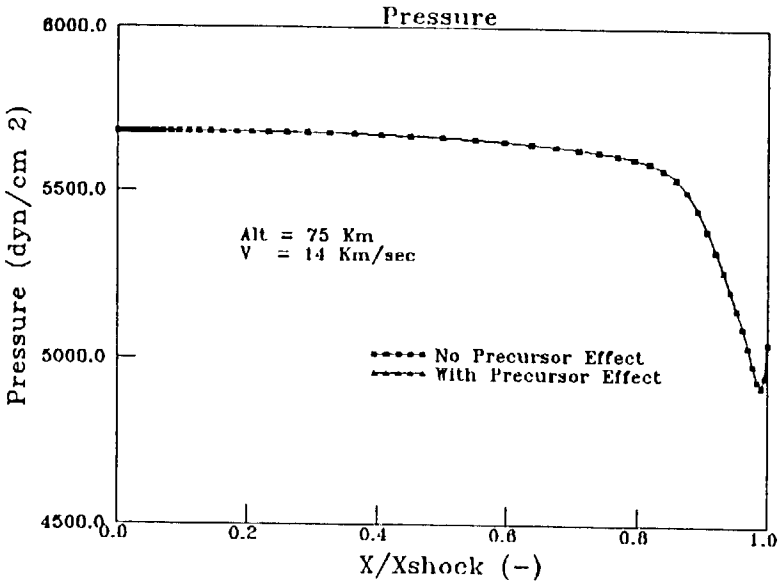
Pressure
Alt = 75 Km
V = 14 Km/sec
No Precursor Effect
With Precursor Effect
Pressure (dyn/cm 2)
X/Xshock (-)
6000.0
5500.0
5000.0
4500.0
0.0
0.2
0.4
0.6
0.8
1.0

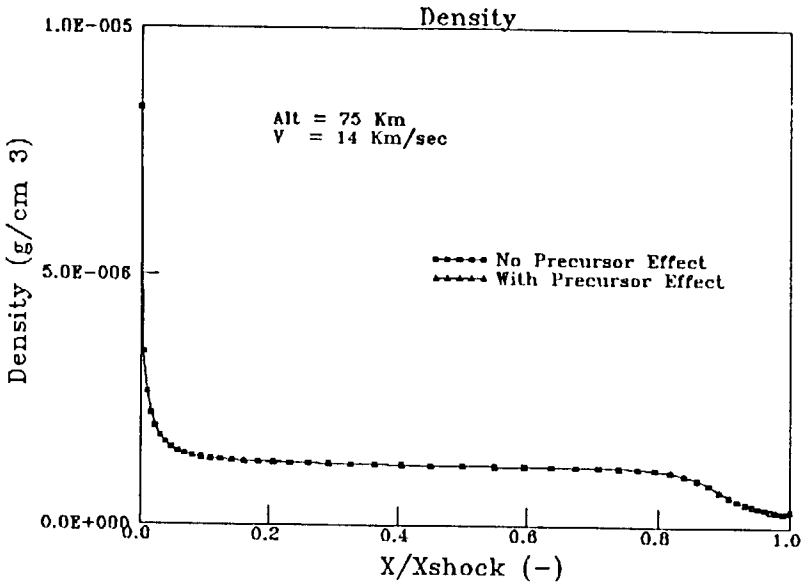
Density
Alt = 75 Km
V = 14 Km/sec
No Precursor Effect
With Precursor Effect
Density (g/cm 3)
X/Xshock (-)
1.0E-005
5.0E-006
0.0E+000
0.0
0.2
0.4
0.6
0.8
1.0

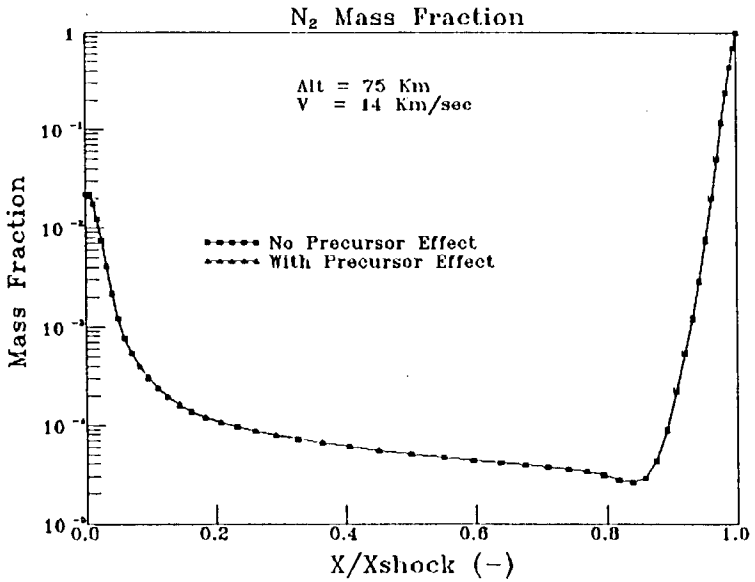
N_2 Mass Fraction
Alt = 75 Km
V = 14 Km/sec
No Precursor Effect
With Precursor Effect
Mass Fraction
X/Xshock (-)

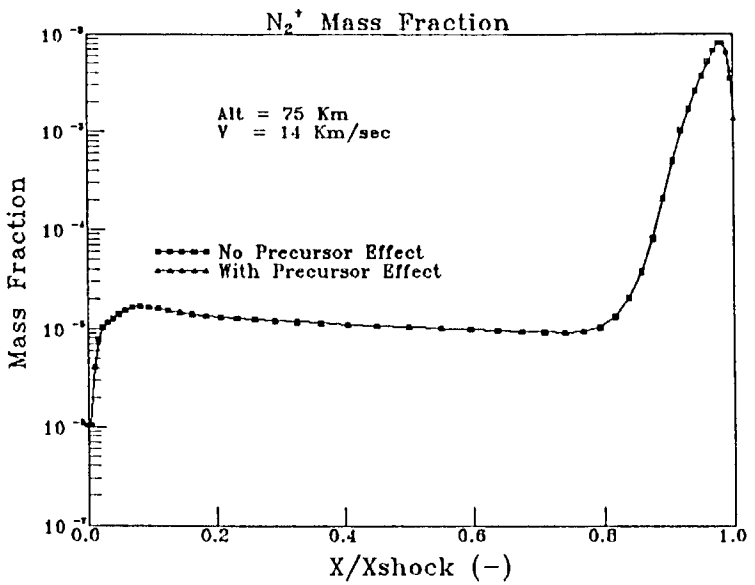
N_2^+ Mass Fraction
Alt = 75 Km
V = 14 Km/sec
No Precursor Effect
With Precursor Effect
Mass Fraction
X/Xshock (-)

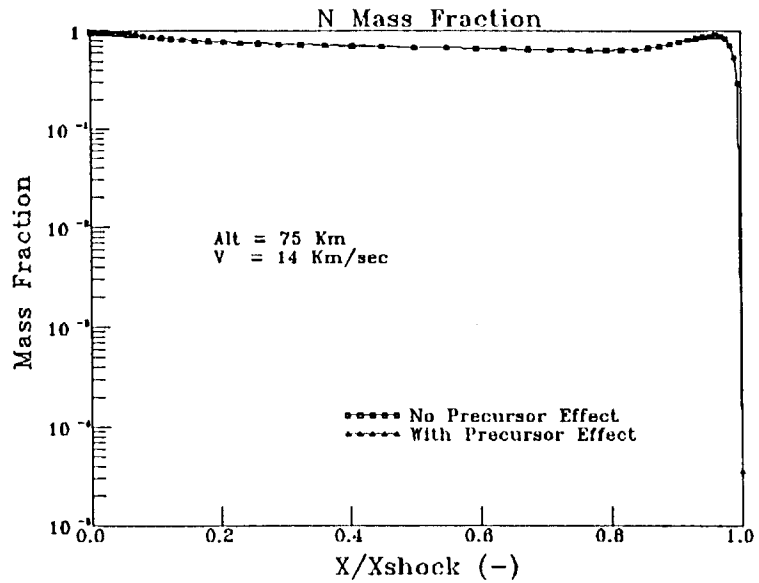
N Mass Fraction
Alt = 75 Km
V = 14 Km/sec
No Precursor Effect
With Precursor Effect
Mass Fraction
X/Xshock (-)

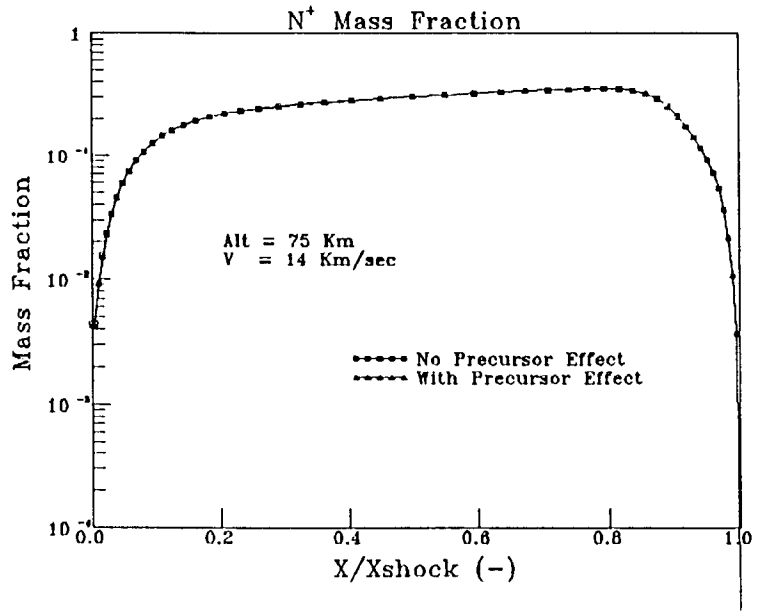
N^+ Mass Fraction
Alt = 75 Km
V = 14 Km/sec
No Precursor Effect
With Precursor Effect
Mass Fraction
X/Xshock (-)

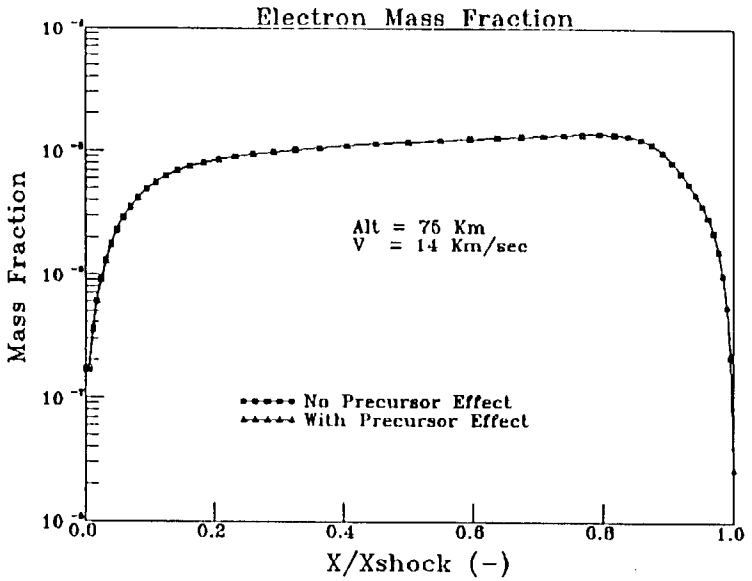
Electron Mass Fraction
Mass Fraction
Alt = 75 Km
V = 14 Km/sec
No Precursor Effect
With Precursor Effect
X/Xshock (-)

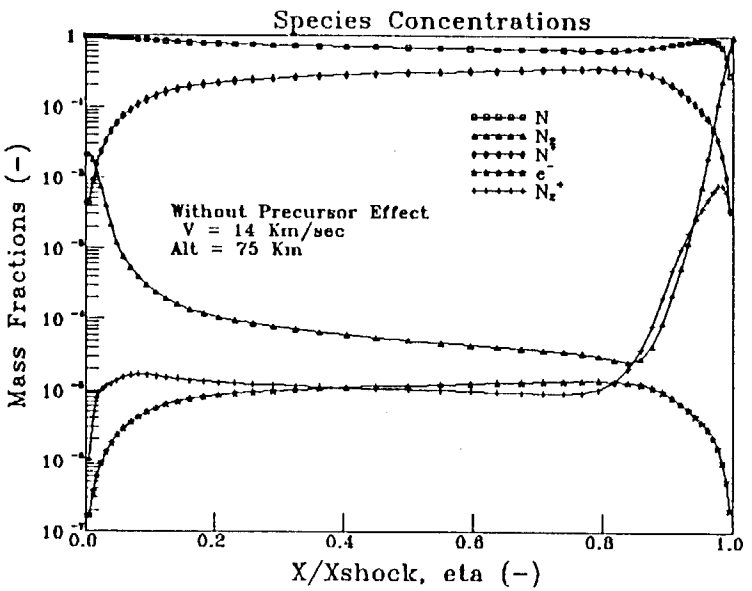
Species Concentrations
Mass Fractions (-)
N
N2
N+
e-
N2+
Without Precursor Effect
V = 14 Km/sec
Alt = 75 Km
X/Xshock, eta (-)

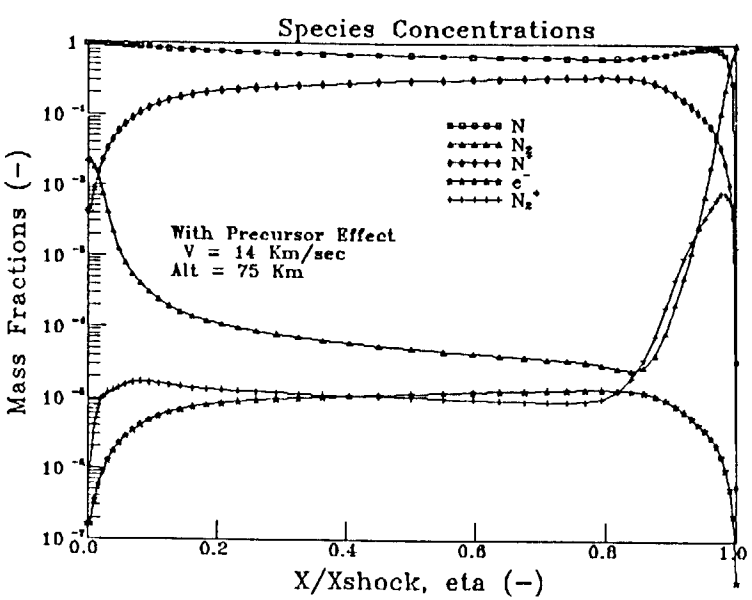
Species Concentrations
Mass Fractions (-)
N
N2
N+
e-
N2+
With Precursor Effect
V = 14 Km/sec
Alt = 75 Km
X/Xshock, eta (-)

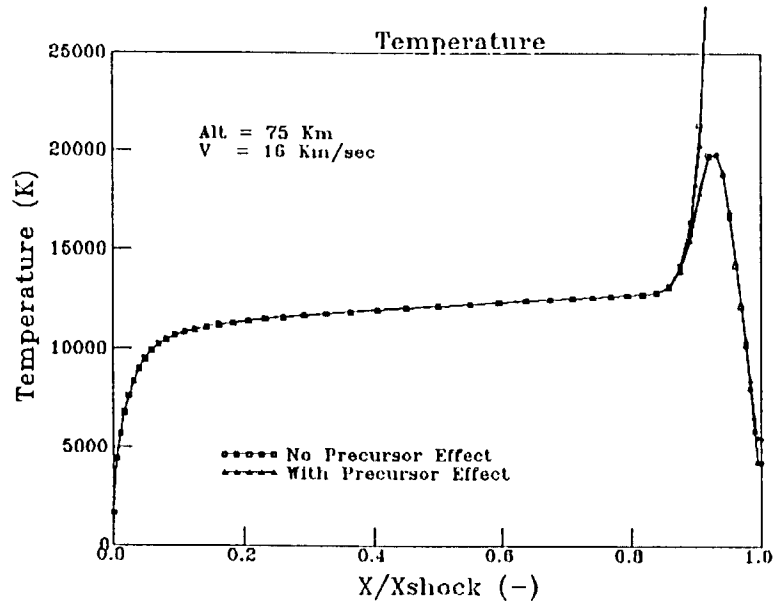
Temperature
Alt = 75 Km
V = 16 Km/sec
No Precursor Effect
With Precursor Effect
Temperature (K)
X/Xshock (-)
25000
20000
15000
10000
5000
0
0.0
0.2
0.4
0.6
0.8
1.0

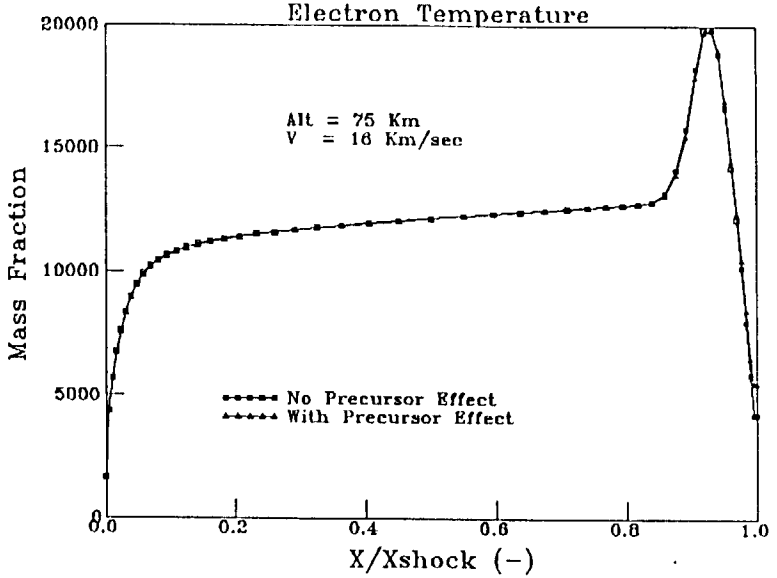
Electron Temperature
Alt = 75 Km
V = 16 Km/sec
No Precursor Effect
With Precursor Effect
Mass Fraction
X/Xshock (-)
20000
15000
10000
5000
0
0.0
0.2
0.4
0.6
0.8
1.0

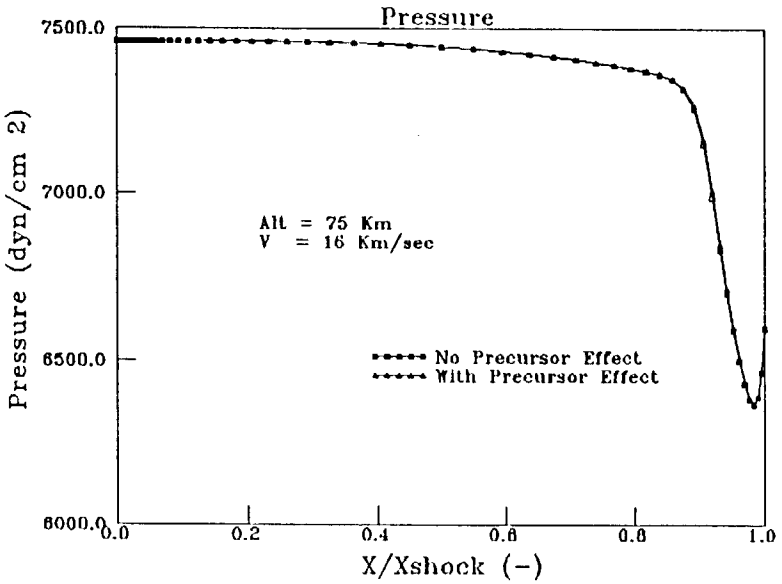
Pressure
Alt = 75 Km
V = 16 Km/sec
No Precursor Effect
With Precursor Effect
Pressure (dyn/cm 2)
X/Xshock (-)
7500.0
7000.0
6500.0
6000.0
0.0
0.2
0.4
0.6
0.8
1.0

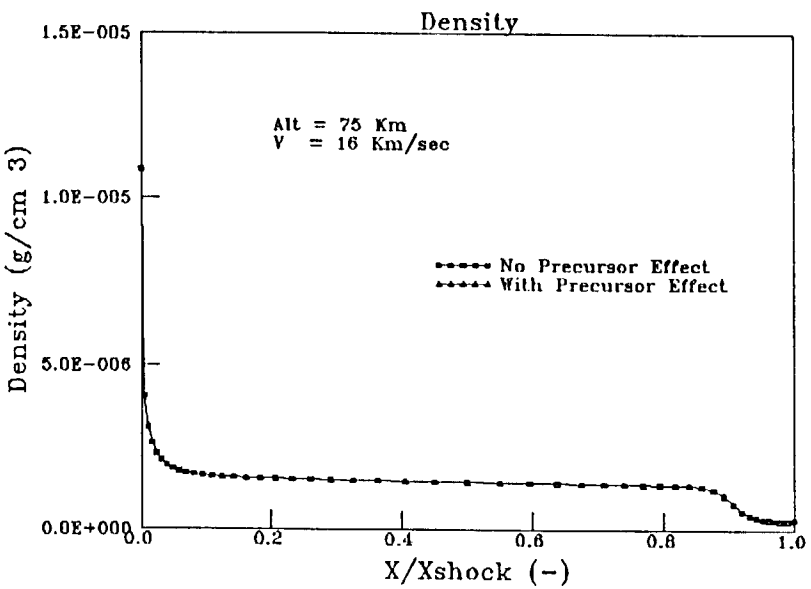
Density
Alt = 75 Km
V = 16 Km/sec
No Precursor Effect
With Precursor Effect
Density (g/cm 3)
X/Xshock (-)
1.5E-005
1.0E-005
5.0E-006
0.0E+000
0.0
0.2
0.4
0.6
0.8
1.0

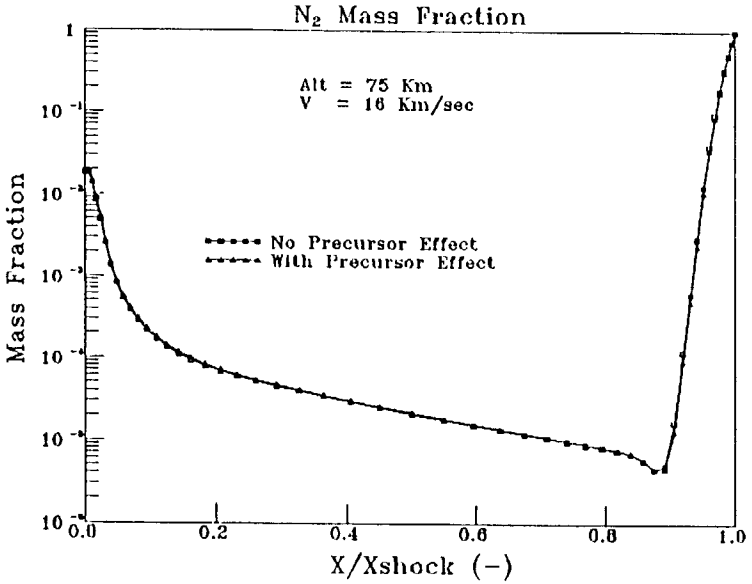
N2 Mass Fraction
Alt = 75 Km
V = 16 Km/sec
No Precursor Effect
With Precursor Effect
Mass Fraction
X/Xshock (-)

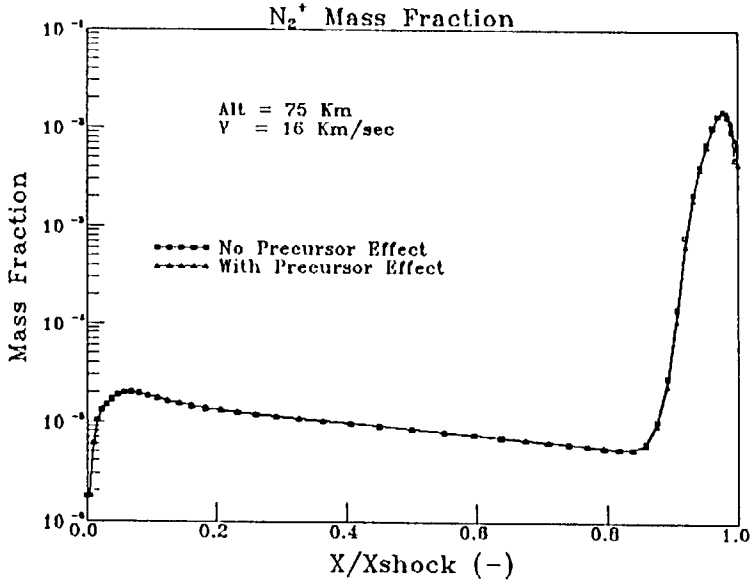
N2+ Mass Fraction
Alt = 75 Km
V = 16 Km/sec
No Precursor Effect
With Precursor Effect
Mass Fraction
X/Xshock (-)

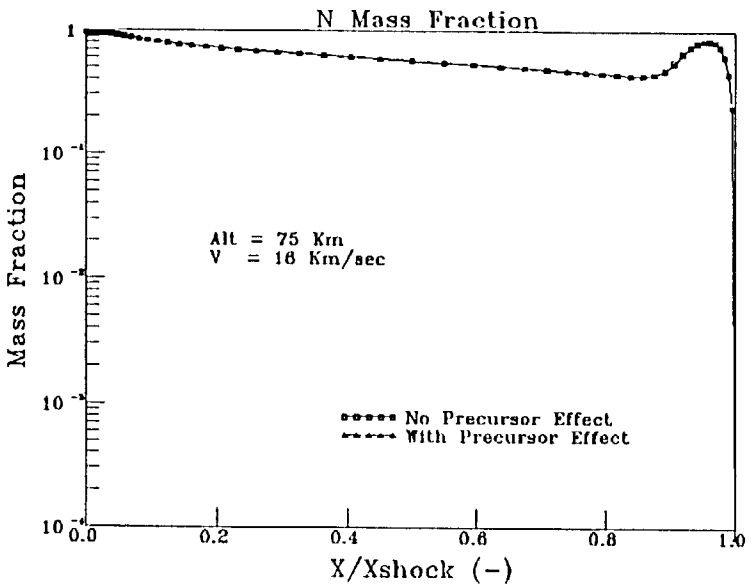
N Mass Fraction
Alt = 75 Km
V = 16 Km/sec
No Precursor Effect
With Precursor Effect
Mass Fraction
X/Xshock (-)

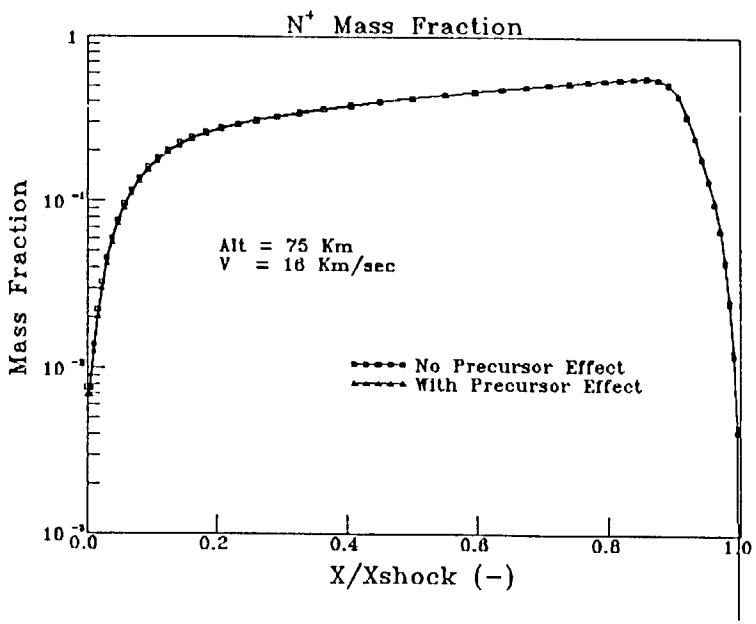
N+ Mass Fraction
Alt = 75 Km
V = 16 Km/sec
No Precursor Effect
With Precursor Effect
Mass Fraction
X/Xshock (-)

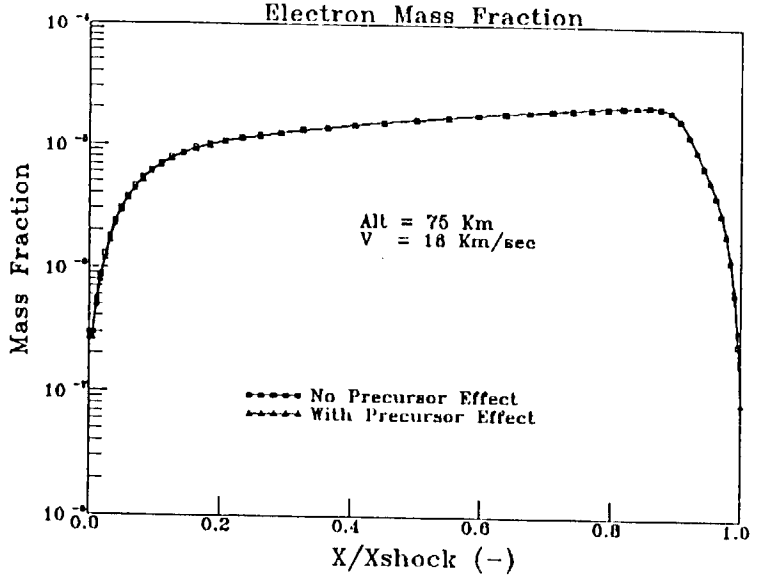
Electron Mass Fraction
Mass Fraction
Alt = 75 Km
V = 16 Km/sec
No Precursor Effect
With Precursor Effect
X/Xshock (-)

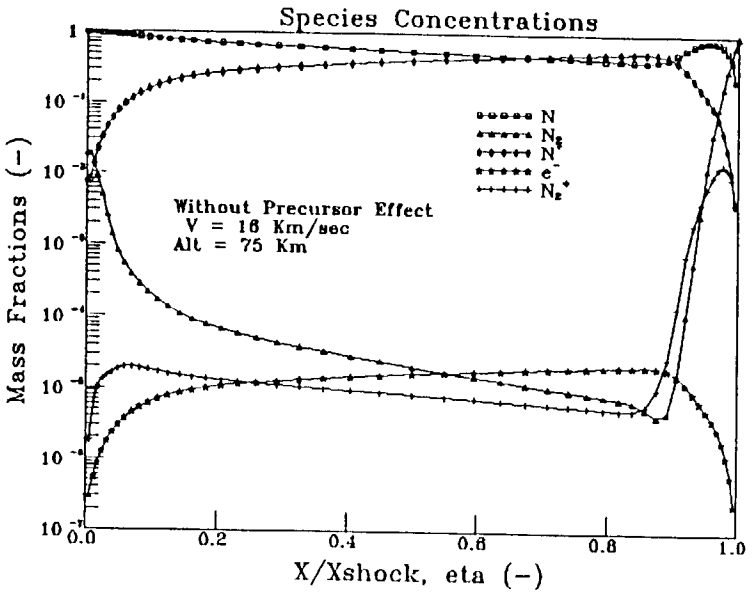
Species Concentrations
Mass Fractions (-)
N
N2
N+
e-
N2+
Without Precursor Effect
V = 16 Km/sec
Alt = 75 Km
X/Xshock, eta (-)

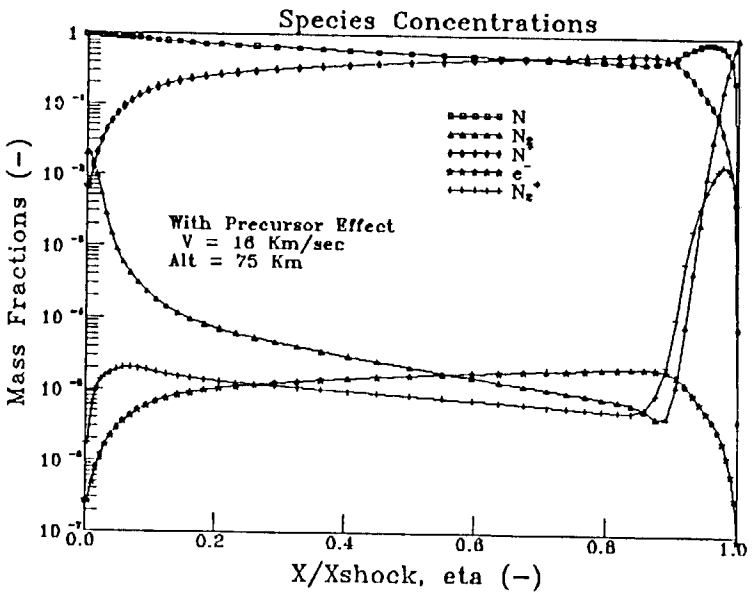
Species Concentrations
Mass Fractions (-)
N
N2
N+
e-
N2+
With Precursor Effect
V = 16 Km/sec
Alt = 75 Km
X/Xshock, eta (-)

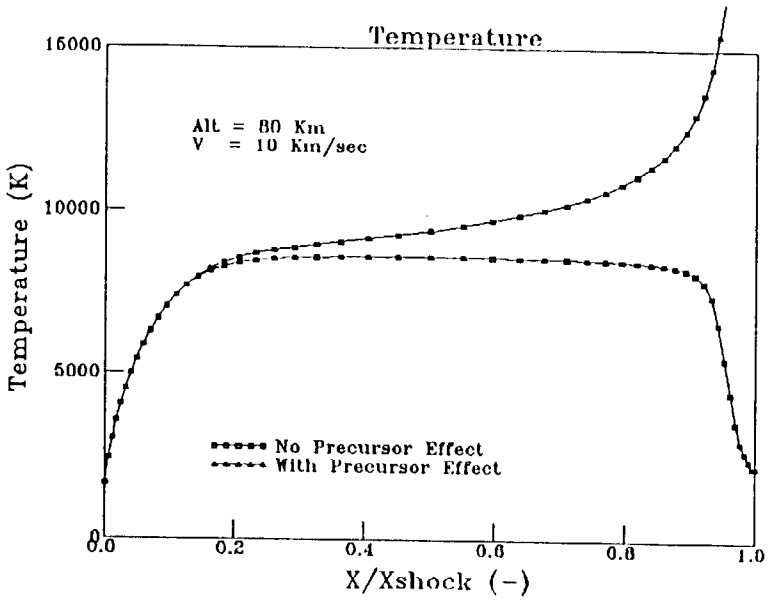
Temperature
Alt = 80 Km
V = 10 Km/sec
No Precursor Effect
With Precursor Effect
Temperature (K)
15000
10000
5000
0
0.0
0.2
0.4
0.6
0.8
1.0
X/Xshock (-)

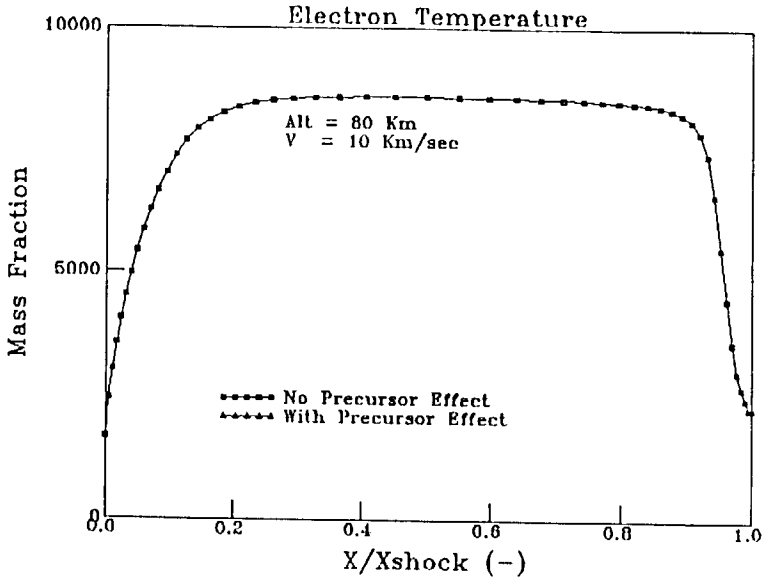
Electron Temperature
Alt = 80 Km
V = 10 Km/sec
No Precursor Effect
With Precursor Effect
Mass Fraction
10000
5000
0
0.0
0.2
0.4
0.6
0.8
1.0
X/Xshock (-)

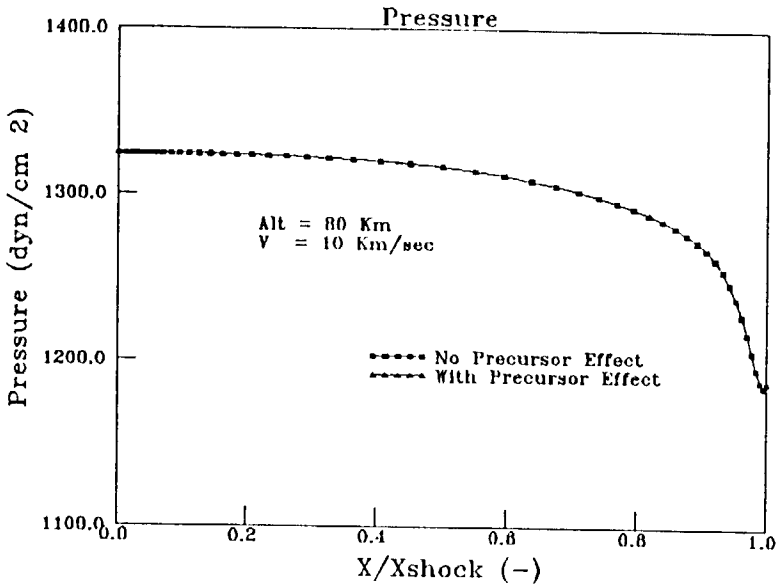
Pressure
Alt = 80 Km
V = 10 Km/sec
No Precursor Effect
With Precursor Effect
Pressure (dyn/cm 2)
1400.0
1300.0
1200.0
1100.0
0.0
0.2
0.4
0.6
0.8
1.0
X/Xshock (-)

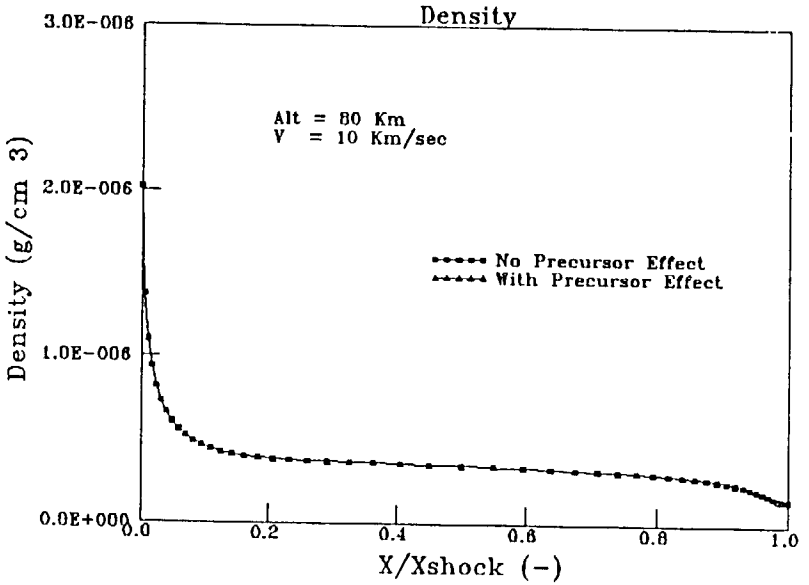
Density
Alt = 80 Km
V = 10 Km/sec
No Precursor Effect
With Precursor Effect
Density (g/cm 3)
3.0E-006
2.0E-006
1.0E-006
0.0E+000
0.0
0.2
0.4
0.6
0.8
1.0
X/Xshock (-)

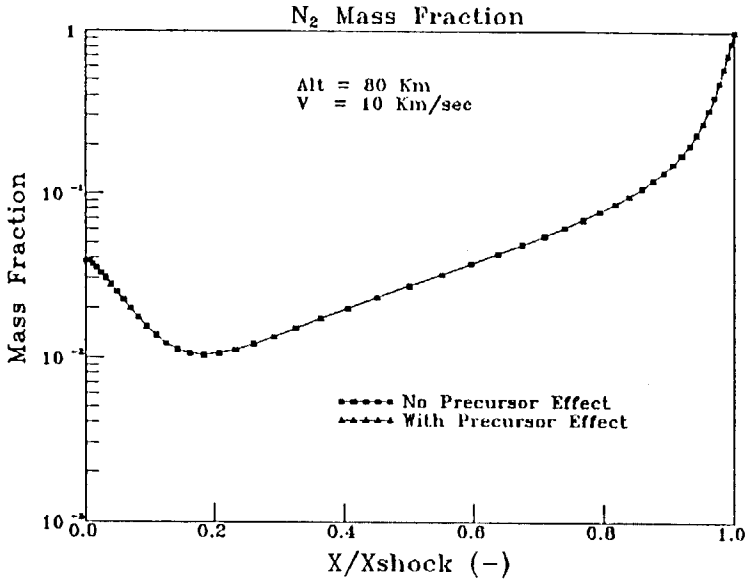
N_2 Mass Fraction
Alt = 80 Km
V = 10 Km/sec
No Precursor Effect
With Precursor Effect
Mass Fraction
X/Xshock (-)

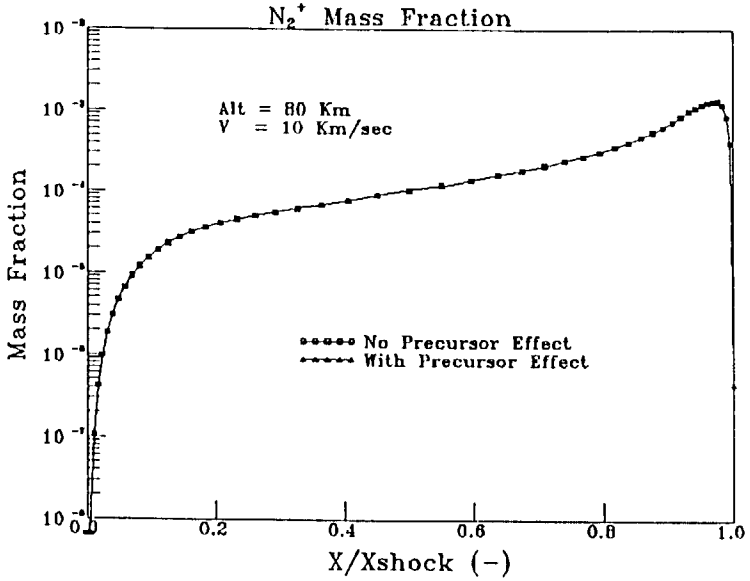
N_2^+ Mass Fraction
Alt = 80 Km
V = 10 Km/sec
No Precursor Effect
With Precursor Effect
Mass Fraction
X/Xshock (-)

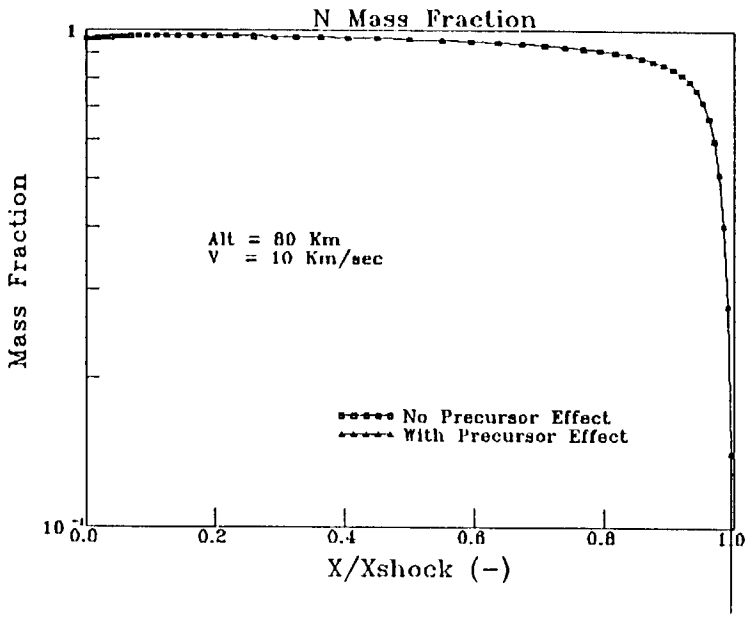
N Mass Fraction
Alt = 80 Km
V = 10 Km/sec
No Precursor Effect
With Precursor Effect
Mass Fraction
X/Xshock (-)

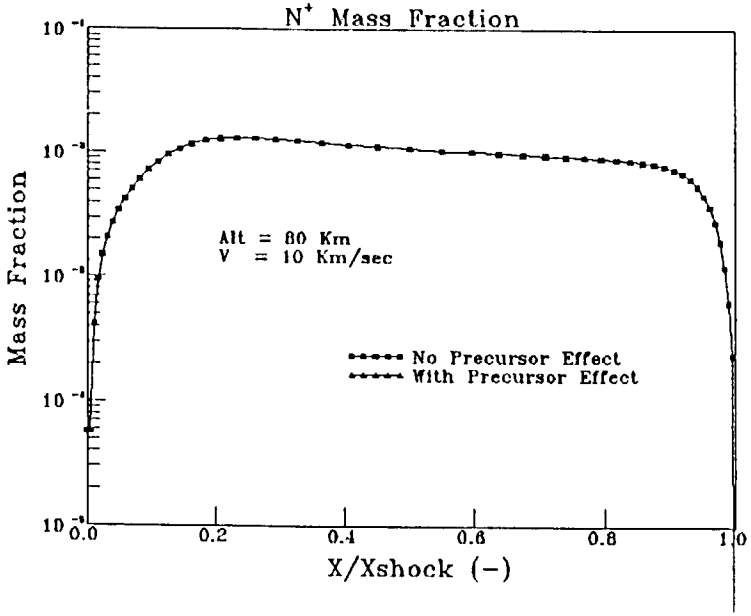
N^+ Mass Fraction
Alt = 80 Km
V = 10 Km/sec
No Precursor Effect
With Precursor Effect
Mass Fraction
X/Xshock (-)

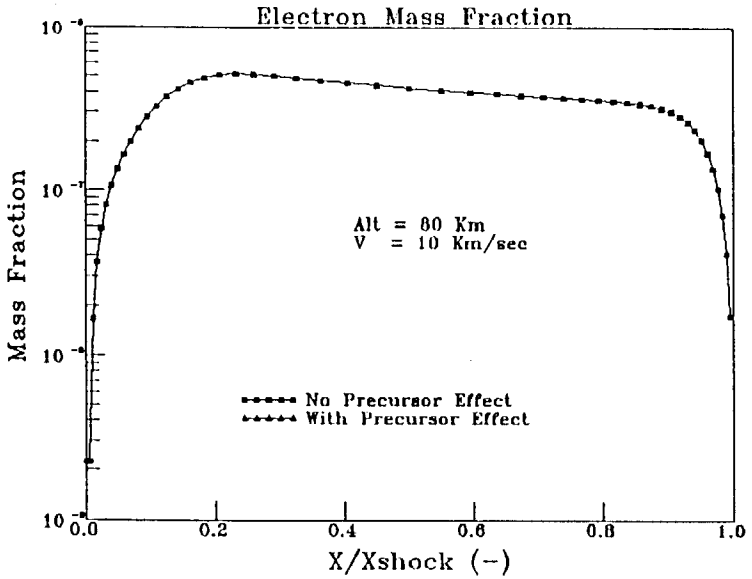
Electron Mass Fraction
Mass Fraction
Alt = 80 Km
V = 10 Km/sec
No Precursor Effect
With Precursor Effect
X/Xshock (-)

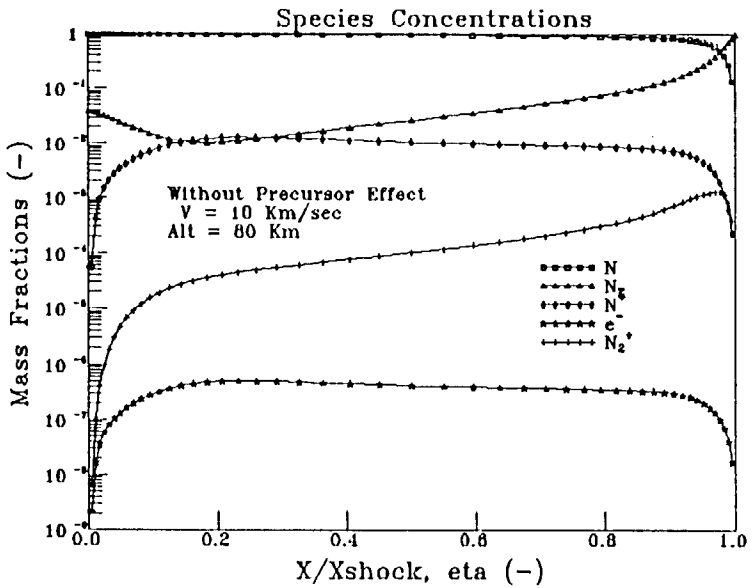
Species Concentrations
Mass Fractions (-)
Without Precursor Effect
V = 10 Km/sec
Alt = 80 Km
N
N2
N+
e-
N2+
X/Xshock, eta (-)

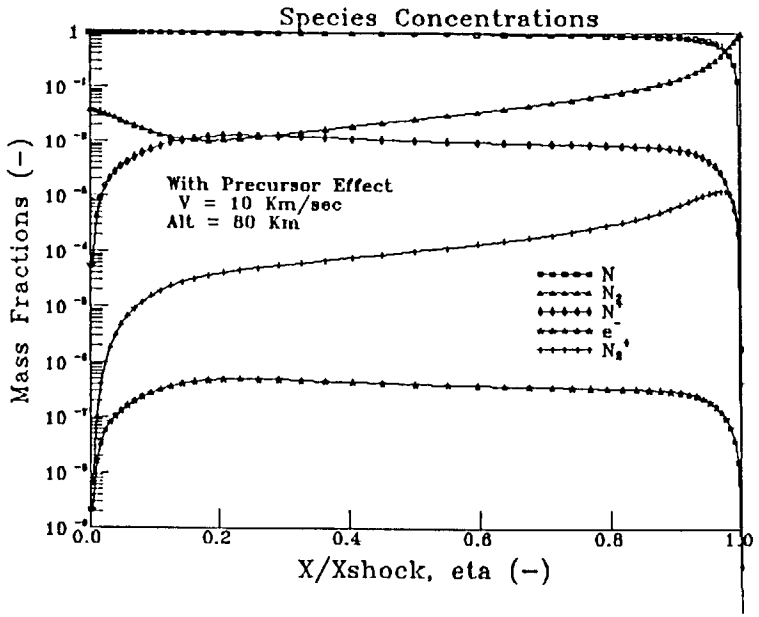
Species Concentrations
Mass Fractions (-)
With Precursor Effect
V = 10 Km/sec
Alt = 80 Km
N
N2
N+
e-
N2+
X/Xshock, eta (-)

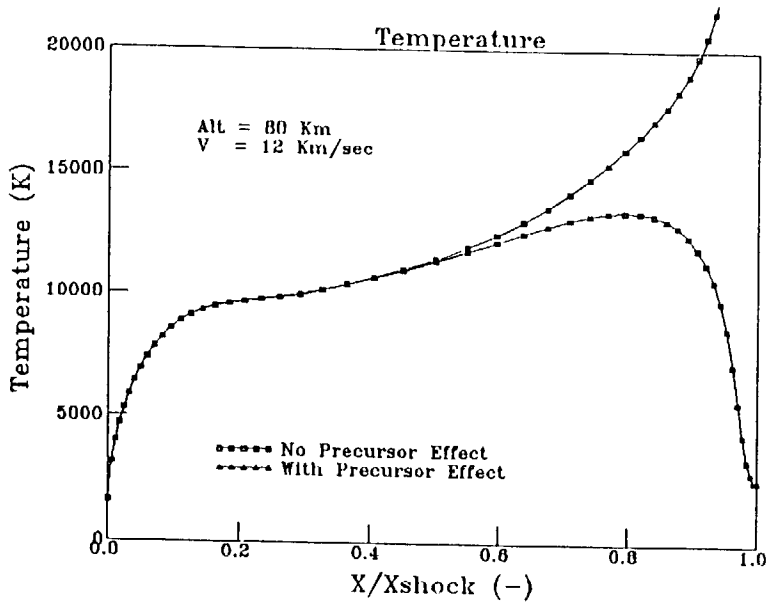
Temperature
Alt = 80 Km
V = 12 Km/sec
No Precursor Effect
With Precursor Effect
Temperature (K)
X/Xshock (-)
20000
15000
10000
5000
0
0.0
0.2
0.4
0.6
0.8
1.0

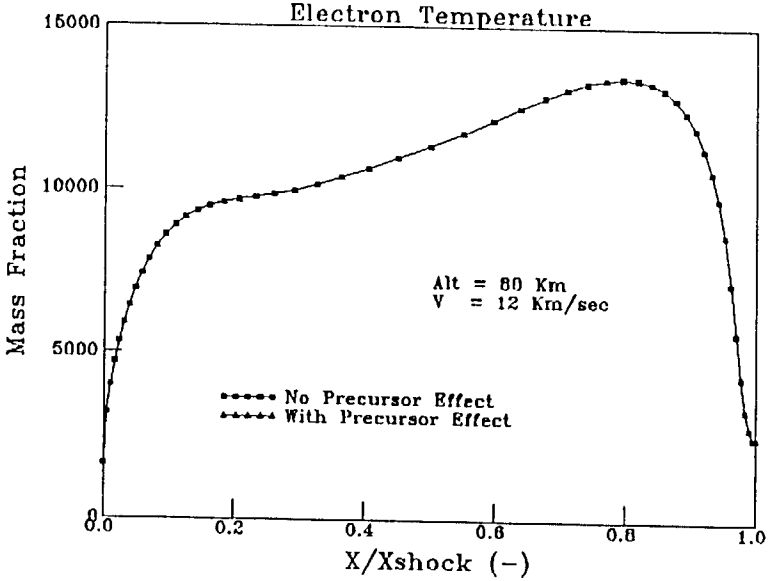
Electron Temperature
Alt = 80 Km
V = 12 Km/sec
No Precursor Effect
With Precursor Effect
Mass Fraction
X/Xshock (-)
15000
10000
5000
0
0.0
0.2
0.4
0.6
0.8
1.0

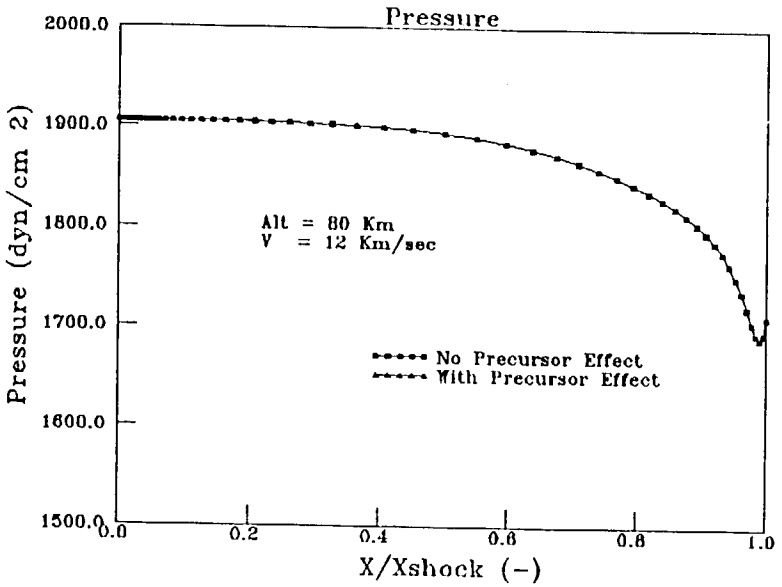
Pressure
Alt = 80 Km
V = 12 Km/sec
No Precursor Effect
With Precursor Effect
Pressure (dyn/cm 2)
X/Xshock (-)
2000.0
1900.0
1800.0
1700.0
1600.0
1500.0
0.0
0.2
0.4
0.6
0.8
1.0

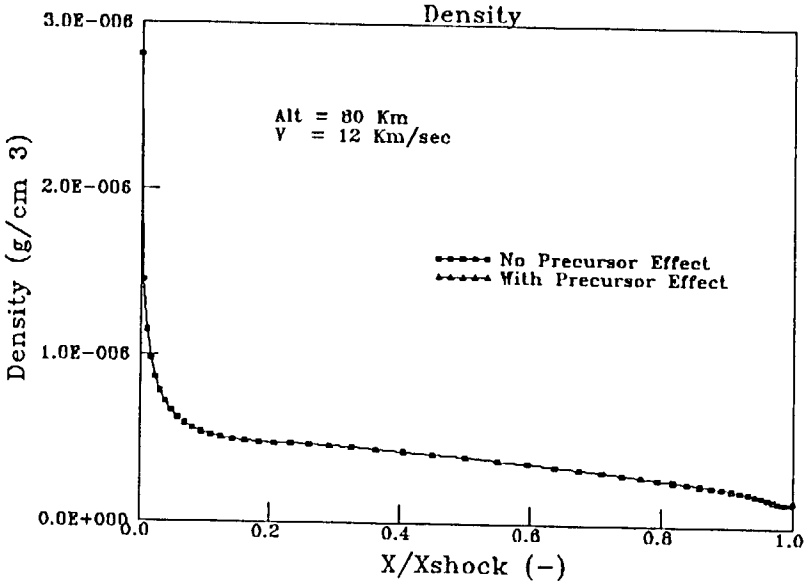
Density
Alt = 80 Km
V = 12 Km/sec
No Precursor Effect
With Precursor Effect
Density (g/cm 3)
X/Xshock (-)
3.0E-006
2.0E-006
1.0E-006
0.0E+000
0.0
0.2
0.4
0.6
0.8
1.0

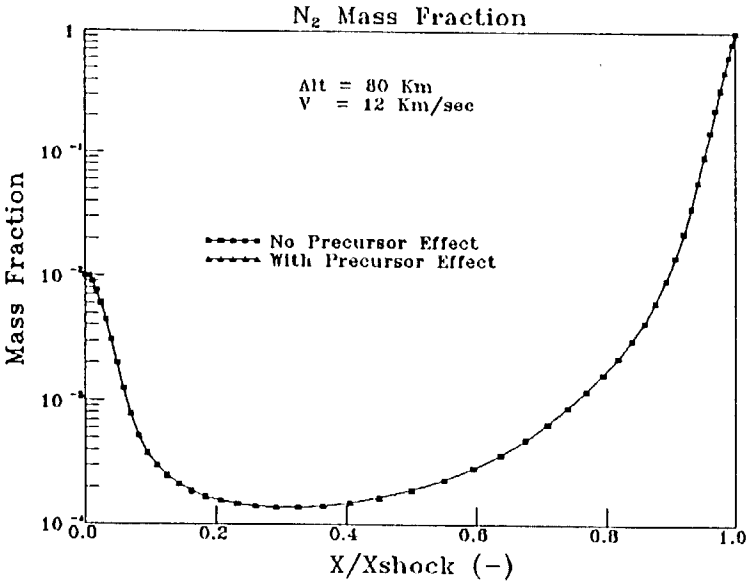
N_2 Mass Fraction
Alt = 80 Km
V = 12 Km/sec
No Precursor Effect
With Precursor Effect
Mass Fraction
X/Xshock (-)

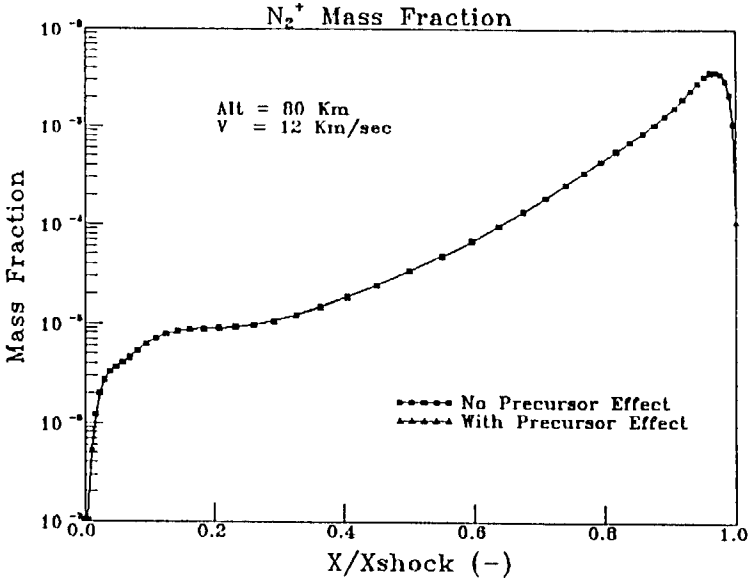
N_2^+ Mass Fraction
Alt = 80 Km
V = 12 Km/sec
No Precursor Effect
With Precursor Effect
Mass Fraction
X/Xshock (-)

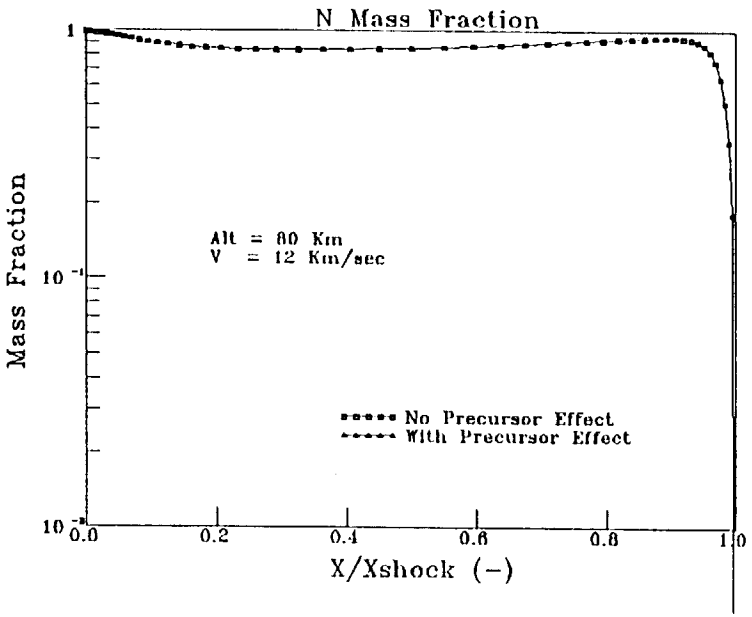
N Mass Fraction
Alt = 80 Km
V = 12 Km/sec
No Precursor Effect
With Precursor Effect
Mass Fraction
X/Xshock (-)

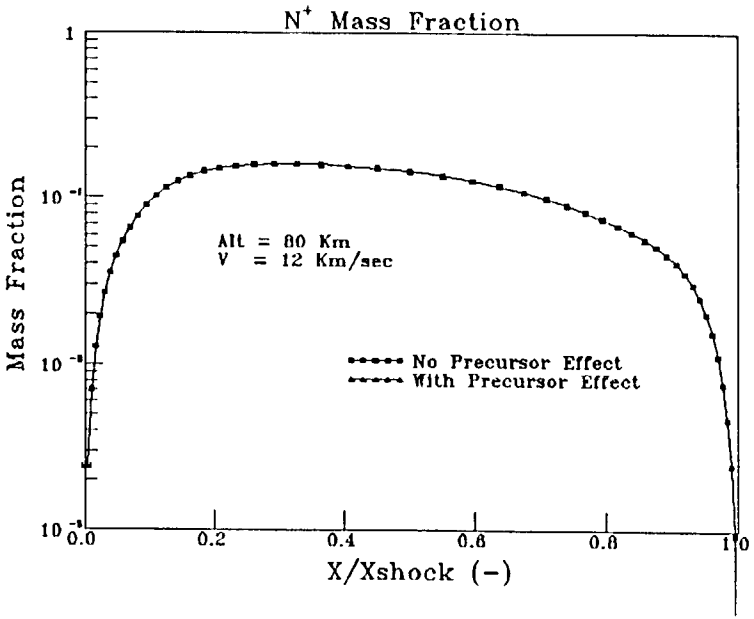
N^+ Mass Fraction
Alt = 80 Km
V = 12 Km/sec
No Precursor Effect
With Precursor Effect
Mass Fraction
X/Xshock (-)

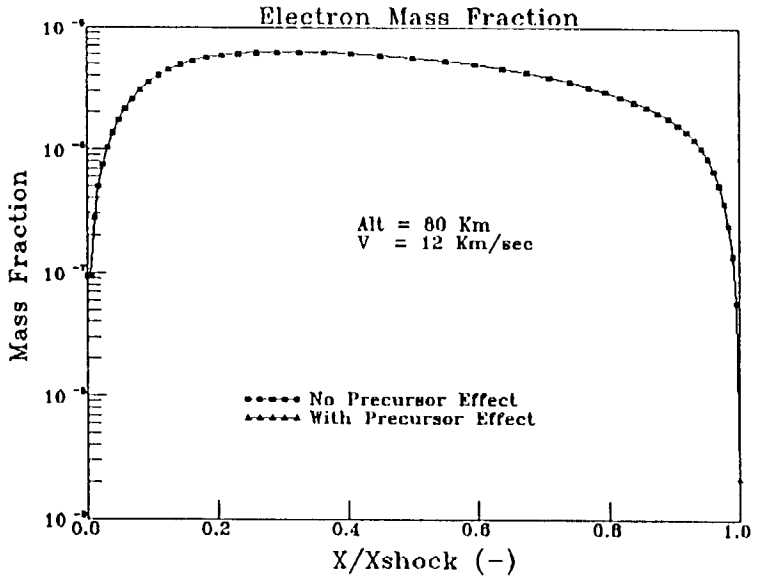
Electron Mass Fraction
Mass Fraction
Alt = 80 Km
V = 12 Km/sec
No Precursor Effect
With Precursor Effect
X/Xshock (-)

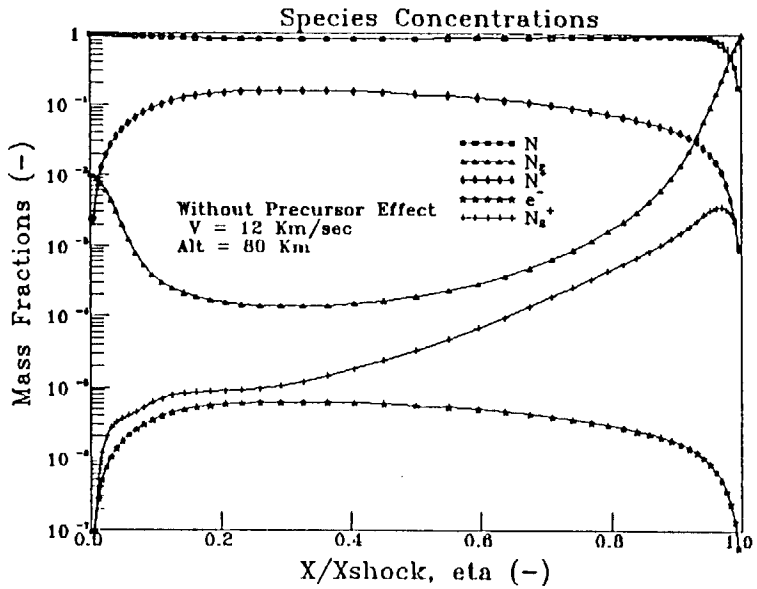
Species Concentrations
Mass Fractions (-)
N
N2
N+
e-
N2+
Without Precursor Effect
V = 12 Km/sec
Alt = 80 Km
X/Xshock, eta (-)

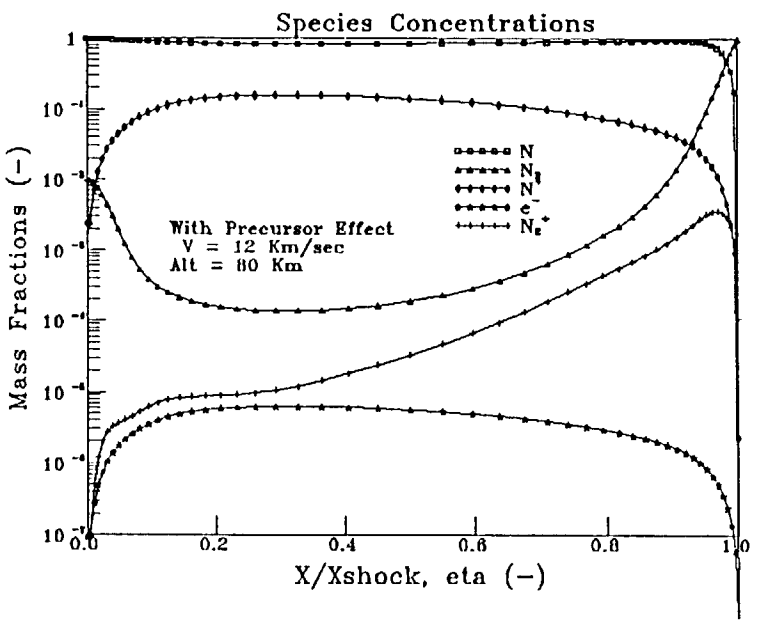
Species Concentrations
Mass Fractions (-)
N
N2
N+
e-
N2+
With Precursor Effect
V = 12 Km/sec
Alt = 80 Km
X/Xshock, eta (-)

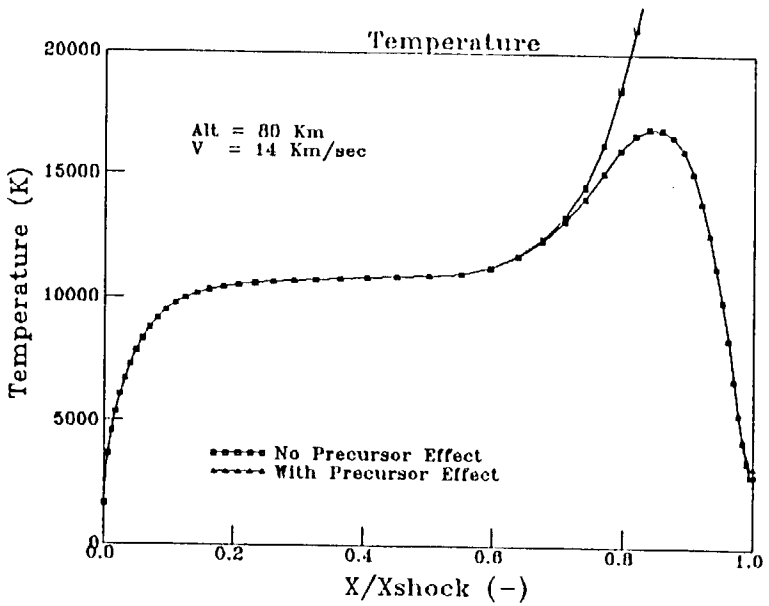
Temperature
Alt = 80 Km
V = 14 Km/sec
No Precursor Effect
With Precursor Effect
Temperature (K)
X/Xshock (-)
20000
15000
10000
5000
0
0.0
0.2
0.4
0.6
0.8
1.0

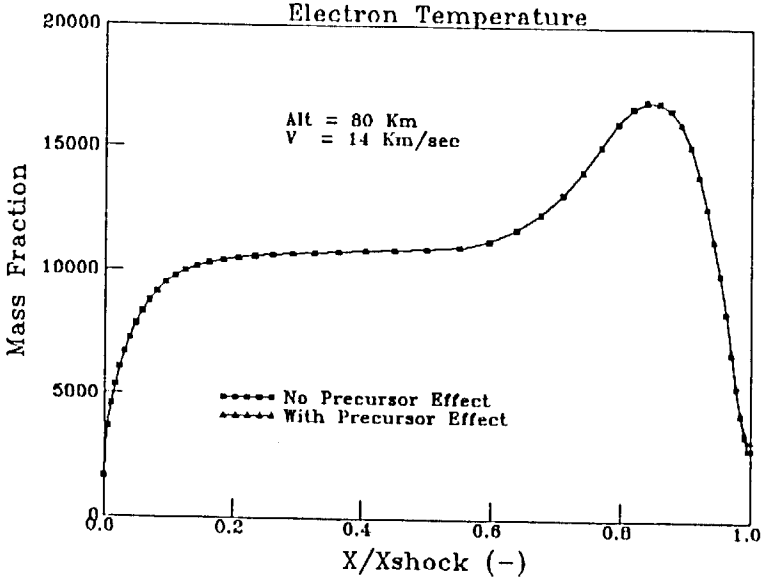
Electron Temperature
Alt = 80 Km
V = 14 Km/sec
No Precursor Effect
With Precursor Effect
Mass Fraction
X/Xshock (-)
20000
15000
10000
5000
0
0.0
0.2
0.4
0.6
0.8
1.0

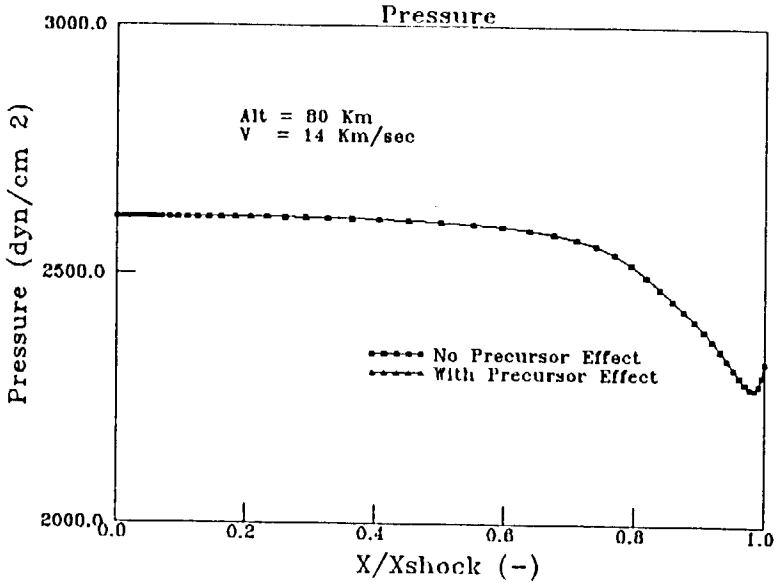
Pressure
Alt = 80 Km
V = 14 Km/sec
No Precursor Effect
With Precursor Effect
Pressure (dyn/cm 2)
X/Xshock (-)
3000.0
2500.0
2000.0
0.0
0.2
0.4
0.6
0.8
1.0

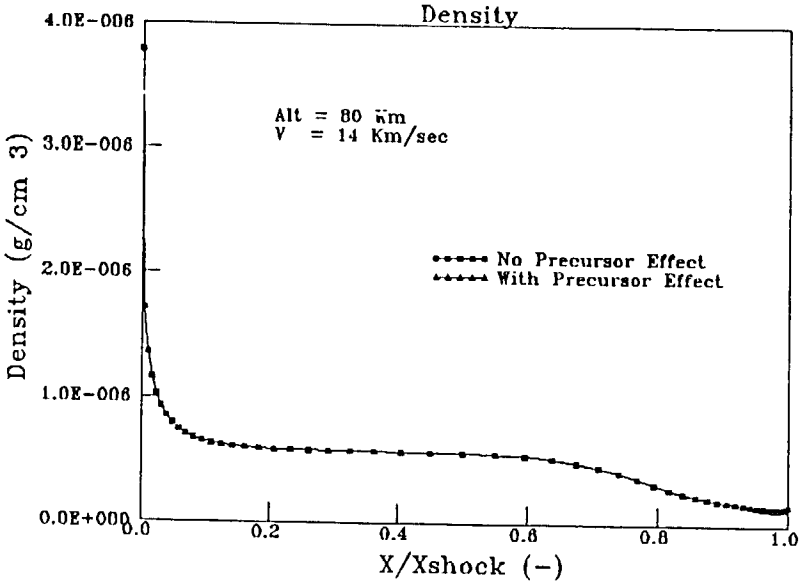
Density
Alt = 80 Km
V = 14 Km/sec
No Precursor Effect
With Precursor Effect
Density (g/cm 3)
X/Xshock (-)
4.0E-006
3.0E-006
2.0E-006
1.0E-006
0.0E+000
0.0
0.2
0.4
0.6
0.8
1.0

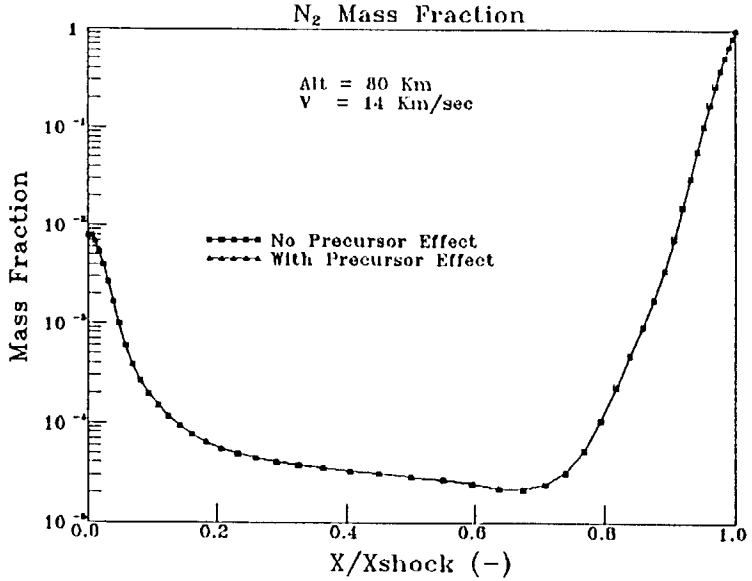
N_2 Mass Fraction
Alt = 80 Km
V = 14 Km/sec
No Precursor Effect
With Precursor Effect
Mass Fraction
X/Xshock (-)

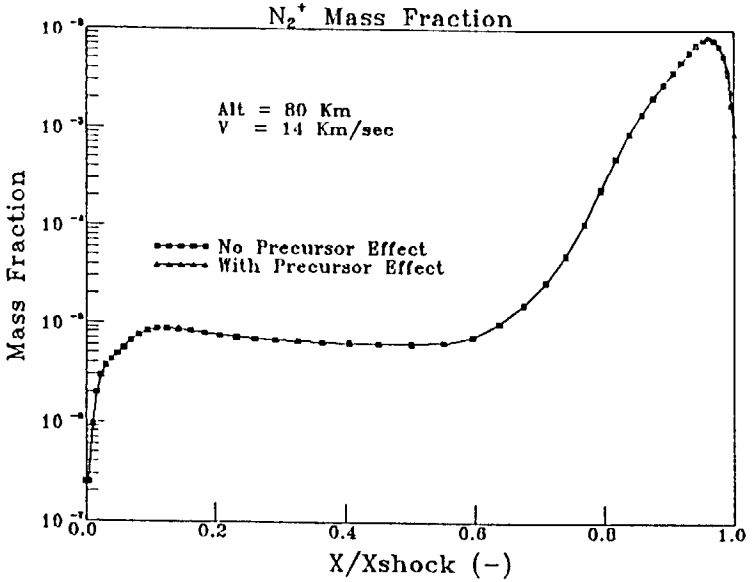
N_2^+ Mass Fraction
Alt = 80 Km
V = 14 Km/sec
No Precursor Effect
With Precursor Effect
Mass Fraction
X/Xshock (-)

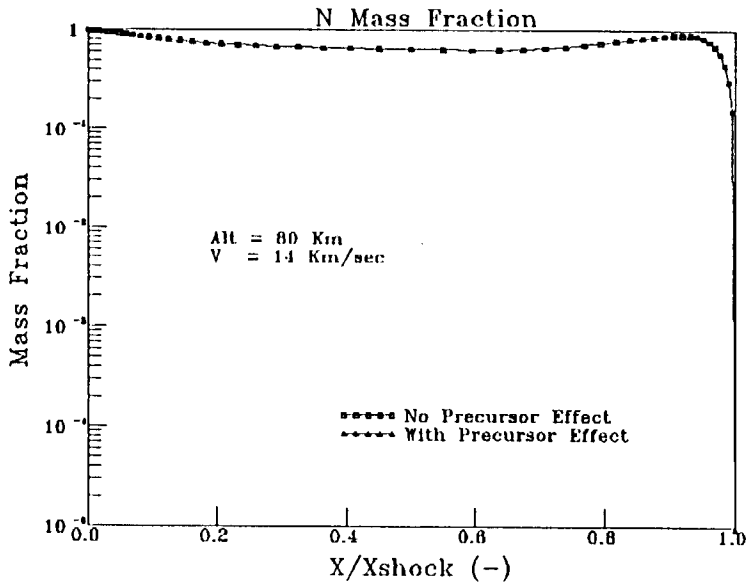
N Mass Fraction
Alt = 80 Km
V = 14 Km/sec
No Precursor Effect
With Precursor Effect
Mass Fraction
X/Xshock (-)

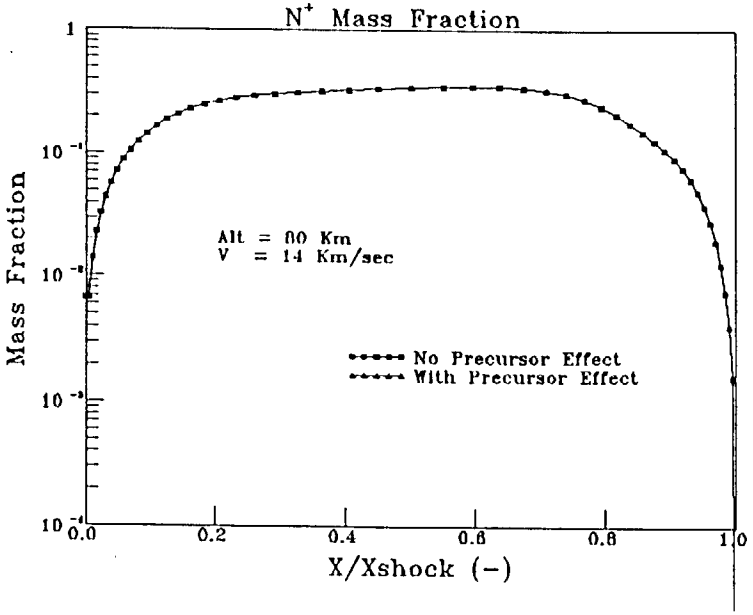
N^+ Mass Fraction
Alt = 80 Km
V = 14 Km/sec
No Precursor Effect
With Precursor Effect
Mass Fraction
X/Xshock (-)

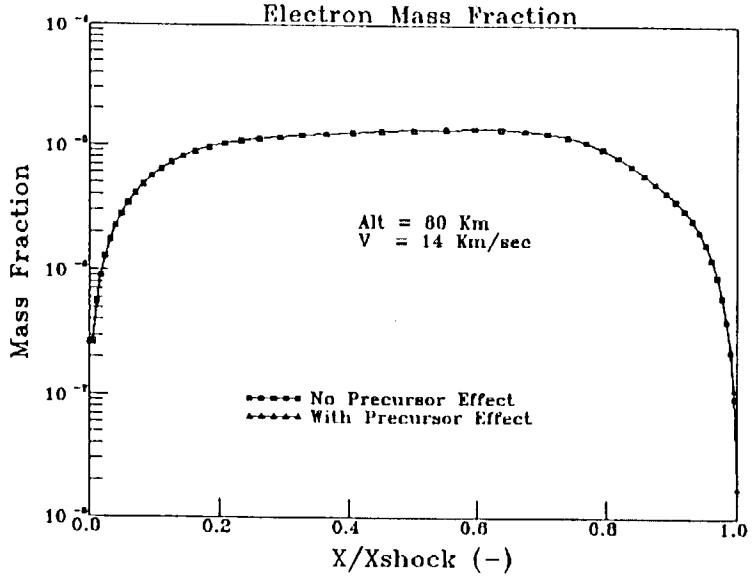
Electron Mass Fraction
Mass Fraction
Alt = 80 Km
V = 14 Km/sec
No Precursor Effect
With Precursor Effect
X/Xshock (-)

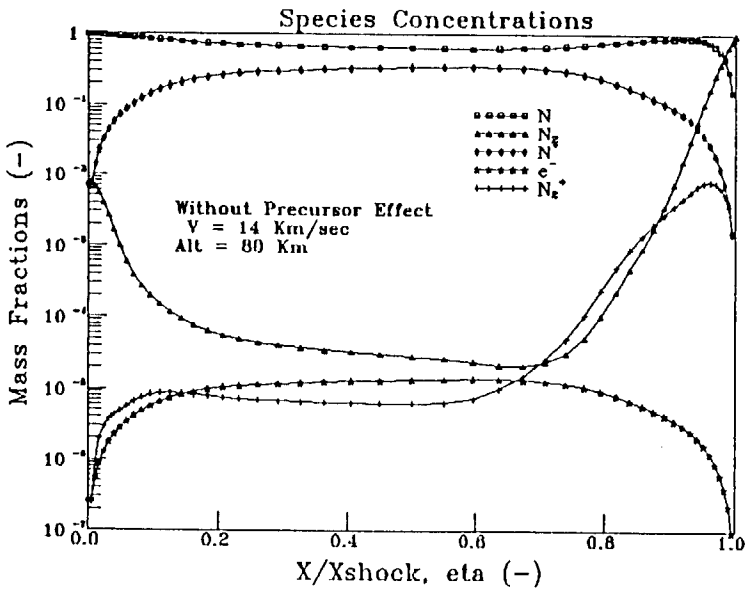
Species Concentrations
Mass Fractions (-)
N
N2
N+
e-
N2+
Without Precursor Effect
V = 14 Km/sec
Alt = 80 Km
X/Xshock, eta (-)

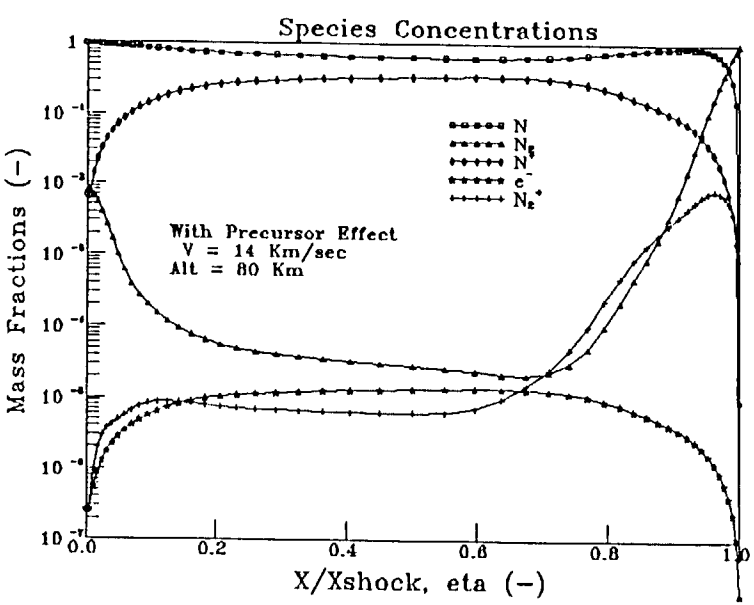
Species Concentrations
Mass Fractions (-)
N
N2
N+
e-
N2+
With Precursor Effect
V = 14 Km/sec
Alt = 80 Km
X/Xshock, eta (-)

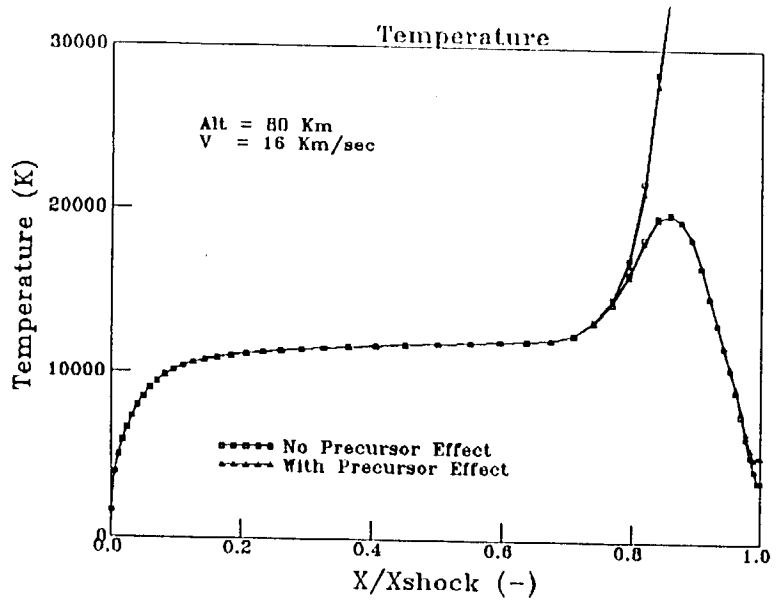
Temperature
Alt = 80 Km
V = 16 Km/sec
No Precursor Effect
With Precursor Effect
Temperature (K)
X/Xshock (-)
30000
20000
10000
0
0.0
0.2
0.4
0.6
0.8
1.0

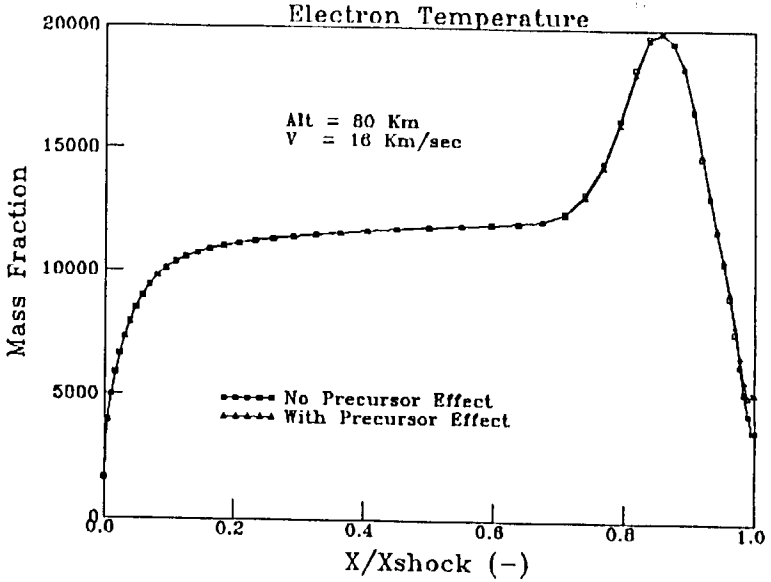
Electron Temperature
Alt = 80 Km
V = 16 Km/sec
No Precursor Effect
With Precursor Effect
Mass Fraction
X/Xshock (-)
20000
15000
10000
5000
0
0.0
0.2
0.4
0.6
0.8
1.0

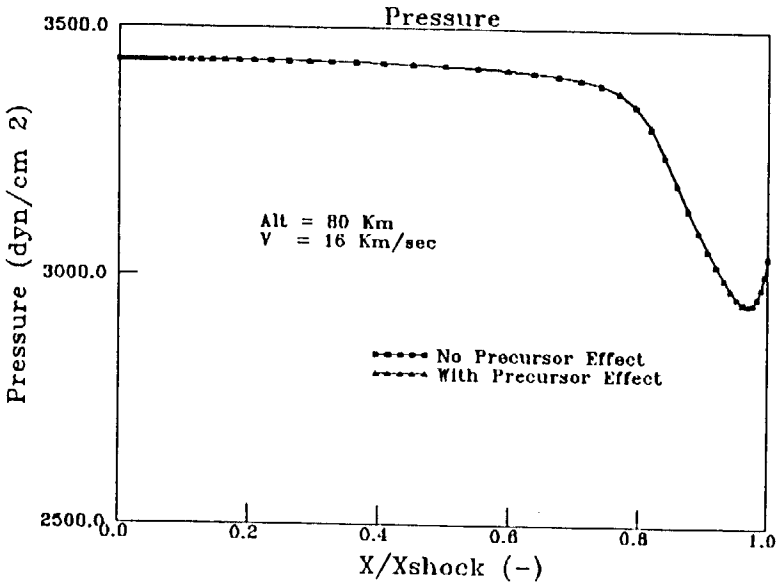
Pressure
Alt = 80 Km
V = 16 Km/sec
No Precursor Effect
With Precursor Effect
Pressure (dyn/cm 2)
X/Xshock (-)
3500.0
3000.0
2500.0
0.0
0.2
0.4
0.6
0.8
1.0

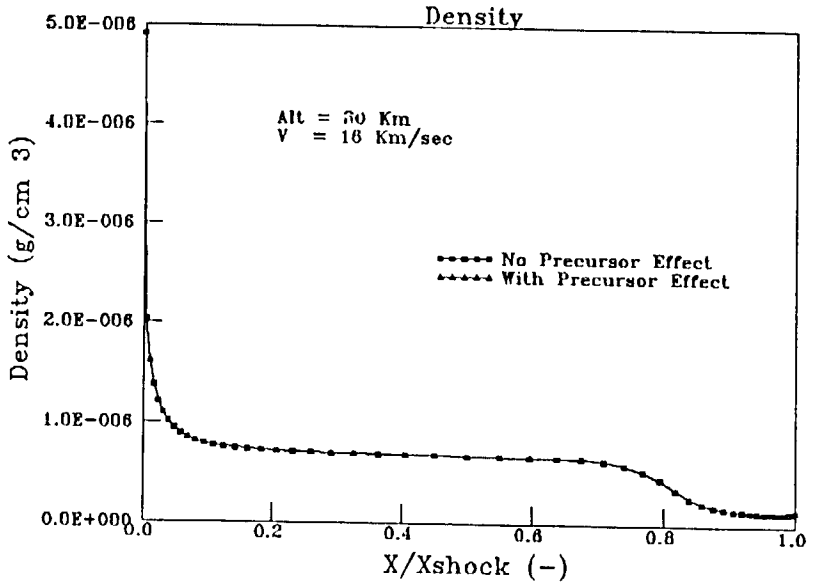
Density
Alt = 80 Km
V = 16 Km/sec
No Precursor Effect
With Precursor Effect
Density (g/cm 3)
X/Xshock (-)
5.0E-006
4.0E-006
3.0E-006
2.0E-006
1.0E-006
0.0E+000
0.0
0.2
0.4
0.6
0.8
1.0

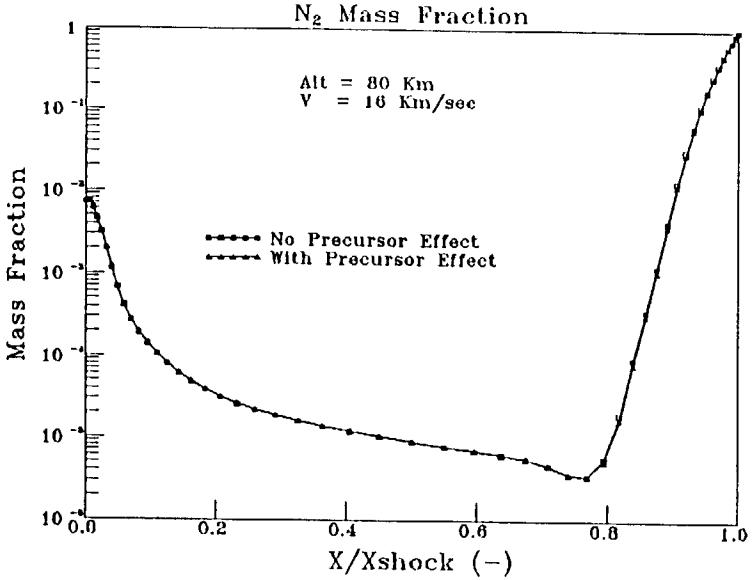
N_2 Mass Fraction
Alt = 80 Km
V = 16 Km/sec
No Precursor Effect
With Precursor Effect
Mass Fraction
X/Xshock (-)

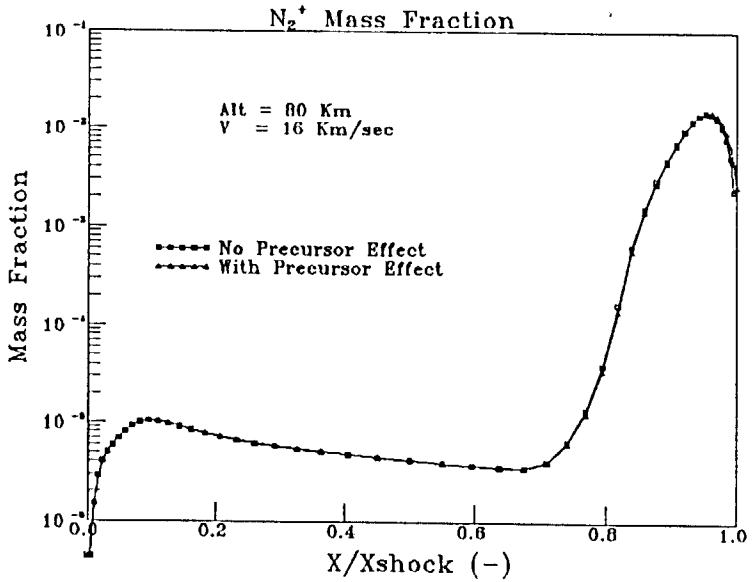
N_2^+ Mass Fraction
Alt = 80 Km
V = 16 Km/sec
No Precursor Effect
With Precursor Effect
Mass Fraction
X/Xshock (-)

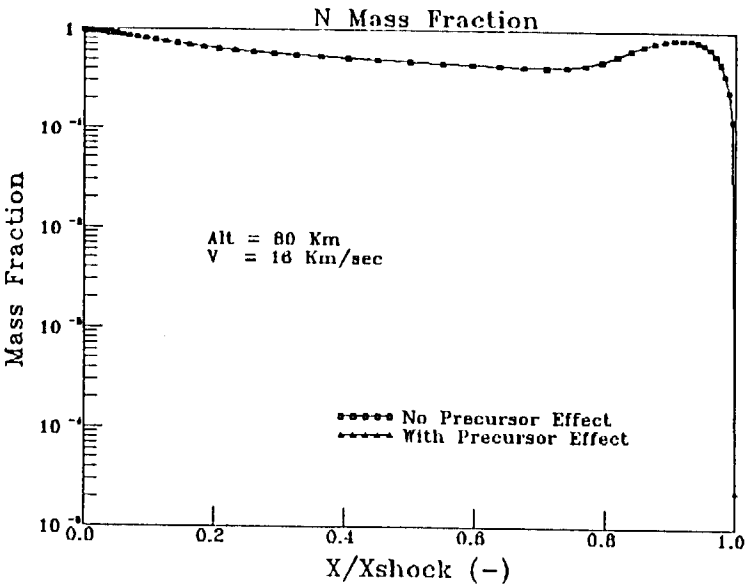
N Mass Fraction
Alt = 80 Km
V = 16 Km/sec
No Precursor Effect
With Precursor Effect
Mass Fraction
X/Xshock (-)

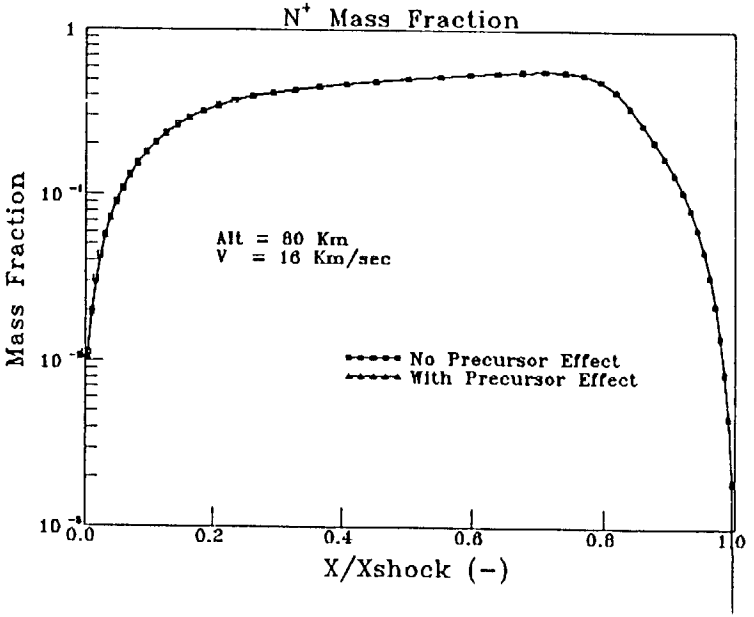
N^+ Mass Fraction
Alt = 80 Km
V = 16 Km/sec
No Precursor Effect
With Precursor Effect
Mass Fraction
X/Xshock (-)

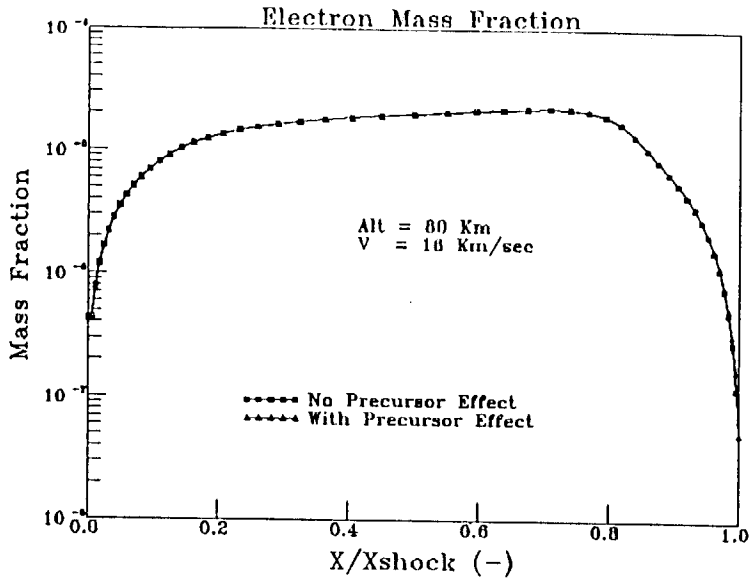
Electron Mass Fraction
Mass Fraction
Alt = 80 Km
V = 16 Km/sec
No Precursor Effect
With Precursor Effect
X/Xshock (-)

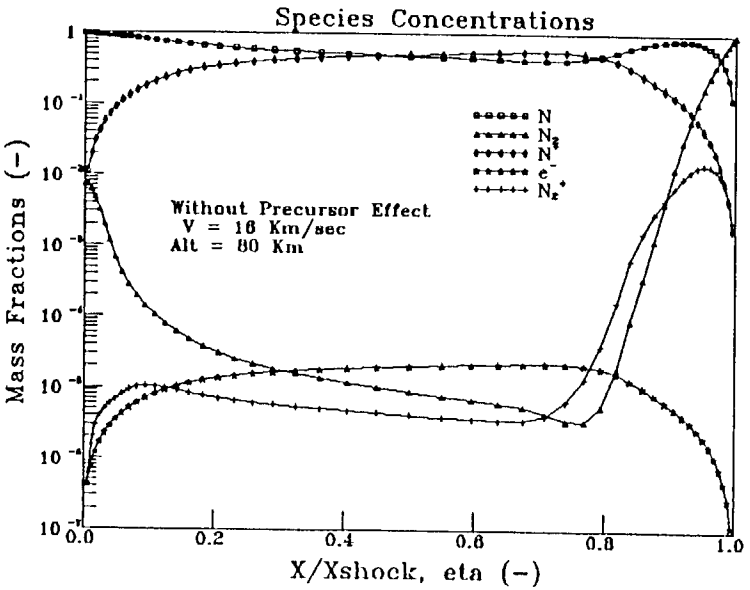
Species Concentrations
Mass Fractions (-)
N
N2
N+
e-
N2+
Without Precursor Effect
V = 16 Km/sec
Alt = 80 Km
X/Xshock, eta (-)

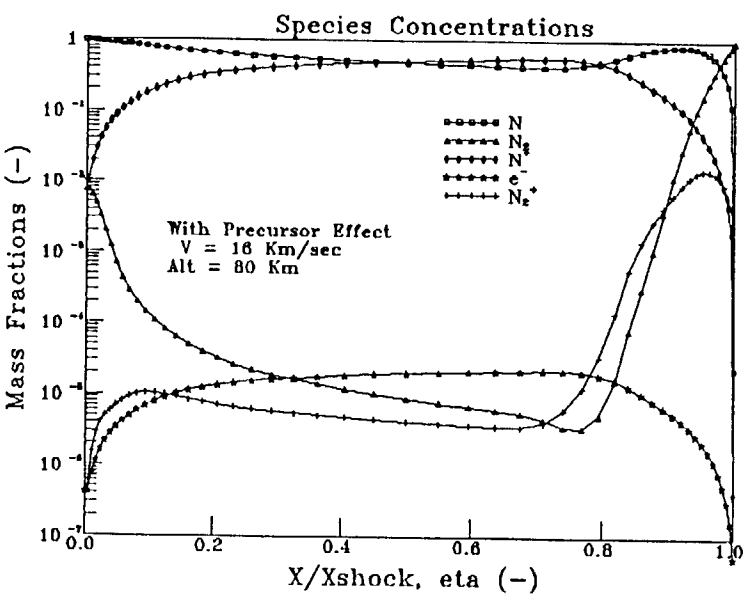
Species Concentrations
Mass Fractions (-)
N
N2
N+
e-
N2+
With Precursor Effect
V = 16 Km/sec
Alt = 80 Km
X/Xshock, eta (-)

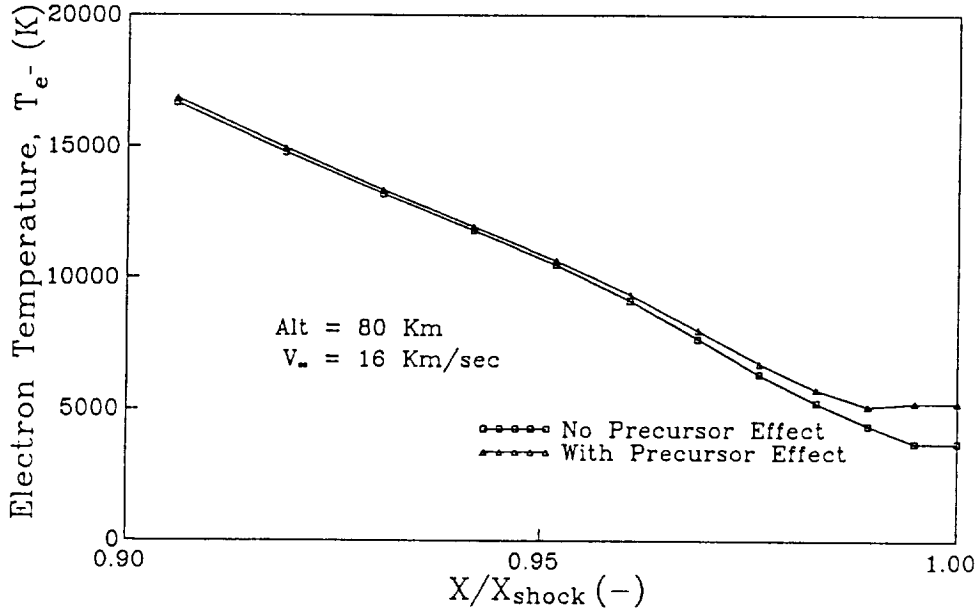
Electron Temperature, T_e - (K)
20000
15000
10000
5000
0
0.90
0.95
1.00
X/X_{shock} (-)
Alt = 80 Km
V_∞ = 16 Km/sec
No Precursor Effect
With Precursor Effect

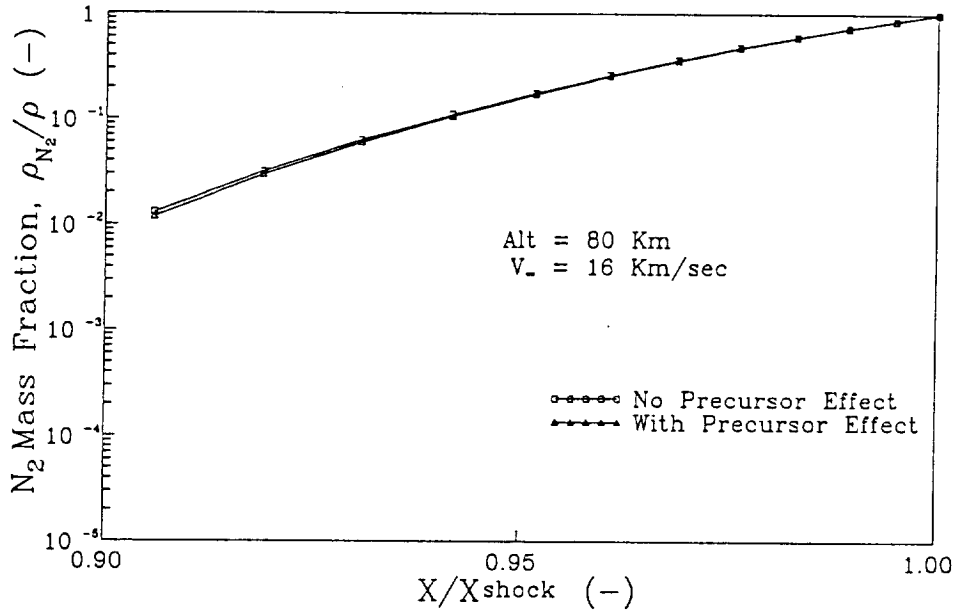
N_2 Mass Fraction, ρ_{N_2}/ρ (-)
1
10^{-1}
10^{-2}
10^{-3}
10^{-4}
10^{-5}
0.90
0.95
1.00
X/X_{shock} (-)
Alt = 80 Km
V_∞ = 16 Km/sec
No Precursor Effect
With Precursor Effect

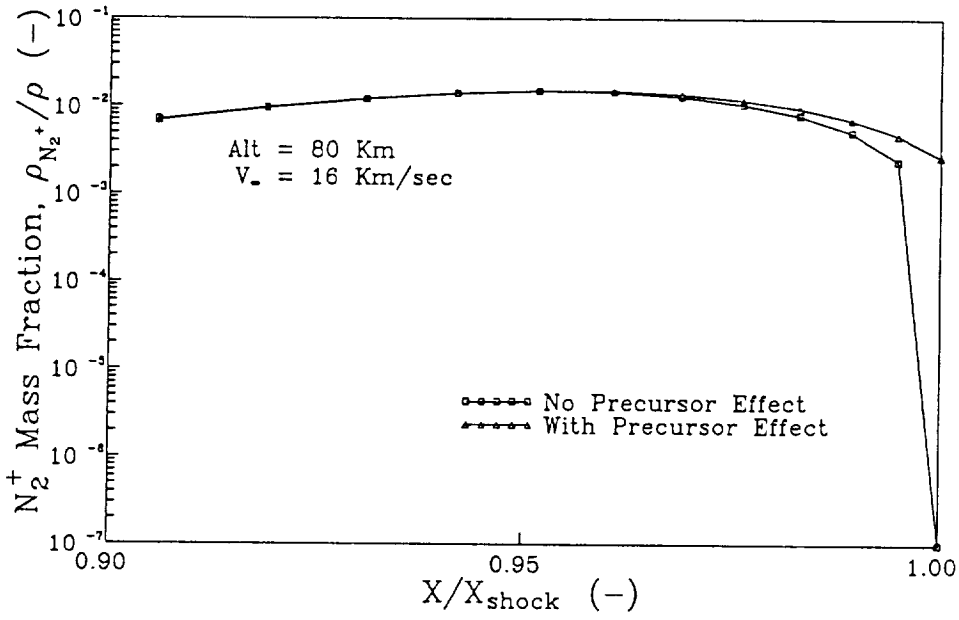
N_2^+ Mass Fraction, $\rho_{N_2^+}/\rho$ (–)
10^{-1}
10^{-2}
10^{-3}
10^{-4}
10^{-5}
10^{-6}
10^{-7}
Alt = 80 Km
V_∞ = 16 Km/sec
No Precursor Effect
With Precursor Effect
0.90
0.95
1.00
X/X_{shock} (–)

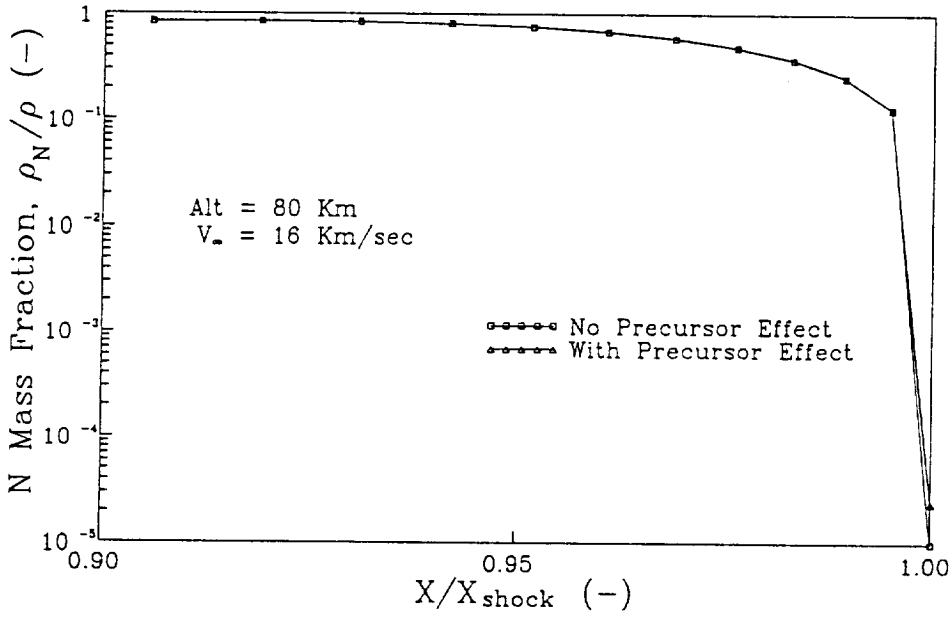
N Mass Fraction, ρ_N/ρ (–)
1
10^{-1}
10^{-2}
10^{-3}
10^{-4}
10^{-5}
Alt = 80 Km
V_∞ = 16 Km/sec
No Precursor Effect
With Precursor Effect
0.90
0.95
1.00
X/X_{shock} (–)

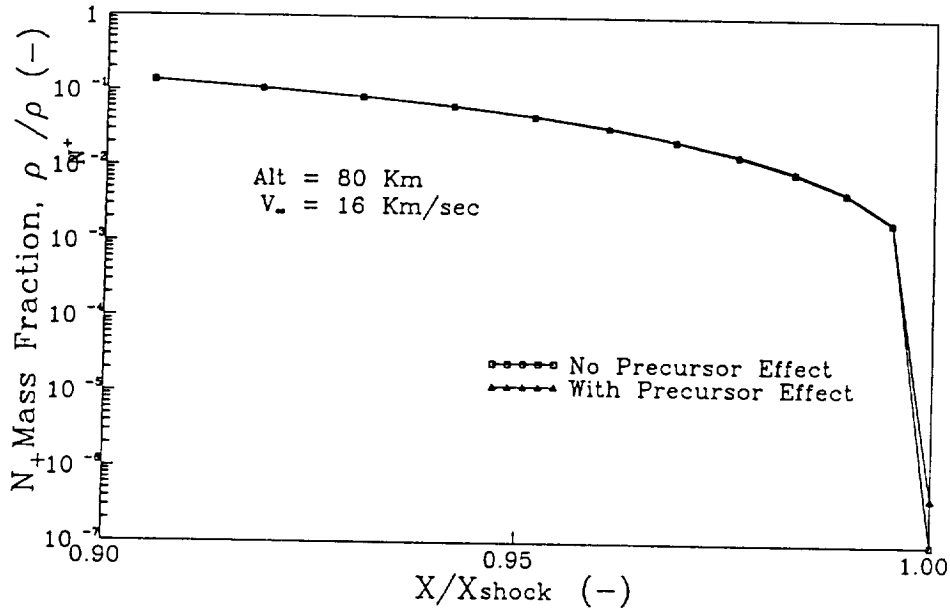
Alt = 80 Km
V∞ = 16 Km/sec
No Precursor Effect
With Precursor Effect
N+ Mass Fraction, ρN+ /ρ (−)
X/Xshock (−)
1
10 -1
10 -2
10 -3
10 -4
10 -5
10 -6
10 -7
0.90
0.95
1.00

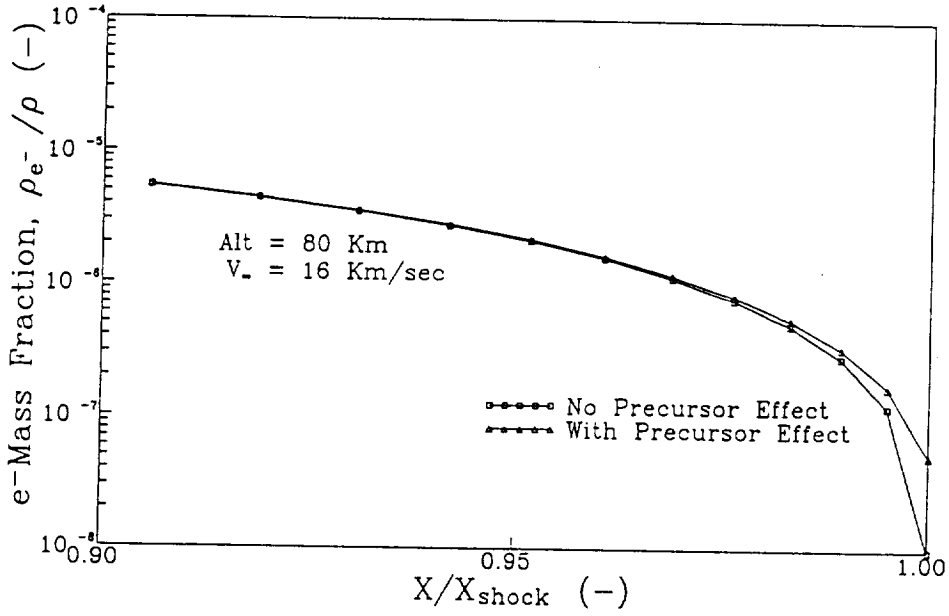
Alt = 80 Km
V∞ = 16 Km/sec
No Precursor Effect
With Precursor Effect
e− Mass Fraction, ρe− /ρ (−)
X/Xshock (−)
10 -4
10 -5
10 -6
10 -7
10 -8
0.90
0.95
1.00

APPENDIX III

Abstract of Paper Submitted to

AIAA 22nd Fluid Dynamics, Plasma Dynamics and Lasers Conference

June 1991

"A Flowfield Coupled Excitation and Radiation Model for Nonequilibrium Reacting Flows"

Thomas A. Gally
Leland A. Carlson
Derek Green

Abstract Submittal Form

Print or type all information

I wish to submit an abstract for (conference/meeting) 22nd Fluid Dynamics, Plasma Dynamics Conf.

Location: Honolulu, Hawaii **Date:** June 24-26, 1991

Session/organizer (this information appears in the call): S. T. Wu,/ L. A. Carlson

Reminders:

1/ AIAA has first publication rights to all papers presented at its meetings.

2/ Authors must inform each organizer if abstract is submitted to more than one session topic organizer.

3/ All nonmember program participants and authors will be charged the nonmember registration fee for the meeting; any *member* program participants and authors are eligible for the member fee.

4/ Authors of accepted papers will be expected to submit a photo-ready manuscript. Deadline dates will be included in author kit packages. Authors desiring journal publication should send five (5) copies of their photo-ready manuscript directly to the Editor in Chief of the journal of their choice (see inside front cover of each journal for correct address), along with a covering letter, before the meeting, if they wish to accelerate the review procedure. Government Program Monitors/Security Officers should be alerted as soon as authors receive formal acceptance of their paper.

5/ It is the responsibility of authors to obtain proper approval if necessary. Please keep in mind that clearances may consume six (6) weeks or more.

6/ Co-authors are grouped by affiliations and do not necessarily reflect amount of author contribution.

Paper title (this title will be published in the program):

A Flowfield Coupled Excitation & Radiation Model for Nonequilibrium Reacting Flows

Author/s' name and title, AIAA membership grade, company, full mailing address, telephone number, FAX number:

1 Principle Author Thomas A. Gally
Aerospace Engr. Dept. Texas A&M Univ.
College Station, TX 77843-3141
(409)845-0821, Student Member

2 Dr. Leland A. CArlson
Aerospace Engr. Dept., Texas A&M Univ.
College Station, TX 77843-3141
(409)845-1426, FAX (409)845-6051
Associate Fellow, AIAA

3 Derek Green
Same Address as No. 1 and 2
(409)845-7541

4

Indicate (one) author to receive all correspondence: ☐ 1 ☒ 2 ☐ 3 ☐ 4

Abstract due date: October 17, 1990

Draft of paper included? ☐ Yes ☒ No No extended abstract only

Similar results previously presented or published elsewhere? ☐ Yes ☒ No

Concise statement of problem (its genesis and objective):

See Attached Summary

Scope and methods of approach, with statement of contribution to the state-of-the-art or an application of existing analytical techniques and theories to a problem.

See Attached Summary

Summary of important conclusions:

See attached summary.

Statement of data used to substantiate conclusions, and freehand sketches of major figures to be used (no more than two typed pages):

A FLOWFIELD COUPLED EXCITATION AND RADIATION MODEL FOR NONEQUILIBRIUM REACTING FLOWS

AN EXTENDED ABSTRACT

Thomas A. Gally*, Leland A. Carlson**, and Derek Green***

Aerospace Engineering Department

Texas A&M University

College Station, Texas 77843-3141

SUMMARY

In this paper, several flowfield coupled electronic excitation models for nonequilibrium atomic radiation suitable for rapid flowfield calculations are presented. Further, due to the sensitivity of results, several electron-electronic energy and diffusion models are presented and their effect on flowfield structure, nonequilibrium electronic excitation, and radiative transfer examined. These models have been incorporated into a computational flowfield program which includes nonequilibrium chemistry, thermal nonequilibrium, viscous, conduction, and diffusion effects, and coupled nongray radiative transfer. The latter has been modified to include local thermodynamic nonequilibrium phenomena resulting from chemical and thermal nonequilibrium.

Comparison with the Fire 2 flight experimental data indicates that the present models are appropriate and reasonable. Subsequently, based upon these models, results are presented for a variety of cases including two AFE cases and a situation representative of

* NASA Graduate Student Researcher
** Professor, Aerospace Engineering
*** Graduate Research Assistant

Martian return aerocapture. These results show the importance of shock slip, chemical and radiative nonequilibrium, and radiative gasdynamic coupling. They also demonstrate the differences between using various electron-electronic energy models and delineate the differences between molecular dominated flows such as AFE and those characterized by ionization such as Martian return.

INTRODUCTION

In the future, various space programs will be conducted which will require the efficient return of large payloads from missions to the moon or to planets such as Mars. To accomplish this task, the return vehicles will either utilize direct entry at very high velocities or aerocapture techniques. In either case, a significant portion of the entry will involve high velocities at high altitudes; and, during this part of the trajectory, the vehicle flowfields will be dominated by chemical, thermal, and radiative nonequilibrium phenomena. In order to design and operate such vehicles, it is essential to develop engineering flowfield models which appropriately and accurately desribe these chemical, thermal, and radiative nonequilibrium processes and the coupling between them.

Previously (Ref. 1), the importance of properly predicting electron temperature and modeling electron impact ionization was investigated and a quasi-equilibrium free electron energy model and a two step ionization model formulated. In addition, an approximate method of handling nonequilibrium atomic radiation, which assumed that the excited states of atoms are in equilibrium with the local free electrons and ions, was developed (Ref. 1-3) and applied to an eight step nongray emission-absorption radiation model. Subsequently, the radiation transport method was replaced with a detailed model, which not only included corrections for nonequilibrium atomic radiation phenomena but also contained modifications to properly account for nonequilibrium molecular radiation. The resultant technique, which also included an improved electron-electronic energy model, was applied

to a wide range of conditions; and the coupling of nonequilibrium chemical and radiation phenomena in high altitude entry vehicle flowfields was studied (Ref. 4). These results showed the importance of these processes and demonstrated that accurate predictions of high altitude flowfields depended upon the number of each species in excited states and the resultant departure from Boltzmann distributions. However, since excited state number densities are sensitive to excitation phenomena, electron temperature, and species concentrations, which are strongly influenced by electron energy, electronic excitation, and diffusion modeling, and since the approach of Ref. 4 used several approximations in its models, it was believed that significant improvements could be made by the development and application of new models.

Thus, the primary objective of this paper is to present a flowfield coupled electronic excitation model for nonequilibirum atomic radiation suitable for rapid flowfield calculations. Further, due to the previously discussed sensitivities, secondary objectives are to examine several electron-electronic energy and diffusion models and to determine their effect on flowfield structure, nonequilibrium electronic excitation, and radiative transfer.

METHODS

The flowfield model used in this investigation is a viscous shock layer analysis which includes the effects of chemical nonequilibrium, multi-temperature thermal nonequilibrium (electron or electron-electronic, vibrational, and heavy particle), viscosity, heat conduction, diffusion, and radiative gasdynamic coupling. The basic method, which has been significantly modified and expanded from the versions used in Ref. 1 and 4, has been coupled with modified versions of the radiation routines of the NASA Langley program, RADICAL (Ref. 5), giving the ability to calculate flowfield solutions with the effects of radiative cooling present. The radiation analysis in RADICAL is a detailed method which

includes atomic continuum radiation, molecular band radiation, and atomic line radiation; and the original model has been expanded to include nonequilibrium chemical and thermal effects and to account for excited state population distributions different from those predicted by a Boltzmann distribution. Thus, the present model includes the effects of local thermodynamic nonequilibrium (LTNE).

One of the advantages of a VSL method is the ability to distribute many flowfield points in regions of large gradients, such as in the region immediately behind the shock front and in the highly nonequilibrium thermal layer near the wall. However, this approach requires proper shock front jump conditions since diffusion and thermal conduction phenomena can be significant in the region immediately behind the shock front. Thus, the present method includes proper shock slip boundary conditions, and the importance of including and utilizing these conditions will be shown later. In addition, the present method permits various wall catalycity properties and includes appropriate spectral variations in the treatment of the wall boundary conditions.

Additional details concerning these methods will be presented in the final paper.

NONEQUILIBRIUM RADIATION MODELS

Molecular Radiation Model

In the present engineering approach, nonequilibrium radiation is computed using the modified RADICAL radiative analysis code and abosprtion coefficient model with actual species concentrations and with correction factors on the effective source function and absorption coefficients. This correction factor approach accounts for the existence of non-Boltzmann distribution state populations (i.e. local thermodynamic nonequilibrium, LTNE) and effectively determines the correct state populations. Previously, approximate correction factors for molecular radiation had been developed (Ref. 3); but it is now believed that these approximate factors overcorrect and for some molecular bands

underestimate the actual radiation. This belief is reenforced by the fact that experimental measurements made in molecular radiation dominated shock flows show a radiation intensity peak behind the shock front in conjunction with the predicted electron temperature peak. Thus, significant depletion of all of the excited molecular states, as predicted by the theory of Ref. 3, is not expected. Consequently, new improved molecular correction factors for molecular nonequilibrium radiation have been developed.

After examing various approaches, a quasi-steady approach similar to that of Ref. 6 has been developed which computes the electronic state populations associated with the radiating molecular bands. Specifically, for N2, the populations of the X, A, B, a, and C states are computed; while for N2+ the X, A, B, and D are included. This approach has been incorporated into the flowfield and radiative transport code; and there is no assumption concerning the existence of equilibrium between excited molecular states and atoms as there was in Ref. 3. Thus, in this new molecular model, both source functions and absorption coefficients associated with molecular band radiation will be modified for nonequilibrium effects. However, in the quasi-steady approach there is the inherent assumption that the rates used to determine the state populations are compatible with the overall rate chemistry. For the molecules, it is believed that the various rates are reasonably well known and that this inherent assumption is satisfied appropriately.

The variation in state population and resultant molecular correction factors will be discussed for several cases in the final paper. In general, however, preliminary results indicate that for many cases that for the N2 Birge-Hopfield band the correction factor for the absorption coefficient is near unity but that for the corresponding source function it is quite small in the nonequilibrium portion of the shock layer immediately behind the shock front. This behavior is what would "normally" be expected since N2(BH) involves absorption to the ground state. Likewise N2(1+) typically displays only a slight correction (from unity) for the source function but a significant decrease from that predicted using

Boltmann distributions in the absorption coefficient. This trend is also "expected" since N2(1+) involves two excited states, B and A. On the other hand, while the absorption coefficient factor for N2(2+) is similar to that for N2(1+), the source function for N2(2+) is typically significantly reduced in the chemical and thermal nonequilibrium region behind the shock front, indicating tht pre-dissociation is significantly depleting the population of the C electronic state.

The most interesting result, however, is that the N2+(1-) radiation is only slightly affected by nonequilibrium phenomena. This result is in agremment with experiments which, at least at lower velociities, have indicated a strong N2+(1-) contribution. However, since the number density of N2+ is often only significant in the region immediately behind the shock front, any N2+(1-) radiation should originate from that region. This feature will be discussed further in the results section and in the final paper.

Atomic Radiation Models

In this paper, local thermodynamic nonequilibrium effects (LTNE) on atomic radiation are also computed by applying to the absorption coefficient and source function values utilized in the radiative analysis, correction factors which account for the deviations in state populations from Boltmann distributions. However, two different models have or are under development; and each will be presented, discussed, and compared in the final paper.

The first model, which should probably be termed a first order approximation, has been presented previously in Ref. 1-4. Briefly, this model assumes that atomic ionization proceeds by excitation from the three low ground states (for nitrogen) to the high excited states followed by rapid ionization. Consequently, the model assumes that excitation from the ground states to the higher states is a rate limiting step for the ionization process

and that the excited states, because of their energy proximity to the ionized state, are in equilibrium with the free electrons and ions.

In contrast, Park (Ref. 6) and Kunc et al (Ref. 7) handle atomic LTNE by using a quasi-steady analysis in which, while rate processes between all the bound states and between the bound states and the ionized state are assumed finite, they are assumed to be fast relative to changes induced by the flowfield. Thus, at any point in a flowfield an equilibrium between the states will exist which is perturbed from a Boltzmann distribution due to radiative effects. Kunc et al have performed calculations in which they specify the electron temperature and the total number of charged particles (defined as two times the number of atoms plus the number of ions plus the number of electrons), leaving the actual number of ions and free electrons to be determined as part of the unknown populations.

Park, on the other hand, in the application of his method (Ref. 8) assumes the number of ions and electrons to be given by a flowfield solution. Under this approach, a non-Boltzmann distribution can be achieved even in the absence of radiation, if the number of ions and electrons differs from equilibrium. To be totally correct, however, the excitation and ionization rates associated with each level must overall be consistent with the ionization rates used in the flowfield solution.

Obviously, the present first order approach and those of Park and Kunc et al represent the extremes of modeling LTNE atomic phenomena. Unfortunately, the present first order approach is overly simplified in its assumption that the rates between the excited states and the free ions and electrons are infinitely fast (i.e. local equilibrium); and the detailed quasi-steady approaches are computationally intensive because they include a large number of electronic levels discretely. In addition, the latter are sensitive to the choice of the individual rates; and it is difficult to know which rate to adjust when comparing with experimental results and attempting to improve the correlation.

After extensively reviewing the work on argon of Foley and Clarke (Ref. 9), Nelson (Ref. 10), etc. and the air and nitrogen work of Park (Ref. 8), Kunc and Soon (Ref. 7), and others, it was decided to develop a second LTNE model for high temperature nitrogen by subdividing atomic nitrogen into two species. The first, termed Ng, for N ground, represents the nitrogen atoms in the first three low lying electronic states of nitrogen. The second, termed N* or N excited, representes those nitrogen atoms populating the remaining upper electronic states. The relative densities of these subspecies will then be determined by appropriate reaction rates between themselves, N+, e−, etc. It is believed that this approach has the potential to be a significant improvment over the present model in that it will allow a finite rate of ionization from excited states while retaining the fundamental two step ionization process. In addition, by determining the excited state number densities directly from the flowfield computation, the appropriate atomic LTNE factors are directly obtainable and more accurate.

Initially, the second order model uses the collisional reaction rate system shown in Table I. In general, reaction rates for the first seven reactions are well known. However, the rates for the electron-atom excitation and electron-atom ionization reactions, numbers 8 - 10, need to be determined. Currently, atom-atom excitation and photo-excitation photo-ionization are not included since it is believed that these reactions are of second order in the stagnation region. However, it is planned to include them later, possibly in time for the final paper.

In this system, care must be taken to properly formulate the species enthalpy of Ng and N*. Specifically,

$$h_{N_g} = \frac{5}{2}\frac{kT}{m_N} + \frac{\sum_{\ell=1}^{3} g_\ell \frac{E_\ell}{k} e^{-E_\ell/kT_e}}{\sum_{\ell=1}^{3} g_\ell e^{-E_\ell/kT_e}} \frac{k}{m_N} + h^\circ_{N_g} \qquad \text{(A-1)}$$

$$h_{N^*} = \frac{5}{2}\frac{kT}{m_N} + \frac{\sum_{\ell=4}^{MAX} g_\ell \frac{E_\ell - E_4}{k} e^{-(E_\ell - E_4)/kT_e}}{\sum_{\ell=4}^{MAX} g_\ell e^{-(E_\ell - E_4)/kT_e}} \frac{k}{m_N} + h^\circ_{N^*} \qquad \text{(A-2)}$$

where

$$h^\circ_{N_g} = 3.36 \times 10^{11} \text{ ergs/gm} \qquad h^\circ_{N^*} = 1.05 \times 10^{12} \text{ ergs/gm}$$

$$E_4 = 83337 \text{ cm}^{-1}$$

For equilibrium conditions, these expressions reduce to the proper forms where

$$h = \sum_{i=1}^{5} \frac{\rho_i}{\rho} h_i \qquad \text{(A-3)}$$

As mentioned above, effective reaction rates have to be obtained for reactions (8) - (10). While in principle, these could be extracted from the work of Park (Ref. 11), the work in Ref. 7 appears to contain information based upon more recent data. Furthermore, it appears to yield excitation rates more compatible with relaxation data behind shock waves. Consequently, a method has been developed and a computer program written to determine from the detailed data of Ref. 7, effective forward rates for reactions (8)-(10). While

complete details of the method and results will be presented in the paper, a preliminary set of results is presented in Figure 1.

Also shown on Figure 1 is the rate of Wilson successfully used in Ref. 1 and 4 in conjunction with the first order LTNE model. As can be seen, the preliminary rates for the new model are faster for excitation from the ground state but are finite for ionization from the excited state to the continuum. Thus, they appear to have the right trend and magnitude. In addition, included on the figure is the effective ionization rate from the ground state directly to the continuum. As previously postulated, this rate is considerably slower than the excitation rate. Finally, the ground to excited forward rate is about two orders of magnitude slower than that which it is believed would be obtained from using the detailed rates in Ref. 11.

Once the chemistry model involving excited species has been developed, the next step is to determine the appropriate LTNE factors which should be utilized in the radiative analysis code. In the final paper the logic behind derivations of these factors will be presented in detail. However, preliminary results are given in the following paragraphs.

For continuum processes involving absorption by an excited state, the absorption coefficient factor is

$$\frac{N_{N^*}}{N_N} \frac{Q^{elec}_{N_g} + Q^{elec}_{N^*} e^{-E_4/kT_e}}{Q^{elec}_{N^*} e^{-E_4/kT_e}}$$

and the factor on the source function is

$$\frac{N_e N_{N^+}}{N_{N^*}} \frac{Q^{elec}_{N^*} e^{(I-E_4)/kT_e}}{Q^{elec}_{N^+} Q_e}$$

Similarly, for continuum absorption involving a "ground" state, the absorption LTNE factor is

$$\frac{N_{N_g}}{N_N} \frac{Q^{elec}_{N_g} + Q^{elec}_{N^*} e^{-E_4/kT_e}}{Q^{elec}_{N_g}}$$

and the corresponding source function factor is

$$\frac{N_e N_{N^+}}{N_{N_g}} \frac{Q_{N_g}^{elec} e^{I/kT_e}}{Q_{N^+}^{elec} Q_e}$$

For line processes involving absorption into an excited state, the present second order theory yields an absorption LTNE factor of

$$\frac{N_{N^*}}{N_N} \frac{Q_{N_g}^{elec} + Q_{N^*}^{elec} e^{-E_4/kT_e}}{Q_{N^*}^{elec} e^{-E_4/kT_e}}$$

while for this case the source function is unchanged. On the other hand, if the line process involves absorption into one of the ground states, the absorption factor is

$$\frac{N_{N_g}}{N_N} \frac{Q_{N_g}^{elec} + Q_{N^*}^{elec} e^{-E_4/kT_e}}{Q_{N_g}^{elec}}$$

and the source function also has the factor

$$\frac{N_{N^*}}{N_{N_g}} \frac{Q_{N_g}^{elec}}{Q_{N^*}^{elec} e^{-E_4/kT_e}}$$

It should be noted that when the N* species is in equilibrium with N+ and e- and the number density of Ng is assumed to be that of N, these expressions reduce to those used with the first order model.

ELECTRON-ELECTRONIC ENERGY MODELS

In the results presented in Ref 1, the electron temperature was determined using a quasi-equilibrium free electron equation; and the electronic temperature was assumed to be equal to the free electron temperature. While it is believed that this approach is a good approximation for many conditions of interest in aerocapture, it was felt that additional models should be developed in an effort to improve the modeling of electron energy, and hence temperature, due to its importance in determining nonequilibrium

ionization chemistry and radiative transfer. Specifically, two electron-electronic energy models have been developed.

The first is termed quasi-electron-electronic and is similar to the first model in that it computes the electron temperature assuming quasi-equilibrium. However, it explicity accounts for the effect of elastic and inelastic collisions on the energy contained in electronic states of each species as well as the free electron energy; and, thus, the resulting temperature is a truly representative of electron-electronic energy.

The second model utilizes a combined electron-electronic energy differential equation which includes the effects of convection, conduction, and diffusion in addition to the production and loss of electron energy through elastic and inelastic collisions. The current full electron-electronic energy equation for the stagnation line is

$$\rho u c_{pe} \frac{\partial T_e}{\partial n} - \frac{\partial}{\partial n}\left(\lambda_e \frac{\partial T_e}{\partial n}\right) - \left(\sum_i \rho D_i c_{pei} \frac{\partial c_i}{\partial n}\right)\frac{\partial T_e}{\partial h} - u \frac{\partial p_e}{\partial h} + \sum_i \dot{w}_i h_{ei} = \sum_i s_{ei} + \dot{w}_{e,ea} E_I/m_e \qquad \text{(E-1)}$$

where c_{pe} is defined as

$$c_{pe} = \frac{\rho_e}{\rho} c_{pe,e} + \sum_i c_{pelec,i} \qquad \text{(E-2)}$$

In this equation, the viscous work terms have not been included due to the fact that they are of lower order. In addition, radiation effects on electron-electronic energy have been neglected as has diffusion effects on collisional energy exchange. The latter is expected to be small in most cases due to the rapid dissociation of N2 and the existence of ambipolar diffusion. However, it might be important at some of the lower AFE velocities.

It should be noted that Eqs. (E-1) is equivalent to that presented by Gnoffo (Ref. 12) and J. H. Lee (Ref. 13). However, it differs slightly from that presented in Ref. (1 and 14) in that the latter contains the additional terms

$$\dot{w}_e \frac{u^2}{2} + U_e \frac{\partial P_e}{\partial n}$$

which arise as a result of the differences in the derivation of the species energy and momentum equations. It is believed that these additional terms occur as a result of using the more detailed approach of Chapman and Cowling (Ref. 15). In any event, these two terms are expected to be small, and their neglect in the present studies should not affect the results.

Another item which needs to be considered in modeling electron-electronic energy is the proper boundary condition on electron temperature at the wall. In most past analyses (Ref. 1 and 12), it has been assumed that at the wall the electron temperature is equal to the wall temperature. Since the heavy particle temperature is also assumed equal to the wall temperature at the wall, this approach effectively assumes that the electron temperature is equal to the heavy particle temperature. At first, this approach seems reasonable and follows the philosophy that in the thermal boundary layer near the wall the flow should be near equilibrium and collision dominated. However, in actuality, the thermal boundary layer is in significant nonequilibrium in that the chemical rection rates are finite and cannot keep up with the true local equilibirum. This lag combined with diffusion leads to atom, ion, and electron densities above equilibrium values and in turn enhanced excited state populations. In addition, as can be seen in the electron-electronic energy equation, ionic recombination yields an increase in electron energy and tends to force the electron temperature above the heavy particle temperature.

Further, since almost all walls are catalytic to ions and electrons, there exists a thin plasma sheath adjacent to the wall across which a potential develops in order to maintain zero charge flux at the sheath edge. Since the thickness of the plasma sheath is negligible

in comparison to that of the wall thermal layer, the edge of the sheath can be construed as being physically at the wall. Thus, the proper wall boundary conditions on the continuum equations should be obtained by matching the particle description in the plasma sheath to the corresponding continuum description at the wall. Examination of appropriate sheath models shows that continuity of electron energy flux requires

$$\left(\lambda_e \frac{\partial T_e}{\partial y} - \rho_e \bar{v}_e h_e\right)_{y=0} = \left[2kT_e + |e\phi|\right] \frac{N_e c_e}{4} e^{-|e\phi|/kT_e} \qquad \text{(E-3)}$$

where the sheath potential is determined by enforcing charge neutrality at the sheath edge. Further analysis indicates that the heavy particle species, being in good contact with the wall, should be at the wall temperature at the wall. This type of electron boundary condition has been incorporated into the present full electron-electronic equation model, and the consequences of using it instead of the usual wall condition will be discussed in the paper.

At lower velocities where molecular processes dominate the flowfield, vibrational energy effects can also be important. In addition, for temperatures near 7500 deg K, vibrational electronic coupling is also known to be important (Ref. 16). Thus, two vibrational energy models are also in the process of being incorporated into the present model. The first of these assumes that vibrational temperature is equal to the electron-electronic temperature and the vibrational energy terms are included in the electron-electronic equation model to yield a combined model. This approach has been successfully used previously by Park (Ref. 8) and Gnoffo (Ref. 12) and eliminates the necessity to explicity account for vibrational-electronic coupling phenomena.

The second model being developed handles vibrational energy separately, includes vibrational electronic coupling as well as collisional and vibration-dissociation coupling effects, and yields a vibrational temperature separate from the heavy particle and

electron-electronic temperatures. Thus, this model when combined with the electron-electronic equation is what would nominally be termed a "three-temperature" model. This model is an extension of the MCVDV model in Ref. 3 and should be applicable over a wide range of entry conditions

Results obtained with these electron-electronic and vibrational energy models will be compared and contrasted in the final paper. In addition, based upon comparisons with available data, recommendations concerning the applications of the models will be stated.

DIFFUSION MODELS

In the stagnation region of a blunt entry vehicle, large gradients in species concentrations occur in the nonequilibrium region behind the shock front and in the thermal boundary layer near the wall. Thus, in these regions species diffusion is significant and needs to be properly modeled. Currently, there are several models which are commonly used, including the single temperature multicomponent model of Moss (Ref. 17), the approximate multi-temperature multi-component model used by Gnoffo (Ref. 12), the multi-temperature binary diffusion model (Ref. 14) based on the work of Fay and Kemp (Ref. 18 and 19), and the constant Lewis number multi-component approximation of Ref. 20. The latter is currently used by the present model.

Fortunately, as discussed in Ref. 14 and 18, an ionized diatomic gas will often be dominated or closely approximated by only two diffusion velocities, that of the molecules and that of the atoms, ions, and electrons. This phenomena occurs because in many cases charge exchange and ambipolar effects cause atoms, ions, and electrons to all have the same diffusion velocity to a first approximation. Thus, results obtained using different models may be very similar. However, in both the wall thermal layer and the nonequilibrium region behind the shock front, it is possible for the gradients of the atom and ion concentrations to have opposite signs. In those situations, the binary diffusion

models of Ref. 14, 18, and 19 should be inadequate; and a multicomponent diffusion model should be used.

Unfortunately, most of the multicomponent models have various limitations. For example, the Moss model in its presented form does not explicitly account for multiple temperatures and is complicated; while the model used by Gnoffo, which includes multi-temperature phenomena is only "exact" if the diffusing species is a trace species (Ref. 21). Likewise the model of Ref. 20, while implicitly accounting for multi-temperature affects only via the species concentrations, is highly approximate in its use of a single constant Lewis number.

In the final paper, results obtained using a new multicomponent diffusion model will be presented and compared to results obtained with the present model and, possibly, with those obtained using the Gnoffo model. This new model will properly account for multicomponent diffusion due to concentration and pressure gradients in a manner which properly includes multitemperature phenomena. Starting with the general diffusion equations in terms of the difference of diffusion velocities (Ref. 15, also Hirschfelder, Curtiss, and Bird), solving them for the differences in diffusion velocities, and combining them with diffusion conservation,

$$\sum \rho_i U_i = 0$$

expressions for the individual diffusion velocities can eventually be obtained. For example, for a gas composed only of molecules, atoms, atomic ions, molecular ions, and electrons, the resultant expressions are

$$\rho U_i = -\sum_{\substack{j=1 \\ j\neq i}}^{3} \frac{\rho_j}{\rho_i \rho_j} \frac{A_{ij}}{A}$$

$1 = m$
$2 = A$
$3 = I + m^+$

where

$$A = \rho_m \mathcal{D}_{AI} + \rho_A \mathcal{D}_{mI} + \rho_{Im} \mathcal{D}_{mA}$$

$$A_{ij} = \mathcal{D}_{ij} \left(\sum_{\substack{K\neq i \\ K\neq j}} \mathcal{D}_{iK} \rho_j d_i - \mathcal{D}_{jK} \rho_i d_j \right)$$

$$\rho_{Im} = \rho_I + \rho_{m+} = \rho_3$$

and $$d_1 = d_m = \rho \frac{\partial \rho_m}{\partial r} - \frac{\rho}{\rho} \rho_m \frac{\partial \rho}{\partial r}$$

$$d_2 = d_A = \rho \frac{\partial \rho_a}{\partial r} - \frac{\rho}{\rho} \rho_A \frac{\partial \rho}{\partial r}$$

$$d_3 = d_m = \rho \frac{\partial}{\partial r}(\rho_I + \rho_{m+} + \rho_e) - \frac{\rho}{\rho}(\rho_I + \rho_{m+} + \rho_e) \frac{\partial \rho}{\partial r}$$

To complete the model these expressions have to be properly expressed in multitemperature form and included properly in the VSL solution scheme. The latter requires in the species concentration equations oc /oy type of terms. Derivations of the appropriate expressions is currently in progress and algebraic and flowfield results will be presented in the final paper.

PRELIMINARY AND PROPOSED RESULTS

In this section, several sets of results which have been obtained using the above methods and models will be presented. However, at this stage these results are very preliminary and should only be considered indicative of the results which will be presented in the final paper. For simplicity, results have only been obtained for the stagnation streamline with nitrogen as the freestream gas. The final paper will utilize air and include full forward face solutions. The present preliminary results utilize ninety-nine points between the shock and the wall and reaction chemistry set of Ref. 1. However, in many cases electron impact dissociation, i.e. $N2 + e = 2\ N + e$, has been added.

Fire 2 Cases

In order to ensure that the present methods and models are reasonably correct and appropriate, results have been obtained for various trajectory points along the Fire 2 entry profile. These results have been computed assuming a fully catalytic wall at the wall temperature measured in flight, and the full electron-electronic energy model has been used in conjunction with an approximate wall sheath boundary condition on the electron temperature. At the shock, slip conditions have been enforced; and throughout the shock layer multi-component diffusion has been included via the constant Lewis number model with a value of 1.4. Nongray emitting and absorbing radiative transfer has been included along with radiative gasdynamic coupling/cooling. In the radiative transfer, local thermodynamic nonequilibrium effects have been accounted for by using the molecular and first order atomic models described above. In addition, the correct wall absorptivity and reflection properties of the wall, as described in Ref. 22, have been included.

Figures 2-6 show temperature and concentration profiles for five trajectory points during the first period of the Fire 2 entry. These points were selected because they cover the time period of the flight involving extensive chemical and thermal nonequilibrium and

changing radiative behavior. At 1634 seconds (Fig. 2), as evidenced by comparing the "coupled" and "uncoupled" profiles, radiation cooling/coupling is insignificant; and the flow never approaches a chemical equilibrium situation. Further, extensive thermal nonequilibrium exists in the region behind the shock front and also in the thermal boundary layer. The latter results from allowing an approximate sheath boundary condition on electron temperature and the fact that three body ion recombination adds energy to both the free electrons and the excited electronic states. Interestingly, results obtained by forcing Te to equal Tw at the wall yielded only slight differences in heating and, with the exception of the electron temperature profile near the wall, flowfield structure.

By 1637.5 seconds, the temperature profile seems to indicate the post shock nonequilibrium region only comprises about twenty percent of the layer and that much of the flowfield is in equilibrium. However, while thermal equilibrium is achieved near y/yshock of 0.75, careful examination reveals that ionization equilibrium is not reached until about y/yshock of 0.55. Further, as indicated by the temperature decrease and changes in species concentrations, radiation coupling/cooling is significant for this case throughout much of the shock layer. These phenomena can be seen more easily on Figure 7 which portrays the enthalpy and degree of ionization behavior along the stagnation streamline. These profiles, which compare results including and excluding radiation coupling, show that radiation cooling is significant for $0.2 < y/yshock < 0.6$ and that the degree of ionization is decreasing in this region due to the loss of energy by radiation.

In Figure 8, the present predictions for various heating rates measured in flight are compared to the flight data. In flight, a total calorimeter measured the sum of the convective heating plus that portion of the radiative heating absorbed by the gage, which is indicated by the QC + ALPHA*QR line on the figure. The present predictions, indicated by the open squares, are in reasonable agreeement with the flight data; and, while not shown, the present predictions for convective heating are in excellent agreement with

corresponding predictions of Ref. 24-26. The high value at 1634 seconds is typical of theoretical predictions; and, since this conditions is dominated by convective heating, the difference may indicate that at this point the wall (or gage) was not fully catalytic. This possibility is suggested by the results of Ref. 27, which obtained good correlation with Fire 2 data by not assuming fully catalytic walls.

Also shown on Figure 8 are comparisons for radiative heating to the wall for two wavelength regions, .02 - 6.2 eV which is in the visible and infrared, and 2 - 4 eV which primarily should be due to N2+(1-) emission. For the latter case, the flight data exhibited extensive scatter, and this is indicated on the figure by the cross-hatching. As can be seen, the present predictions in the 2-4 eV range are within the data scatter at early times and slightly low at the later times; while the predictions for the visible and infrared regions are low throughout the times considered. However, the data do appear to have the correct trends.

At first glance, the radiation results appearing on Figure 8 are distrubing due to their underprediction. However, the Fire 2 data is a single experiment, and thus must be viewed with care; and the present results are for a nitrogen freesteam and not air. While it is generally true that equilibrium nitrogen and equilibrium air will yield almost identical wall radiative heating rates if they are at the same temperature and pressure, identical freestream conditions will yield cooler equilibrium temperatures for nitrogen than for air. For example, for the 1637.5 sec case, the equilibrium temperature for a nitrogen freestream would be 10155 K while for an air freestream it would be 11021 K. This small 4.5% difference, however, leads to a radiative heating rate for air 60% higher than that for nitrogen. Since the present results were obtained matching freestream conditions on velocity, temperature, and pressure and not post shock conditions, the present radiative heating predictions should be below the flight values, particularly at the later times where the flow is approaching equilibrium. As can be seen on Figure 8, this is indeed the case.

To further test this conjecture, a case was run using a slightly different freestream velocity and pressure that were designed to match the 1637.5 case in air. While this test was not completely successful in that the resultant temperature was still slightly low, the radiative heating results from this case, shown as solid symbols on Figure 8, were higher and closer to the flight data.

To further identify the characteristics of the radiative heating of Fire 2, the stagnation point radiative flux is presented in Figures 9-11 as a function of energy (frequency) for three trajectory points. On these plots, the line and continuum contributions are plotted jointly. Also, for convenience, the line radiation is presented for lines that are close together as an average value over an appropriate width. It should be noted, however, that in the actual calculations the lines are treated individually using appropriate line shapes.

As can be seen, at 1634 seconds most of the radiative flux is in continuum radiation between 2 and 4 eV and in infrared lines, with about 20% of the total being from lines. In fact, for this condition seventy percent of the predicted stagnation point radiation is below 6.2 eV. At 1636 sec, the results indicate the presence of more line radiation overall and increasing continuum radiation in the vacuum ultraviolet (VUV); and by 1637.5 sec there is extensive line and VUV flux. In fact, at the latter time the character of the radiation has changed so that 53% is from lines and only 43% of the total is below 6.2eV. However, in all three cases there is extensive radiation in the 2-4eV range.

The latter range (2 - 4 eV or 0.3 - 0.6 microns) was spectrally measured in flight, and the present predictions for this range are shown on Figure 12. For this region most of the continuum contribution is from N2+(1-). Notice that at 1634 sec most of the flux is between 3 and 3.5 eV (.35 - .4 microns), but that by 1637.5 sec the flux is relatively constant. This trend and the relative levels are in excellent agreement with the flight data presented in Ref. 23.

Based upon these comparisons with the Fire 2 flight data, it is believed that the present method and models are reasonable and appropriate. Thus, they should be useful in studying a wide variety of entry vehicle flowfield situations.

AFE CFD Point 2

This condition corresponds to what is often referred to as the "max Q" computational point for one of the initial AFE trajectories at which the freestream velocity is 8.915 km/sec, freestream pressure is 15.715 dyne/sq cm and temperature is 197.101 K. For this case, the free stream is considered to be nitrogen and the nose radius has been assumed to be 2.3 meters. Also, the wall has been assumed to be radiatively black, catalytic to ionic recombination but noncatalytic to atomic recombination, and at a temperature of 1650 K. Figures 13-15 show stagnation line results obtained for this case under various assumptions. In all cases, nongray radiative transfer has been included and LTNE has been accounted for using the molecular and first order atomic models previously described. Also, for these cases the electron temperature was required to equal the heavy particle temperature at the wall.

The results presented on Figures 13 (a) and (b) were obtained using the quasi-equilibrium free electron energy model without the electron impact molecular dissociation reaction, and profiles obtained with both fixed and slip shock jump conditions using a Lewis number of 1.4 are portrayed. As shown, the electron temperature rapidly rises behind the shock front and equilibrates with the heavy particle temperature. However, as evidenced by the continual decrease in temperature and the variations in composition across the shock layer, the stagnation flow for this case is always in chemical nonequilibrium. Also, the wall thermal layer comprises approximately twenty percent of the 12.2 cm thick shock layer. For this case, the convective heating was 13.55 watts/sq cm and the total radiative heat flux to the wall was 1.56 watts/sq cm.

With respect to temperature, the effects of slip versus fixed shock jump conditions seems to be confined to a small region immediately behind the shock front. However, as can be seen, the effects on concentration and particularly on total enthalpy are significant. In fact, the total enthalpy profiles clearly show that the fixed shock boundary condition results in an incorrect value for enthalpy in the interior of the shock layer, leading to incorrect species concentration values. Interestingly, with the fixed shock boundary conditions, when a Lewis number of one is used the enthalpy profile appears to be correct and when a value less than unity is used, the enthalpy is high in the flow interior. However, for the slip shock condition, the enthalpy profiles are unaffected by Lewis number. Since a Lewis number of 1.4 is more appropriate for describing atom molecule diffusion, which is the dominant diffusion mechanism in this flow, and since the enthalpy in the flow interior in the absence of significant radiative cooling should be unity, these results indicate that only the slip boundary condition is appropriate for these conditions.

Figure 14 shows the same case but with the electron energy modeled using the qausi-equilibrium electron-electronic model. As can be seen, this model leads to a significant decrease in electron temperature and increase in the extent of thermal nonequilibrium. In fact, almost the entire shock layer is in thermal nonequilibrium for this condition and model. As a result of the electron temperature decrease the shock layer is slightly thicker at 12.5 cm and the total radiative heating is reduced to 0.61 watts/sq cm. The convective heating to the partially catalytic wall is relatively unchanged at 13.65 watts/sq cm.

On Figure 15 results are also presented for this case using the quasi-equilibrium electron-electronic model, but for this calculation electron impact dissociation ($N_2 + e = 2N + e$) has been included. Since this reaction uses free electron energy to dissociate nitrogen molecules, it has a slightly lower electron temperature than the previous result.

Consequently, the radiative heat transfer is predicted to be only 0.43 watts/sq cm. For this model, the shock layer thickness was 12.5 cm and the convective heating rate was 13.62watts/sq cm, which are essentially the same as the previous case.

These results demonstrate the importance of using slip shock boundary conditions at these conditions and the sensitivity of radiative heating to electron temperature modeling. Since at these conditions, vibrational nonequilibrium should also be important, it is planned in the final paper to include results which include vibrational nonequilibrium. Also, it should be noted that since the results shown on Figs. 13-15 were for a nitrogen freestream, the radiative heating values in air, based upon the Fire 2 data, will probably be slightly higher.

AFE CFD Point 4

This condition corresponds to a "max Q" point for a heavier AFE vehicle at which the freestream velocity is 9.326 km/sec, freestream pressure is 26.4 dynes/ sq cm and temperature is 200 K. Again the freestream is nitrogen, the nose radius is 2.3 m, the wall is assumed to be partially catalytic at 1650 K, and both molecular and atomic nongray radiation have been include using the molecular and first order LTNE models. Stagnation line temperature and concentration profiles are presented on Figure 16, which compares results obtained using the quasi-equilibrium electron-electronic model (QEEE) including the electron impact dissociation reaction with those using the quasi-equilibrium electron (QEE) energy model only. As for CFD Point 1, the primary effect of using the QEEE model is more extensive thermal nonequilibrium and a lower electron temperature thru much of the shock layer. Also, the combined effect of electron impact dissociation and the QEEE model leads to a more dissociated flow having slightly different N2 and N2+ profiles.

Again, the most significant difference in the two models is the radiative heat transfer. For the QEEE case, the lower electron temperature yielded a total radiative flux of 1.18 watts/sq cm, a shock standoff distance of 11.96 cm, and a convective heating of 25.8

watts/sq cm. For the QEE model it was 2.91 watts/sq cm., 11.89 cm, and 25.7 watts/sq cm respectively.

Figure 17(a) shows the stagnation point continuum and line radiation distributions predicted with the QEEE model. In the actual radiative transfer analysis, lines are considered and integrated individually, but they are presented on Fig. 17 as average values for various line groups for convenience. As can be seen, there are many infrared line groups and some in the ultra-violet. However, compared to the continuum, the line contributions are negligible. For the continuum, most of the radiation (about 90%) is in the visible and infrared below 6.2 ev; and most of that is between 2 and 4 ev. At these conditions, this radiation is due to the N2+(1-) band. Also, there is some continuum contributions in the ultra-violet, probably due to nitrogen free-bound processes and N2(BH) bands.

Figure 17(b) shows the same information as Figure 17(a) except each line is shown individually. As can be seen, many of the VUV lines are absorbing in their line centers and the IR lines are essentially transparent. However, for this case line radiation is insignificant compared to the continuum contribution.

As part of this study, computations were conducted using the QEE model without including molecular LTNE effects; and the resulting radiative heat transfer result was 8.90 watts/sq cm. Obviously, molecular LTNE is important at AFE conditions and leads to lower radiative heating. Examination of the results which included LTNE effects indicate that the LTNE induced by chemical and thermal nonequilibirum drastically reduces radiation from the N2(1+) and N2(2+) bands and significantly decreases that due to N2(BH). However, N2+(1-) is virtually unaffected by chemical and thermal nonequilibrium phenomena. Thus, on Fig. 17, the primary stagnation point radiation is in the continuum between 2 and 4 eV and is from the N2+(1-) band.

At shock speeds below 10 km/sec, shock tube photomultiplier results indicate a sharp rise in intensity to a peak immediately behind the shock front followed by a decrease until equilibrium is achieved (Ref. 28). Similar results have been obtained computationally for nonequilibrium flows for the visible region of the spectrum assuming the gas to transparent (Ref. 16). Figure 18 shows for the present QEEE model the variation along the stagnation line in radiative flux towards the stagnation point, QR+, and its negative derivative, -DQR+/DY. The latter is essentially what Candler (Ref. 16) and others have termed radiation intensity. As can be seen, -DQR(+)/DY is similar to observed photomultiplier traces in having a peak near the shock front followed by a steady decrease towards the wall. For this case, no equilibrium plateau is achieved since the flow never reaches chemical equilibrium prior to the wall thermal boundary layer. (The oscillations near the wall are an artifact due to significant digit error resulting from providing the plot routine formatted data. The actual curve is smooth.) Comparison with the temperature plots indicates that the "intensity" peak corresponds to the maximum value in electron temperature; and near the wall the "intensity" is negative, indicating absorption. However, as shown by only the slight decrease in QR(+), the amount of absorption near the wall is negligible at these conditions.

AOTV -- 14 Km/sec, 80 km

This case is representative of a small Mars return aerocapture vehicle. (In the final paper, results for several cases representative of Mars/Lunar return will be included. At present, it is planned to cover entry speeds of 11 - 16 km/sec and altitudes of 70 - 80 km.) For this preliminary result, the freestream is considered to be nitrogen at 180.65K and 10.35 dynes/sq cm. The nose radius is 2.3 m, the wall is assumed to be partially catalytic at 1650 K, and both molecular and atomic nongray radiation have been include using the molecular and first order LTNE models. Stagnation line temperature and concentration profiles obtained using the exact electron-electronic energy model are presented on Figure

19, which compares results obtained with and without radiative gasdynamic coupling/cooling. Further, shock slip and an approximate sheath representation were used as boundary conditions; and electron impact dissociation was included in the reaction chemistry.

As can be seen, the post shock electron-electronic temperature peaks at a value several thousand degrees above the equilibrium temperature, and the wall sheath representation only affects the electron temperature in a small zone near the wall. For this case, the shock layer thickness was 9.03 cm, the covective heating was 56.8 watts/sq cm, and the radiative heating was 111.7 watts/sq cm. Interestingly, especially when compared to the AFE cases, only about ten percent of this radiative heating is due to molecular processes.

As part of this study, several cases were also conducted at this condition using the quasi-equilibirum electron-electronic and quasi-equilibrium electron energy models; and the primary difference between the models was that the peak in electron temperature was slightly higher and slightly further from the shock front with the exact model than with the quasi-equilibrium models. This behavior has been observed at freestream velocities of 12 Km/sec and higher and is in sharp contrast to the trends displayed at the AFE velocities. Apparently, at the higher velocities there are more electrons and the flow is dominated by ionization processes. Consequently, the electron-electronic energy is dominated by the free electrons. At the lower AFE speeds, there is very little ionization and the electronic energy portion dominates the combination. Thus, the shape and character of the electron temperature profiles appears to be significantly different at Martian return velocities than at AFE speeds.

Figure 19 also shows that that radiation cooling at this condition (coupled results) is significant, leading to cooler temperatures and different concentration profiles. The magnitude of radiation cooling is quite evident in the total enthalpy and degree of ionization profiles displayed on Figure 20. As can be seen, radiative cooling is present

throughout most of the shock layer and significantly decreases the amount of ionization. Also, the effects of diffusion near the shock front can be seen in the enthalpy changes in that region. Similar diffusion effects exist near the wall, but the decrease in enthalpy due to thermal conduction dominates the profile and prevents them being observed on the figure.

The spectral variation in radiative heat flux to the wall is shown on Figure 21, where the contributions due to line and continuum processes have been combined and the convenient representation of lines as group averages has been utilized. Here, the heating due to continuum and lines is similar in magnitude with extensive infrared and UV lines as well as significant VUV bound-free processes. In fact, only about twenty-eight percent of the wall flux is from the visible and infrared below 6.2 eV. Notice that a measureable portion of the visible radiation is between 2 and 4 eV and is due to N2+(1-) molecular radiation. Nevertheless, while this type of presentation is informative and useful, especially for continuum radiation, the characteristics and number of lines is not evident on this type of plot.

As mentioned previously, the actual radiative transfer analysis treats lines individually, and Figure 22 displays the same information as Figure 21 but with each line shown separately. From this representation, it is evident that in the visible and infrared the line radiation is primarily transparent. However, in the VUV, many of the line centers are highly absorbing with most of the emission reaching the wall emanating from the line wings.

In contrast to results below 10 km/sec, shock tube photomultiplier results at higher speeds show that the radiative intensity peak behind a shock front changes from a single peak to a double hump peak system (Ref. 28). Experimental spectral data indicates that the first is due to molecular radiation near the shock front while the second is atomic radiation coupled to the ionization process. Figure 23 shows for the present case

theoretical predictions of the radiative flux towards the wall, QR+, and the negative of its derivative, - DQR(+),DY. As discussed previously, the latter is closely related to radiative intensity.

As can be seen on the plot, the present profile clearly exhibits this double hump behavior. The first peak corresponds to the maximum value of the electron temperature, while the second occurs at the onset of thermal equilibrium and the establishment of near Boltzmann distributions in the excited states. Subsequently, radiative cooling occurs and the "intensity" rapidly decreases. During this period, examination of the species concentrations and of LTNE phenomena indicates nonequilibrium recombination is induced with resultant overpopulation, compared to a Boltzmann distribution, of the excited states. Around y/yshock of 0.3 the flow begins to absorb more than it emits and QR+ begins to decrease. However, as shown by the QR+ profile, which only decreases slightly between 0.3 and the wall, the absorption in the wall thermal layer only results in a mild decrease in QR+ at this condition.

Finally, Figure 24 present some very preliminary results obtained using the second order nonequilibrium atomic radiation model in conjunction with the nonequilibrium molecular model. The flowfield conditions and boundary conditions for this case are 14 Km/sec at 80 Km and are identical to those of Figure 19. Examination of these preliminary data indicates that compared to those obtained with the first order model, the post shock chemical nonequilibrium region is smaller and the electron temperature peaks slightly quicker at a slightly lower value. Also, the outer twenty-five percent and inner ten percent of the stagnation region is in local thermodynamic nonequilibrium in that the N* population is not that predicted by a Boltzmann distribution. Further, unlike Figure 19, the new excitation rate is sufficiently fast to maintain local thermodynamic equilibrium in the interior of the flowfield, even with extensive radiative cooling/coupling. In fact the new rates actually lead to higher radiative cooling in the outer portions of the shock layer.

However, the effect is to cool the shock layer and this leads to slightly lower wall radiative heating than with the previous model. For this result, the radiative heating was 105.6 watts/sq cm, the covective was 60.3 watts/sq cm. and the standoff distance was 8.82 cm. The final paper will also include air results and, for several cases, flowfield computations involving the front face of representative vehicles.

CONCLUSIONS

In this paper, several flowfield coupled coupled electronic excitation models for nonequilibrium atomic radiation suitable for rapid flowfield calculations have been presented. Further, due to the sensitivity of results, several electron-electronic energy and diffusion models have been presented and their effect on flowfield structure, nonequilibrium electronic excitation, and radiative transfer have been examined. These models have been incorporated into a computational flowfield program which includes nonequilibrium chemistry, thermal nonequilibrium, viscous, conduction, and diffusion effects, and coupled nongray radiative transfer. The latter has been modified to include local thermodynamic nonequilibrium phenomena resulting from chemical and thermal nonequilibrium.

Comparison with the Fire 2 flight experimental data indicates that the present models are appropriate and reasonable. Subsequently, based upon these models, results are presented for a variety of cases including two AFE cases and a situation representative of Martian return aerocapture. These results show the importance of shock slip, chemical and radiative nonequilibrium, and radiative gasdynamic coupling. They also demonstrate the differences between using various electron-electronic energy models and delineate the differences between molecular dominated flows such as AFE and those characterized by ionization such as Martian return.

Table V -- Collisional Reaction Rate System

Number	Reaction	
1.	$N_2 + M \rightleftharpoons 2N_g + M$	$(M = N_g, N^*)$
2.	$N_2 + N_2 \rightleftharpoons 2N_g + N_2$	
3.	$N_2 + M \rightleftharpoons 2N + M$	$(M = N^+, N_2^+)$
3a	$N_2 + e \rightleftharpoons 2N + e$	
4.	$N_2 + N^+ \rightleftharpoons N_2^+ + N_g$	
5.	$N_g + N_g \rightleftharpoons N_2^+ + e^-$	
6.	$N_g + N \rightleftharpoons N^+ + e^- + N$	
7.	$N_g + N^+ \rightleftharpoons 2N^+ + e^-$	
8.	$N_g + e^- \rightleftharpoons N^+ + 2e^-$	
9.	$N_g + e^- \rightleftharpoons N^* + e^-$	
10.	$N^* + e^- \rightleftharpoons N^+ + 2e^-$	

REFERENCES

1. Carlson, L. A. and Gally, T. A., "The Effect of Electron Temperature and Impact Ionization on Martian Return AOTV Flowfields," AIAA Paper 89-1729, June 1989.

2. Carlson, L. A., "Approximations for Hypervelocity Nonequilibrium Radiating, Reacting, and Conducting Stagnation Regions," Journal of Thermophysics and Heat Transfer, Vol. 3, No. 4, October 1989, pp. 380-388.

3. Carlson, L. A., Bobskill, G. J., and Greendyke, R. B., "Comparison of Vibration Dissociation Coupling and Radiative Transfer Models for AOTV/AFE Flowfields," Journal of Thermophysics and Heat Transfer, Vol. 4, No. 1, January 1990, pp. 16-26.

4. Carlson, L. A. and Gally, T. A., "Nonequilibrium Chemical and Radiation Coupling Phenomena in AOTV Flowfields," AIAA Paper 91-0569, January 1991.

5. Nicolet, W., "User's Manual for the Generalized Radiation Transfer Code (RAD/EQUIL or RADICAL)," NASA CR 116353, October 1969.

6. Park, C., "Calculation of Nonequilibrium Radiation in the Flight Regimes of Aeroassisted Orbital Transfer Vehicles," in Thermal Design of Aeroassisted Orbital Transfer Vehicles, Progress in Astronautics and Aeronautics, Vol. 96, Ed. by H. F. Nelson, AIAA, New York, 1985, pp. 395 - 418.

7. Kunc, J. A. and Soon, W. H., "Collisional Radiative Nonequilibrium in Partially Ionized Atomic Nitrogen," Physical Review A, Vol. 40, No. 10, November 15, 1989, pp. 5822 ff.

8. Park, C., "Assesment of Two Temperature Kinetic Model for Ionizing Air," AIAA Paper 87-1574, June 1987.

9. Foley, W. H. and Clarke, J. H., "Shock Waves Structered by Nonequilibrium Ionizing and Thermal Phenomena," Physics of Fluids, Vol. 16, No. 3, March 1973, pp. 1612-1620.

10. Nelson, H. F., "Nonequilibrium Structure of Argon Shock Waves," Physics of Fluids, Vol. 16, No. 12, December 1973, pp. 2132 - 2142.

11. Park, C., "Nonequilibrium Air Radiation (NEQAIR) Program: User's Manual," NASA TM B6707, July 1985.

12. Gnoffo, P. A., Gupta, R. N., and Shinn, J. L., "Conservation Equations and Physical Models for Hypersonic Air Flows in THermal and Chemical Nonequilibrium," NASA TP 2867, February 1987.

13. Lee, J. H., "Basic Governing Equations for the Flight Regimes of Aeroassisted Orbital Transfer Vehicles," in Thermal Design of Aeroassisted Orbital Transfer Vehicles, Progress in Astronautics and Aeronautics, Vol. 96, Ed. by H. F. Nelson, AIAA, New York, 1985, pp. 3 - 53.

14. Carlson, L. A., "Radiative Gasdynamic Coupling and Nonequilibrium Effects Behind Reflected Shock Waves," AIAA Journal, vol. 9, No. 5, May 1971, pp. 858-865.

15. Chapman, S. and Cowling, T. G., The Mathematical Theory of Non-Uniform Gases, Cambridge, 1964.

16. Candler, G. and Park, C., "The Computation of Radiation from Nonequilibrium Hypersonic Flows," AIAA 88-2678, June 1988.

17. Moss, James N., "Reacting Viscous Shock Layer Solutions with Multicomponent Diffusion and Mass Injection," NASA TR - R - 411, June 1974.

18. Fay, J. A. and Kemp, N. H., "Theory of Stagnation Point Heat Transfer in a Partially Ionized Diatomic Gas," AIAA Journal, Vol. 1, No. 12, December 1963, pp. 2741-2751.

19. Camac, M. and Kemp, N. H., "A Multi-temperature Boundary Layer," Avco Research Report 184, August 1964.

20. Miner, E. W. and Lewis, C. H., "Hypersonic Ionizing Air Viscous Shock Layer FLows over Nonanalytic Blunt Bodies," NASA CR-2550, May 1975.

21. Curtiss, C. F. and Hirschfelder, J. O., "Transport Properties of Multi-Component Gas Mixture," Journal of Chemical Physics, Vol. 17, No. 6, June 1949, pp. 550-555.

22. Cauchon, D. L., "Radiative Heating Results from the Fire II Flight Experiments at a Reentry Velocity of 11.4 Kilometers Per Second,", NASA TM X-1402, 1966.

23. Cauchon, D. L., McKee, C. W., and Cornette, E. S., "Spectral Measurements of Gas-Cap Radiation During Project Fire Flight Experiments at Reentry Velocities Near 11.4 Kilometers per Second," NASA TM X-1389, October 1967.

24. Gupta, R. N., "Navier Stokes and Viscous Shock Layer Solutions for Radiating Hypersonic Flows," AIAA Paper No. 87-1576, June 1987.

25. BalaKrishnan, A., C. Park, and Green, J. M., "Radiative Viscous Shock Layer Analysis of Fire, Apollo, and PAET Flight Data," AIAA Paper 85-1064, 1985.

26. Sutton, K., "Air Radiation Revisited," AIAA Paper 84-1733, 1984.

27. Bird, G. A., "Nonequilibrim Radiation During Re-Entry at 10 km/sec," AIAA Paper No. 87-1543.

28. Wilson, J., "Ionization Rate of Air Behind High Speed Shock Waves," The Physics of Fluids, Vol. 9, No. 10, October 1966, pp. 1913-1921.

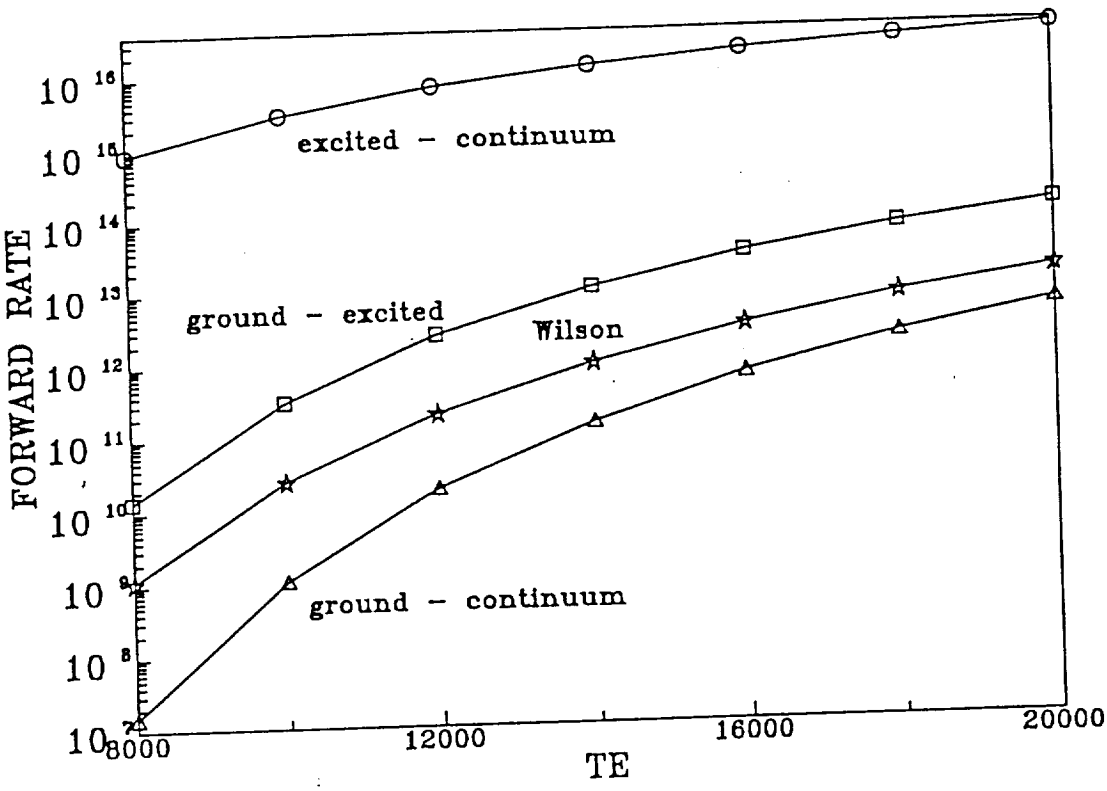

Fig. 1 -- Effective Forward Reaction Rates for Excitation and Ionization from N(ground) and N(excited)

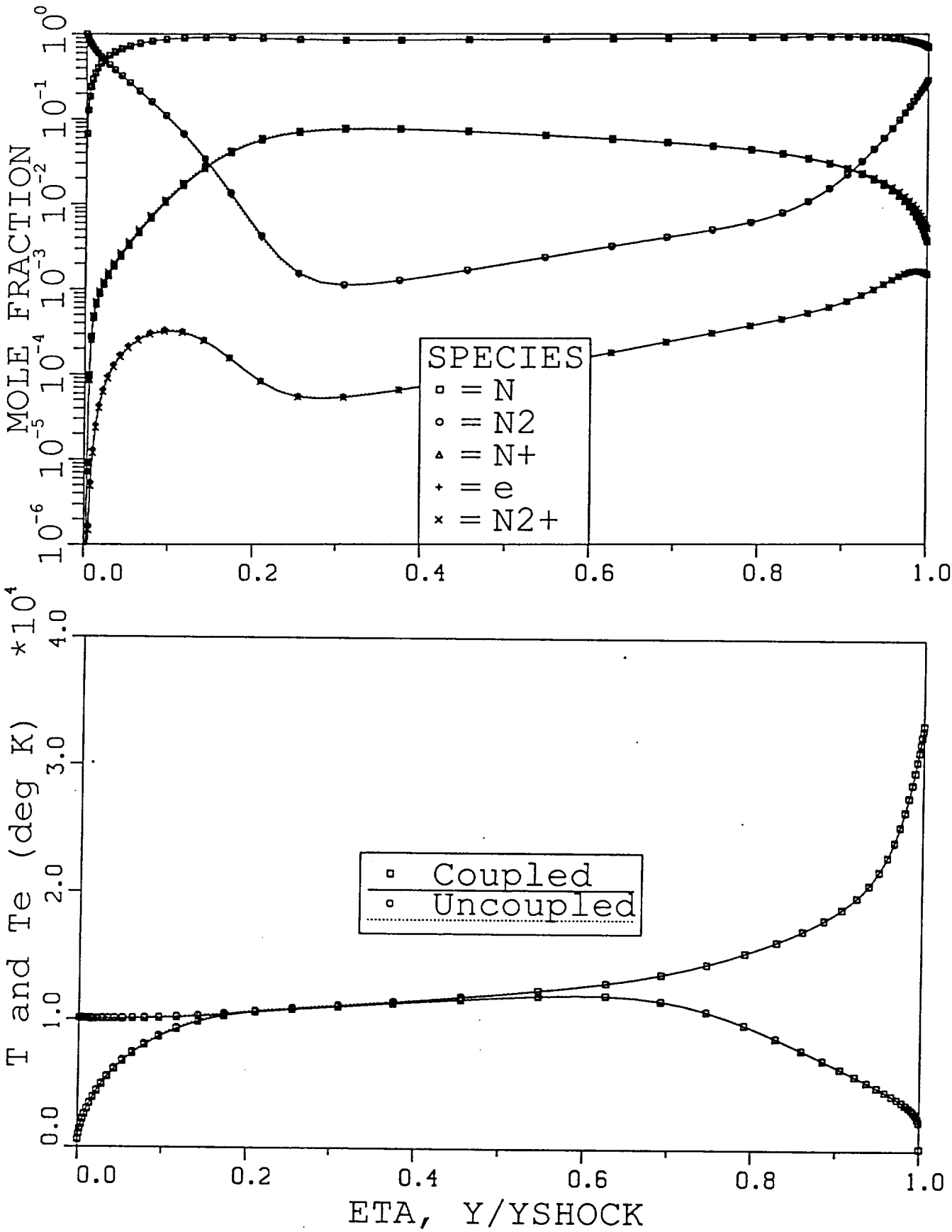

Fig.2 -- Stagnation Profiles for Fire 2 at 1634 Seconds
δ = 4.12 cm

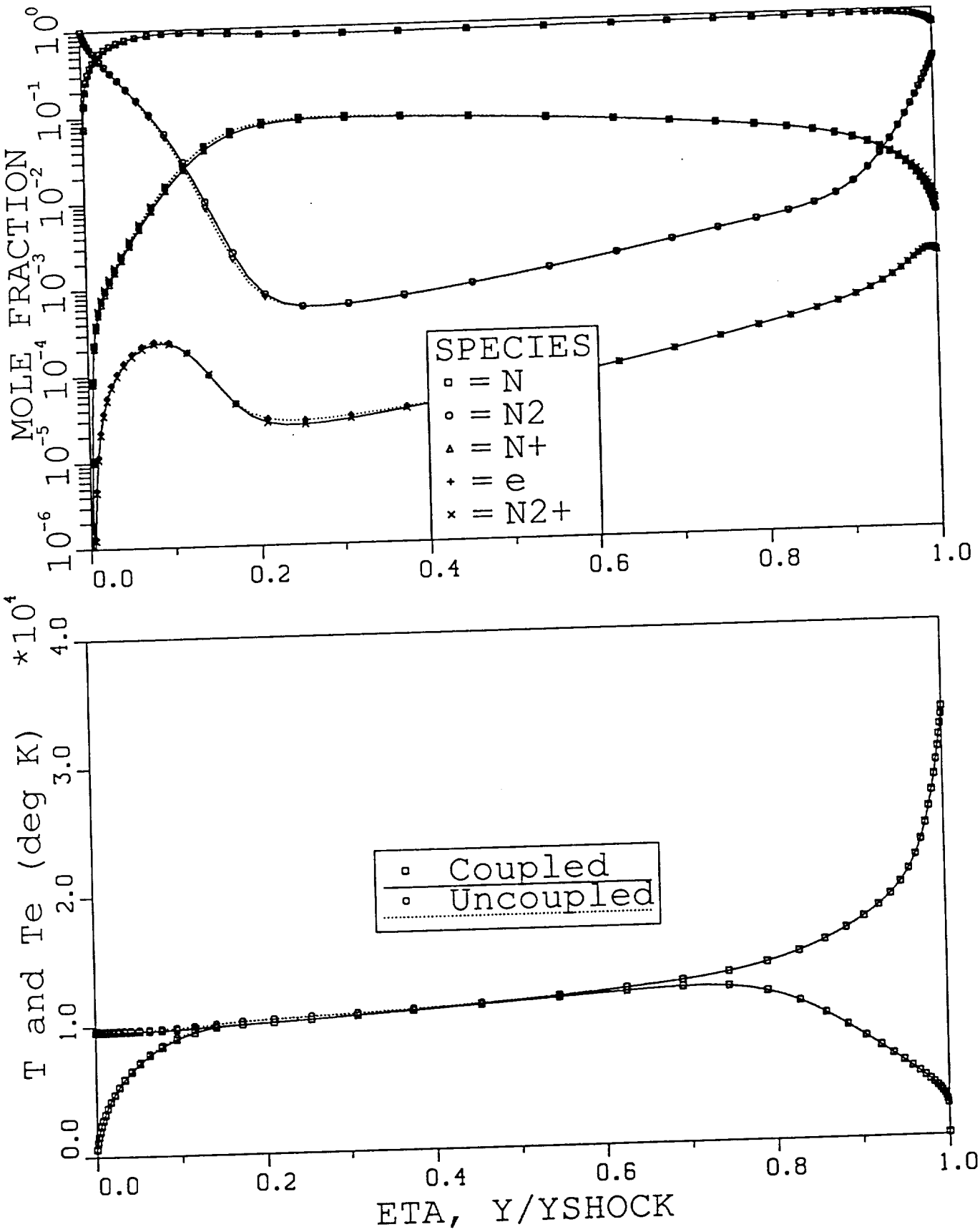

Fig. 3 -- Stagnation Profiles for Fire 2 at 1635 Seconds
δ = 3.91 cm

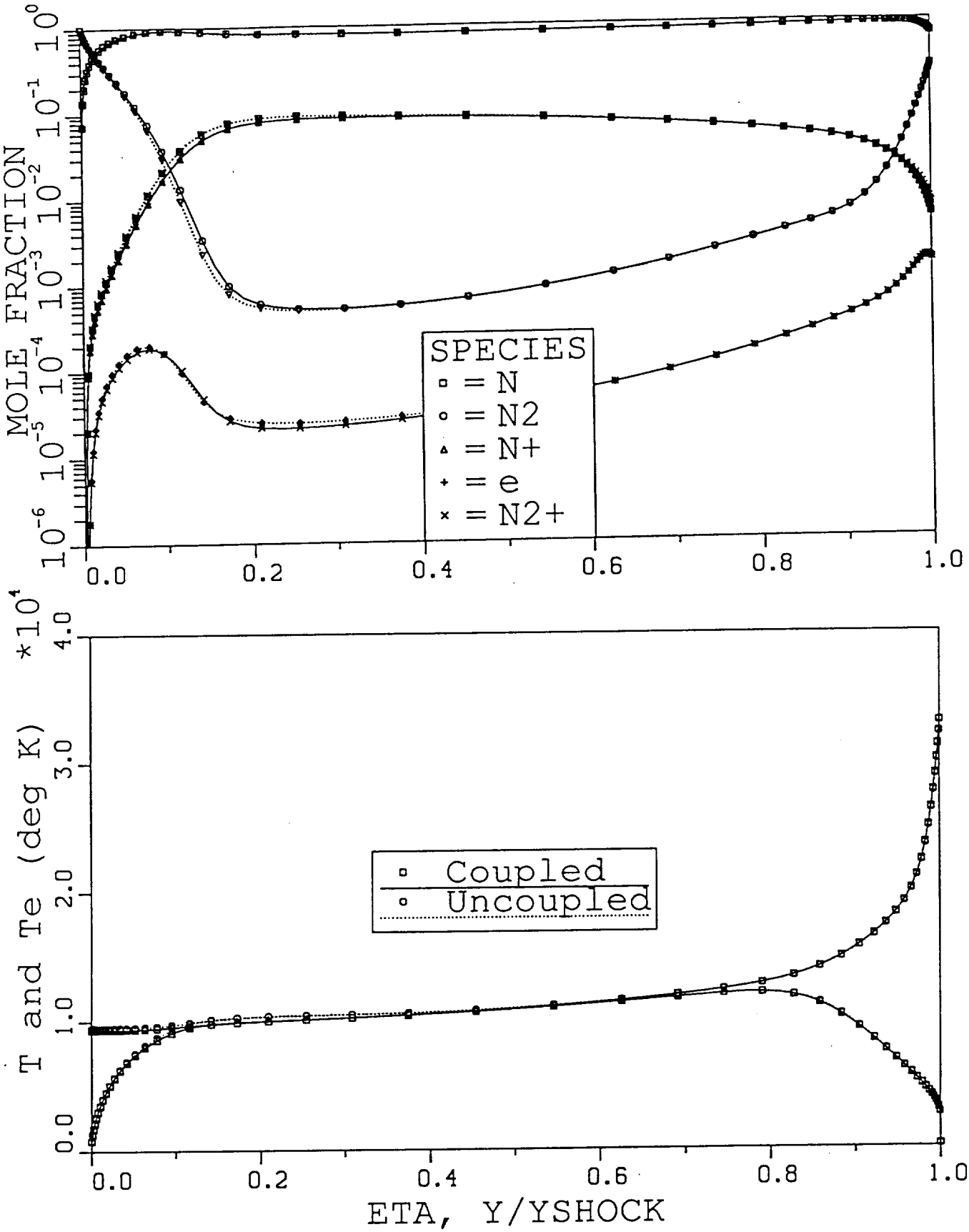

Fig. 4 -- Stagnation Profiles for Fire 2 at 1636 Seconds
δ = 3.80 cm

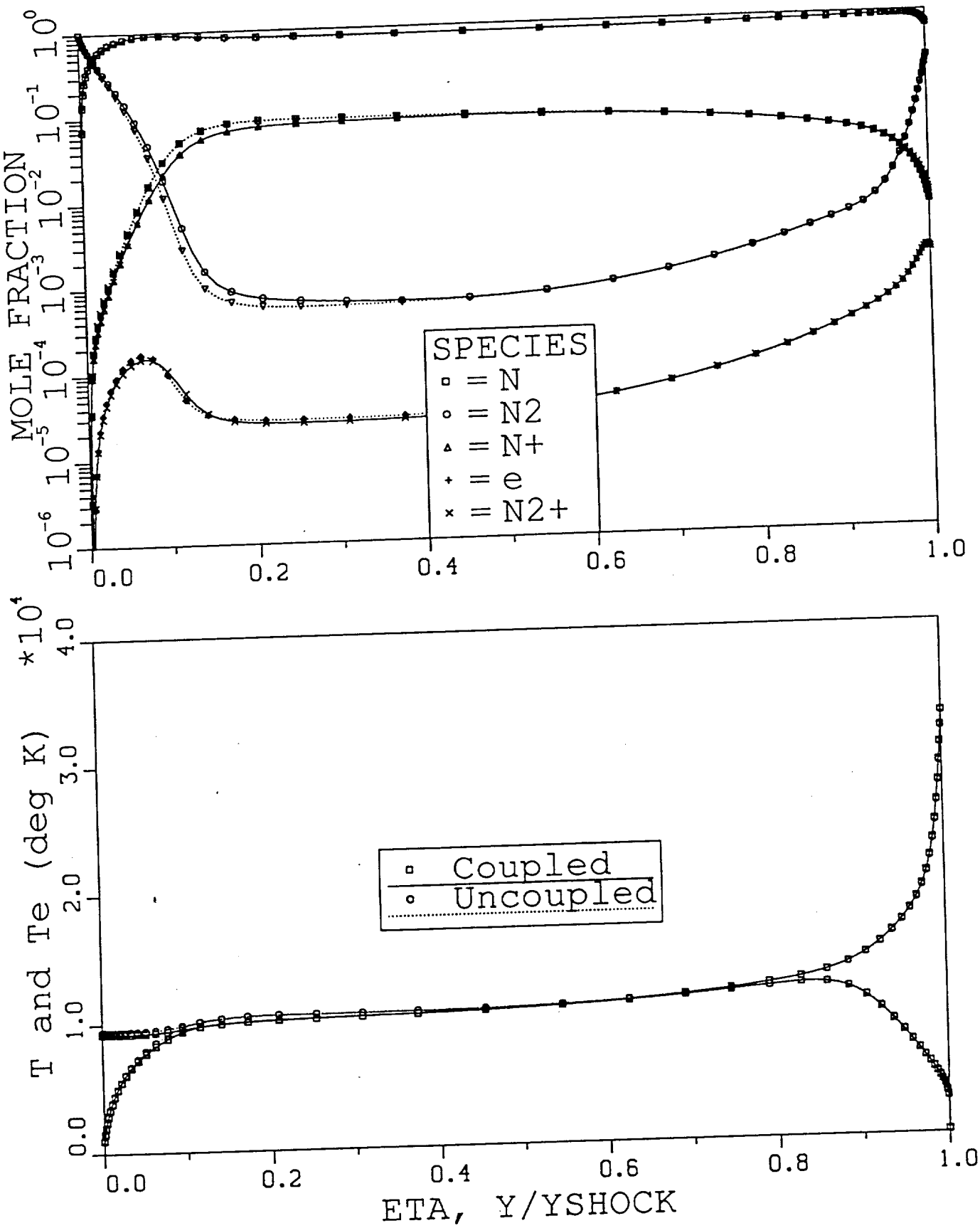

Fig. 5 -- Stagnation Profiles for Fire 2 at 1637 Seconds
δ = 3.73 cm

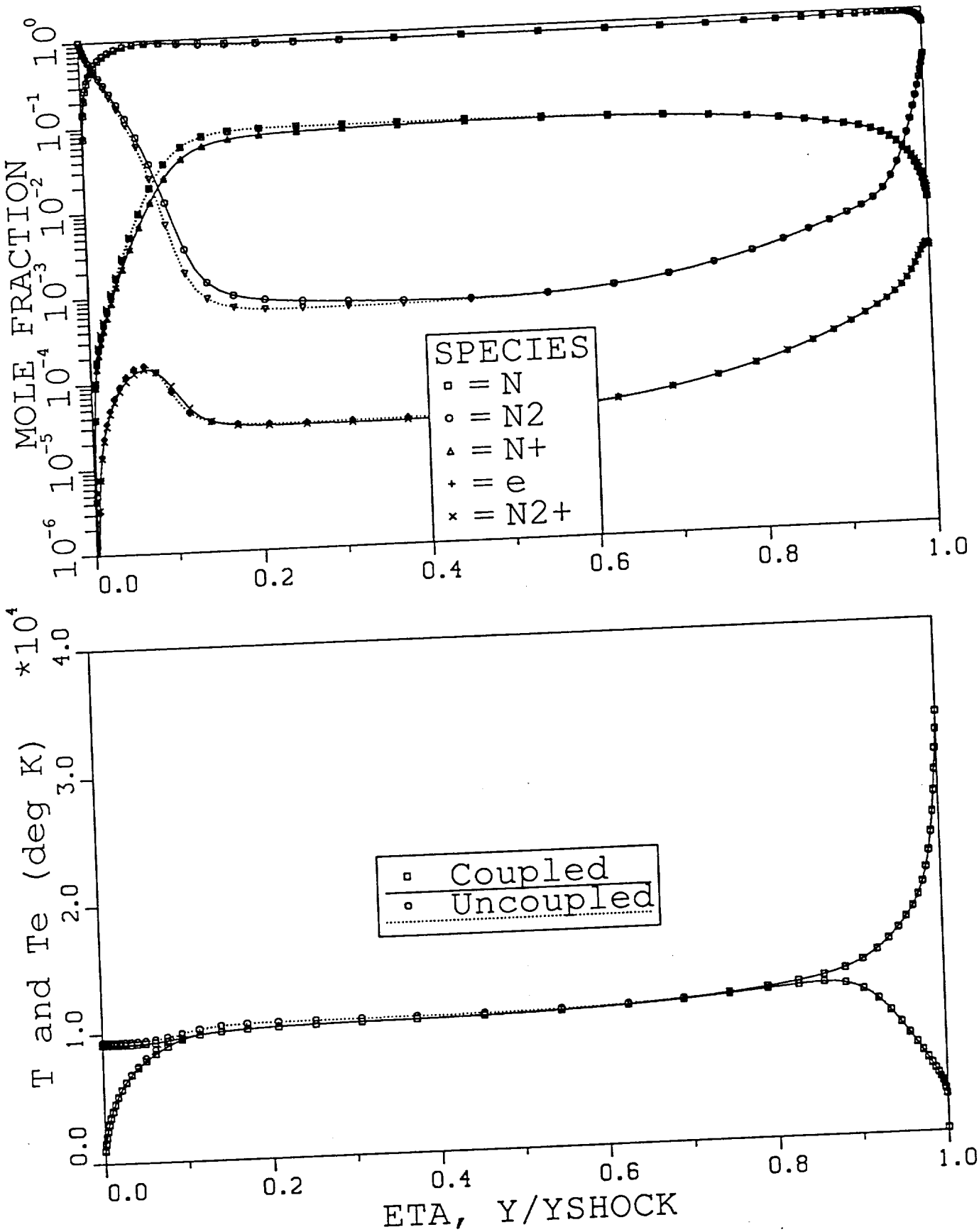

Fig. 6 -- Stagnation Profiles for Fire 2 at 1637.5 Seconds
δ = 3.72 cm

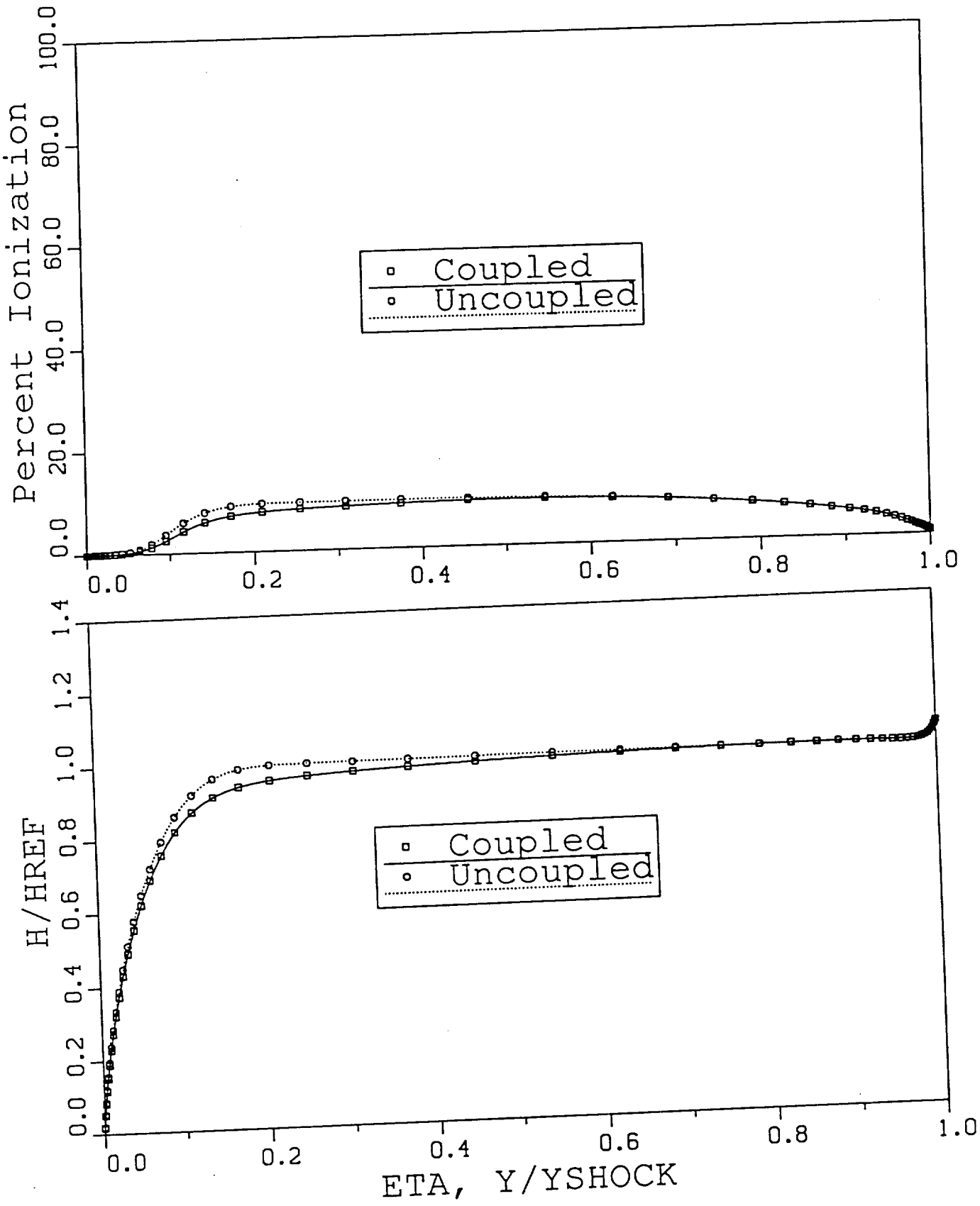

Fig. 7 -- Enthalpy and Ionization Profiles for Fire 2 at 1637.5 Seconds

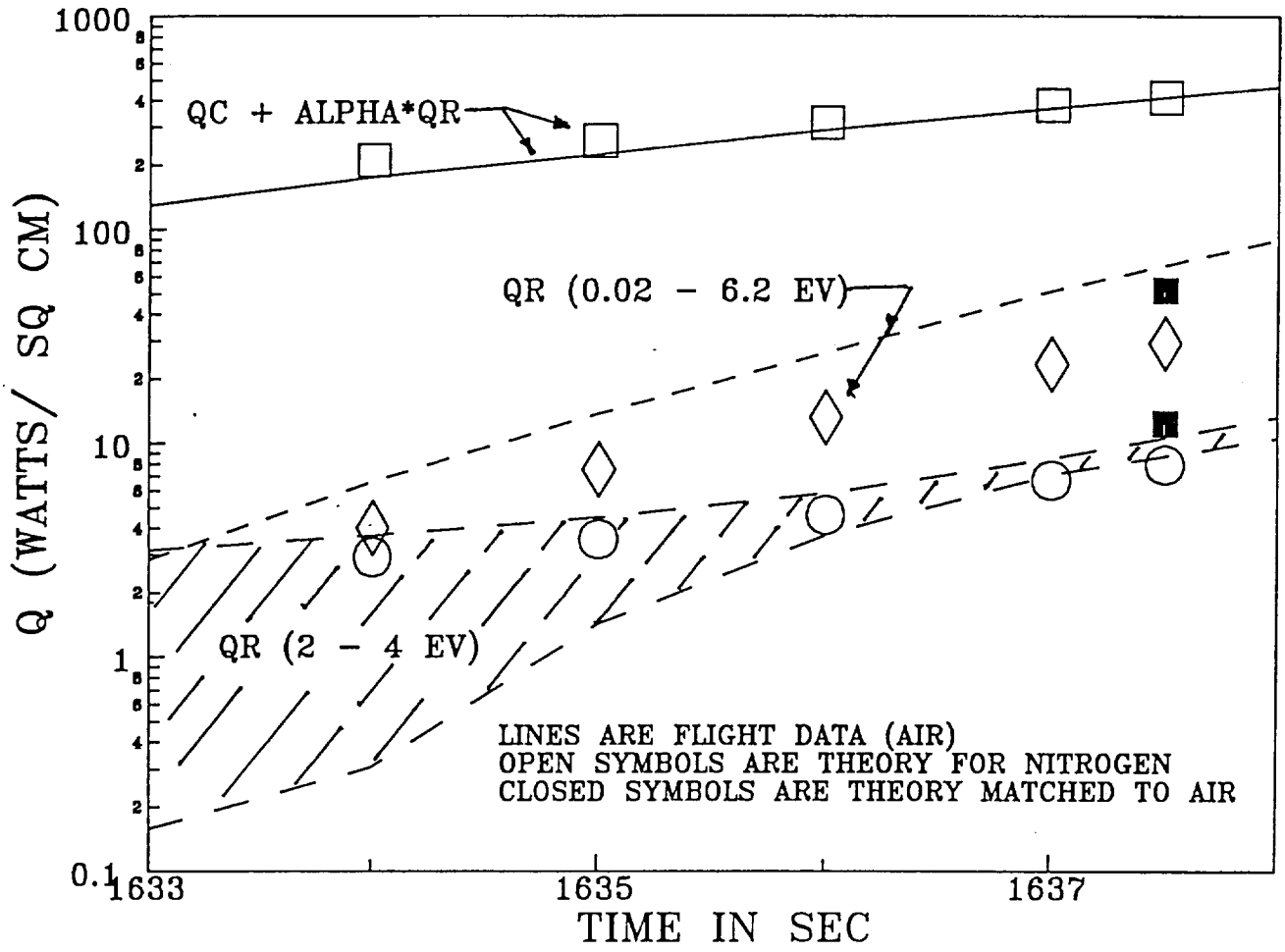

Fig. 8 -- Comparison of Present Fire 2 Predictions (Nitrogen) with Flight Data (Air)

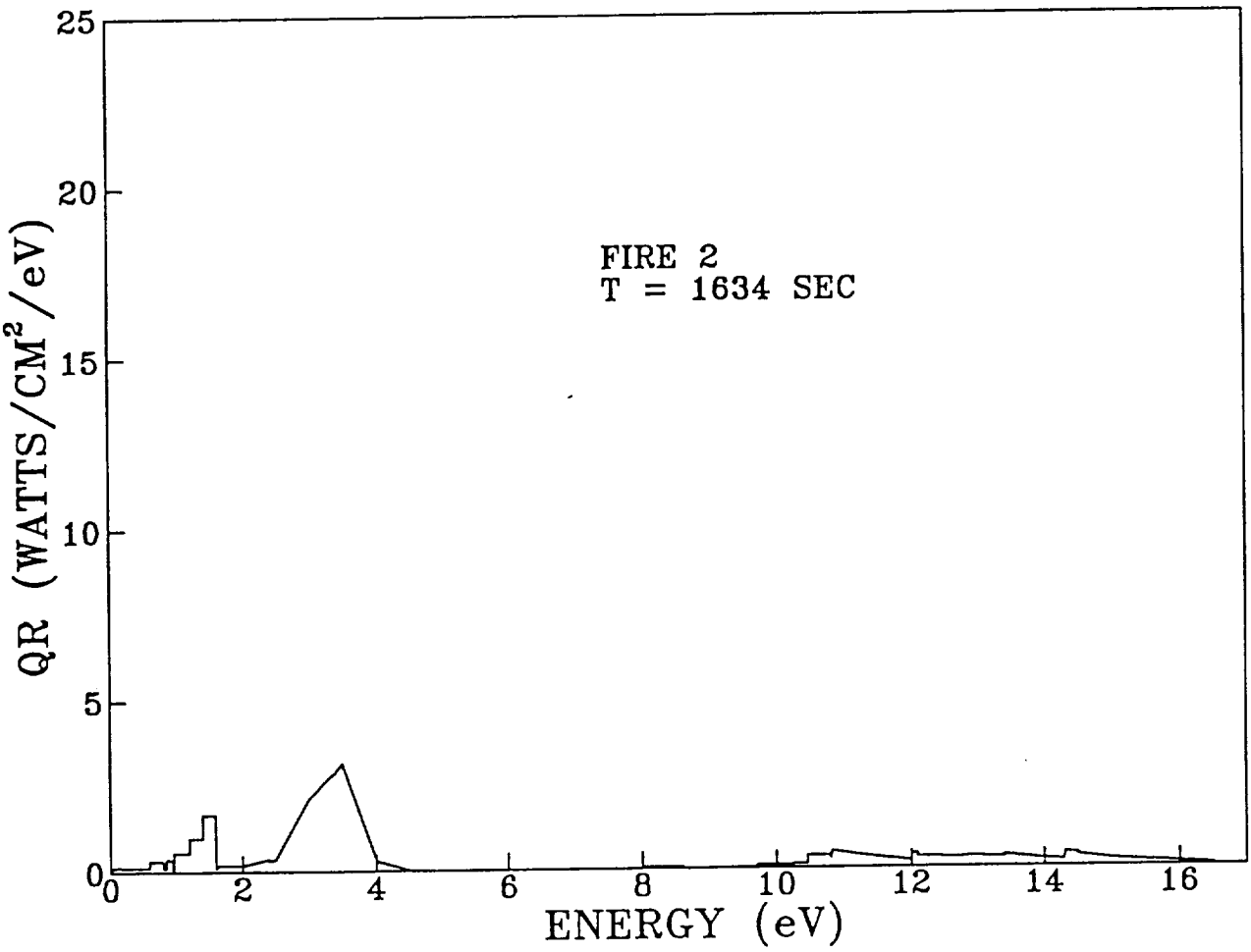

Fig. 9 -- Spectral Variation of Stagnation Point Radiative Heat Transfer for Fire 2 at 1634 Seconds

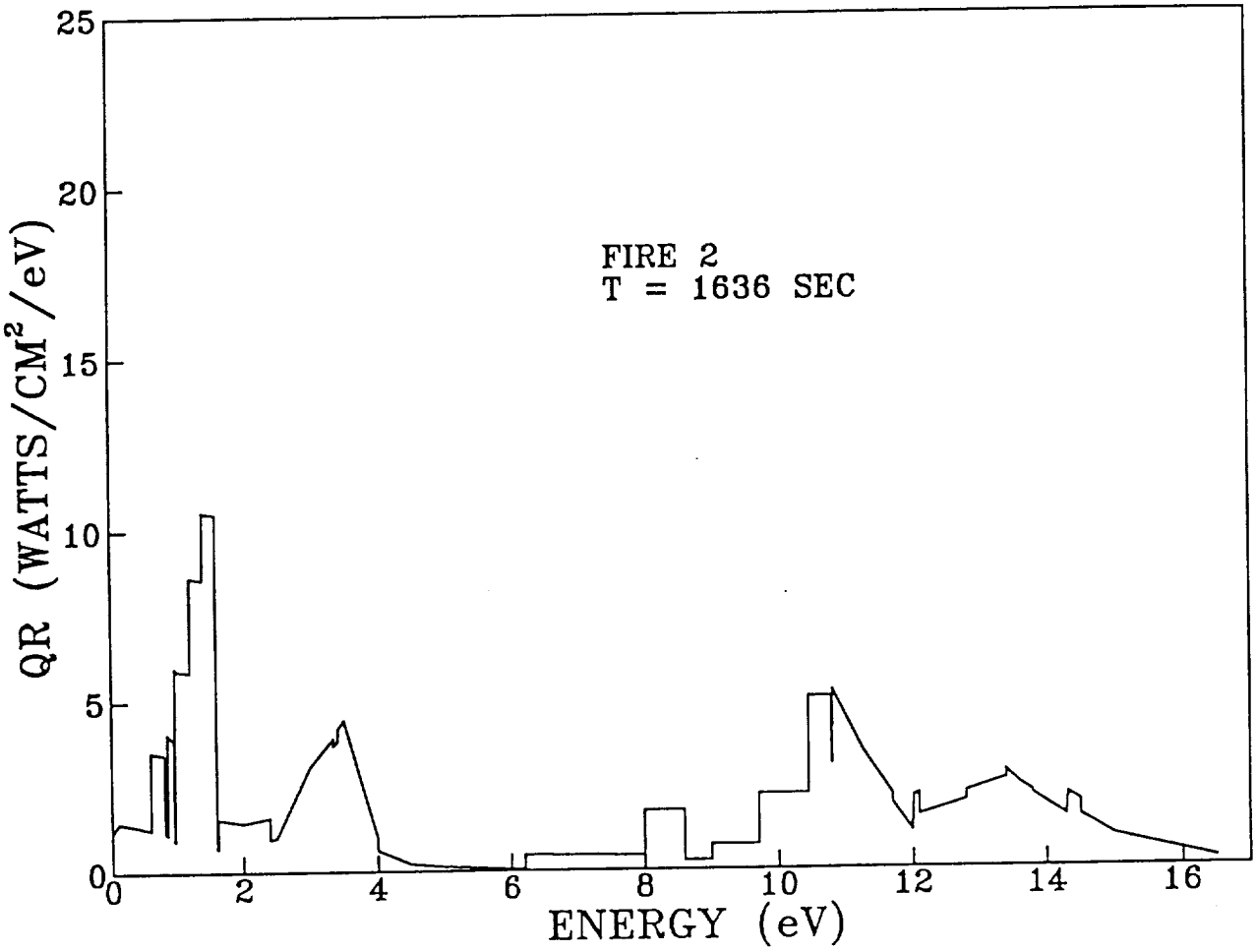

Fig. 10 -- Spectral Variation of Stagnation Point Radiative Heat Transfer for Fire 2 at 1636 Seconds

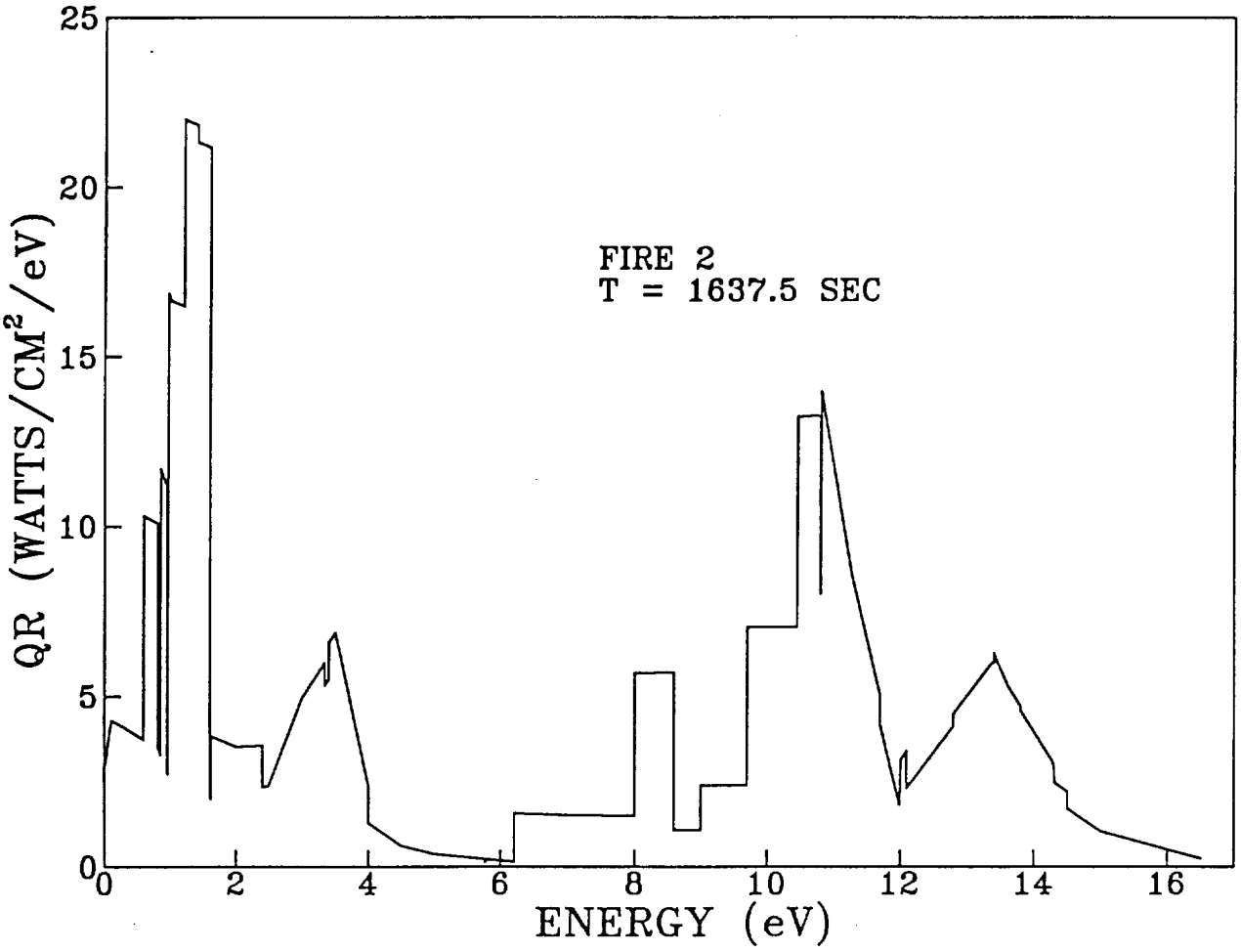

Fig. 11 -- Spectral Variation of Stagnation Point Radiative Heat Transfer for Fire 2 at 1637.5 Seconds

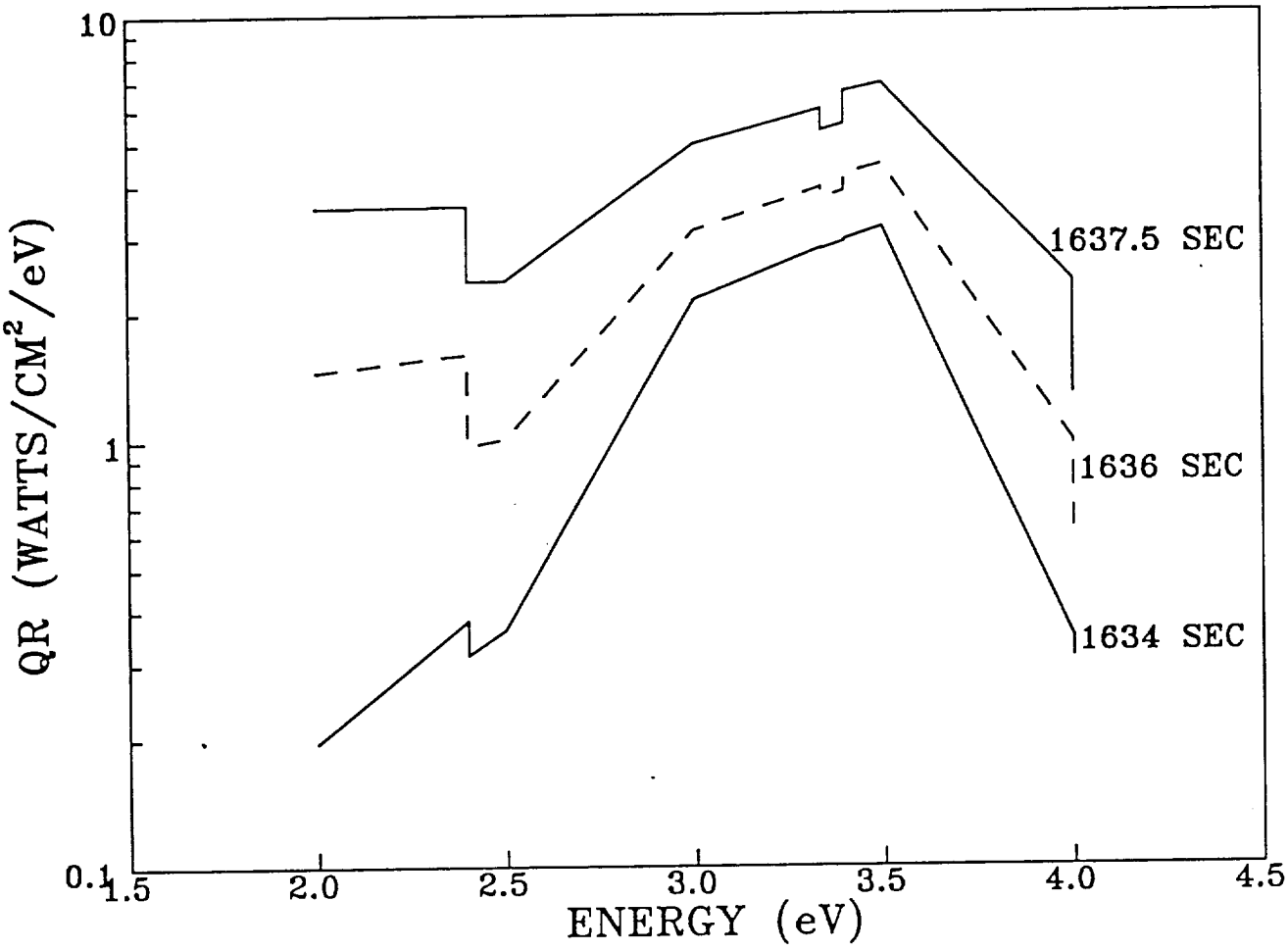

Fig. 12 -- Spectral Variation of Stagnation Point Radiative Heating Between 2 and 4 eV at Various Times

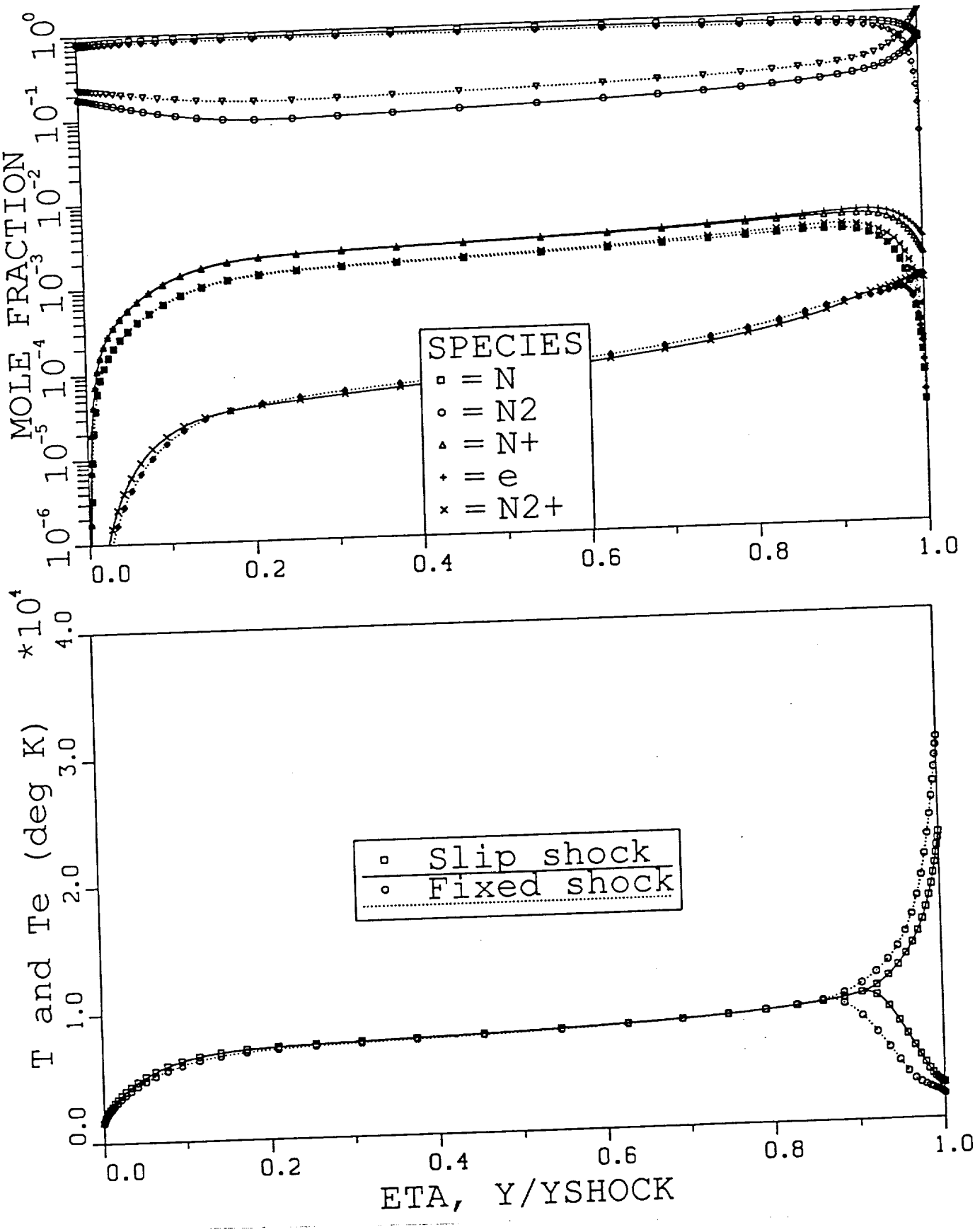

Fig. 13(a) -- Stagnation Profiles for AFE CFD Point 2 Using QEE Model
U = 8.915 km/sec, H = 77.9 km, Rnose = 2.3 m
QR = 1.56 watts/sq cm, QC = 13.6 watts/sq cm, δ = 12.2 cm

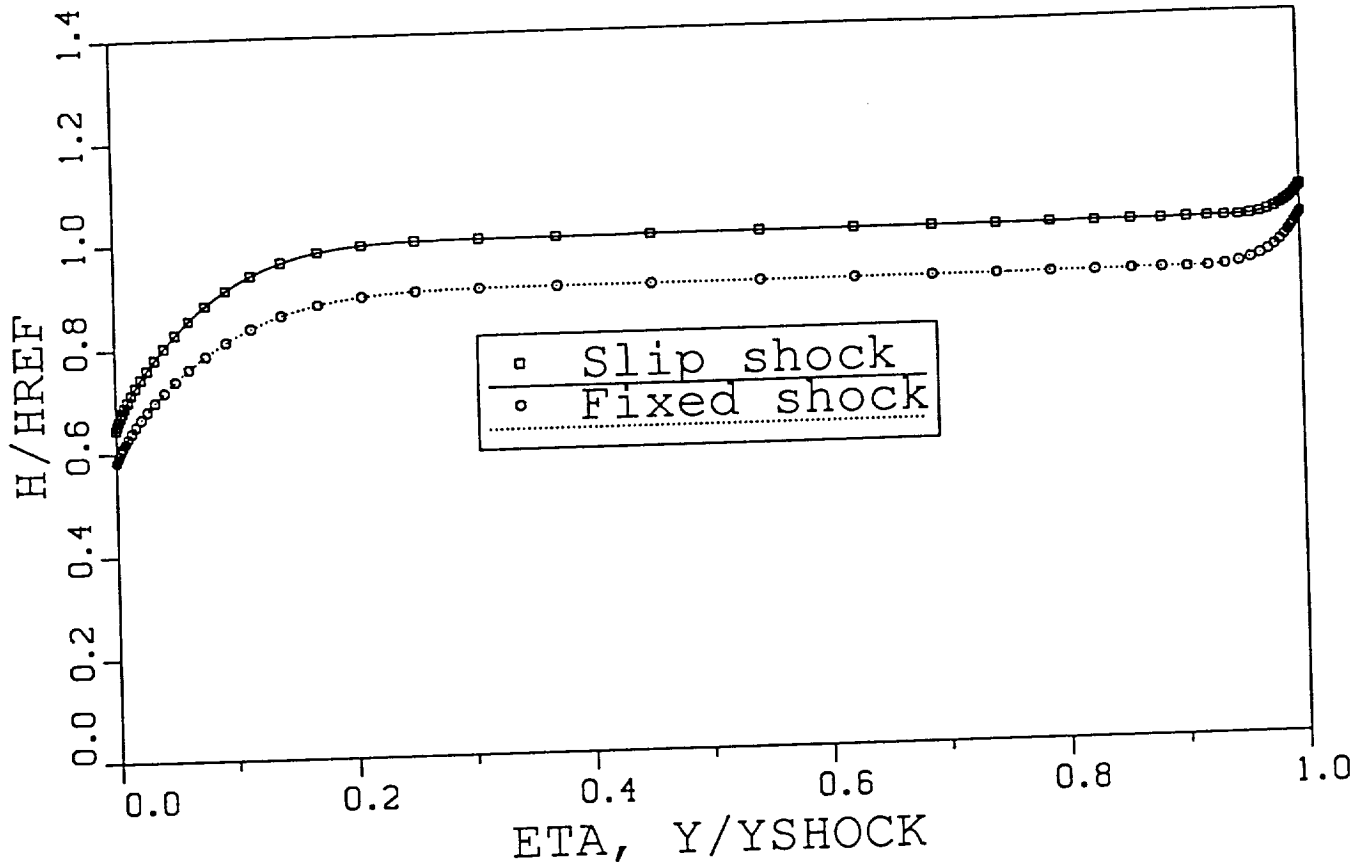

Fig. 13(b) -- Stagnation Profiles for AFE CFD Point 2 Using QEE Model
U = 8.915 km/sec, H = 77.9 km, Rnose = 2.3 m
QR = 1.56 watts/sq cm, QC = 13.6 watts/sq cm, δ = 12.2 cm

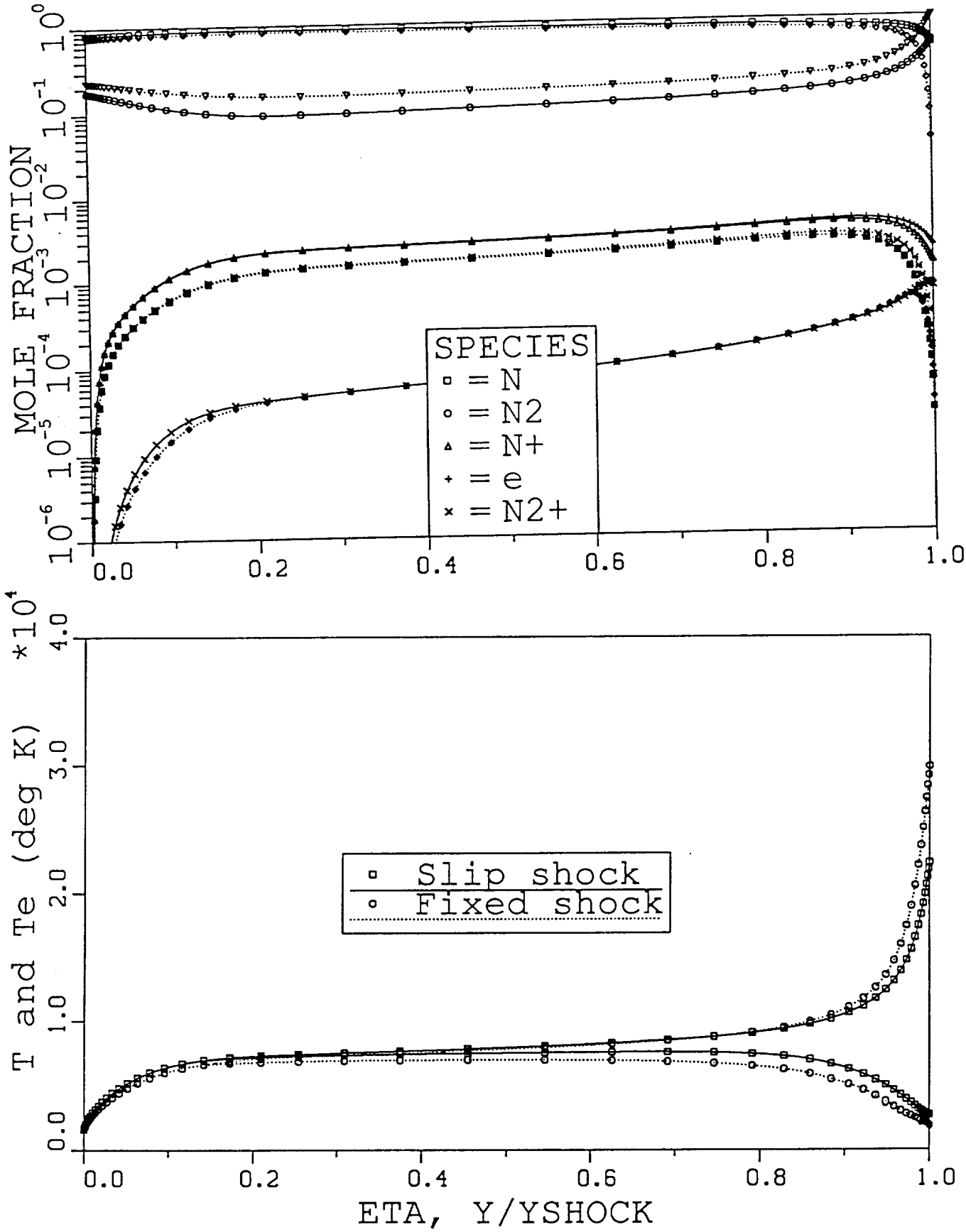

Fig. 14 -- Stagnation Profiles for AFE CFD Point 2 Using QEEE Model
U = 8.915 km/sec, H = 77.9 km, Rnose = 2.3 m
QR = 0.61 watts/sq cm, QC = 13.6 watts/sq cm, δ = 12.5 cm

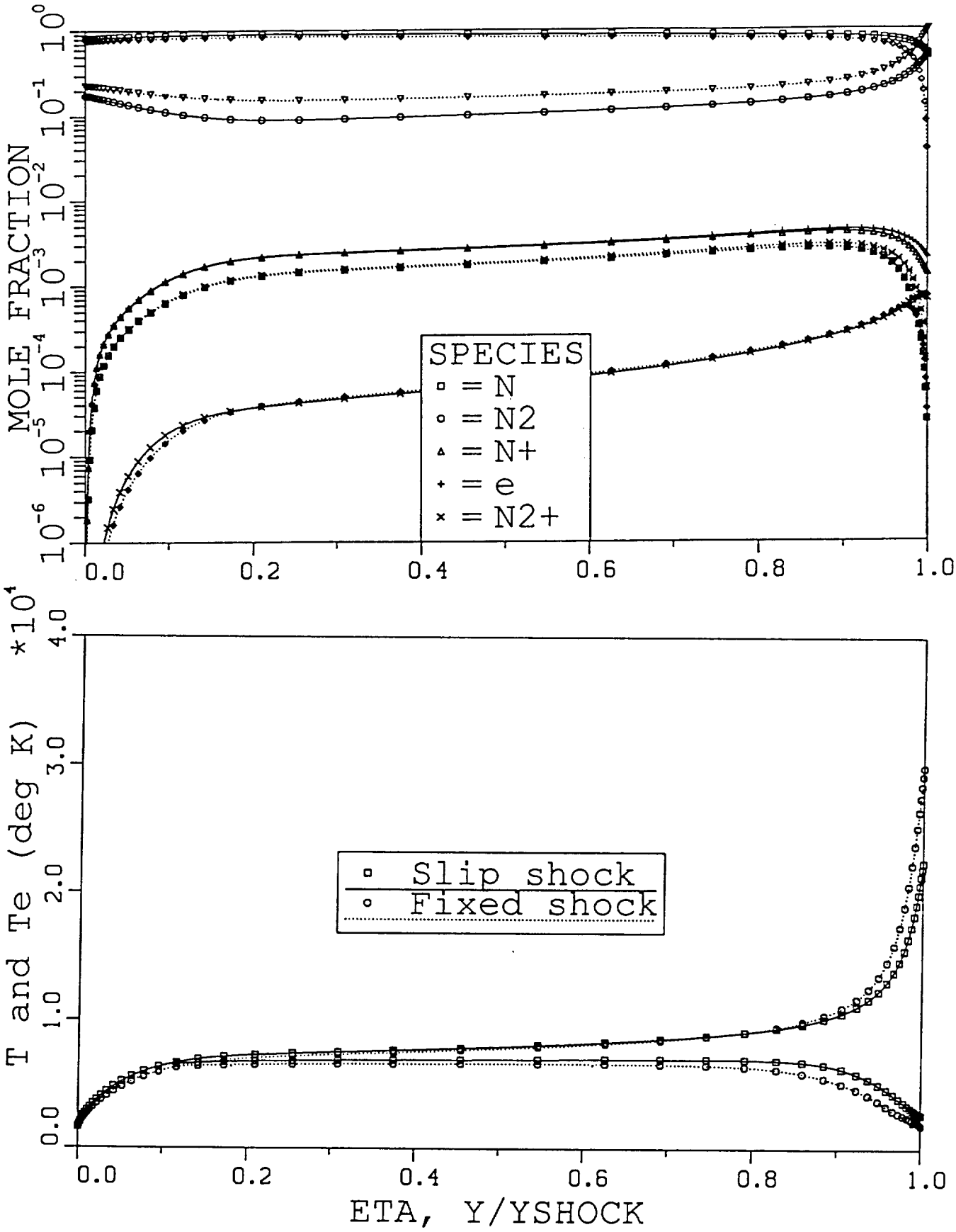

Fig. 15 -- Stagnation Profiles for AFE CFD Point 2 Using QEEE Model with Electron Impact Dissociation Included
U = 8.915 km/sec, H = 77.9 km, Rnose = 2.3 m
QR = 0.43 watts/sq cm, QC = 13.6 watts/sq cm, δ = 12.5 cm

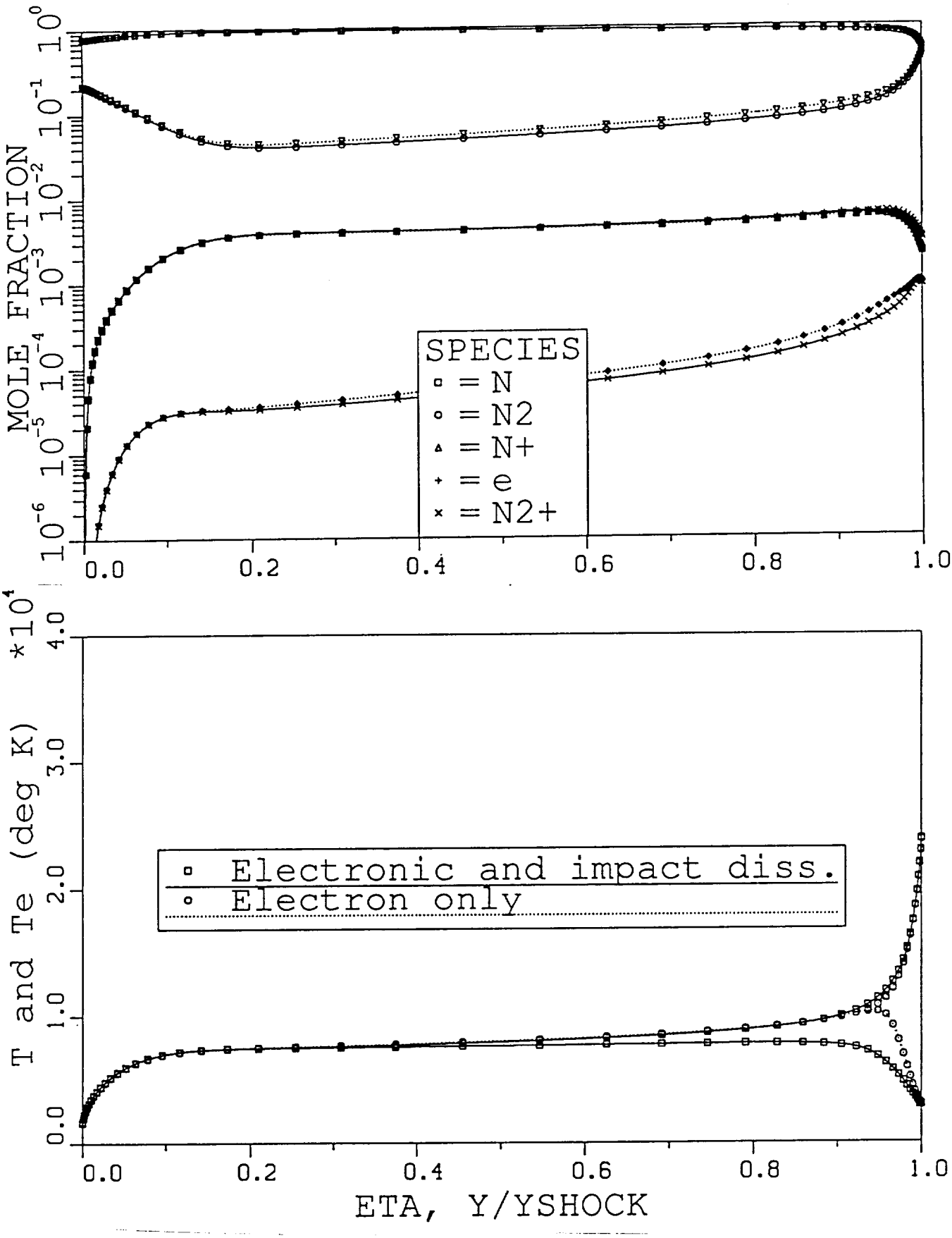

Fig. 16 -- Stagnation Profiles for AFE CFD Point 4
U = 9.326 km/sec, H = 75.2 km, Rnose = 2.3 m
For QEEE case: QR = 1.18 watts/sq cm, QC = 25.8 watts/sq cm, δ = 11.96 cm
For QEE case: QR = 2.91 watts/sq cm, QC = 25.7 watts. sq cm, δ = 11.89 cm

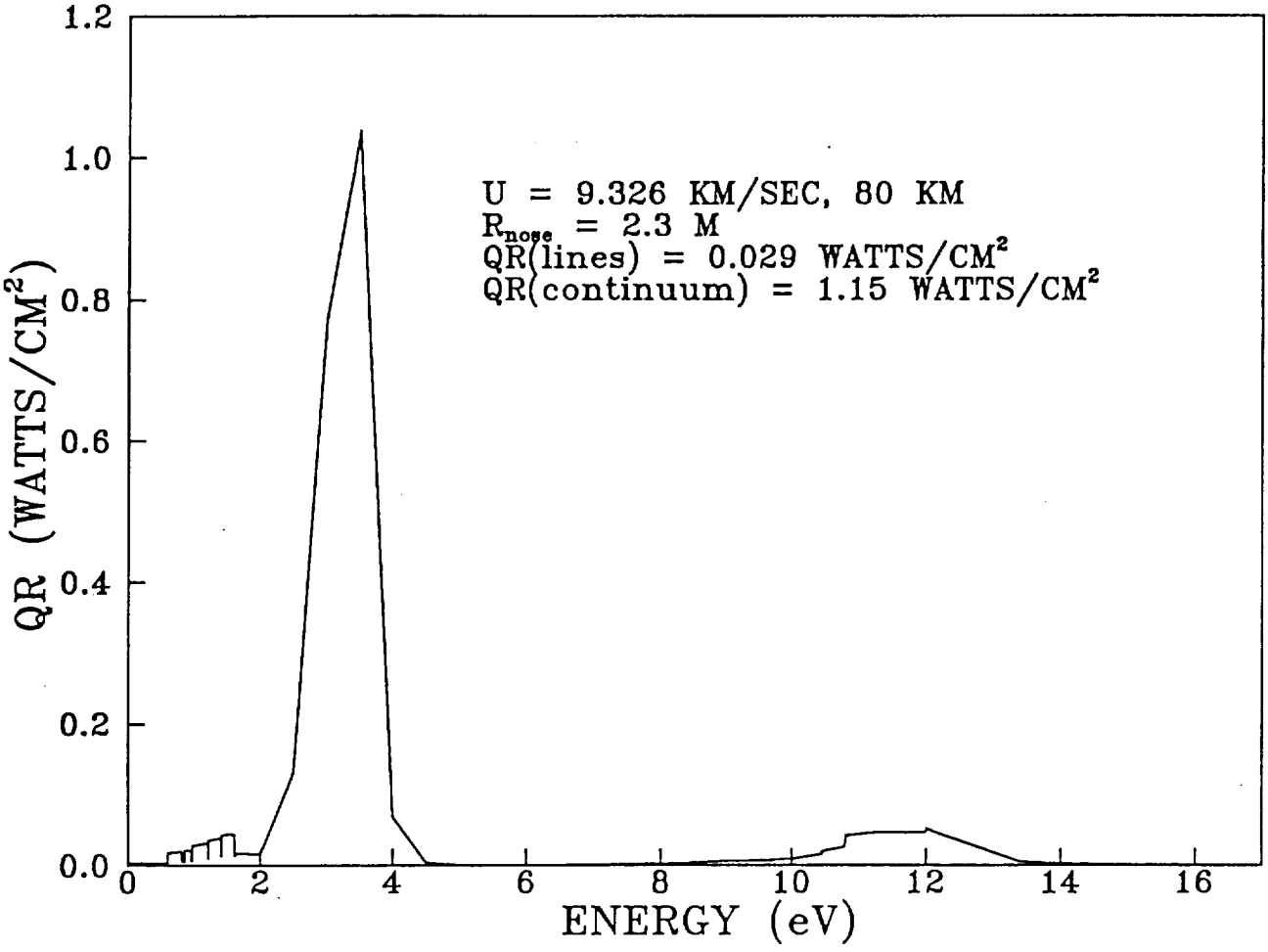

Fig. 17(a) -- Usual Presentation of Spectral Variation of Stagnation Point Heat Transfer
AFE CFD Point 4, QEEE Model

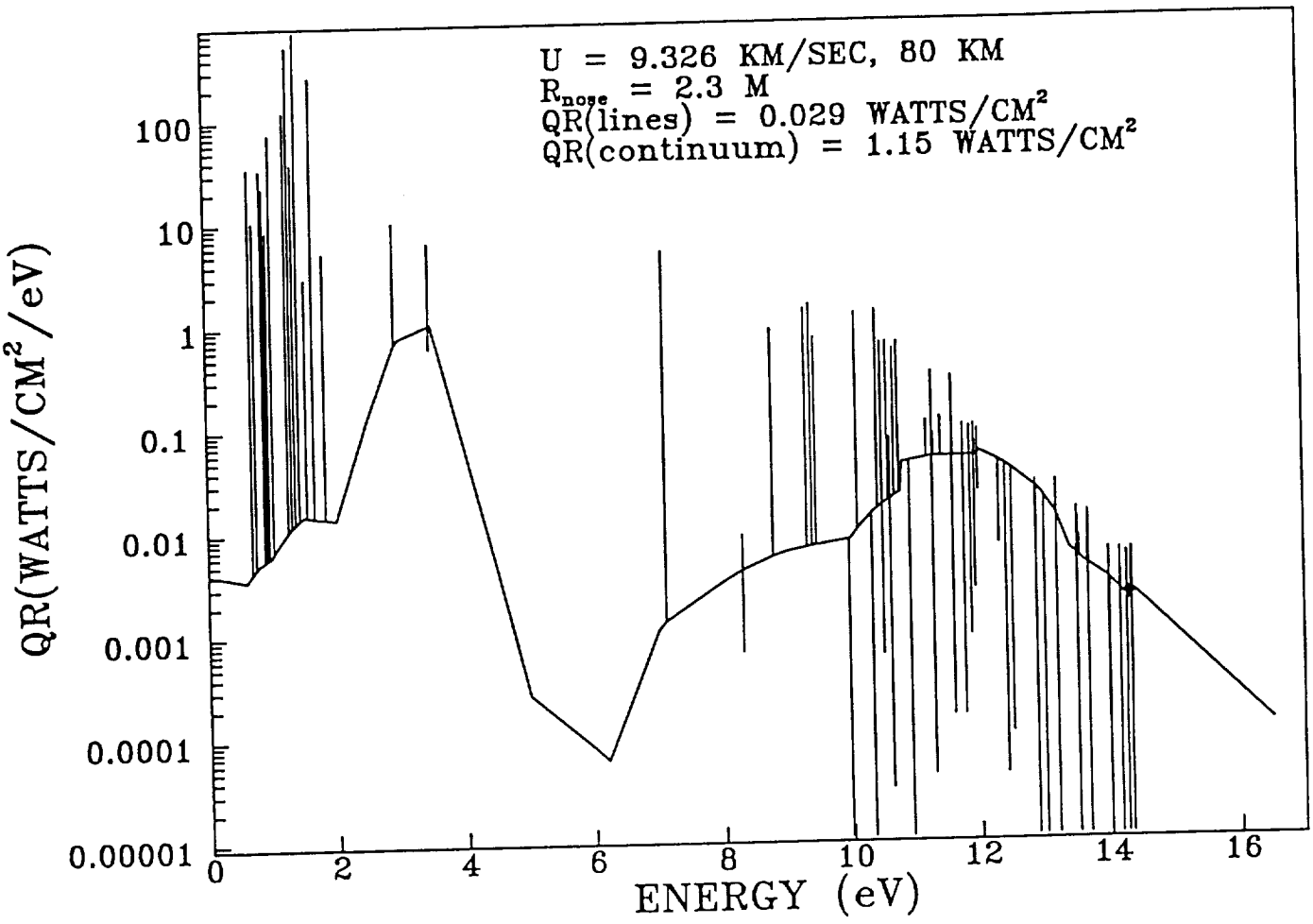

Fig. 17(b) -- Detailed Spectral Variation of Stagnation Point Heat Transfer
AFE CFD Point 4, QEEE Model

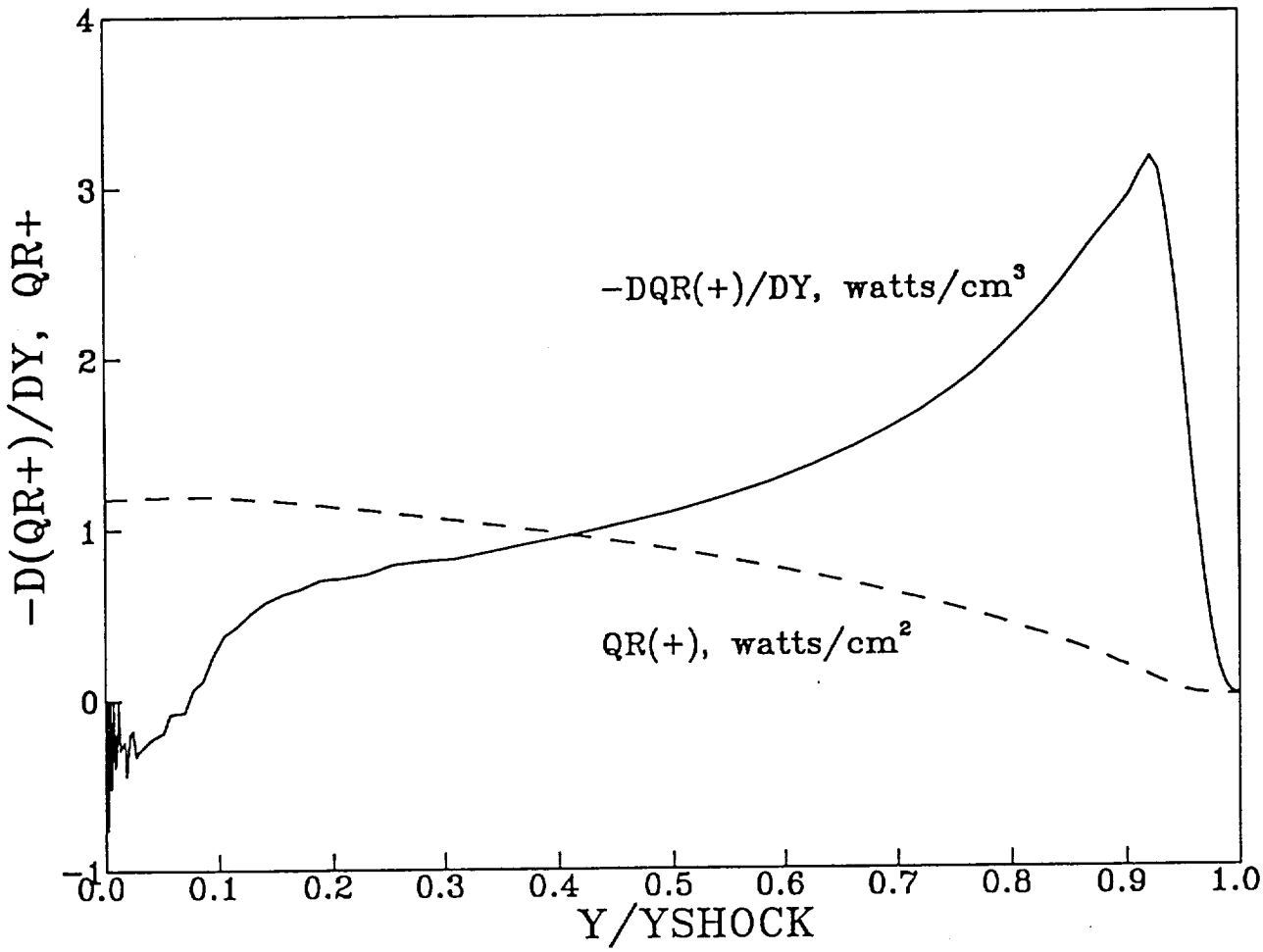

Fig. 18 -- "Intensity" and Radiative Flux Towards Stagnation Point
AFE CFD Point 4, QEEE Model

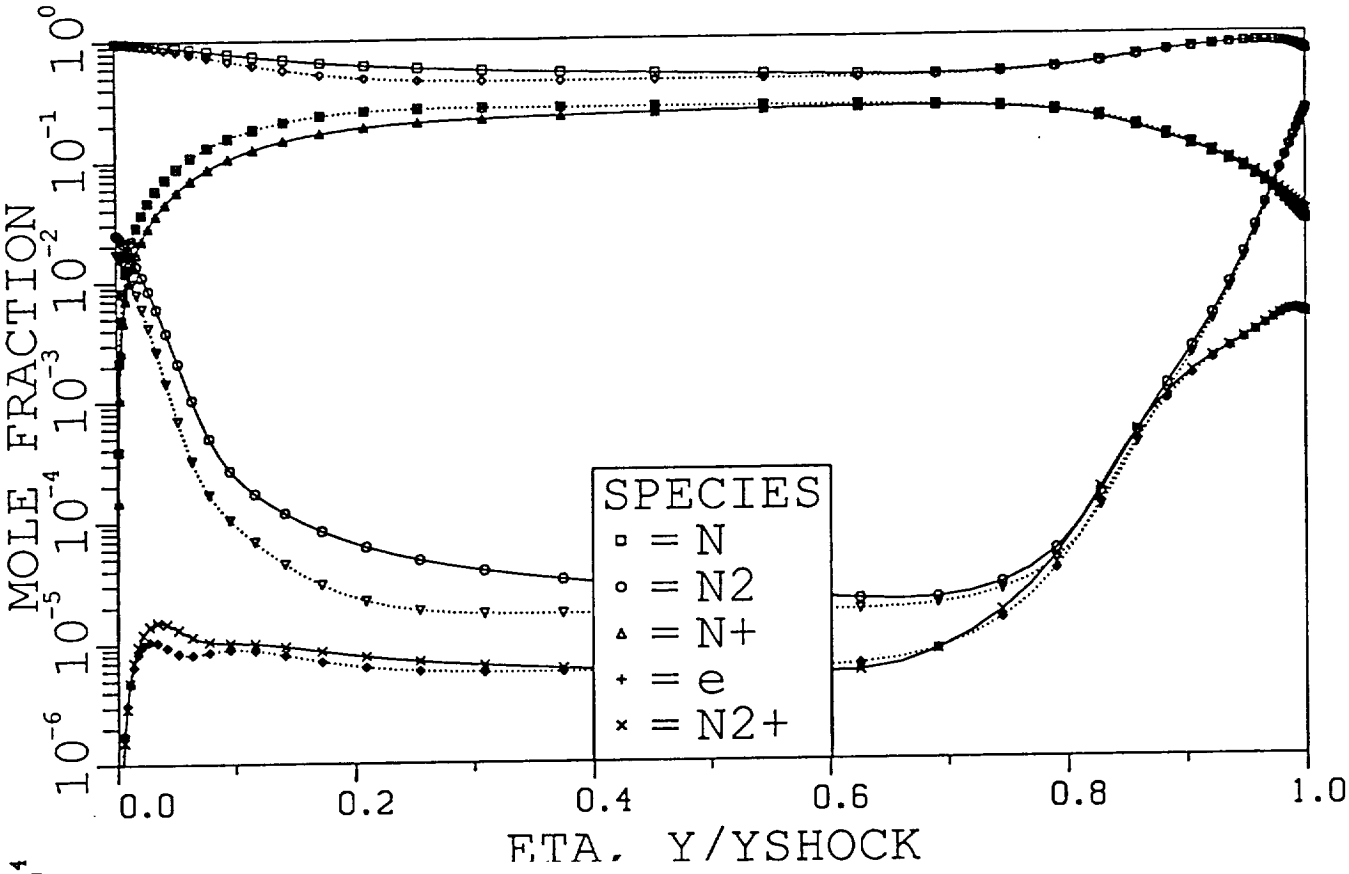

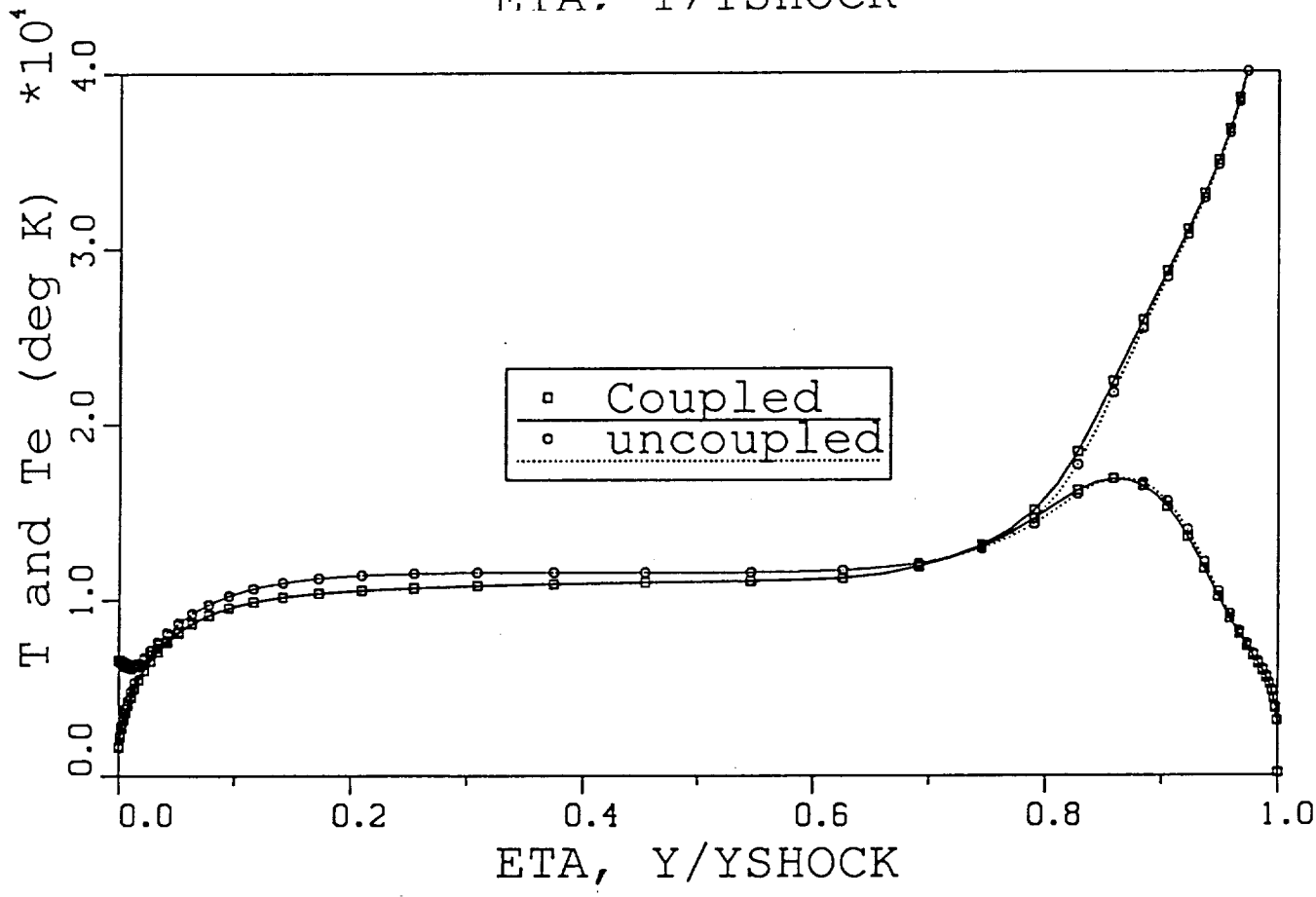

Fig. 19 -- Stagnation Profiles at 14 km/sec, 80 km, Rnose = 2.3 m
Full Electron-Electronic Equation Model with
Radiative Cooling and LTNE Effects
QR = 111.7 watts/sq cm, QC 56.8 watts/sq cm, δ = 9.03 cm

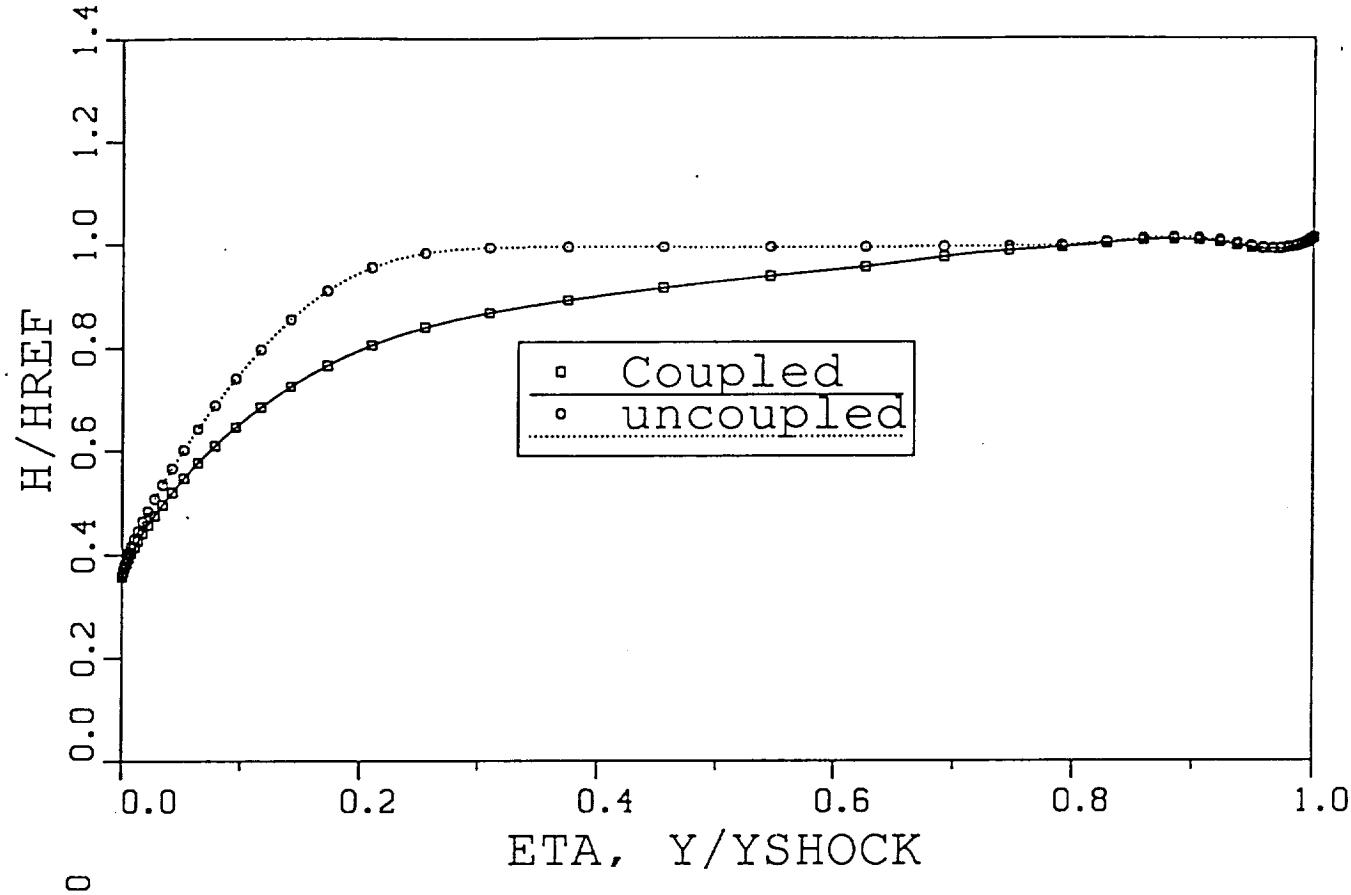

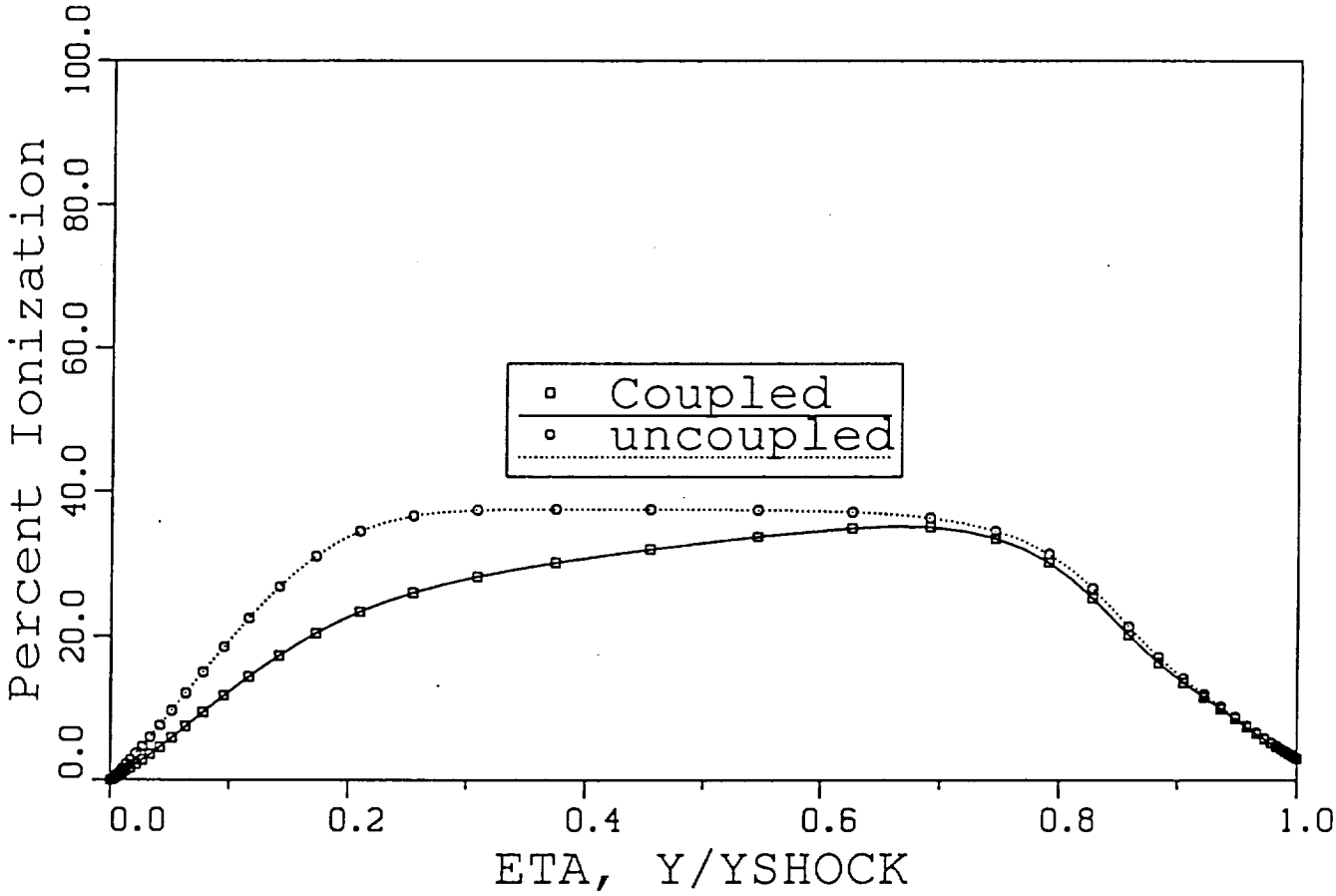

Fig. 20 -- Enthalpy and Ionization Profiles at 14 km/sec, 80 km, Rnose = 2.3 m
Full Electron-Electronic Equation Model with Radiative Cooling and LTNE Effects

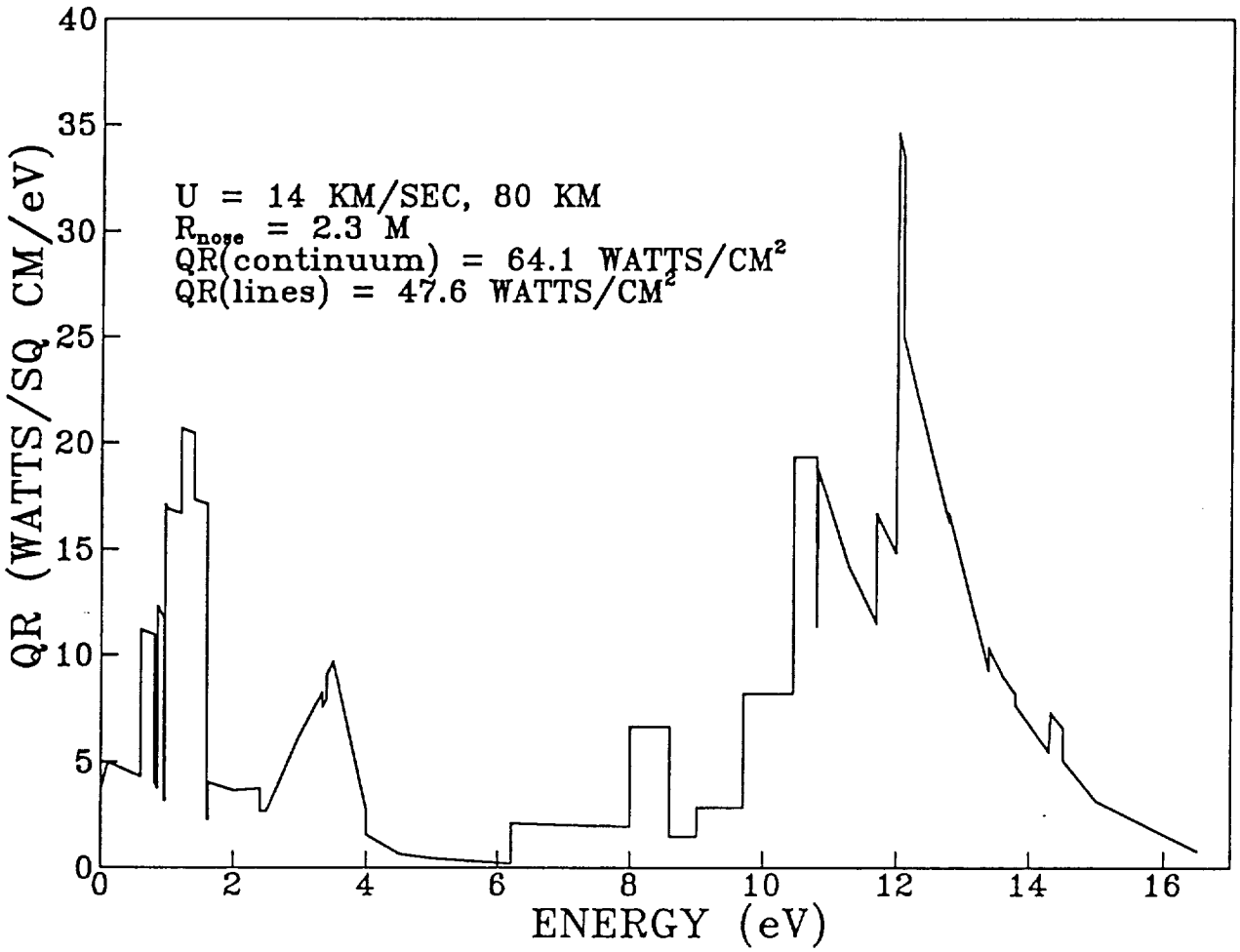

Fig. 21 -- Usual Presentation of Spectral Variation of Stagnation Point Heat Transfer, 14 km/sec, 80 km, Full Electronic Equation Model with Radiative Cooling and LTNE Effects

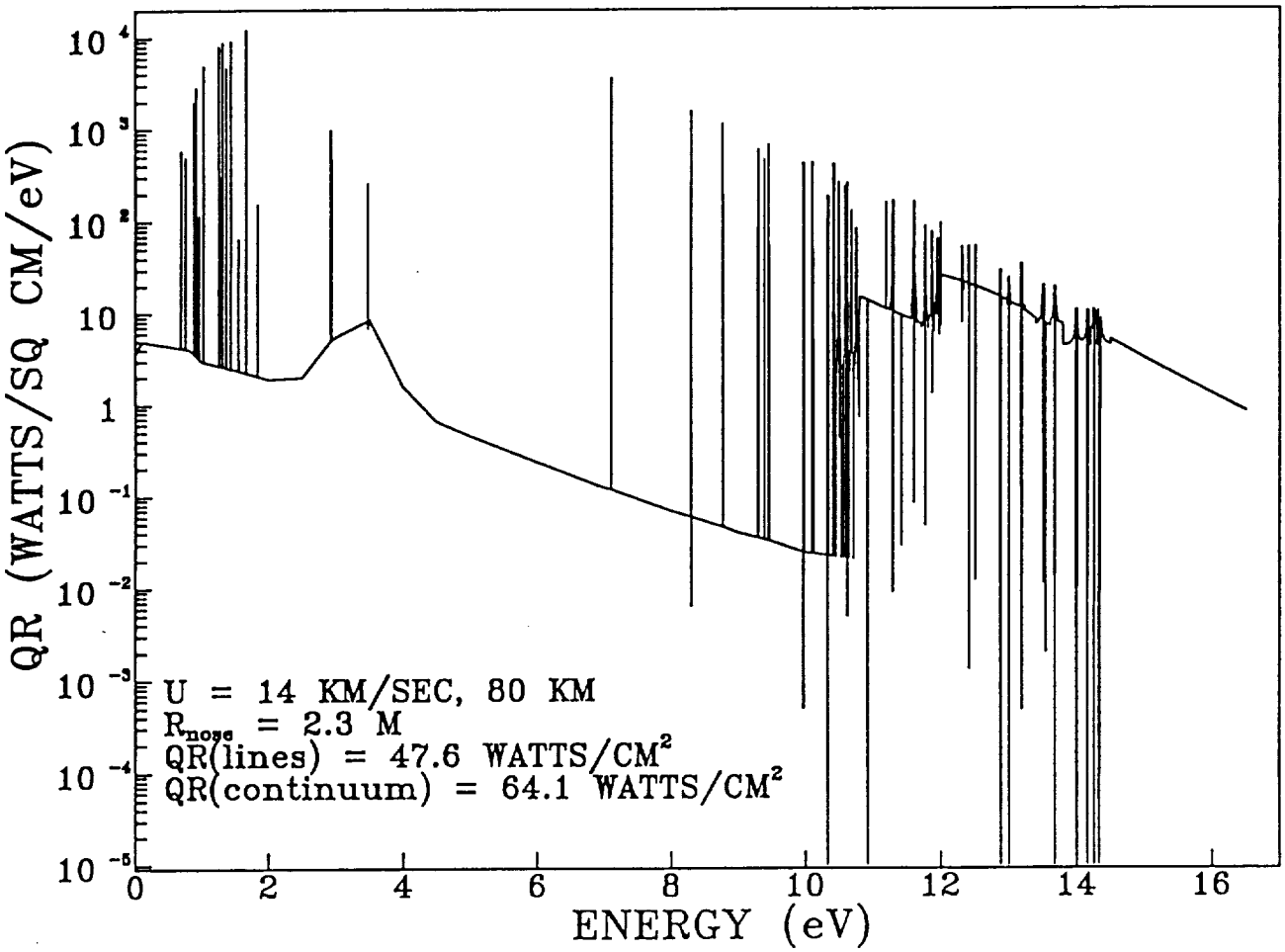

Fig. 22 -- Detailed Spectral Variation of Stagnation Point Heat Transfer
14 km/sec, 80 km, Full ELectronic Equation Model
with Radiative Cooling and LTNE Effects

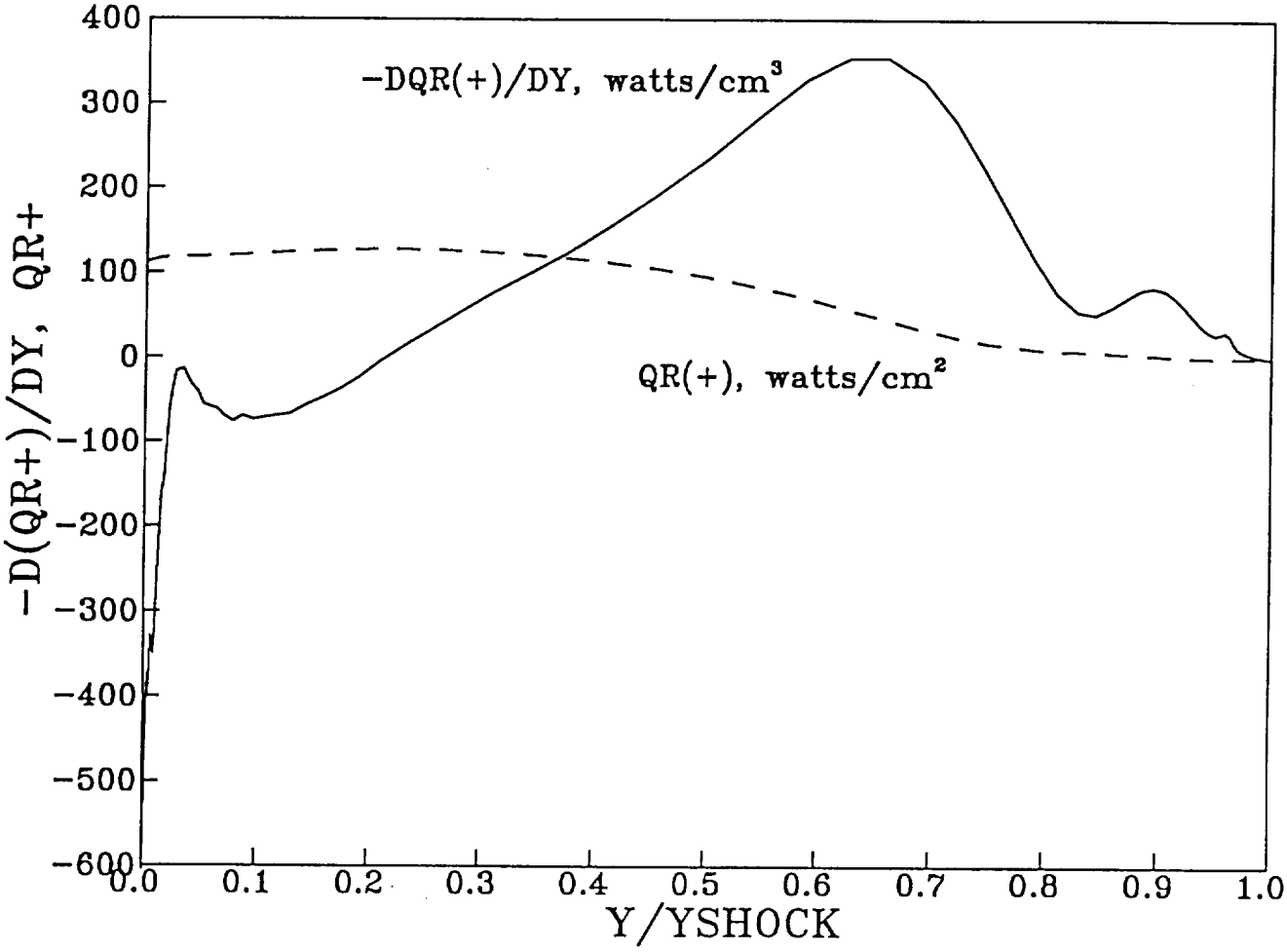

Fig. 23 -- "Intensity" and Radiative Flux Towards Stagnation Point
14 km/sec, 80 km

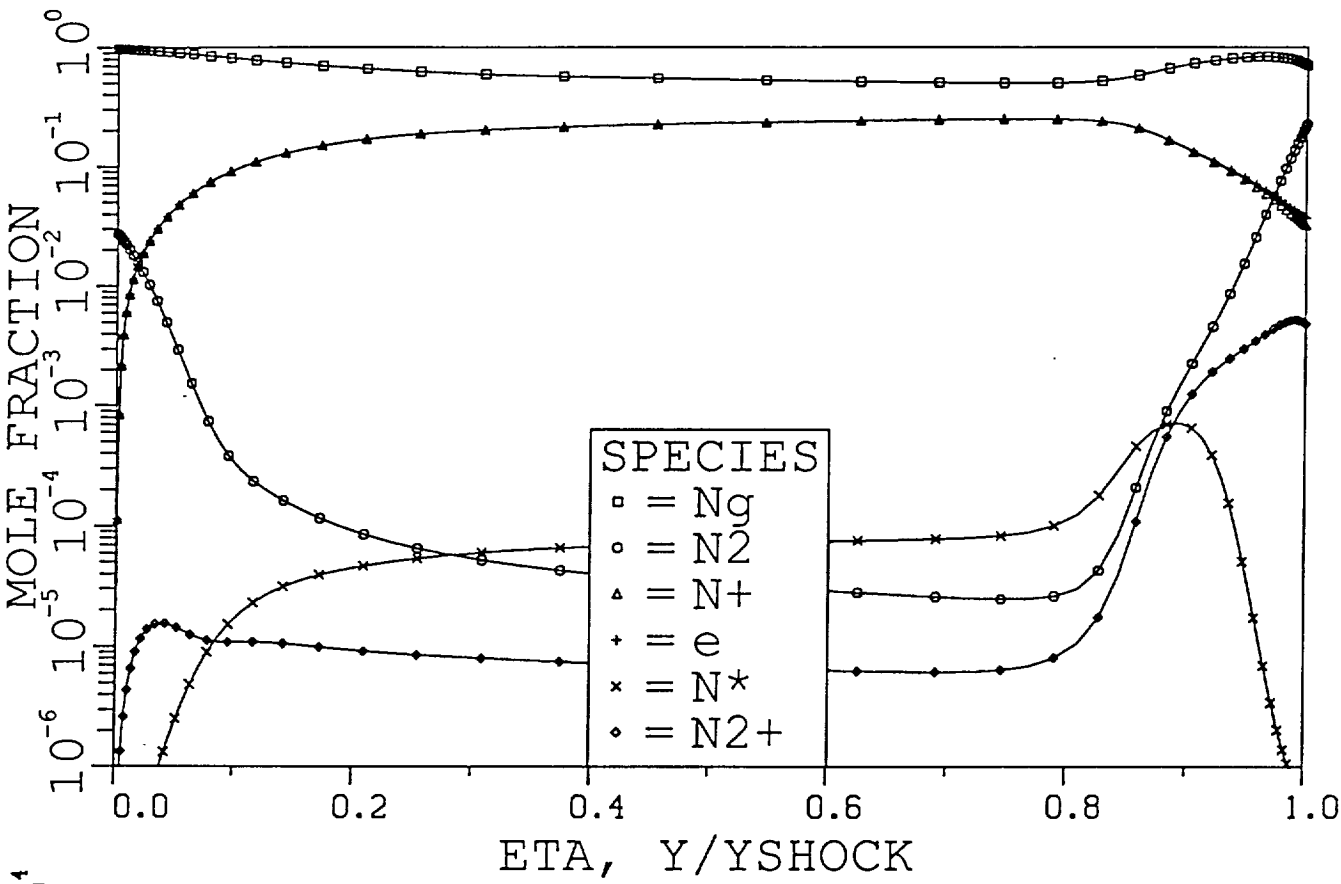

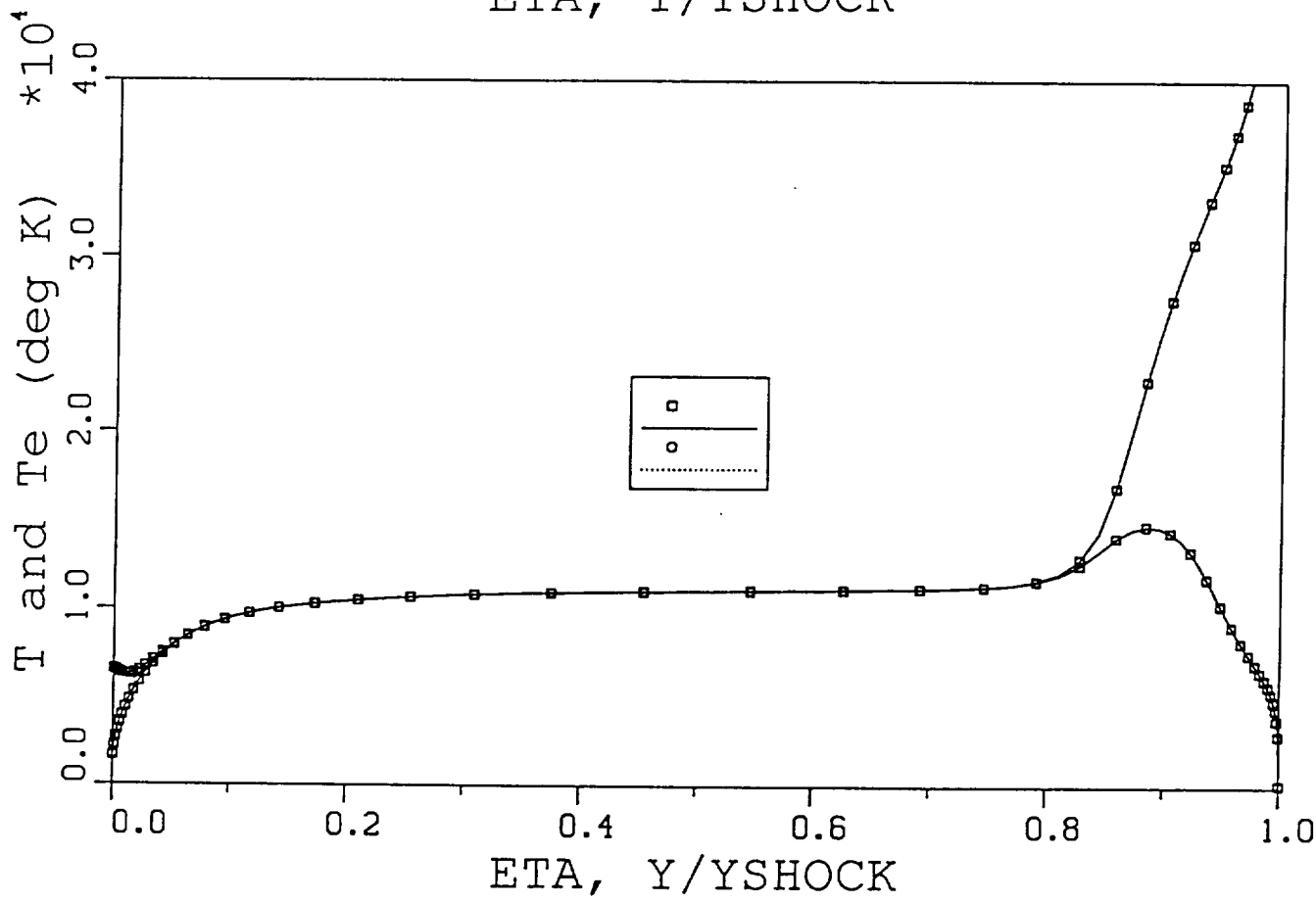

Fig. 24 -- Stagnation Profiles at 14 km/sec, 80 km, Rnose = 2.3 m
Second Order Nonequilibrium Atomic Radiation Model
QR = 105.6 watts/sq cm, QC = 60.3 watts.sq. cm, ζ = 8.82 cm

ACKNOWLEDGEMENT

The research discussed in this abstract is primarily supported by NASA Grant No. NAG 1-1003, with Lin Hartung, Aerothermodynamics Branch, NASA Langley, as technical monitor. In addition, Mr. Gally is partially supported by NASA Graduate Student Researchers Fellowship thru the NASA Johnson Space Center, with Dr. Carl Scott, Aerosciences Branch, as technical monitor.

APPENDIX IV

Abstract of Paper Submitted to

AIAA 22nd Fluid Dynamics, Plasma Dynamics and Lasers Conference

June 1991

"The Effects of Shock Wave Precursors Ahead of Hypersonic Entry Vehicles"

Scott A. Stanley
Leland A. Carlson

Abstract Submittal Form

Print or type all information

I wish to submit an abstract for (conference/meeting) 22nd Fluid Dynamics, Plasma Dynamics and Lasers

Location: Honolulu, Hawaii **Date:** June 24-26, 1991

Session/organizer (this information appears in the call):

Reminders:

1/ AIAA has first publication rights to all papers presented at its meetings.

2/ Authors must inform each organizer if abstract is submitted to more than one session topic organizer.

3/ All nonmember program participants and authors will be charged the nonmember registration fee for the meeting; any *member* program participants and authors are eligible for the member fee.

4/ Authors of accepted papers will be expected to submit a photo-ready manuscript. Deadline dates will be included in author kit packages. Authors desiring journal publication should send five (5) copies of their photo-ready manuscript directly to the Editor in Chief of the journal of their choice (see inside front cover of each journal for correct address), along with a covering letter, before the meeting, if they wish to accelerate the review procedure. Government Program Monitors/Security Officers should be alerted as soon as authors receive formal acceptance of their paper.

5/ It is the responsibility of authors to obtain proper approval if necessary. Please keep in mind that clearances may consume six (6) weeks or more.

6/ Co-authors are grouped by affiliations and do not necessarily reflect amount of author contribution.

Paper title (this title will be published in the program):
The Effects of Shock Wave Precursors Ahead of Hypersonic Entry Vehicles

Author/s' name and title, AIAA membership grade, company, full mailing address, telephone number, FAX number:

1 Principle Author
Scott A. Stanley (Student Member)
Graduate Research Assistant, Aero. Engr.
Texas A&M University
401 H.R. Bright Bldg.
College Station, TX 77843
(409) 845-0708
Fax: (409) 845-6051

2
Leland A. Carlson
Professor, Aero. Engr. Dept.
Texas A&M University
College Station, TX 77843
(409) 845-1426
Fax: (409) 845-6051

3

4

Indicate (one) author to receive all correspondence: ☐ 1 ☒ 2 ☐ 3 ☐ 4

Abstract due date: October 17, 1990

Draft of paper included? ☐ Yes ☒ No

Similar results previously presented or published elsewhere? ☐ Yes ☒ No

Concise statement of problem (its genesis and objective): To determine the nonequilibrium as properties in the radiation absorption dominated precursor region head of an earth entry vehicle, as well as the resulting effects n the shock layer and radiative flux to the body. The specific low conditions considered are for an aerocapture vehicle entering he earth's atmosphere upon return from Mars.

Scope and methods of approach, with statement of contribution to the state-of-the-art or an application of existing analytical techniques and theories to a problem.

computational method has been developed to calculate the thermal nd chemical nonequilibrium gas properties on the stagnation streamline n the precursor region. Expressions have been developed for the ass production rates due to chemical reactions and the effects of adiation absorption on each individual energy mode of the gas.

Summary of important conclusions:

ee enclosed abstract.

Statement of data used to substantiate conclusions, and freehand sketches of major figures to be used (no more than two typed pages):

ee enclosed abstract.

The Effects of Shock Wave Precursors Ahead of Hypersonic Entry Vehicles

An Extended Abstract

Scott A. Stanley* and Leland A. Carlson**
Texas A&M University
College Station, Texas

SUMMARY

In order to determine the effects of the shock wave precursor on the flow field around an aerocapture vehicle entering the earth's atmosphere, a computational method has been developed to calculate the gas properties in the precursor region. A viscous shock layer program was used to predict the gas properties in the shock layer, and a spectrally detailed radiation model has been used to predict the emission and absorption of radiation. Expressions have been developed for the mass production rates due to photoprocesses and the effects of absorption and emission on the individual energy modes of the gas. The flow field properties in the precursor are shown and discussed for a representative case. The changes in the shock layer properties and the radiative flux to the body, resulting from including the precursor effects, are also discussed.

INTRODUCTION

With the recent emphasis placed on the future exploration of the planet Mars and the subsequent return of men and samples to earth, there has been increased interest in the development of accurate prediction methods for the fluid flow around hypersonic entry vehicles. This renewed interest is a result of the plan to use an aerocapture technique to provide the

* Graduate Research Assistant, Aerospace Engineering Department
** Professor, Aerospace Engineering Department

velocity reduction necessary to place the spacecraft in earth orbit. The benefit of this approach is that aerodynamic drag, resulting from the interaction of the spacecraft with the high altitude atmosphere, can be used instead of propulsive braking to slow the vehicle to orbital speeds. This technique permits a reduction in the fuel necessary for the mission and increases the return payload capability.

A portion of hypersonic flow fields which has received little attention in recent years is the shock wave precursor, the radiation dominated region of cold gas ahead of the shock. Recent work in hypersonic flow field predictions has concentrated on the shock layer, the region between the shock wave and the body. In the precursor, radiation emitted by the gas in the shock layer is reabsorbed; this absorption of radiation causes a heating as well as excitation, ionization and dissociation of the gas ahead of the shock. These changes in the conditions ahead of the shock in turn might effect the gas behind the shock. The preheating of the gas in the precursor, as well as the introduction of electrons and ions could potentially increase the rate at which the gas behind the shock approaches equilibrium. For certain cases, it has been predicted that the precursor causes significant increases in the radiative heating to the body.[1,2] The primary objective of this research was to properly model and ascertain the effects of the precursor ahead of an entry type vehicle in the earth's atmosphere.

METHOD

Precursor Formulation

For this engineering model, it was decided that treating the earth's atmosphere as a nitrogen gas was an acceptable approximation. Due to the predominance of nitrogen in the

atmosphere, as well as the low levels of radiation present in the strong absorption region for the oxygen dissociation continuum it is believed that a nitrogen gas will sufficiently model the absorption of cool air.

In order to determine the effects of the precursor on the gas in the shock layer and the radiative heat transfer to the body, a computational method and program was developed to solve the one-dimensional Euler equations for the gas composition, temperature, pressure, density and velocity on the stagnation streamline in the precursor, including the effects of thermal and chemical nonequilibrium. The basic governing equations for the inviscid flow in the precursor region are:

Continuity,

$$\frac{\partial}{\partial x}(\rho v) = 0 \tag{1}$$

Momentum,

$$\rho v \frac{\partial v}{\partial x} + \frac{\partial p}{\partial x} = 0 \tag{2}$$

Energy,

$$\rho v \frac{\partial H}{\partial x} + \frac{\partial q}{\partial x} = 0 \tag{3}$$

where, H, is the total enthalpy of the gas given by:

$$H = h + \frac{1}{2}v^2 \tag{4}$$

and,

$$h = \frac{P}{\rho} + \sum_{n=1}^{n_s} (e_{tr_n} + e_{rot_n} + e_{vib_n} + e_{elct_n} + e_n^o) \tag{5}$$

In the energy equation above, q is the radiative flux; and the term $\partial q/\partial x$ is the change in the radiative flux due to the absorption of radiation and not that due to the geometry of the problem. This will be discussed in further detail later in the text.

In order to include the effects of chemical nonequilibrium, a continuity equation for each species is added to the above set of equations. The dominate chemical reactions in the precursor region are those due to the absorption of radiation; therefore, the effects of collisional reactions in the cool precursor are neglected in comparison to the effects of the radiative reactions. The photoreactions used in this model include the dissociation of molecular nitrogen and the ionization of both molecular and atomic nitrogen:

$$N_2 + h\nu \rightleftarrows^{k_{\nu 1}} 2\,N$$
$$N_2 + h\nu \rightleftarrows^{k_{\nu 2}} N_2^+ + e^-$$
$$N + h\nu \rightleftarrows^{k_{\nu 3}} N^+ + e^-$$

The species continuity equations are of the form:

$$\rho v \frac{\partial\left(\frac{\rho_n}{\rho}\right)}{\partial x} = -m_n \int_0^{\infty} \frac{Y^s_{\nu_n}}{h\nu} \frac{\partial q_\nu}{\partial x}\, \partial\nu \tag{6}$$

where the term on the right hand side is the mass production rate of the nth species due to radiative reactions. The variable, $Y^s_{\nu,n}$, in this term is a factor accounting for the proportion of

the total radiation absorbed at the frequency ν which is associated with the production of the nth species. These terms are given by:

$$Y^s_{\nu_{N_2}} = -\frac{k'_{\nu_1} + k'_{\nu_2}}{k'_{\nu_{tot}}} \qquad Y^s_{\nu_{N_2^+}} = \frac{k'_{\nu_2}}{k'_{\nu_{tot}}}$$

$$Y^s_{\nu_N} = \frac{2k'_{\nu_1} - k'_{\nu_3}}{k'_{\nu_{tot}}} \qquad Y^s_{\nu_{N^+}} = \frac{k'_{\nu_3}}{k'_{\nu_{tot}}} \tag{7}$$

$$Y^s_{\nu_{e^-}} = \frac{k'_{\nu_3} + k'_{\nu_2}}{k'_{\nu_{tot}}}$$

where the absorption coefficients, $k'_{\nu,1}$, $k'_{\nu,2}$ and $k'_{\nu,3}$ are those associated with the three radiative reactions above. $k'_{\nu,tot}$ is the total absorption coefficient for all absorption and emission processes.

The effects of thermal nonequilibrium are included through the use of an electron/electronic energy equation:

$$\frac{\partial}{\partial x}(\rho v e''_e) = -p_e \frac{\partial v}{\partial x} + \sum_{n=1}^{n_s} \xi_{e,n} + \dot{w}_e \frac{v^2}{2} - \frac{\partial q}{\partial x}$$

$$+ \sum_{i=1}^{n_{diss}} \int_0^\infty \frac{Y^p_{\nu_i}(h\nu - \Delta E_{elct_i} - D_i)}{h\nu} \frac{\partial q_\nu}{\partial x} d\nu \tag{8}$$

$$+ \sum_{i=1}^{n_{mb}} \int_0^\infty \frac{Y^p_{\nu_i}(h\nu - E^{upp}_{elct_i} + E^{low}_{elct_i})}{h\nu} \frac{\partial q_\nu}{\partial x} d\nu$$

where,

$$e''_e = \frac{\rho_{e^-}}{\rho} e_{e^-} + \sum_{n=1}^{n_s} (e_{elct_n} + e^o_n) \tag{9}$$

The last three terms in equation (8) account for the effects of absorption and emission on the free

electron kinetic energy, the electronic energy and the zero point energy.

In this model, the excited electronic states are assumed to be in thermal equilibrium with the free electrons. This is a good engineering approximation for the shock layer and is frequently used in this region. However, as discussed by Nelson and Goulard[3], in the precursor region the temperature governing the electronic states is expected to be greater than the heavy particle temperature but less than the electron temperature. Ideally, a three temperature model should be used allowing a separate electronic temperature; however, the mechanisms and expressions for the transfer of energy between the electronic states and free electrons are not well known or understood. In order to correct for the local thermodynamic nonequilibrium between the free electrons and the electronic states, a collision limiting correction[4] is applied to the populations of the molecular electronic states.

The equation of state for a two temperature gas is necessary in addition to the above equations to calculate a complete solution. This equation is:

$$p = \rho \hat{R} T \sum_{n=1}^{n_s} \left(\frac{\rho_n}{\rho} \frac{1}{M_n} \right) + \rho \frac{\hat{R}}{M_{e^-}} \frac{\rho_{e^-}}{\rho} (T_e - T) \qquad (10)$$

where the last term allows for thermal nonequilibrium between the electrons and the heavy particles.

Radiative Transfer Calculations

In computing the shock layer radiative phenomena, the usual engineering approach is to use the tangent slab approximation. Since the ratio of the shock layer thickness to the vehicle radius or diameter is small, this approach is appropriate. However, in the precursor region ahead of the shock front, important phenomena occur at significant distances from the vehicle;

at these points the radiating shock layer only comprises a small portion of the spherical field of view. In other words, as the point of interest in the precursor moves away from the shock front, the radiating shock layer and body do not appear to be infinite slabs and the actual solid angle over which the radiation should be spatially integrated must be properly computed.

By assuming that there is no emission in the precursor region, it can be shown that the appropriate expression for the radiative flux at a point in the precursor is:

$$q_{\nu} = 2\pi I_{\nu}^{w} E_3(\tau_{\nu}) \left[1 - Cos^2\beta \frac{E_3(\tau_{\nu} Sec\beta)}{E_3(\tau_{\nu})} \right] + 2\pi \int_0^{\tau_{\nu}^s} S_{\nu} E_2(\tau_{\nu} - \tau_{\nu}') d\tau_{\nu}' \left[1 - Cos^2\beta \frac{E_3((\tau_{\nu} - \tau_{\nu}^s) Sec\beta) - E_3(\tau_{\nu} Sec\beta)}{E_3(\tau_{\nu} - \tau_{\nu}^s) - E_3(\tau_{\nu})} \right] \tag{11}$$

where β is one-half of the angle subtended by the body as viewed from the point in the precursor. It should be noted that this equation is essentially the tangent slab expression except that each term has been modified by an attenuation factor which depends upon the vehicle size and the location of the point of interest. In this equation, the first term in brackets is the attenuation factor related to the wall radiation and the second term in brackets is the attenuation factor related to the shock layer radiation. Since it is anticipated that the radiation from the shock layer, rather than the "cool" wall, is absorbed in the precursor, the present engineering model utilizes the shock layer attenuation factor on all of the radiative terms. Using this attenuation factor, the radiative flux in the precursor can be expressed as:

$$q_{\nu} = AF_{\nu}\, q_{\nu}^{TS} \tag{12}$$

where AF_ν is the attenuation factor and q_ν^{TS} is the radiative flux at the point assuming tangent slab.

In the species continuity and energy equations, the terms involving the radiation appear as a divergence of the flux and are defined to account for the absorption and emission of radiation at a point. However, simple differentiation of equation (12) yields:

$$\frac{\partial q_\nu}{\partial x} = AF_\nu \frac{\partial q_\nu^{TS}}{\partial x} + q_\nu^{TS} \frac{\partial AF_\nu}{\partial x} \tag{13}$$

In this expression, the first term on the right hand side is the change in the radiative flux due to the emission and absorption of radiation, but the second term is the change due to the geometry of the problem and should not affect gas. If the second term were included in the species continuity and energy equations, an essentially transparent radiation would appear to be absorbed due to the spatial variation of the attenuation factor.

The NASA Langley program, RADICAL, is used to perform the tangent slab radiation calculations in this model and these results are corrected in the precursor region for the geometric attenuation of the radiation. RADICAL uses a spectrally detailed absorption coefficient model and includes the effects of atomic continuum, molecular continuum and atomic lines. The absorption coefficient model in RADICAL has been modified to include the effects of absorption in the Lyman-Birge-Hopfield molecular band of nitrogen as well as photoionization of molecular nitrogen. For the relatively cool nitrogen gas in the precursor region, photodissociation occurs primarily through absorption in the Lyman-Birge-Hopfield band and the subsequent predissociation out of the $a'\Pi_g$ excited state.

The radiative processes included in the calculation of the emission and absorption in the shock layer and precursor are given in Table 1. In the shock layer, the continuum processes for molecular and atomic nitrogen, as well as the lines associated with the nitrogen atom are included. In the precursor region, however, the absorption and emission of radiation through the atomic lines is neglected; however, absorption through the atomic lines is expected to have only a small influence on the precursor due to the low atomic concentrations in this region.

Shock Layer Calculations

For this model, the conditions of the gas in the shock layer are found using a viscous shock layer, VSL, program written by Thompson[5]. This program has been modified extensively by Carlson and Gally[6] and includes the effects of chemical nonequilibrium, thermal nonequilibrium, atomic local thermodynamic nonequilibrium and radiative gasdynamic coupling.

Table I: Radiative Processes Included in the Shock Layer and Precursor

	Radiative Process	Frequency Range (eV)
Shock Layer:		
	Free-Free, Bremsstrahlung	$0.0 \leq h\nu$
N	- Low Frequency Ionization (Highly excited states)	$0.0 \leq h\nu$
	- High Frequency Ionization (Ground and first two excited states)	$10.8 \leq h\nu$
	- Atomic Lines	--
N_2	- Birge-Hopfield Molecular Band	$6.50 \leq h\nu \leq 12.77$
	- 1st Positive Molecular Band	$0.75 \leq h\nu \leq 4.5$
	- 2nd Positive Molecular Band	$0.75 \leq h\nu \leq 4.5$
N_2^+	- 1st Negative Molecular Band	$2.23 \leq h\nu \leq 4.46$
Precursor:		
	Free-Free, Bremsstrahlung	$0.0 \leq h\nu$
N	- Low Frequency Ionization (Highly excited states)	$0.0 \leq h\nu$
	- High Frequency Ionization (Ground and first two excited states)	$10.8 \leq h\nu$
N_2	- Ionization Continuum	$8.24 \leq h\nu$
	- Birge-Hopfield Molecular Band	$6.5 \leq h\nu \leq 12.77$
	- 1st Positive Molecular Band	$0.75 \leq h\nu \leq 4.5$
	- 2nd Positive Molecular Band	$0.75 \leq h\nu \leq 4.5$
	- Lyman-Birge-Hopfield Molecular Band	$4.77 \leq h\nu \leq 9.78$
	- Dissociation Continuum (Adjoining Lyman-Birge-Hopfield molecular band)	$9.78 \leq h\nu$
N_2^+	- 1st Negative Molecular Band	$2.23 \leq h\nu \leq 4.46$

TYPICAL RESULTS

The results enclosed herein are for the stagnation streamline of a 2.3 m nose radius vehicle at a velocity of 16 Km/sec and an altitude of 80 Km. These conditions are within the possible range associated with an aerocapture vehicle returning from Mars. The freestream conditions associated with this altitude are:

$$T_\infty = 180.65\ K$$
$$P_\infty = 10.72\ dyn/cm^2$$
$$\rho_\infty = 1.99x10^{-8}\ g/cm^3$$

Figures 1 to 6 show the heavy particle temperature, electron/electronic temperature, pressure, total enthalpy, density and velocity in the precursor for this case; figures 7 to 11 show the variations of the mass fractions through the precursor for the five species, N_2, N_2^+, N, N^+ and e^-. The radiative flux through the shock wave for this case was $264.5\ Watt/cm^2$. As can be seen in figures 5 and 6, the density and velocity were constant in the precursor. This verifies what was shown by Tiwari and Szema[7,2] and assumed by many other researchers.[8,9,10] Through the precursor region, there was a steady increase in the heavy particle temperature, pressure and total enthalpy of the gas due to absorption of radiative energy by the gas; however, for this case the changes in the heavy particle temperature and total enthalpy were very small. The increase in these properties was less than one percent through the precursor; the pressure, on the other hand, increased by greater than five percent.

The variation in the electron/electronic temperature as seen in figure 2 was not the steady increase exhibited by the other properties. The high electron/electronic temperature far ahead of the shock wave was a result of the fact that the electrons due to photoionization far from the shock were created by the absorption of high energy photons. However, as shown in figure 11,

in this region there were very few electrons present. The electron temperature increased slightly to a peak value of *4620 K* approximately *140* shock standoff distances ahead of the shock and then decreased to a value of *3350 K* immediately ahead of the shock. This decrease in the electron temperature in the region from 126 shock standoff distances ahead of the shock to the shock wave was due to the production of "low" energy electrons in this region. These electrons resulted from the absorption of photons much closer to the ionization threshold than those absorbed further from the shock. Since the electron temperature is a measure of the average energy of the electrons, the introduction of these "low" energy electrons resulted in a decrease in the average electron energy.

By comparison of the relative magnitudes of the species mass fractions in the precursor, it can be seen that the dominate photoprocess in the precursor was photoionization of the nitrogen molecule. The presence of the electrons produced through this process at the elevated electron temperature discussed above was expected to have the greatest effect on the gas behind the shock wave.

The frequency variation of the radiative flux through the shock front for this case is shown in figure 12. As can be seen in this figure, the radiation passing through the shock was primarily in the infra-red and ultra-violet frequency ranges. The majority of the infra-red radiation was due to emission by the body; although, a small portion of this was due to the 1st and 2nd positive molecular bands of the nitrogen molecule, the 1st negative band of the ionized nitrogen molecule and the atomic lines of the nitrogen atom. The cool gas in the precursor was essentially transparent to this infra-red radiation; the radiative energy absorbed in the precursor region was primarily in the ultra-violet frequency range. This radiation was due primarily to

the Birge-Hopfield molecular band of the nitrogen molecule and the ionization continuum of atomic nitrogen.

Figures 13 to 21 show the variation of the heavy particle and electron temperatures, pressure, density and mass fractions for each species through the shock layer both including and neglecting the effect of the precursor on the conditions directly in front of the shock. From these figures, it can be seen that the precursor had negligible effect on the shock layer in this case. The primary effect of the precursor was to change the conditions of the gas immediately after passing through the shock wave. As can be seen in the figures there was a slight change in the electron temperature; likewise, the mass fractions for the electrons, atomic and ionic species were nonzero immediately behind the shock due to the precursor. These changes, however, had negligible influence on the rest of the flow field. It should also be mentioned that there was no perceptible change in the radiative flux through the shock or to the wall due to the precursor for this case.

In addition to the case presented herein, a series of parametric studies will be conducted over a velocity range of 12 to 16 Km/sec and at altitudes ranging from 70 to 80 Km. This range of conditions should provide an idea of the precursor effects for a broad range of aerocapture trajectories.

CONCLUSIONS

Although this precursor model does neglect the effects of collisional chemistry and the absorption of radiation through the atomic lines, it is believed to be one of the more detailed models applicable to aerocapture type flow fields. In this analysis, no assumptions are made

regarding any of the flow field properties in the precursor, as is done in much of the previous work on precursors. The effects of both chemical and thermal nonequilibrium are included in this method, and a detailed spectral analysis is used in the calculation of the emission and absorption of the radiation. This analysis also involves a nitrogen gas in order to model the earths atmosphere; the majority of the previous work involving monatomic gases.

Although this study dealt with the radiative effects in the precursor region, the terms developed in this study for mass production rates due to radiative reactions are also applicable in the shock layer. Likewise, the analysis in this study of the radiative effects on each energy mode of the gas is applicable in the shock layer.

REFERENCES

1. Lasher, L.E. and Wilson, K.H., "Effects of Shock Precursor Heating on Radiative Flux to Blunt Bodies", Lockheed Missiles and Space Co., Palo Alto, CA, NASA-CR-1265, 1969.

2. Tiwari, S.N. and Szema, K.Y., "Effects of Precursor Heating on Chemical and Radiative Nonequilibrium Viscous Flow around a Jovian Entry Body", AIAA Paper 78-907, May 1978.

3. Nelson, H.F. and Goulard, R., "Structure of Shock Waves with Nonequilibrium Radiation and Ionization", Physics of Fluids, Vol. 12, August 1969.

4. Horton, T.E., "Radiative Coupled Nonequilibrium Flow Fields Associated with Aeroassisted Orbital Transfer", Final Contractors Report for NASA Grant NAG-1-496, March 1986.

5. Thompson, R.A., "Comparison of Nonequilibrium Viscous Shock Layer Solutions with Windward Surface Shuttle Heating Data", AIAA Paper 87-1473, June 1987.

6. Carlson, L.A. and Gally, T.A., "The Effect of Electron Temperature and Impact Ionization on Martian Return AOTV Flowfields", AIAA Paper 89-1729, June 1989.

7. Tiwari, S.N. and Szema, K.Y., "Radiation Induced Precursor Flow Field Ahead of a Jovian Entry Body", AIAA Paper 77-768, June 1977.

8. Ferrari, C. and Clarke, J.H., "On Photoionization Ahead of a Strong Shock Wave", Supersonic Flow, Chemical Processes and Radiative Transfer, Pergamon Press, New York, 1964.

9. Murty, S.S.R., "Effect of Line Radiation on Precursor Ionization", Journ. Quant. Spect. Rad. Transf., Vol. 8, 1968.

10. Nelson, H.F., "Nonequilibrium Structure of Argon Shock Waves", Phys. of Fluids, Vol 16 No. 12, December 1973.

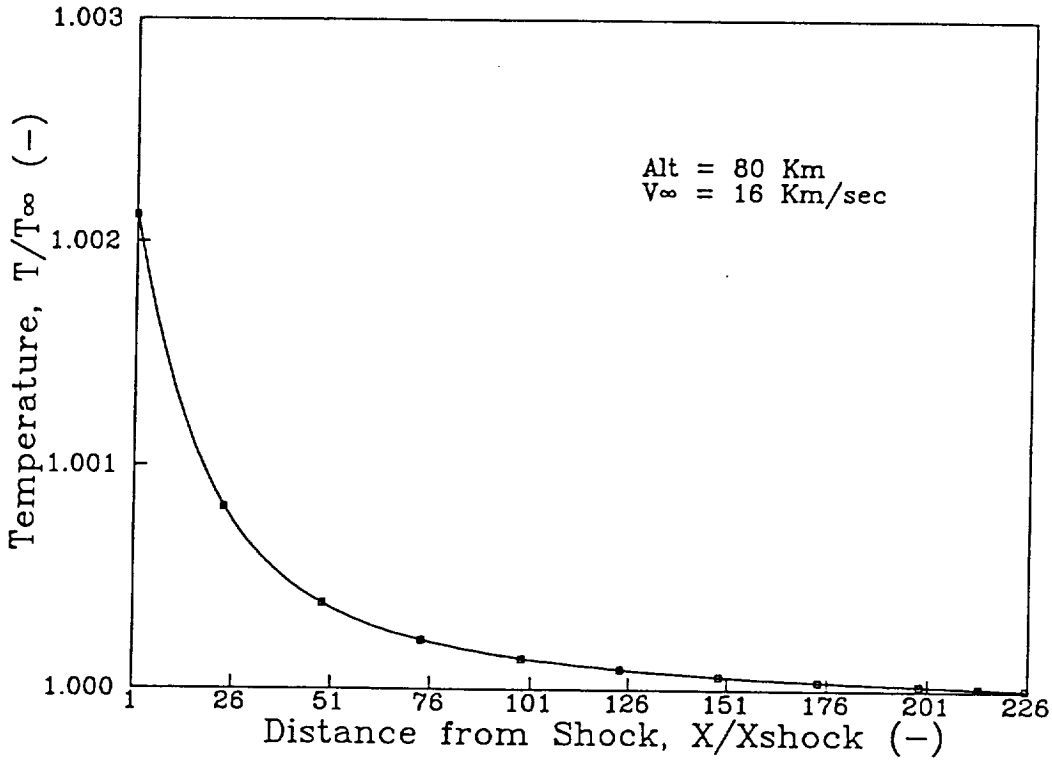

Figure 1: Heavy Particle Temperature in the Precursor Region;
V_∞ = *16 Km/sec, Alt = 80 Km*

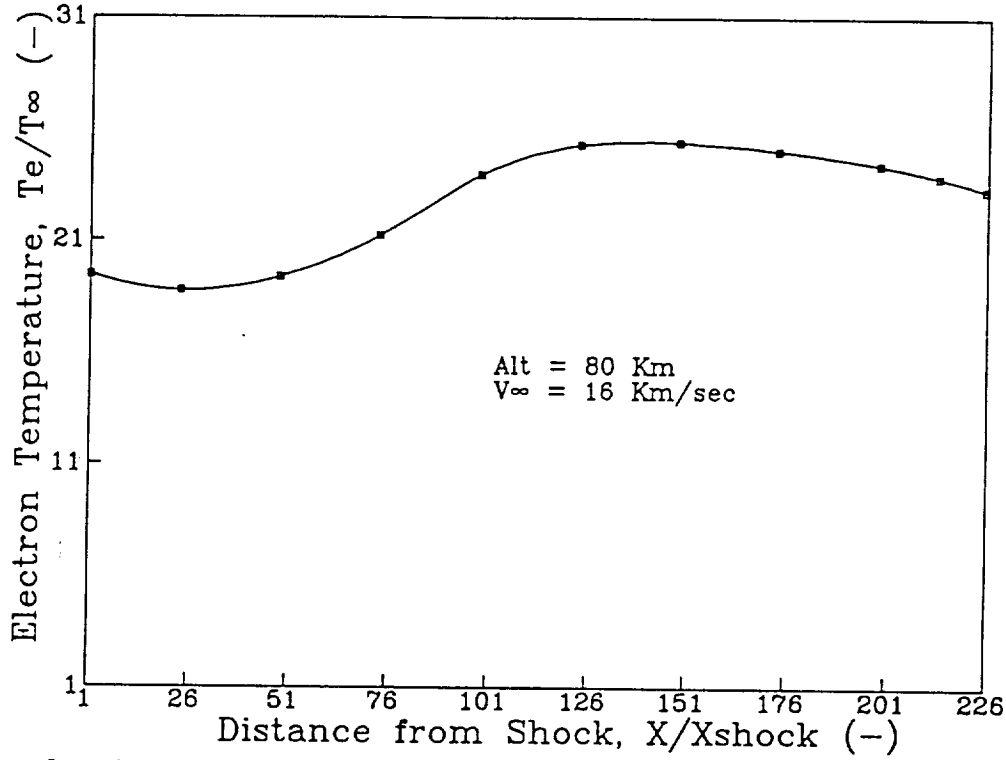

Figure 2: Electron Temperature in the Precursor Region;
V_∞ = *16 Km/sec, Alt = 80 Km*

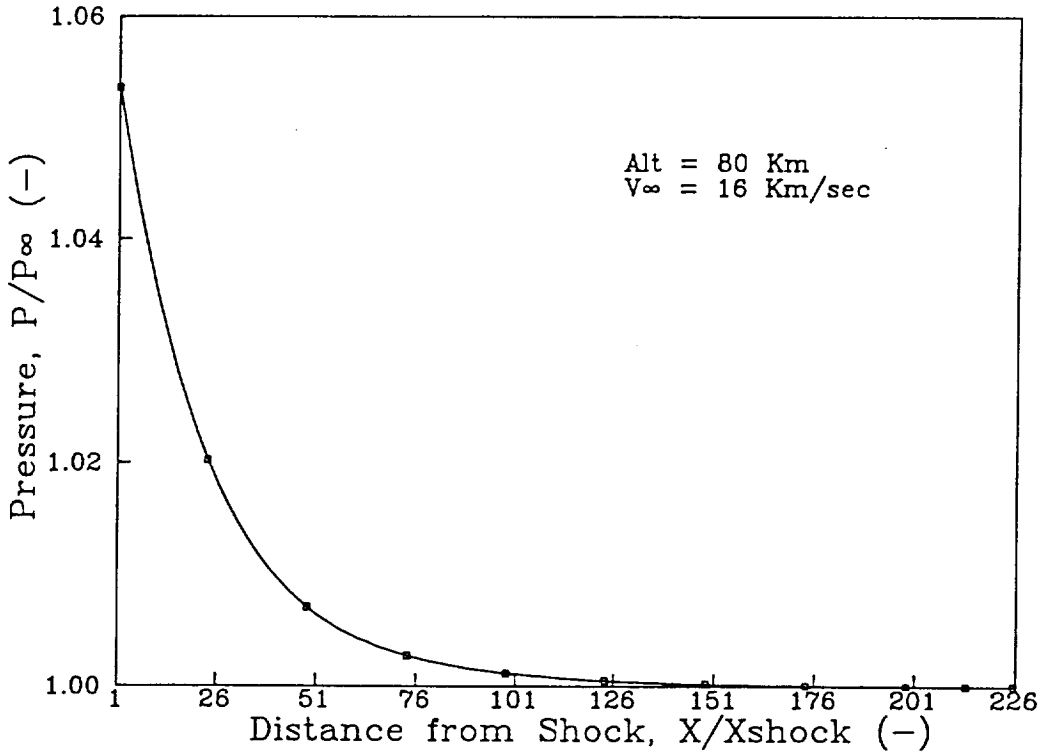

Figure 3: Pressure in the Precursor Region;
V_∞ = 16 Km/sec, Alt = 80 Km

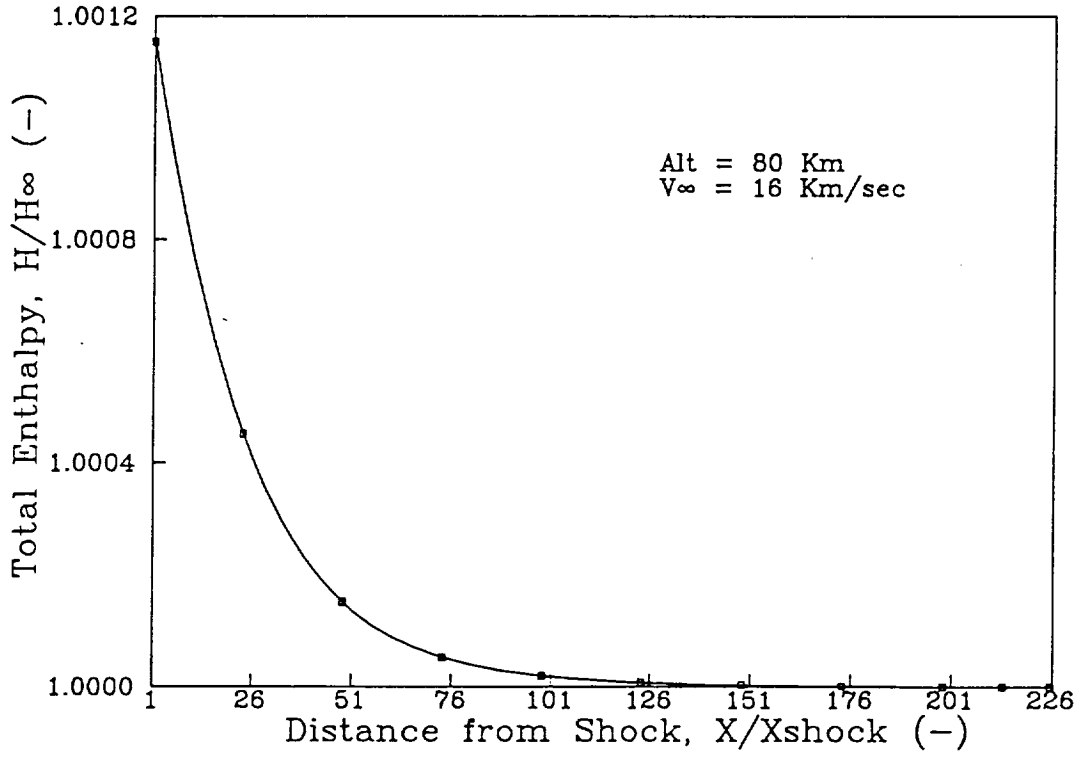

Figure 4: Total Enthalpy in the Precursor Region;
V_∞ = 16 Km/sec, Alt = 80 Km

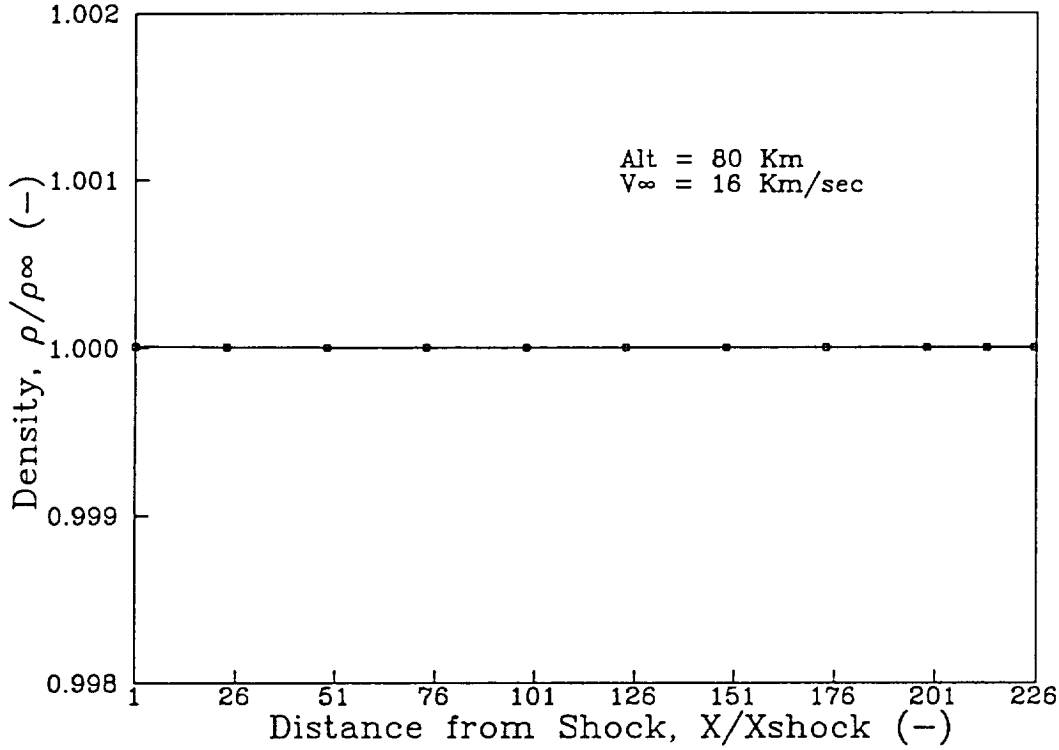

Figure 5: Density in the Precursor Region;
V_∞ = 16 Km/sec, Alt = 80 Km

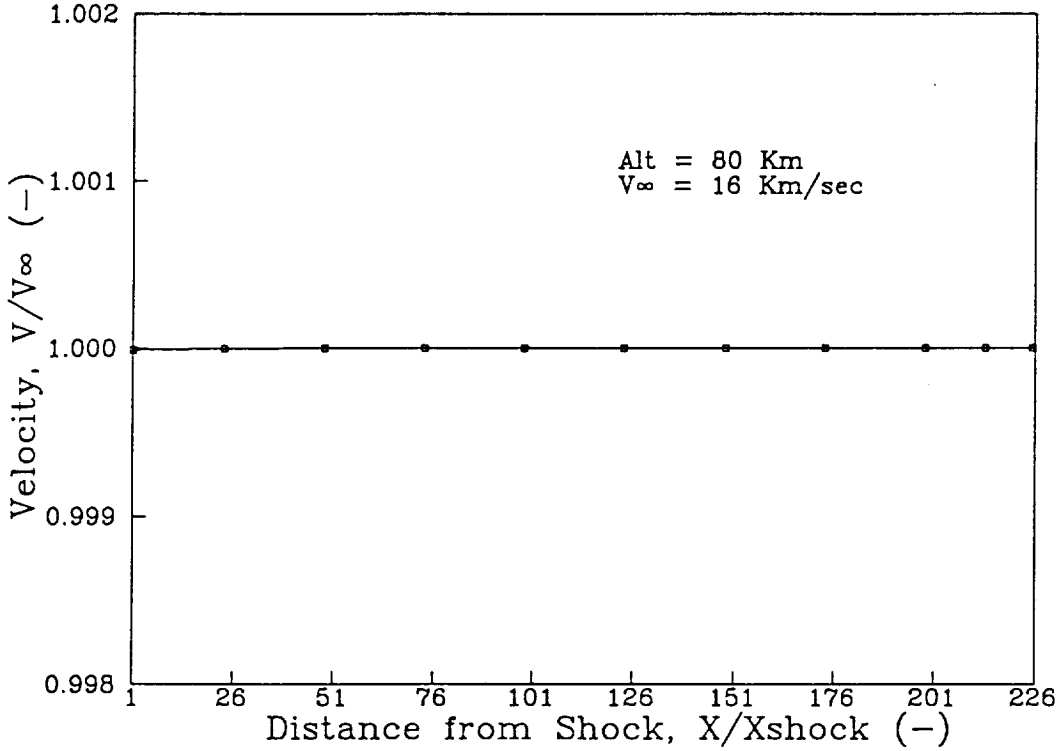

Figure 6: Velocity in the Precursor Region;
V_∞ = 16 Km/sec, Alt = 80 Km

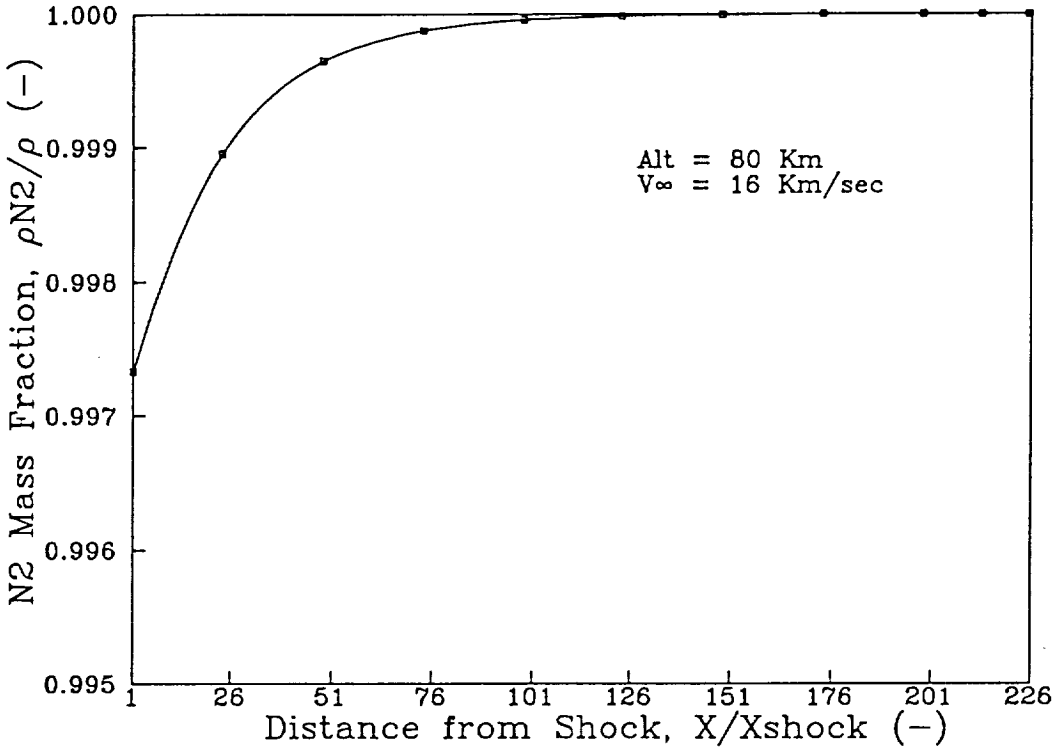

Figure 7: N_2 Mass Fraction in the Precursor Region;
V_∞ = 16 Km/sec, Alt = 80 Km

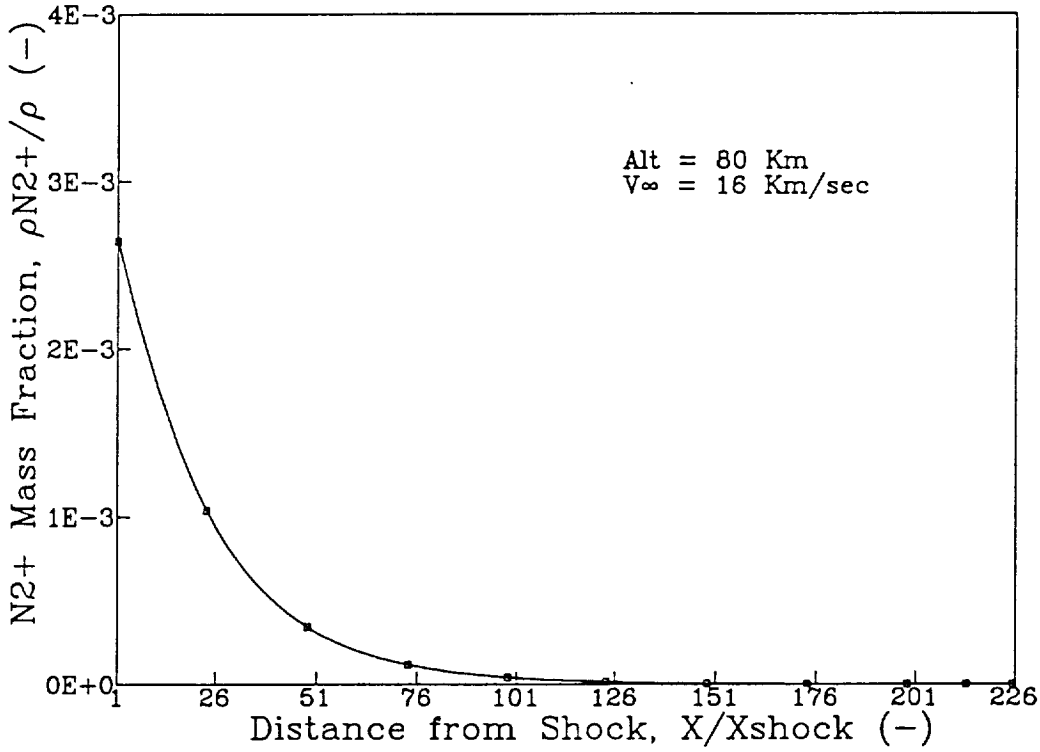

Figure 8: N_2^+ Mass Fraction in the Precursor Region;
V_∞ = 16 Km/sec, Alt = 80 Km

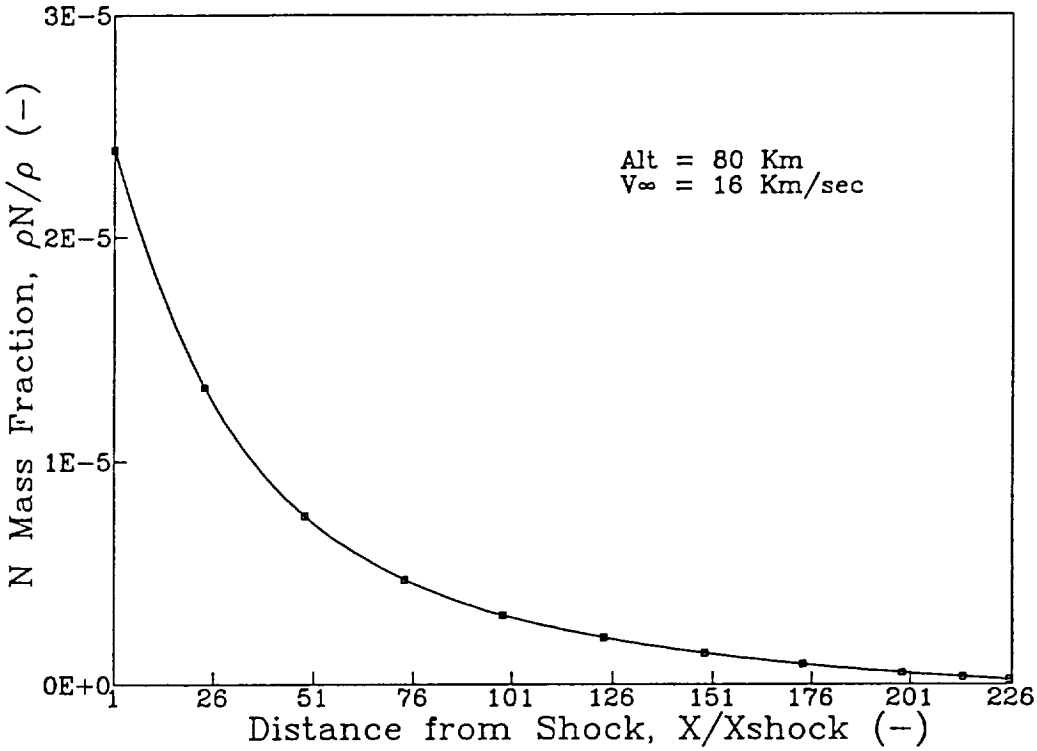

Figure 9: N Mass Fraction in the Precursor Region;
V_∞ = 16 Km/sec, Alt = 80 Km

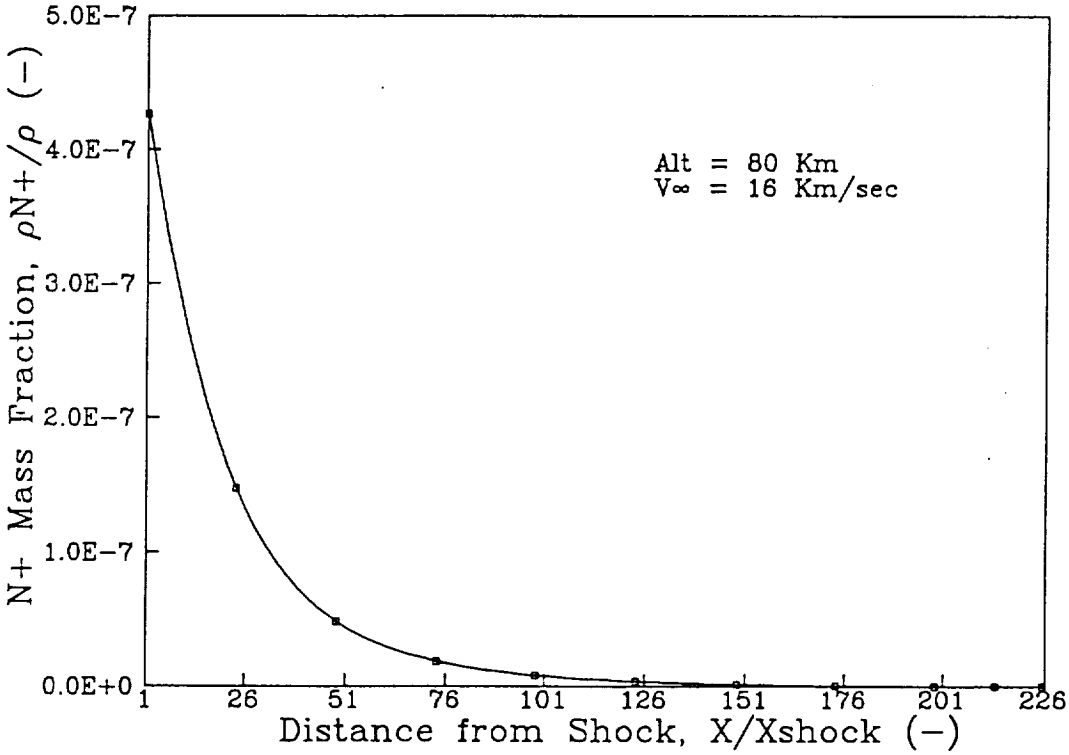

Figure 10: N^+ Mass Fraction in the Precursor Region;
V_∞ = 16 Km/sec, Alt = 80 Km

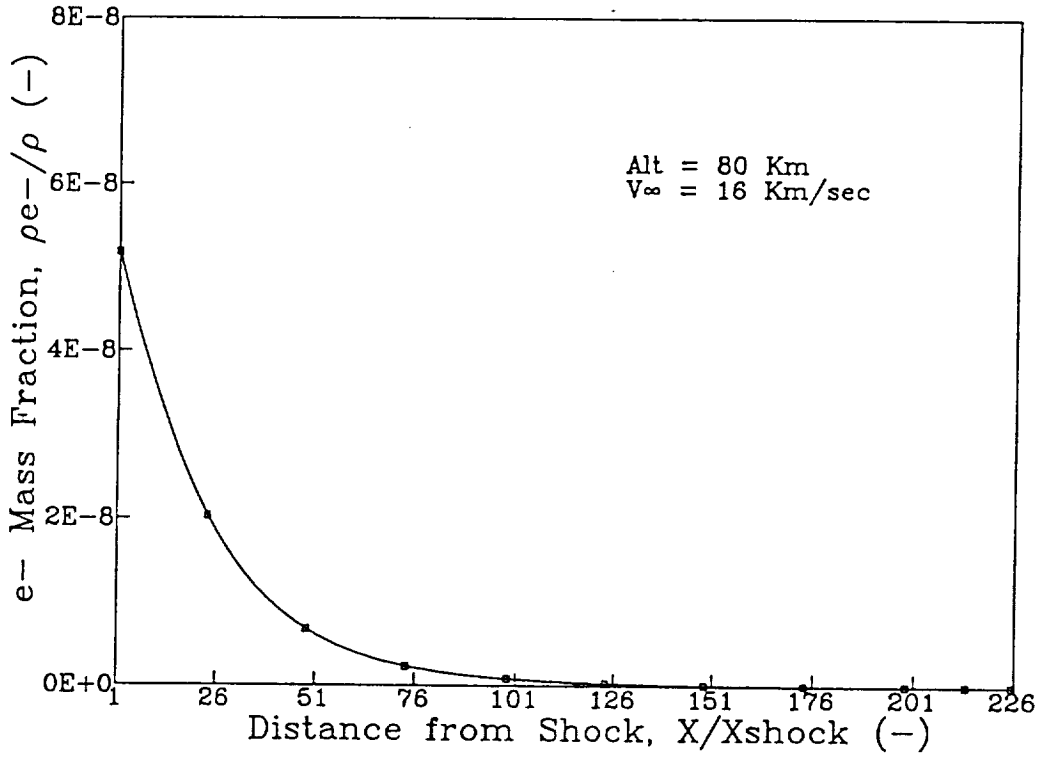

Figure 11: e^- Mass Fraction in the Precursor Region;
V_∞ = 16 Km/sec, Alt = 80 Km

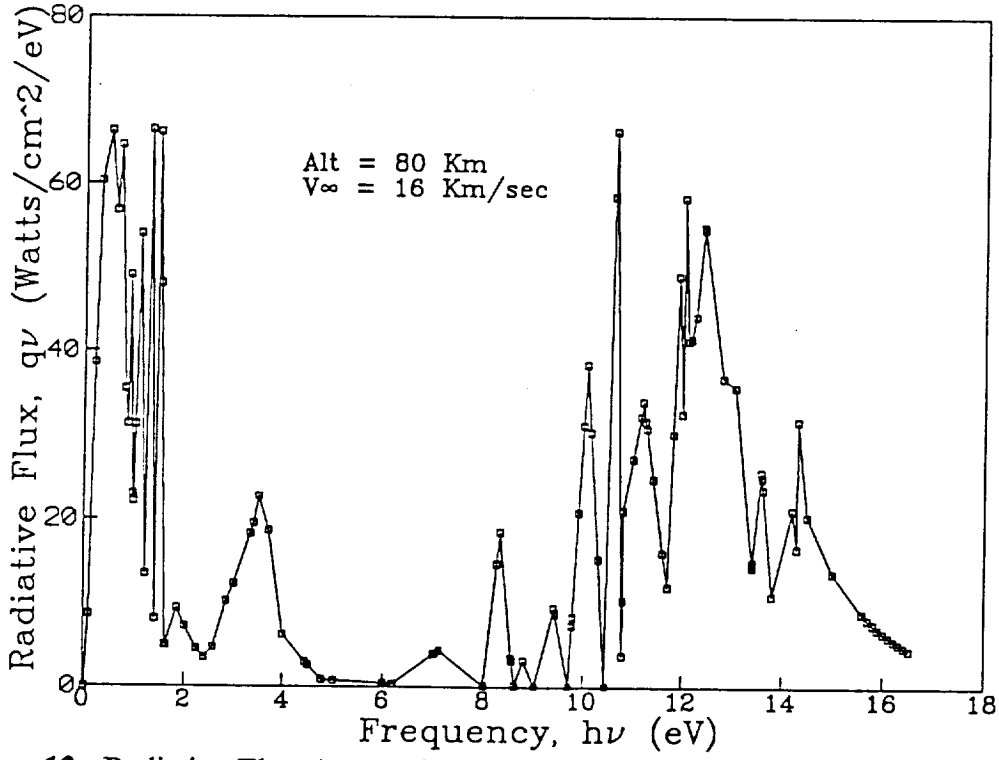

Figure 12: Radiative Flux Across the Shock Front;
V_∞ = 16 Km/sec, Alt = 80 Km

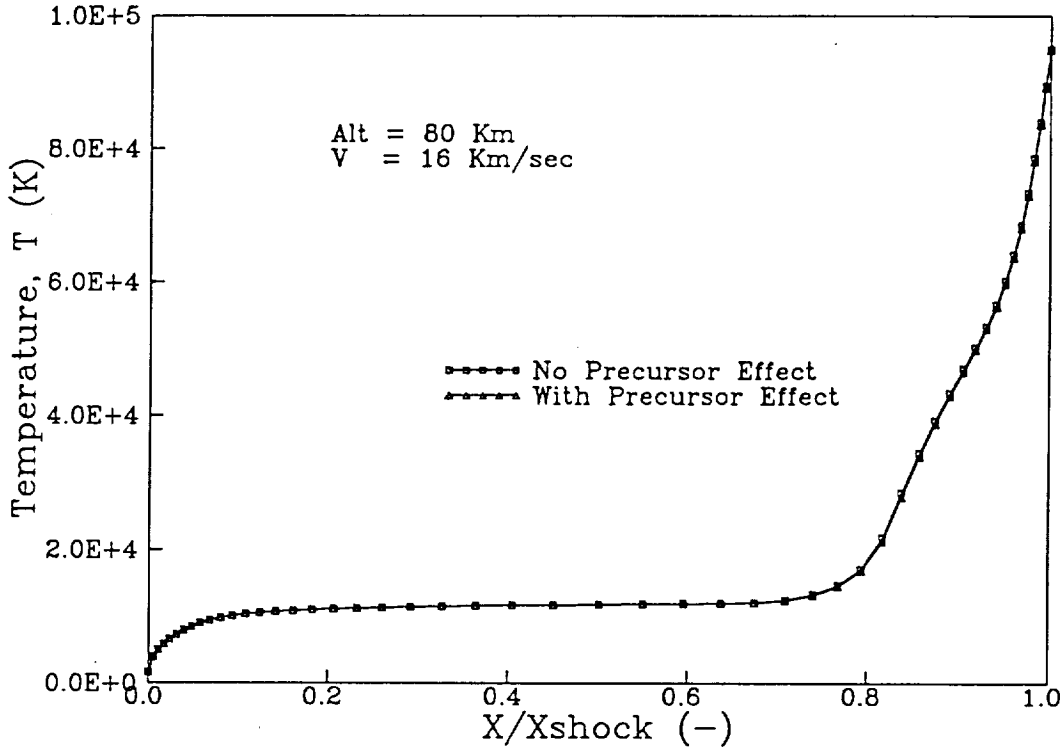

Figure 13: Heavy Particle Temperature in the Shock Layer;
V_∞ = 16 Km/sec, Alt = 80 Km

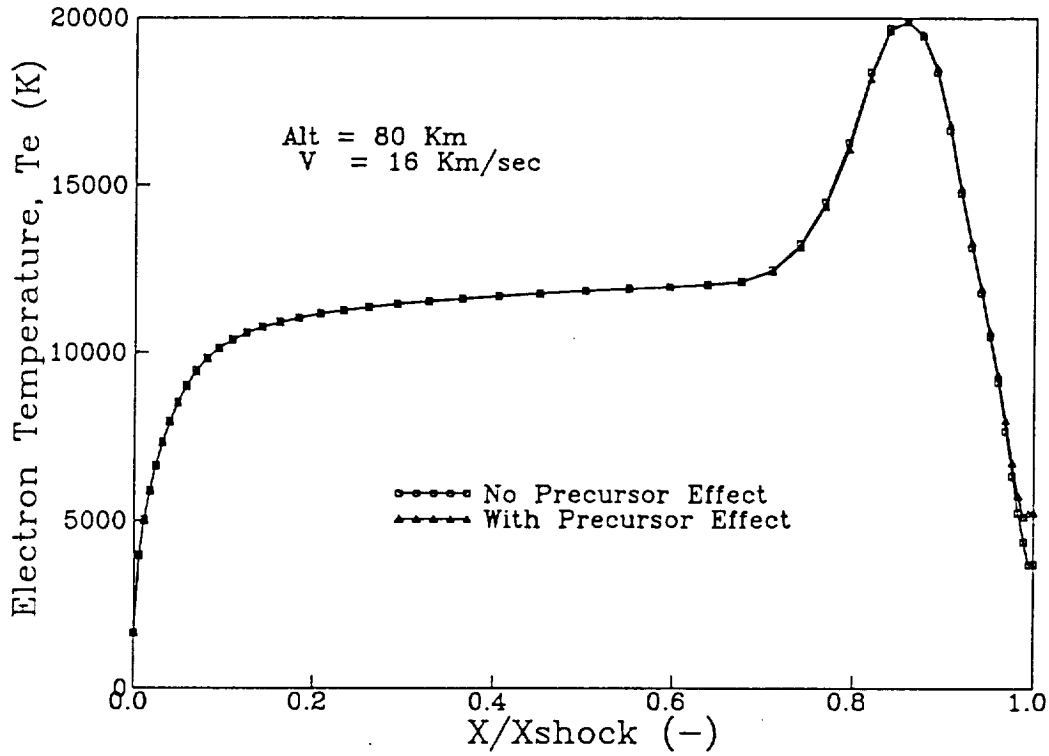

Figure 14: Electron Temperature in the Shock Layer;
V_∞ = 16 Km/sec, Alt = 80 Km

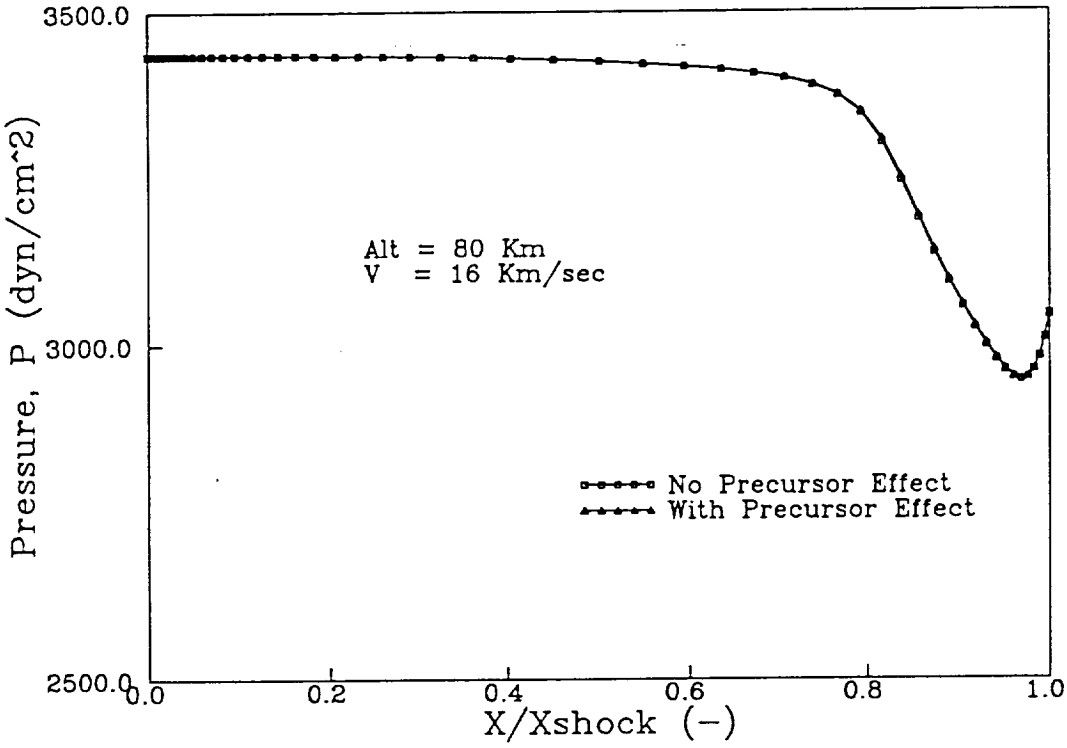

Figure 15: Pressure in the Shock Layer;
V_∞ = 16 Km/sec, Alt = 80 Km

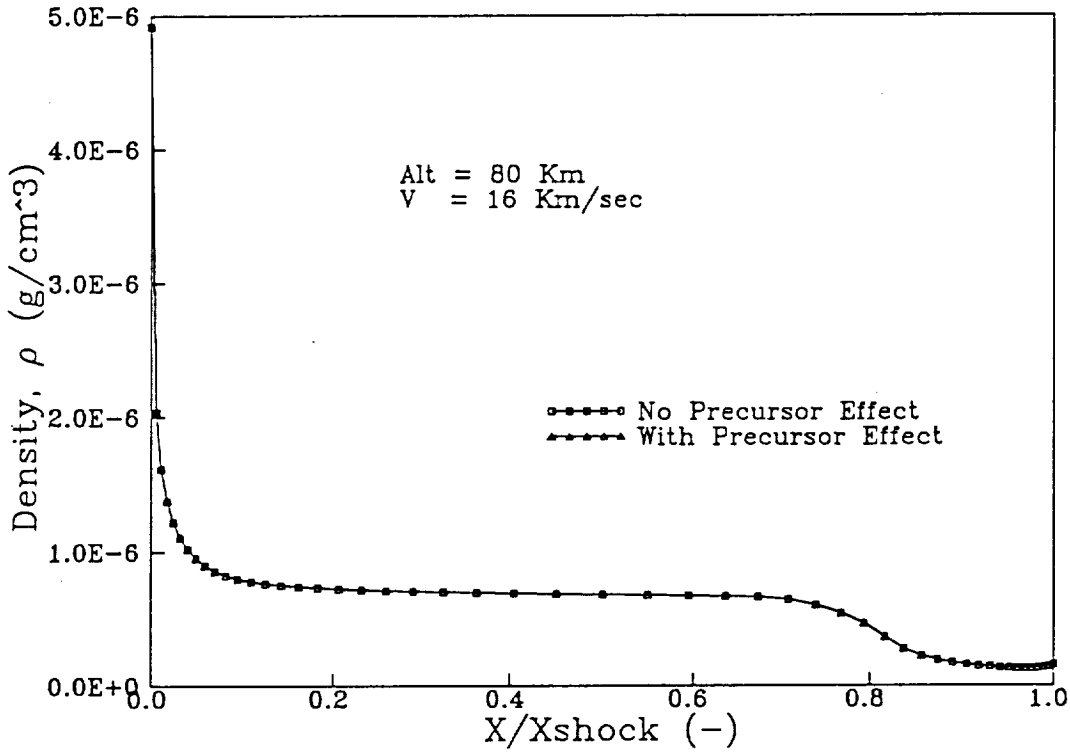

Figure 16: Density in the Shock Layer;
V_∞ = 16 Km/sec, Alt = 80 Km

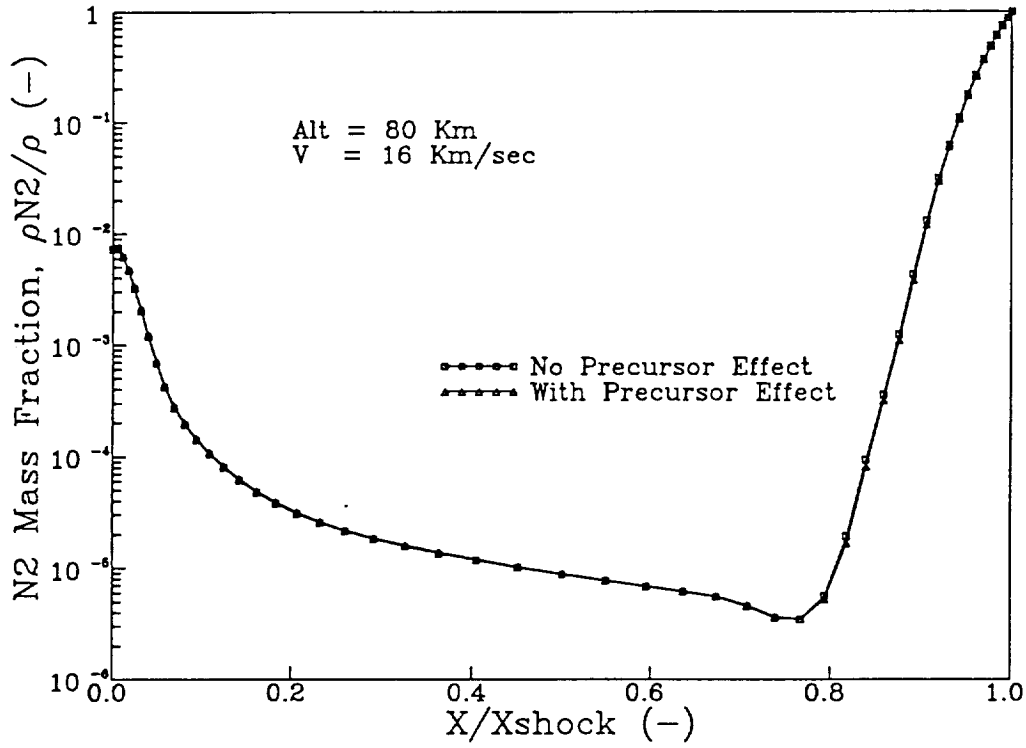

Figure 17: N_2 Mass Fraction in the Shock Layer;
V_∞ = *16 Km/sec, Alt = 80 Km*

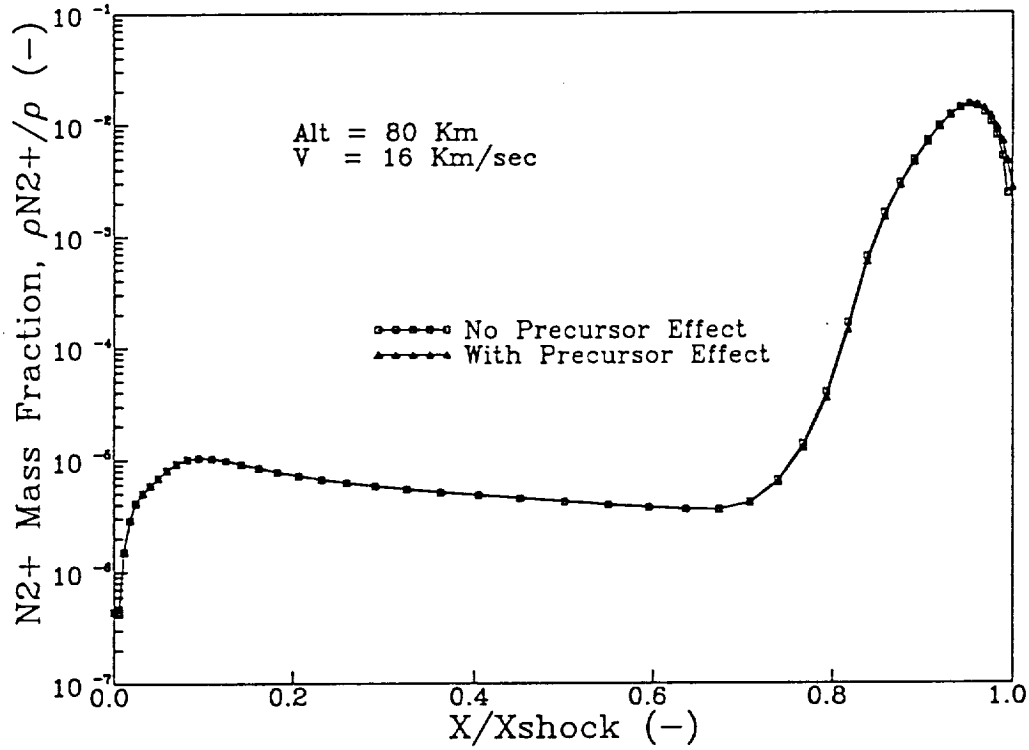

Figure 18: N_2^+ Mass Fraction in the Shock Layer;
V_∞ = *16 Km/sec, Alt = 80 Km*

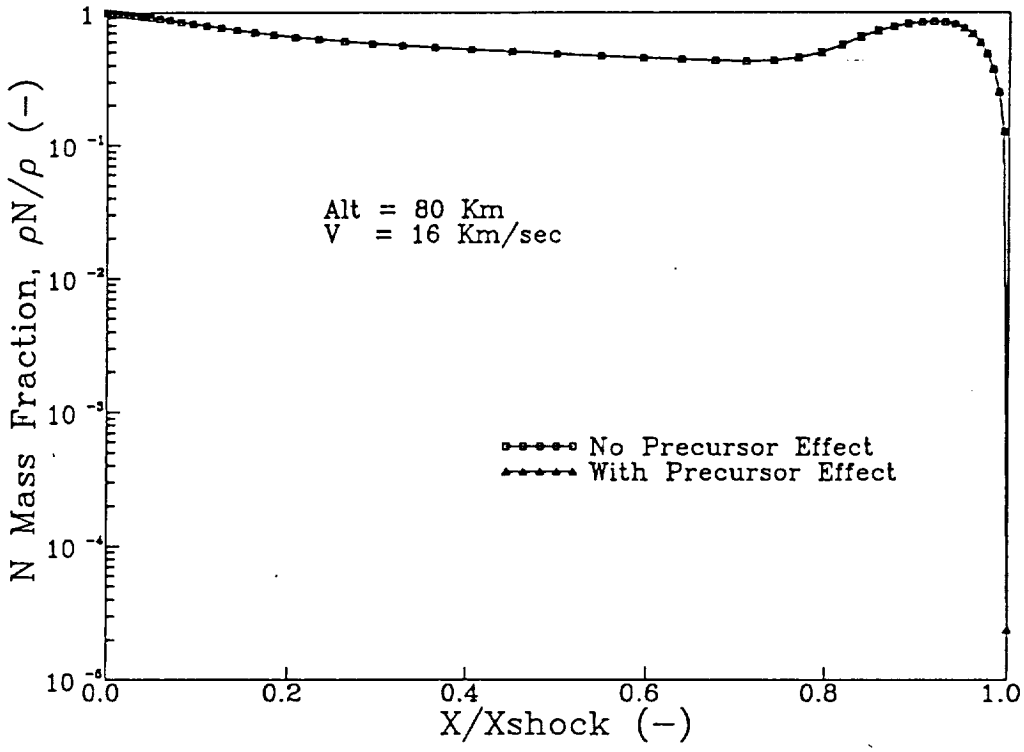

Figure 19: N Mass Fraction in the Shock Layer;
V_∞ = *16 Km/sec, Alt = 80 Km*

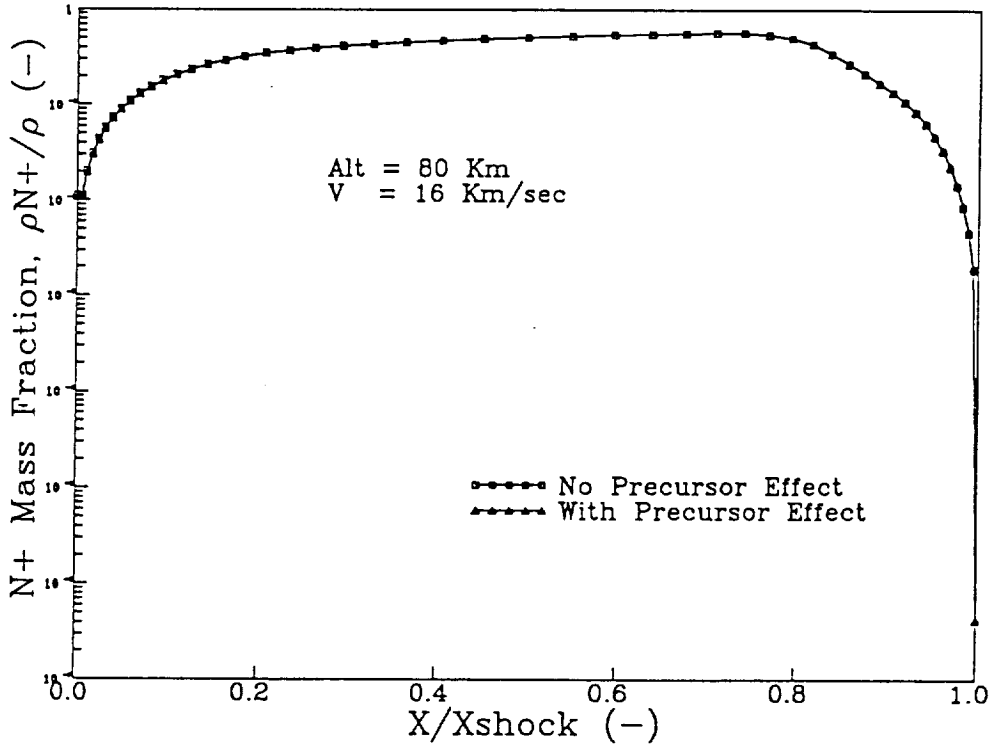

Figure 20: N^+ Mass Fraction in the Shock Layer;
V_∞ = *16 Km/sec, Alt = 80 Km*

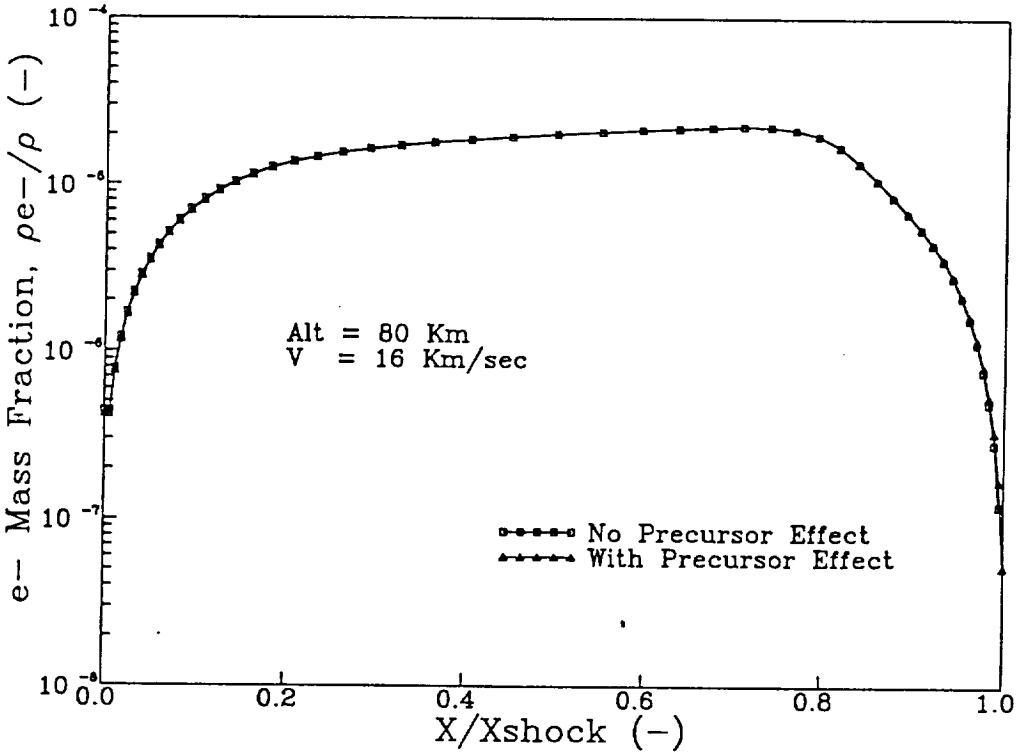

Figure 21: e^- Mass Fraction in the Shock Layer;
V_∞ = 16 Km/sec, Alt = 80 Km